Numerical simulation of lubricated wire rolling and drawing

Škurić, Vanja

University of Zagreb

Faculty of Mechanical Engineering and Naval Architecture

Vanja Škurić

Numerical Simulation of Lubricated Wire Rolling and Drawing

DOCTORAL THESIS

Zagreb, 2019.

University of Zagreb

Faculty of Mechanical Engineering and Naval Architecture

Vanja Škurić

Numerical Simulation of Lubricated Wire Rolling and Drawing

DOCTORAL THESIS

Supervisor: prof. Hrvoje Jasak, PhD

Zagreb, 2019.

Sveučilište u Zagrebu

Fakultet strojarstva i brodogradnje

Vanja Škurić

Numerička simulacija valjanja i vučenja žice uz podmazivanje

DOKTORSKI RAD

Mentor: prof. dr. sc. Hrvoje Jasak

Zagreb, 2019.

Acknowledgements

I would like to express my gratitude to my supervisor, Prof. Hrvoje Jasak, for his continuous interest and support during this study, and for motivating me to finish it. I am also grateful to Prof. Željko Tuković for his help and guidance, especially at the beginning of this study.

Abstract

A numerical framework for simulation of lubricated contact between two rough surfaces in metal forming simulations is presented in this work. The framework is implemented as a contact condition for the hyperelastoplastic finite volume deformation solver within the `foam-extend` software package, a community driven fork of the open source OpenFOAM software.

The main features of the model are: calculation of film thickness, hydrodynamic pressure and shear stress of the lubricant, estimation of asperity contact pressure and contact area ratio for a realistic rough surface, solution of the heat transfer problem considering the liquid film shear stress and asperity contact, and calculation of pressure– and temperature–dependent transport properties of the lubricant. The lubricant pressure is calculated by solving the Reynolds equation, using the Finite Area Method of discretisation. A mass–conserving cavitation algorithm is implemented for the liquid lubricant in the finite area formulation. Contact between the asperities is calculated with a deterministic elastic–perfectly plastic contact model using a measured surface roughness profile or a three–dimensional surface scan as an input. Temperature increase of the lubricant is calculated using a two–dimensional thin film energy equation, discretised with the Finite Area Method.

Each model is verified and validated against available analytical, other numerical or experimental results. Very good agreement is achieved between the calculated values and results from the literature. In order to assess the accuracy of the complete numerical framework, extensive verification and validation is performed on point contact test cases, where film thickness and friction coefficients are compared to experimental results of ball–on–disc tribometer tests. The study shows that acceptable accuracy can be achieved using the implemented numerical framework, provided that complete information regarding lubricant transport properties is available and surface roughness has been measured.

Finally, the numerical framework is tested on industrial–grade wire drawing and wire rolling simulations. The framework is capable of calculating hydrody-

namic pressure, film thickness, asperity contact pressure, contact area ratio, and other fields useful for designing a metal forming process. The increase of computational time when using the lubricated contact model is around 40%, compared to the non–lubricated penalty contact model. The increase is acceptable considering the complexity of the implemented model. Stability of the lubricated contact model is shown to be similar to the stability of the penalty contact.

Prošireni sažetak

Ovaj rad predstavlja numerički model za izračun podmazanog kontakta između hrapavih površina prilikom provedbe numeričke simulacije obrade metala deformiranjem.

I   Uvod

Donedavno je projektiranje procesa obrade metala deformiranjem bilo isključivo temeljeno na skupim i zahtjevnim eksperimentalnim metodama izvođenim na stvarnim objektima. S napretkom računala, numeričko modeliranje procesa obrade metala polako postaje upotrebljivi konstruktorski alat koji potencijalno može zamijeniti barem dio eksperimentalnih ispitivanja.

Trenje je važan čimbenik prilikom samog procesa obrade metala deformiranjem, međutim neoptimalne vrijednosti sile trenja dovode do smanjenja učinkovitosti procesa i pada kvalitete konačnog proizvoda. Jedan od načina za postizanje odgovarajućih uvjeta trenja je dodavanje maziva određenih svojstava u zonu kontakta između proizvodnog alata (npr. valjak, matrica) i obratka (npr. žica). Postojeći računalni paketi koji omogućuje provođenje simulacija procesa obrade metala deformiranjem koriste napredne modele deformacije materijala i detekcije kontakta, ali često koriste relativno jednostavne formulacije kojima opisuju koeficijente trenja (npr. Coulombov ili Trescin zakon), koje ne pružaju rezultate zadovoljavajuće točnosti, pogotovo u slučaju modeliranja podmazanog kontakta.

Numerička analiza postupka obrade metala deformiranjem uz podmazivanje je izrazito zahtjevna budući da podrazumijeva rješavanje spregnutog sustava jednadžbi deformacije čvrstog tijela i strujanja maziva u području kontakta. Ovakav sustav je izrazito nelinearan zbog velikih deformacija tijela, očvršćivanja materijala, kompliciranosti geometrija, nepoznatih lokacija kontakta, itd. Podmazani kontakt između površina u relativnom gibanju može se podijeliti u tri režima: hidrodinamički, mješoviti i granični režim podmazivanja. U graničnom režimu podmazivanja površinska hrapavost nosi gotovo cijeli kontaktni tlak, te

se taj režim uobičajeno modelira pomoću poluempirijskih izraza. Kod hidro-
dinamičkog režima mazivo podnosi cjelokupno kotaktno opterećenje, te nema
kontakta između hrapavosti dviju površina. Ovaj režim se uobičajeno modelira
pomoću Reynoldsove jednadžbe. Kod mješovitog režima podmazivanja kontakt-
no opterećenje se dijeli između maziva i hrapavosti u kontaktu, te se taj režim
može modelirati sprezanjem Reynoldsove jednadžbe i modela čvrstog kontakta.

Cilj ovoga rada je razvoj i implementacija numeričkog modela za simulaciju
podmazanog kontakta prilikom simulacije obrade metala deformiranjem koji obu-
hvaća sve režime podmazivanja. Model je implementiran u obliku rubnog uvjeta
kontakta koji se koristi prilikom provedbe algoritma za izračun deformacije čvrstog
tijela, implementiranog unutar softverskog paketa OpenFOAM u okviru metode
kontrolnih volumena i kontrolnih površina.

II Numerički modeli i implementacija

Hidrodinamički tlak maziva računa se rješavanjem Reynoldsove jednadžbe, koja
se diskretizira metodom kontrolnih površina. Metoda kontrolnih površina je
dvodimenzionalni pandan metodi kontrolnih volumena gdje se prostorna diskreti-
zacija vrši preko zakrivljenih površina. Reynoldsova jednadžba je diskretizirana
u obliku u kojem je očuvana konzervativnost mase prilikom kavitacije, po uzoru
na algoritam Elroda i Adamsa. Reynoldsova jednažba se rješava za varijablu gu-
stoće, a iz vrijednosti gustoće se računa hidrodinamički tlak pomoću analitičkih
jednadžbi koje opisuju odnose tlaka, gustoće i temperature.

Kontakt između površinskih hrapavosti računa se pomoću determinističkog
modela elastično–idealno plastičnog kontakta. Izmjereni profil ili trodimenzio-
nalna površinska snimka hrapavosti su ulazni podaci za model, na temelju kojih
se računaju kontaktni tlakovi, kontaktne površine i debljine mazivnog sloja za
unaprijed određeni raspon nominalnih udaljenosti između dvije površine. Izraču-
nate vrijednosti se pohranjuju u obliku tablica, iz kojih se vrijednosti interpoliraju
prilikom same provedbe simulacija, čime se smanjuje proračunsko vrijeme.

Prirast temperature maziva se računa pomoću dvodimenzionalne energetske
jednadžbe za tanki film, koja se diskretizira pomoću metode kotrolnih površina te
podrazumijeva parabolični temperaturni profil po debljini filma. Svojstva maziva

se računaju pomoću izraza koji ovise o njegovoj vrsti, tj. za određeni tip maziva dani su izrazi i vrijednosti koje ta svojstva opisuju. Na temelju poznatih vrijednosti tlaka i temperature mogu se računati: viskoznost, specifični toplinski kapacitet, koeficijent prijenosa topline, tlak kavitacije, itd.

III   Validacija i verifikacija

Detaljna validacija i verifikacija je provedena za svaki implementirani model. Prvo je validirana i verificirana implementacija Reynoldsove jednadžbe i modela kavitacije. Prva tri testna slučaja su jednodimenzionalni modeli kliznog ležaja različitih konfiguracija. Rezultati su uspoređeni s analitičkim i drugim numeričkim rješenjima iz literature, te je postignuto njihovo izvrsno poklapanje. Verifikacija je provedena pomoću analize konvergencije proračunske mreže, gdje je pokazano da s povećanjem gustoće mreže rješenja konvergiraju prema vrijednostima iz literature. Utvrđeno je da slučajevi koji imaju oštre promjene debljine mazivnog filma te u kojima dolazi do kondenzacije kavitacijske smjese, zahtijevaju gušće mreže kako bi postigli istu razinu točnosti kao i slučajevi kod kojih tih pojava nema. Sljedeća dva testna slučaja su dvodimenzionalne geometrije, od kojih je prvi klizni ležaj s džepom, a drugi je brtveni ležaj sa sitnim ulegnućima. U oba slučaja poklapanja s rezultatima iz literature su izvrsna.

Deterministički model elasto–idealno plastičnog kontakta je validiran pomoću testnog slučaja kontakta između valovite površine izrađene od silikonske gume i krutog ravnog bloka. Izračunate vrijednosti površine u elastičnom kontaktu su uspoređene s eksperimentalnim mjerenjima i vrijednostima drugih numeričkih simulacija iz literature. Srednje odstupanje rezultata od eksperimentalnih mjerenja iznosi 4,27%, a od numeričkih rješenja 0,22%. Kontaktne površine u slučaju elasto–idealno plastičnog kontakta su uspoređene s rezultatima trodimenzionalne simulacije provedene pomoću algoritma za proračun deformacije čvrstog tijela, te je poklapanje i u tom slučaju vrlo dobro, s relativnim odstupanjem od 3,98%. Rezultati tri implementirana statistička modela kontakta su uspoređeni s determinističkim modelom pomoću tri primjera hrapavih površina. Rezultati značajno odstupaju od determinističkog modela, poglavito kod većih kontaktnih površina. Statistički modeli kontakta općenito daju značajno niže vrijednosti kontaktne

površine za određeni tlak, u odnosu na deterministički model, te nisu u mogućnosti točno predvidjeti tlak pri kojem dolazi do potpunog kontakta. Na temelju dobivenih rezultata zaključeno je da bi deterministički model trebalo koristiti kada god je to moguće, a statistički model, ako je nužno, kod isključivo malih kontaktnih površina.

Na kraju je provedena zbirna validacija modela koristeći testne slučajeve točkastog kontakta. Točkasti kontakt u provedenim simulacijama predstavlja kontakt između kuglice i diska koji rotiraju, a zapravo su osnovni dijelovi tribometra, uređaja za mjerenje trenja. Provedene su dvije skupine simulacija. U prvoj skupini analiziran je isključivo hidrodinamički režim podmazivanja, te je kao mazivo korišteno ulje Turbo T9. Gotovo sva svojstva ovoga ulja, te njihove ovisnosti o temperaturi i tlaku, su navedeni u literaturi. Debljina filma je mjerena za dvije vrijednosti opterećenja, 23 i 95 N, te za širok raspon brzina rotacije. Za opterećenje od 23 N relativno odstupanje izračunate minimalne debljine filma iznosi 2,3%, a centralne debljine 3%, u odnosu na eksperimentalna mjerenja. Za opterećenje od 95 N, odstupanje minimalne debljine iznosi 13,6%, a cetralne 7,8%. Za opterećenja od 38 i 154 N, te za brzine od 0,8 i 2 m/s izračunati su koeficijenti trenja za raspon omjera klizanja kontaktnih površina od 0 do 1. Izračunati koeficijenti trenja su uspoređeni s vrijednostima numeričkih proračuna iz literature, te s eksperimentalnim mjerenjima. Za prvi testni slučaj (38 N i 0,8 m/s) relativna odstupanja izračunatih koeficijenata trenja su 0,8% od numeričkih rezultata i 7,4% od eskperimentalnih mjerenja, za drugi slučaj (38 N i 2 m/s) odstupanja su 5,9% i 11,2%, za treći slučaj (154 N i 0,8 m/s) su 1,8% i 5,7%, te za četvrti slučaj (154 N i 2 m/s) odstupanja iznose 3,1% i 5%. Općenito, dobivena su vrlo dobra poklapanja, i s eksperimentalnim mjerenjima i s numeričkim rezultatima iz literature.

U drugoj skupini simulacija točkastog kontakta analizirani su hidrodinamički i mješoviti režim podmazivanja, te je kao mazivo korišteno ulje Turbo T68. Za ovo ulje u literaturi nisu navedeni svi podaci koji opisuju njegova svojstva. Simulacije su provedene za tri različite longitudinalne hrapavosti kuglice, za dvije vrijednosti omjera klizanja kontaktnih površina, te za široki raspon brzina. Simulacije su provedene za slučaj izmjerenong profila hrapavosti i za slučaj pojednostavljenog profila hrapavosti u obliku sinus funkcije. Poklapanja izračunatih koeficijenata

trenja s eksperimentalnim mjerenjima su vrlo dobra za prvi i treći profil hrapavosti. Za drugi profil hrapavosti odstupanja su mala pri visokim brzinama gdje vlada hidrodinamički režim, ali izrazito velika kod nižih brzina gdje nastupa mješoviti režim podmazivanja. S obzirom na razultat moguće je da drugi profil hrapavosti ne odgovara stvarnoj hrapavosti za koju su mjerenja izvršena. S obzirom na nepotpune informacije vezane uz svojstva maziva, poklapanje rezultata i eksperimentalnih mjerenja je prihvatljivo.

Na temelju provedene validacije i verifikacije modela, može se zaključiti da implementirani numerički modeli daju dovoljno točne rezultate uz uvjet da su dostupne potpune informacije vezane uz svojstva maziva i hrapavosti površina.

IV Primjena modela na simulacije vučenja i valjanja žice

Numerički model podmazanog kontakta primjenjen je u sklopu simulacija vučenja i valjanja žice. Model je implementiran u obliku rubnog uvjeta kontakta koji se koristi prilikom provedbe algoritma za izračun deformacije čvrstog tijela. Implementacija je provedena u dva dijela, gdje se prvi dio izvršava prije početka, a drugi tijekom izvođenja simulacije. Prije početka simulacije, na temelju izmjerenog profila hrapavosti, računaju se kontaktni tlakovi hrapavosti, kontaktne površine i debljine mazivnog sloja za određeni raspon nominalnih udaljenosti između hrapavih površina. Izračunate vrijednosti su spremljene u obliku tablica. Tijekom izvođenja simulacije, model podmazanog kontakta se poziva prilikom svakog vrednovanja rubnih uvjeta. S obzirom na nominalne udaljenosti između površina u kontaktu, vrijednosti kontaktnog tlaka između hrapavosti, kontaktne površine i debljine mazivnog filma se interpoliraju iz spremljenih tablica. Nakon toga se računaju svojstva maziva, te se rješava Reynoldsova jednadžba. Izračunate normalne i tangencijalne površinske sile se šalju nazad u algoritam za izračun deformacije čvrstog tijela. Postupak se ponavlja do željene razine konvergencije.

Simulacije vučenja žice provedene su na dvije geometrije: aksisimetrična i jedna četvrtina pune geometrije. Ispitano je četrnaest brzina vučenja i pet postavki kontakta. Utvrđeno je da veće brzine vučenja i veće vrijednosti viskoznosti

povećavaju nosivost maziva, što rezultira smanjenjem sile trenja. Koristeći finije proračunske mreže pad tlaka u središtu kontakta se značajno smanjuje. Proračunsko vrijeme potrebno za provedbu simulacije poraste za 40%, u odnosu na proračunsko vrijeme kada se koristi postojeći model penaliziranja kontakta. S obzirom na kompleksnost modela podmazanog kontakta ovoliko povećanje proračunskog vremena je prihvatljivo. Stabilnost modela ispitana je usporedbom prosječnog broja korektora deformacije tijela između modela podmazanog kontakta i modela penaliziranja kontakta. Broj korektora je povećan, u prosjeku, za 10% prilikom korištenja modela podmazanog kontakta, što je prihvatljivo s obzirom na dodatne nelinearnosti unesene u sustav. Uspoređujući rezultate sile trenja između aksisimetričnih simulacija i simulacija jedne četvrtine geometrije, razlike su ispod 1%. Za provedbu simulacije jedne četvrtine geometrije potrebno je 15 puta više proračunskog vremena u odnosu na aksisimetričnu simulaciju.

Simulacije valjanja žice provedene su za dvije brzine vrtnje valjka (150 i 300 o/min) te za iste postavke kontakta kao i kod simulacija vučenja žice. Tri gustoće proračunske mreže su uspoređene. Visoki hidrodinamički tlakovi maziva su postignuti u blizini prednjeg vrha kontakta između valjka i žice, dok u unutrašnjosti kontakta nisu utvrđeni značajni porasti tlaka maziva. Polja hidrodinamičkog tlaka i kontaktnog tlaka hrapavosti imaju karakterističan oblik potkove. Lokalni koeficijenti trenja poprimaju niže vrijednosti u području visokog hidrodinamičkog tlaka, što je očekivano budući da na tim mjestima mazivo nosi dobar dio opterećenja. Srednje povećanje proračunskog vremena iznosi 33%, u odnosu na model penaliziranja kontakta. Broj korektora deformacije čvrstog tijela je niži 4%, u odnosu na model penaliziranja kontakta. Na temelju smanjenja broja korektora može se zaključiti da je model podmazanog kontakta u slučaju valjanja žice stabilniji od postojećeg modela penaliziranja kontakta.

V   Zaključak

Za numeričku analizu podmazanog kontakta između hrapavih površina potrebno je ostvariti spregu između modela strujanja maziva, modela kontakta hrapavosti, modela prijenosa topline i modela koji opisuju svojstva maziva.

Na temelju provedene validacije i verifikacije modela podmazanog kontakta

može se zaključiti da implementirani numerički model daje vrlo dobre rezultate uz uvjet da su dostupne kompletne informacije vezane uz svojstva maziva i hrapavosti površina.

Upotrebom modela podmazanog kontakta u simulacijama vučenja i valjanja žice pokazano je da model može izračunati hidrodinamičke tlakove, debljine maziva, kontakne tlakove hrapavosti, i dodatne vrijednosti koje mogu biti od koristi prilikom analize i planiranja procesa obrade metala deformiranjem. Povećanje proračunskog vremena od 40% upotrebom modela je prihvatljivo, dok je njegova stabilnost gotovo jednaka kao i stabilnost postojećeg modela penaliziranja kontakta. Ovisno o željenoj točnosti proračuna potrebno je koristiti proračunske mreže dovoljne gustoće.

Ključne riječi
Numerička analiza, Obrada metala deformiranjem, Podmazivanje, Reynoldsova jednadžba, Metoda kontrolnih površina, Valjanje žice, Vučenje žice, OpenFOAM, Metoda kontrolnih volumena

Contents

List of Figures

List of Tables

Nomenclature

Calligraphy letters

$\nabla_{\mathrm{s}}\bullet$	surface divergence operator	–
∇_{s}	surface gradient operator	–
$\top$	transpose operator	–

Greek letters

α	cavitation switch function	–
α	non–orthogonality angle of finite area edge	–
α	pressure–viscosity coefficient	–
α^*	pressure–viscosity coefficient	–
β	fluid bulk modulus	Pa
β^*	temperature–viscosity coefficient	–
β_{f}	thermal expansion coefficient of the lubricant film	$\mathrm{K^{-1}}$
β_{K}	thermal expansion coefficient	–
$\dot{\boldsymbol{\gamma}}$	shear rate vector	$\mathrm{s^{-1}}$
$\dot{\gamma}$	total shear strain rate	$\mathrm{s^{-1}}$
$\dot{\gamma}_{\mathrm{e}}$	elastic strain rate	$\mathrm{s^{-1}}$
$\dot{\gamma}_{\mathrm{v}}$	viscous shear strain rate	$\mathrm{s^{-1}}$
γ	Peklenik surface parameter	–
Γ_{ρ}	diffusion coefficient of property ρ	–

$\boldsymbol{\Delta}_e$	vector of orthogonal contribution to normal surface gradient	–
δ	elastic deflection	m
δ_e	elastic deformation	m
η	asperity density	m^{-2}
η	high–shear dynamic viscosity	Pa s
η'	Jacobson–Vinet parameter	–
η_C	Carreau shear–thinning dynamic viscosity	Pa s
η_RE	Ree–Eyring shear–thinning dynamic viscosity	Pa s
θ	fractional film content	–
θ_form	fractional film content next to the formation boundary	kg/m^3
κ_s	thermal diffusivity of a solid	m^2/s
λ	characteristic time	s
λ	correlation length	m
$\lambda_{0.5}$	half–correlation length	m
μ	dynamic viscosity	Pa s
μ	low–shear dynamic viscosity	Pa s
μ_∞	viscosity coefficient for T9 oil	Pa s
μ_0	dynamic viscosity at ambient pressure and temperature	Pa s
μ_B	dynamic viscosity calculated using Barus' law	Pa s
μ_g	dynamic glass viscosity	Pa s
μ_H	dynamic viscosity calculated using Houpert's equation	Pa s
μ_R	dynamic viscosity at reference state	Pa s

μ_{R}	dynamic viscosity calculated using Roelands' equation	$\mathrm{Pa\,s}$
μ_0	characteristic dynamic viscosity	$\mathrm{Pa\,s}$
μ_f	film dynamic viscosity	$\mathrm{Pa\,s}$
$\overline{\mu}$	dimensionless dynamic viscosity	–
ν	Poisson's ratio	–
ν	limiting shear stress parameter	–
ξ	heat partition coefficient	$\mathrm{W/mK}$
$\overline{\rho}$	dimensionless density	–
ρ	density	$\mathrm{kg/m^3}$
ρ_0	density at ambient pressure	$\mathrm{kg/m^3}$
ρ_{cav}	density at cavitation pressure	$\mathrm{kg/m^3}$
ρ_{form}	density of gas–liquid mixture next to the formation boundary	$\mathrm{kg/m^3}$
ρ_{ref}	reference density	$\mathrm{kg/m^3}$
ρ_{s}	specific heat capacity of a solid	$\mathrm{J/kgK}$
ρ_0	characteristic density	$\mathrm{kg/m^3}$
σ_{s}	squeeze number	–
τ	shear stress	Pa
τ_{E}	Eyring stress	Pa
τ_{f}	film shear stress	Pa
τ_{L}	limiting shear stress	Pa
τ_{m}	mean shear stress across the film thickness	Pa
τ_{tot}	total traction	Pa

ϕ_η	viscosity flow factor	–
ϕ_∞	viscosity coefficient for T9 oil	–
ϕ_s	shear flow factor	–
ϕ_{xy}	pressure flow factor	–
φ	asperity height distribution function	m^{-1}
ψ	calculated property	–
ψ^ref	reference property	–
Ω	full–film region	–
ω	asperity interference	m
Ω_cav	cavitating region	–
ω_c	critical interference	–

Latin letters

a	Yasuda parameter	–
a	asperity contact radius	m
A_1	Yasutomi parameter	°C
A_2	Yasutomi parameter	GPa^{-1}
A_r	contact area ratio	–
B	lubricant–dependent constant in Doolittle viscosity relation	–
B_0	Jacobson–Vinet parameter	Pa
b_1	improved Yasutomi parameter	GPa^{-1}
b_2	improved Yasutomi parameter	–
B_form	formation boundary	–

B_{F}	viscosity coefficient for T9 oil	–
B_{rup}	rupture boundary	–
$\tilde{C}_1$	integration constant	Pa
$\tilde{C}_2$	integration constant	m/s
$\tilde{C}_3$	integration constant	Pa
$\tilde{C}_4$	integration constant	m/s
$\mathbf{C}$	transformation tensor	–
C	critical yield coefficient	–
C	specific heat capacity	J/kgK
C_1	Dowson–Higginson coefficient	Pa
C_1	WLF parameter	–
C_2	Dowson–Higginson coefficient	–
C_2	WLF parameter	°C
c_{s}	specific heat capacity of a solid	J/kgK
C_p	specific heat capacity of lubricant film	J/kgK
D_{k}	normal surface gradient corrector due to curvature	–
E'	equivalent elastic modulus	Pa
E_{r}	reduced elastic modulus	Pa
E_{ψ}	relative error	–
F_{f}	friction force	N
$\mathbf{g}$	vector of gravitational acceleration	m/s^2
G	effective shear modulus	Pa

G	surface gap	m
g	cavitation switch function	–
G_0	initial gap	m
g_x	gravitational acceleration component in x–direction	m/s^2
g_y	gravitational acceleration component in y–direction	m/s^2
g_z	gravitational acceleration component in z–direction	m/s^2
$\overline{\mathbf{H}}$	non–dimensional film thickness	–
$\overline{\mathbf{H}}_{\mathrm{c}}$	non–dimensional film thickness at percolation threshold	–
H	material hardness	Pa
h	film thickness	m
h_0	characteristic length in z–direction	m
h_{cf}	fluid thermal conductance	W/m^{2}K
h_{cs}	solid thermal conductance	W/m^{2}K
h_{c}	thermal conductance	W/m^{2}K
h_{l}	local film thickness	m
H_{v}	Vickers hardness	HV
$\mathbf{k}_e$	vector of non–orthogonal correction	–
K	thermal conductivity	W/mK
K'_0	rate of change of the bulk modulus	–
K_0	bulk modulus at ambient pressure	Pa
k_{f}	thermal conductivity of lubricant film	W/mK
k_{s}	thermal conductivity of a solid	W/mK

l_0	characteristic length in x–direction	m
L_e	length of finite area edge	m
$\mathbf{m}_e$	unit binormal vector of finite area edge	–
m_0	zero order spectral moment	m^2
m_2	second order spectral moment	–
m_4	fourth order spectral moment	–
$\mathbf{n}_e$	unit normal vector of finite area edge	–
$\mathbf{n}_P$	unit normal vector of finite area face P	–
n	Carreau power law exponent	–
P	dimensionless pressure	–
p	pressure	Pa
p^*	contact pressure at the point of complete contact	Pa
P_a	asperity contact pressure	Pa
p_cav	cavitation pressure	Pa
P_f	film hydrodynamic pressure	Pa
p_ref	reference pressure	Pa
P_tot	total pressure	Pa
q	heat flux	W
q_f	friction generated heat flux	W
q'_x	flow rate in x–direction	m^2/s
q'_y	flow rate in y–direction	m^2/s
R	asperity radius	m

r	pressure flow factor constant	–
R_0	lubricant–dependent constant in Doolittle viscosity relation	–
R_{G}	gap residual	–
$R_{\mathrm{q_a}}$	root mean squared roughness of surface a	m
$R_{\mathrm{q_b}}$	root mean squared roughness of surface b	m
R_{q}	combined root mean squared surface roughness	m
Re	Reynolds number	–
$\mathrm{Re_x}$	Reynolds number in x–direction	–
$\mathrm{Re_y}$	Reynolds number in y–direction	–
$\mathrm{Re_z}$	Reynolds number in z–direction	–
$\dot{s}$	flux through finite area edge	$\mathrm{m^3/s}$
$\mathbf{S}$	boundary face area vector	$\mathrm{m^2}$
S_0	Roelands and Houpert temperature exponent	–
S_P	surface area of finite area face P	m
ΔT	temperature increase	K
Δt	timestep	s
$\mathbf{T}$	second rank tensor variable	–
T	dimensionless time	–
T	temperature	K
t	time	s
T_0	ambient temperature	K
t_0	characteristic time	s

T_∞	ambient temperature	K
T_g	glass transition temperature	°C
T_m	mean film temperature	K
T_ref	reference temperature	K, °C
$\overline{\mathbf{U}}$	mean velocity of two surfaces	–
$\overline{U}_x$	dimensionless velocity component in x–direction	–
$\overline{U}_y$	dimensionless velocity component in y–direction	–
$\overline{U}_z$	dimensionless velocity component in z–direction	–
$\mathbf{U}$	velocity vector	m/s
$\mathbf{U}_\mathrm{a}$	velocity vector of surface a	m/s
$\mathbf{U}_\mathrm{b}$	velocity vector of surface b	m/s
U_d	drawing speed	m/s
U_s	slip velocity magnitude	m/s
U_x	velocity component in x–direction	m/s
U_y	velocity component in y–direction	m/s
U_z	velocity component in z–direction	m/s
U_{0_x}	characteristic velocity in x–direction	m/s
U_{0_y}	characteristic velocity in y–direction	m/s
U_{0_z}	characteristic velocity in z–direction	m/s
$\mathbf{V}$	vector variable	–
V	volume at specific pressure and temperature state	m^3
V_∞	occupied volume at specific pressure and temperature state	m^3

V_R	volume at reference state	m^3
V_r	variance ratio of a surface	–
$V_{\infty R}$	occupied volume at reference state	m^3
w_0	characteristic length in y–direction	m
X	dimensionless x–coordinate	–
Y	dimensionless y–coordinate	–
Y	material yield strenght	Pa
y_s	distance between the mean surface and mean asperity height planes	m
Z	Roelands and Houpert pressure exponent	–
Z	dimensionless z–coordinate	–
z	surface height	m
z_0	initial surface height	m
Z_T	target contact plane	m

Superscripts

q^n	new timestep or iteration	–
q^{oo}	timestep or iteration before old timestep or iteration	–
q^o	old timestep or iteration	–

Subscripts

q_a	value at surface a	–
q_b	value at surface b	–
q_e	edge interpolated value	–
q_in	value at the inlet	–

$\mathbf{q}_n$	normal component of the vector	–
q_N	neighbouring finite area face–centred value	–
q_{out}	value at the outlet	–
q_P	current finite area face–centred value	–
$\mathbf{q}_t$	tangential component of the vector	–

1. Introduction

1.1. Background

Until recently, design of a metal forming process has been mainly performed by a costly trial–and–error–based experimental methods carried out on real physical models. With the advancement of computational resources, numerical modelling of metal forming processes is becoming a viable design tool which can potentially replace costly trials on real models by performing numerical experiments on virtual models.

Rolling is a forming operation where plastic deformation of a work piece is achieved by compression between two rotating rolls in a mill. Friction between the roller and the work piece is an integral part of the rolling process. Roll bite of the mill is lubricated using a special rolling lubricant to control friction and wear. While friction is essential for a rolling process, its unoptimised parameters can lead to lower productivity and inferior surface quality of rolled products. Roller wear has negative impact on productivity of the mills and lifetime of rolling equipment.

Although the importance of an appropriate friction model during the simulation of a metal forming processes is well known, a required interaction between tribology and computational mechanics is rarely present. The computer codes generally use sophisticated models for the treatment of plasticity and contact but poor friction laws, like the Coulomb's or Tresca's laws for the modelling of frictional contact [13], which are easy to implement but their results are generally not reliable or sufficiently accurate for this purpose.

The complete resolution of lubricated contact problem is a challenging task: it implies the resolution of the coupled system composed of the equilibrium equations of bodies in contact and motion of the lubricant in the contact area. The lubricated contact between surfaces in relative motion can be divided into three main regimes [14]: full film hydrodynamic lubrication regime, mixed lubrication regime and boundary lubrication regime. While boundary lubrication regime is

usually modelled using semi–empirical relations, lubrication in the full film hydro-dynamic regime can be modelled using averaged Reynolds lubrication equation. In the mixed lubrication regime, the applied load is shared between the lubricant and the contacting asperities. Lubricant flow in the mixed regime can also be modelled by averaged Reynolds lubrication equation, but in order to determine the asperity contact pressure, appropriate form of the asperity flattening model should be applied.

The most widely employed method for numerical modelling of metal forming processes is the Finite Element Method [15]. Nonetheless, the Finite Volume Method, conservative in nature, has become a viable alternative in many solid mechanics applications, specifically in simulations of strongly non–linear phenom-ena [8]. Notable work on stress analysis employing Finite Volume Method started two decades ago. Jasak and Weller [16] discretised the linear stress analysis prob-lem using the Finite Volume Method and applied it on three cases. They used a second–order accurate discretisation scheme and a segregated solution proce-dure. The same authors derived and implemented a coupling algorithm for con-tact stress problems of linear elastic solids [17]. Tuković and Jasak [18] presented a structural component of the Fluid Structure Interaction solver in the updated Lagrangian formulation. They used a fully implicit second–order accurate three–time–level scheme for temporal discretisation and the second–order cell–centred spatial discretisation scheme, and validated the solver on three–dimensional case of cantileverd elastic beam. Karač and Ivanković [19] performed a simulation of a fluid–filled polyethylene container under base drop using a two–system fluid–structure interaction procedure based on the Finite Volume Method. Cardiff et al. [20] developed a frictionless contact stress solver based on the penalty method used in finite element algorithms. Tuković et al. [21] described and implemented a procedure for accurately calculating traction at the interface of bonded or joined materials with different material properties.

Cardiff et al. [22] developed a large strain hyperelastoplastic finite volume deformation solver within the OpenFOAM framework. The solver is primarily used for metal forming simulations, e.g. wire rolling and drawing. At the moment, the available contact boundary conditions are: Dirichlet–Neumann and penalty–based contact. In the framework of the proposed dissertation, this method shall

be extended by including lubrication modelling in the hydrodynamic and mixed lubrication regime and calculation of frictional contact forces resulting from the presence of lubricant between two surfaces in contact.

1.2. Previous and Related Studies

Numerical simulations of metal forming processes gained ground in the last three decades due to rapid development of computational performance [8]. Liu et al. [23] were one of the first authors to perform numerical simulations of cold strip rolling using the Finite Element Method (FEM) under transient and steady–state conditions. Hwu and Lenard [24] performed a flat rolling simulation using an Eulerian finite element formulation. Cescutti et al. [25] carried out finite element simulations of a hot forging process, where they utilised a continuous remeshing procedure in order to rectify high distortions of finite elements. Hu and Liu [26] used a Lagrangian–Eulerian approach within the Finite Element Method for calculating ring rolling processes where they analysed the distribution of stresses and strains on the rolled ring and transient fluctuations of the roll separating force. Huetink et al. [27] gave a detailed review of their own Lagrangian–Eulerian method for simulating metal forming processes via the finite element framework. They used a special smoothing procedure in order to avoid numerical instabilities and diffusion, and demonstrated their method by calculating upsetting and wire drawing process. Gratacos et al. [28] derived and implemented a general coupled finite element model for analysing thin strip rolling processes. The authors used a plane–strain elastoplastic material model and applied their method to temper rolling and thin film rolling process. Sa and Wilson [29] developed a mathematical model for calculating liquid lubricated strip rolling in the full–film regime, which combined slab plasticity method, hydrodynamic lubrication and thermal analysis. The authors compared their results to the experimental measurements and achieved a very good agreement. Boman and Ponthot [13] used their own arbitrary Lagrangian–Eulerian formulation written within the finite element framework for calculating lubricated strip rolling process, where they used an extended hydrodynamic lubrication procedure together with the averaged Reynolds equation for representing lubricant flow. Liu and Tieu [30] used

3

a thermal lubrication model based on the averaged Reynolds equation for calculating thin strip rolling process. Their methodology required a division of the computational domain into three separate zones (inlet zone, work zone and outlet zone) with predetermined positions, where each zone was simulated using different equations. Khan et al. [31] combined the equivalent interfacial layer with an existing finite element code in order to calculate mixed lubrication phenomena during a two–dimensional sheet rolling simulation. The authors used a statistical Hertzian–based asperity contact model and the averaged Reynolds equation. Wu et al. [32] used a similar approach and performed a three–dimensional sheet rolling simulation, where they compared hydrodynamic and contact pressures for different lubricant properties and rolling speeds. Later, the same authors [33] expanded their method and incorporated elastic–perfectly–plastic single asperity contact model. Recently, a finite volume large strain hyperelastoplastic deformation solver was developed by Cardiff et al. [22]. The authors tested their solver on several cases and achieved a very good agreement with finite element calculations. They also performed a three–dimensional wire rolling simulation using a penalty contact model [20] and constant friction coefficient.

Modern treatment of lubricated rough surface contact can be divided into two essential parts:

- modelling of liquid film,

- contact modelling for a pair of rough surfaces.

Modelling of liquid film generally encompasses calculation of film pressure, characterisation of lubricant transport properties, cavitation modelling and heat transfer. Contact modelling is usually done in two ways: statistically and deterministically. Review of the previous relevant work in each of these fields is presented in Chapter 2.

1.3. Present Contributions

The present study contributes to the field of numerical contact modelling by providing a framework for calculating lubricated contact between rough surfaces during numerical analysis of a metal forming process. The methods that are developed and implemented in this study are combined to create a unique framework in a form of a contact boundary condition for the existing large strain hyperelastoplastic finite volume deformation solver [22].

The lubricant flow is modelled using the Reynolds equation. In the present study the Reynolds equation is discretised using the Finite Area Method [1], as opposed to the previous implementations carried out in the finite element and finite difference frameworks. Special discretisation of the Poiseuille coefficient is formulated in order to satisfy cavitation rupture and formation boundary conditions within the finite area framework. The model is implemented to work efficiently on parallel distributed memory computer architectures.

The lubricant flow model, thermal model and asperity contact model are coupled together enabling the calculation of normal contact pressure and traction continuously throughout all lubrication regimes. The asperity contact procedure is created in a way that enables the user to input measured surface roughness profile, or surface scan, from which the information regarding surface topology is determined and contact data (pressures, area ratios and film thicknesses) is automatically calculated for a selected range of surface separations. A detailed description of all the implemented models and procedures is given.

A numerical framework combining all presented models is developed and implemented as a contact boundary condition used by the finite volume deformation solver for the purpose of metal forming simulations. The main task of the framework is to calculate contact pressures and traction during the evaluation of boundary conditions. The framework also provides additional information like film thickness, temperature, contact area, etc., which can be valuable when planning a new manufacturing process or choosing between different lubricants. To the best of author's knowledge, the mentioned combination of models has not been implemented so far.

Numerical models and procedures are implemented in a metal forming soft-

ware package based on the open source object–oriented C++ `foam-extend` library (community driven fork of the OpenFOAM software for general computational continuum mechanics [34]). Special attention has been given to object–oriented programming pattern to ensure straightforward maintenance and further development.

An extensive validation and verification is carried out for each of the implemented models, i.e. parts of the contact framework, in order to analyse their applicability to engineering applications and to minimise the possibility of programming errors. The main validation is carried out on point contact (ball–on–disc) cases by comparing the results to the available experimental measurements. The implemented contact boundary condition is tested on two metal forming geometries: wire drawing and wire rolling. The results are compared to the existing penalty contact model.

1.4. Thesis Outline

The rest of this thesis is organised as follows.

Chapter 2. presents an overview of different elements and models required for calculating rough surface lubricated contact. These elements are: lubricant flow model (Reynolds equation), flow factors, contact model, thin film thermal model and characterisation of the lubricant transport properties.

Chapter 3. presents the numerical method called Finite Area Method used for discretising the Reynolds equation and thin film energy equation. Finite Area Method is a two–dimensional counterpart of the Finite Volume Method, discretised over a curved surface. Discretisation of the spatial domain and of the transport equation is given.

Chapter 4. presents the numerical modelling framework and implementation. Finite area discretisation of the Reynolds equation is presented first, with the emphasis on cavitation boundaries. Implemented equations describing lubricant transport properties are given next. Implementations of three thermal models are described: thin film energy equation, deterministic surface temperature model and thermal boundary condition for rough lubricated contact. Finally, equations and numerical procedures for statistical and deterministic contact models are

presented.

Chapter 5. presents test cases used to validate and verify implemented numerical models. The first five bearing cases are used for validating the lubricant flow model, i.e. the implementation of the Reynolds equation. Next, the deterministic contact model is validated using a two–dimensional wavy surface test case. Results of statistical contact models are compared to the results of deterministic model for three rough surfaces. Deterministic surface temperature model is validated against exact numerical solutions for two types of heat sources, square and parabolic. Finally, a point contact analysis is carried out for two lubricants: Turbo T9 and Turbo T68. Point contact simulations in this study represent comprehensive analyses utilising almost all implemented models. Cases in which the hydrodynamic lubrication is examined consider Turbo T9 oil, while the mixed lubrication cases consider Turbo T68 oil.

Chapter 6. presents the numerical framework in which the rough surface lubricated contact model is implemented as a contact boundary condition for an existing finite volume deformation solver. The application of the lubricated contact boundary condition is presented on two wire drawing cases (axisymmetric and quarter–symmetric) and on a simple wire rolling case. The simulations are conducted for different lubricant viscosities, and their results are compared to the values calculated using the penalty contact model with a constant friction coefficient.

Chapter 7. presents the summary and conclusions regarding the work presented this study. Proposals for future research are briefly discussed.

2. Lubricated Contact Models for Rough Surfaces

2.1. Introduction

In this chapter an overview of numerical models required for calculating lubricated rough surface contact is given. First, Reynolds equation used for calculating thin film flow is presented, with its complete derivation from Navier–Stokes and continuity equations. A literature survey of cavitation boundary conditions and algorithms used in conjuction with Reynolds equation is given. Next, the averaged Reynolds equation and flow factors are presented. The averaged Reynolds equation takes into account surface roughness effects, while the original Reynolds equation assumes smooth surface contact. An overview of asperity contact models is given, where advantages and disadvantages of statistical and deterministic models are stated. A brief summary of the most used thin film thermal models is given, as well as different methods for characterising lubricant transport properties.

2.2. Reynolds Equation

In this section the Reynolds equation is introduced with its complete derivation from Navier-Stokes and continuity equations. A literature survey of the calculation of thin film cavitation is given.

The Reynolds equation is a partial differential equation governing the pressure distribution in thin film flows. It was first derived in 1886 by Osborne Reynolds [35], where he formulated a governing equation which describes the pressure distribution in a fluid film lubricated bearing and referred to Beauchamp Tower's friction experiments. In its original form the Reynolds equation had the following assumptions:

- Newtonian fluid;

- Laminar flow;

- Viscous forces dominate over fluid body, inertia and surface tension forces;

- Fluid film curvature can be neglected, i.e. thickness of the film is significantly smaller compared to the width and length of the film;

- The variation of pressure across the fluid film thickness is negligibly small.

Some of the assumptions (e.g. Newtonian fluid) were alleviated later, yielding more general forms of the Reynolds equation [36].

Engineering applications for which the Reynolds equation is utilised are various [37]: journal bearings, thrust bearings, mechanical seals, cylinder liners, etc. The majority of publications from the 1960s to the late 1990s were mostly theoretical [37], with models based on steady–state Reynolds equation, non–mass–conserving cavitation algorithms and constant fluid properties. Since the early 2000s, following the increase in computational power, more sophisticated models were developed and utilised.

Modern numerical thin film models based on the Reynolds equation consider temperature and pressure dependent fluid density [38, 3, 39], non-Newtonian viscosity [10, 39, 40], thermal effects [41, 42, 43, 44], surface roughness effects [45, 46, 32, 47], etc.

2.2.1. Derivation from Navier–Stokes and Continuity Equations

A starting point for the derivation of the Reynolds equation [48] is the Navier–Stokes momentum equation for compressible fluids [49]:

$$\frac{\partial \rho \mathbf{U}}{\partial t} + \nabla \bullet (\rho \mathbf{U}\mathbf{U}) = \rho \mathbf{g} - \nabla \left(p + \frac{2}{3}\mu \nabla \bullet \mathbf{U} \right) + \nabla \bullet \left[\mu \left(\nabla \mathbf{U} + (\nabla \mathbf{U})^\top \right) \right], \quad (2.1)$$

and the continuity equation:

$$\frac{\partial \rho}{\partial t} + \nabla \bullet (\rho \mathbf{U}) = 0. \quad (2.2)$$

The derivation of the Reynolds equation is performed using the order–of–magnitude analysis [48], therefore it is more convenient to rewrite Eqs. 2.1 and 2.2 in Cartesian component notation.

Cartesian Component Notation

First, a reorganisation of the left hand side of Eq. 2.1 is required:

$$\frac{\partial \rho \mathbf{U}}{\partial t} + \nabla \bullet (\rho \mathbf{U} \mathbf{U}), \tag{2.3}$$

where $\mathbf{U}\mathbf{U}$ is a dyad [50], resulting in a second rank tensor. Divergence of a dyad is calculated as follows:

$$\nabla \bullet (\mathbf{p}\mathbf{q}) = \mathbf{p} \bullet \nabla \mathbf{q} + (\nabla \bullet \mathbf{p}) \, \mathbf{q}. \tag{2.4}$$

Using Eq. 2.4 in Eq. 2.3 results in:

$$
\begin{aligned}
\frac{\partial \rho \mathbf{U}}{\partial t} + \nabla \bullet (\rho \mathbf{U} \mathbf{U}) \rightarrow & \rho \frac{\partial \mathbf{U}}{\partial t} + \mathbf{U} \frac{\partial \rho}{\partial t} + \rho \mathbf{U} \nabla \bullet \mathbf{U} + \mathbf{U} \bullet \nabla (\rho \mathbf{U}) \\
\rightarrow & \rho \frac{\partial \mathbf{U}}{\partial t} + \mathbf{U} \frac{\partial \rho}{\partial t} + \rho \mathbf{U} \nabla \bullet \mathbf{U} + \mathbf{U} \mathbf{U} \bullet \nabla \rho + \rho \mathbf{U} \bullet \nabla \mathbf{U},
\end{aligned} \tag{2.5}
$$

which, by rearranging and substituting $\rho \nabla \bullet \mathbf{U} + \mathbf{U} \bullet \nabla \rho$ with $\nabla \bullet (\rho \mathbf{U})$, becomes:

$$
\begin{aligned}
& \rho \left(\frac{\partial \mathbf{U}}{\partial t} + \mathbf{U} \bullet \nabla \mathbf{U} \right) + \mathbf{U} \left(\frac{\partial \rho}{\partial t} + \rho \nabla \bullet \mathbf{U} + \mathbf{U} \bullet \nabla \rho \right) \rightarrow \\
& \rho \left(\frac{\partial \mathbf{U}}{\partial t} + \mathbf{U} \bullet \nabla \mathbf{U} \right) + \mathbf{U} \left(\frac{\partial \rho}{\partial t} + \nabla \bullet (\rho \mathbf{U}) \right).
\end{aligned} \tag{2.6}
$$

By taking into account the continuity equation, the second term of Eq. 2.6 is equal to zero, therefore Eq. 2.3 is written as:

$$\frac{\partial \rho \mathbf{U}}{\partial t} + \nabla \bullet (\rho \mathbf{U} \mathbf{U}) \rightarrow \rho \left(\frac{\partial \mathbf{U}}{\partial t} + \mathbf{U} \bullet \nabla \mathbf{U} \right) \tag{2.7}$$

In order to write the previous expression in Cartesian component notation the scalar product of the velocity vector and its gradient is expanded as follows:

$$
\begin{aligned}
\mathbf{U} \bullet \nabla \mathbf{U} &= \begin{bmatrix} U_x & U_y & U_z \end{bmatrix} \bullet \left(\begin{bmatrix} \frac{\partial}{\partial x} \\ \frac{\partial}{\partial y} \\ \frac{\partial}{\partial z} \end{bmatrix} \begin{bmatrix} U_x & U_y & U_z \end{bmatrix} \right) \\
&= \begin{bmatrix} U_x & U_y & U_z \end{bmatrix} \bullet \begin{bmatrix} \frac{\partial U_x}{\partial x} & \frac{\partial U_y}{\partial x} & \frac{\partial U_z}{\partial x} \\ \frac{\partial U_x}{\partial y} & \frac{\partial U_y}{\partial y} & \frac{\partial U_z}{\partial y} \\ \frac{\partial U_x}{\partial z} & \frac{\partial U_y}{\partial z} & \frac{\partial U_z}{\partial z} \end{bmatrix} \\
&= \begin{bmatrix} U_x \frac{\partial U_x}{\partial x} + U_y \frac{\partial U_x}{\partial y} + U_z \frac{\partial U_x}{\partial z} \\ U_x \frac{\partial U_y}{\partial x} + U_y \frac{\partial U_y}{\partial y} + U_z \frac{\partial U_y}{\partial z} \\ U_x \frac{\partial U_z}{\partial x} + U_y \frac{\partial U_z}{\partial y} + U_z \frac{\partial U_z}{\partial z} \end{bmatrix}^{\top} .
\end{aligned} \tag{2.8}
$$

Now, Eq. 2.7 written in Cartesian component notation states:

$$\rho \frac{\partial U_x}{\partial t} + \rho \left(U_x \frac{\partial U_x}{\partial x} + U_y \frac{\partial U_x}{\partial y} + U_z \frac{\partial U_x}{\partial z} \right), \tag{2.9}$$

$$\rho \frac{\partial U_y}{\partial t} + \rho \left(U_x \frac{\partial U_y}{\partial x} + U_y \frac{\partial U_y}{\partial y} + U_z \frac{\partial U_y}{\partial z} \right), \tag{2.10}$$

$$\rho \frac{\partial U_z}{\partial t} + \rho \left(U_x \frac{\partial U_z}{\partial x} + U_y \frac{\partial U_z}{\partial y} + U_z \frac{\partial U_z}{\partial z} \right). \tag{2.11}$$

Next, expanding the third term on the right-hand side of Eq. 2.1 results in:

$$
\begin{aligned}
\nabla \left(\frac{2}{3} \mu \nabla {\cdot} \mathbf{U} \right) &= \begin{bmatrix} \frac{\partial}{\partial x} \\ \frac{\partial}{\partial y} \\ \frac{\partial}{\partial z} \end{bmatrix} \left(\frac{2}{3} \mu \begin{bmatrix} \frac{\partial}{\partial x} & \frac{\partial}{\partial y} & \frac{\partial}{\partial z} \end{bmatrix} {\cdot} \begin{bmatrix} U_x \\ U_y \\ U_z \end{bmatrix} \right) \\[2mm]
&= \frac{2}{3} \begin{bmatrix} \frac{\partial}{\partial x} \\ \frac{\partial}{\partial y} \\ \frac{\partial}{\partial z} \end{bmatrix} \left(\mu \frac{\partial U_x}{\partial x} + \mu \frac{\partial U_y}{\partial y} + \mu \frac{\partial U_z}{\partial z} \right) \\[2mm]
&= \begin{bmatrix} \frac{2}{3} \frac{\partial}{\partial x} \left[\mu \left(\frac{\partial U_x}{\partial x} + \frac{\partial U_y}{\partial y} + \frac{\partial U_z}{\partial z} \right) \right] \\ \frac{2}{3} \frac{\partial}{\partial y} \left[\mu \left(\frac{\partial U_x}{\partial x} + \frac{\partial U_y}{\partial y} + \frac{\partial U_z}{\partial z} \right) \right] \\ \frac{2}{3} \frac{\partial}{\partial z} \left[\mu \left(\frac{\partial U_x}{\partial x} + \frac{\partial U_y}{\partial y} + \frac{\partial U_z}{\partial z} \right) \right] \end{bmatrix},
\end{aligned}
\tag{2.12}
$$

while expanding the fourth term gives:

$$\nabla\bullet\left[\mu\left(\nabla\mathbf{U}+(\nabla\mathbf{U})^{\top}\right)\right]=$$

$$=\begin{bmatrix}\frac{\partial}{\partial x} & \frac{\partial}{\partial y} & \frac{\partial}{\partial z}\end{bmatrix}\bullet\left\{\mu\left[\begin{bmatrix}\frac{\partial}{\partial x}\\\frac{\partial}{\partial y}\\\frac{\partial}{\partial z}\end{bmatrix}\begin{bmatrix}U_x & U_y & U_z\end{bmatrix}+\left(\begin{bmatrix}\frac{\partial}{\partial x}\\\frac{\partial}{\partial y}\\\frac{\partial}{\partial z}\end{bmatrix}\begin{bmatrix}U_x & U_y & U_z\end{bmatrix}\right)^{\top}\right]\right\}$$

$$=\begin{bmatrix}\frac{\partial}{\partial x} & \frac{\partial}{\partial y} & \frac{\partial}{\partial z}\end{bmatrix}\bullet\left[\mu\left(\begin{bmatrix}\frac{\partial U_x}{\partial x} & \frac{\partial U_y}{\partial x} & \frac{\partial U_z}{\partial x}\\\frac{\partial U_x}{\partial y} & \frac{\partial U_y}{\partial y} & \frac{\partial U_z}{\partial y}\\\frac{\partial U_x}{\partial z} & \frac{\partial U_y}{\partial z} & \frac{\partial U_z}{\partial z}\end{bmatrix}+\begin{bmatrix}\frac{\partial U_x}{\partial x} & \frac{\partial U_y}{\partial x} & \frac{\partial U_z}{\partial x}\\\frac{\partial U_x}{\partial y} & \frac{\partial U_y}{\partial y} & \frac{\partial U_z}{\partial y}\\\frac{\partial U_x}{\partial z} & \frac{\partial U_y}{\partial z} & \frac{\partial U_z}{\partial z}\end{bmatrix}^{\top}\right)\right]$$

$$=\begin{bmatrix}\frac{\partial}{\partial x} & \frac{\partial}{\partial y} & \frac{\partial}{\partial z}\end{bmatrix}\bullet\left[\mu\left(\begin{bmatrix}\frac{\partial U_x}{\partial x} & \frac{\partial U_y}{\partial x} & \frac{\partial U_z}{\partial x}\\\frac{\partial U_x}{\partial y} & \frac{\partial U_y}{\partial y} & \frac{\partial U_z}{\partial y}\\\frac{\partial U_x}{\partial z} & \frac{\partial U_y}{\partial z} & \frac{\partial U_z}{\partial z}\end{bmatrix}+\begin{bmatrix}\frac{\partial U_x}{\partial x} & \frac{\partial U_x}{\partial y} & \frac{\partial U_x}{\partial z}\\\frac{\partial U_y}{\partial x} & \frac{\partial U_y}{\partial y} & \frac{\partial U_y}{\partial z}\\\frac{\partial U_z}{\partial x} & \frac{\partial U_z}{\partial y} & \frac{\partial U_z}{\partial z}\end{bmatrix}\right)\right]$$

$$=\begin{bmatrix}\frac{\partial}{\partial x} & \frac{\partial}{\partial y} & \frac{\partial}{\partial z}\end{bmatrix}\bullet\begin{bmatrix}2\mu\frac{\partial U_x}{\partial x} & \mu\left(\frac{\partial U_y}{\partial x}+\frac{\partial U_x}{\partial y}\right) & \mu\left(\frac{\partial U_z}{\partial x}+\frac{\partial U_x}{\partial z}\right)\\\mu\left(\frac{\partial U_y}{\partial x}+\frac{\partial U_x}{\partial y}\right) & 2\mu\frac{\partial U_y}{\partial y} & \mu\left(\frac{\partial U_z}{\partial y}+\frac{\partial U_y}{\partial z}\right)\\\mu\left(\frac{\partial U_z}{\partial x}+\frac{\partial U_x}{\partial z}\right) & \mu\left(\frac{\partial U_z}{\partial y}+\frac{\partial U_y}{\partial z}\right) & 2\mu\frac{\partial U_z}{\partial z}\end{bmatrix}$$

$$=\begin{bmatrix}2\frac{\partial}{\partial x}\left(\mu\frac{\partial U_x}{\partial x}\right)+\frac{\partial}{\partial y}\left[\mu\left(\frac{\partial U_y}{\partial x}+\frac{\partial U_x}{\partial y}\right)\right]+\frac{\partial}{\partial z}\left[\mu\left(\frac{\partial U_z}{\partial x}+\frac{\partial U_x}{\partial z}\right)\right]\\\frac{\partial}{\partial x}\left[\mu\left(\frac{\partial U_y}{\partial x}+\frac{\partial U_x}{\partial y}\right)\right]+2\frac{\partial}{\partial y}\left(\mu\frac{\partial U_y}{\partial y}\right)+\frac{\partial}{\partial z}\left[\mu\left(\frac{\partial U_z}{\partial y}+\frac{\partial U_y}{\partial z}\right)\right]\\\frac{\partial}{\partial x}\left[\mu\left(\frac{\partial U_z}{\partial x}+\frac{\partial U_x}{\partial z}\right)\right]+\frac{\partial}{\partial y}\left[\mu\left(\frac{\partial U_z}{\partial y}+\frac{\partial U_y}{\partial z}\right)\right]+2\frac{\partial}{\partial z}\left(\mu\frac{\partial U_z}{\partial z}\right)\end{bmatrix}^{\top}.$$

(2.13)

Finally, combining Eqs. 2.9 to 2.13 results in the Navier–Stokes momentum equation written in Cartesian component notation:

$$\rho\frac{\partial U_x}{\partial t}+\rho\left(U_x\frac{\partial U_x}{\partial x}+U_y\frac{\partial U_x}{\partial y}+U_z\frac{\partial U_x}{\partial z}\right)=$$

$$\rho g_x-\frac{\partial p}{\partial x}-\frac{2}{3}\frac{\partial}{\partial x}\left[\mu\left(\frac{\partial U_x}{\partial x}+\frac{\partial U_y}{\partial y}+\frac{\partial U_z}{\partial z}\right)\right]$$

$$+2\frac{\partial}{\partial x}\left(\mu\frac{\partial U_x}{\partial x}\right)+\frac{\partial}{\partial y}\left[\mu\left(\frac{\partial U_y}{\partial x}+\frac{\partial U_x}{\partial y}\right)\right]+\frac{\partial}{\partial z}\left[\mu\left(\frac{\partial U_z}{\partial x}+\frac{\partial U_x}{\partial z}\right)\right],$$

(2.14)

$$\rho\frac{\partial U_y}{\partial t} + \rho\left(U_x\frac{\partial U_y}{\partial x} + U_y\frac{\partial U_y}{\partial y} + U_z\frac{\partial U_y}{\partial z}\right) =$$

$$\rho g_y - \frac{\partial p}{\partial y} - \frac{2}{3}\frac{\partial}{\partial y}\left[\mu\left(\frac{\partial U_x}{\partial x} + \frac{\partial U_y}{\partial y} + \frac{\partial U_z}{\partial z}\right)\right]$$

$$+ \frac{\partial}{\partial x}\left[\mu\left(\frac{\partial U_y}{\partial x} + \frac{\partial U_x}{\partial y}\right)\right] + 2\frac{\partial}{\partial y}\left(\mu\frac{\partial U_y}{\partial y}\right) + \frac{\partial}{\partial z}\left[\mu\left(\frac{\partial U_z}{\partial y} + \frac{\partial U_y}{\partial z}\right)\right],$$

$$(2.15)$$

$$\rho\frac{\partial U_z}{\partial t} + \rho\left(U_x\frac{\partial U_z}{\partial x} + U_y\frac{\partial U_z}{\partial y} + U_z\frac{\partial U_z}{\partial z}\right) =$$

$$\rho g_z - \frac{\partial p}{\partial z} - \frac{2}{3}\frac{\partial}{\partial z}\left[\mu\left(\frac{\partial U_x}{\partial x} + \frac{\partial U_y}{\partial y} + \frac{\partial U_z}{\partial z}\right)\right]$$

$$+ \frac{\partial}{\partial x}\left[\mu\left(\frac{\partial U_z}{\partial x} + \frac{\partial U_x}{\partial z}\right)\right] + \frac{\partial}{\partial y}\left[\mu\left(\frac{\partial U_z}{\partial y} + \frac{\partial U_y}{\partial z}\right)\right] + 2\frac{\partial}{\partial z}\left(\mu\frac{\partial U_z}{\partial z}\right),$$

$$(2.16)$$

Terms on the left hand side of Eqs. 2.14 to 2.16 represent inertia effects and convective transport, while terms on the right hand side represent body force, pressure gradient and viscous term, respectively. These equations are written in the general form for a Newtonian fluid and are valid for compressible viscous flow with varying viscosity. The continuity equation written in Cartesian component notation states:

$$\frac{\partial \rho}{\partial t} + \frac{\partial(\rho U_x)}{\partial x} + \frac{\partial(\rho U_y)}{\partial y} + \frac{\partial(\rho U_z)}{\partial z} = 0. \qquad (2.17)$$

Order–of–Magnitude Analysis

Problems of the fluid film lubrication fall in the special class of flow conditions called "slow viscous motion" [48], in which the pressure and viscous terms are dominant. In order to demonstrate that the previous statement is true, Hamrock et al. [48] performed an order–of–magnitude analysis of the Navier-Stokes momentum and continuity equations for the previously mentioned flow conditions. A summary of their analysis is presented here.

The following characteristic parameters are defined:

l_0 characteristic length in x–direction   [m]

w_0 characteristic length in y–direction   [m]

h_0 characteristic length in z–direction   [m]

t_0 characteristic time   [s]

U_{0_x} characteristic velocity in x–direction   [m/s]

U_{0_y} characteristic velocity in y–direction   [m/s]

U_{0_z} characteristic velocity in z–direction   [m/s]

ρ_0 characteristic density   [kg/m^3]

μ_0 characteristic dynamic viscosity   [Pa s]

In Fig. 2.1 the given parameters are graphically represented. The lubricant, characterised by density ρ_0 and dynamic viscosity μ_0, flows with velocity $\mathbf{U}_0$ between two surfaces, a and b. Length, width and height of the domain are defined by characteristic parameters l_0, w_0 and h_0, respectively.
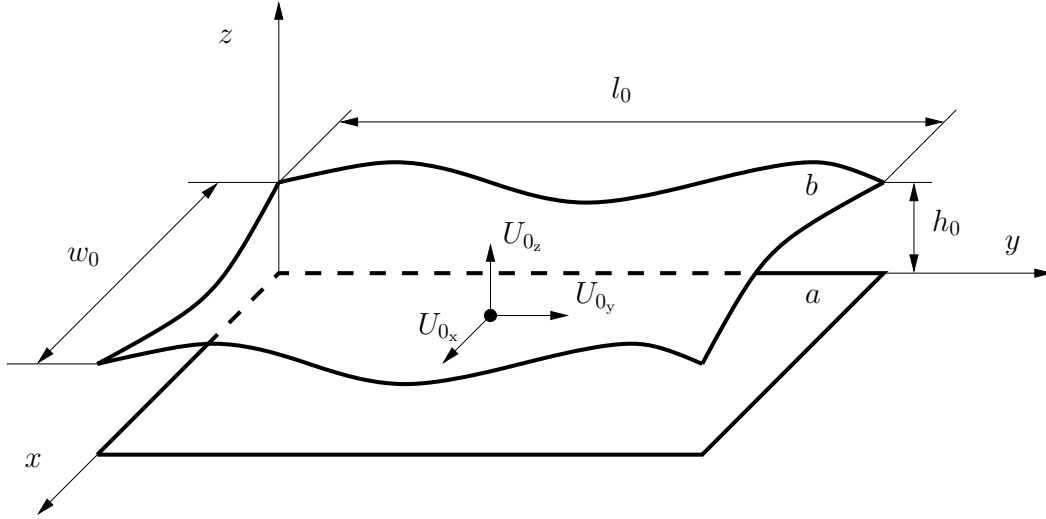
Figure 2.1: With the definition of characteristic parameters.

Using the specified characteristic parameters the following dimensionless parameters are defined:

$$X = \frac{x}{l_0} \qquad Y = \frac{y}{w_0} \qquad Z = \frac{z}{h_0} \qquad T = \frac{t}{t_0} \qquad \sigma_{\mathrm{s}} = \frac{\rho_0 h_0^2}{\mu_0 t_0}$$

$$\overline{U}_x = \frac{U_x}{U_{0_x}} \qquad \overline{U}_y = \frac{U_y}{U_{0_y}} \qquad \overline{U}_z = \frac{U_z}{U_{0_z}} \qquad \overline{\rho} = \frac{\rho}{\rho_0} \qquad \overline{\mu} = \frac{\mu}{\mu_0}$$

$$P = \frac{h_0^2 p}{\mu_0 U_{0_x} l_0}$$

Introducing dimensionless parameters into Eqs. 2.14 to 2.16 results in:

$$
\frac{l_0}{U_{0_x} t_0} \frac{\partial \overline{U}_x}{\partial T} + \left(\overline{U}_x \frac{\partial \overline{U}_x}{\partial X} + \frac{l_0}{w_0} \frac{U_{0_y}}{U_{0_x}} \overline{U}_y \frac{\partial \overline{U}_x}{\partial Y} + \frac{l_0}{h_0} \frac{U_{0_z}}{U_{0_x}} \overline{U}_z \frac{\partial \overline{U}_x}{\partial Z} \right) =
$$

$$
\frac{l_0 g_x}{U_{0_x}^2} - \frac{\mu_0}{\rho_0 U_{0_x} l_0} \left(\frac{l_0}{h_0} \right)^2 \frac{1}{\overline{\rho}} \frac{\partial P}{\partial X}
$$

$$
- \frac{2}{3} \frac{\mu_0}{\rho_0 U_{0_x} l_0} \frac{1}{\overline{\rho}} \frac{\partial}{\partial X} \left[\overline{\mu} \left(\frac{\partial \overline{U}_x}{\partial X} + \frac{U_{0_y}}{U_{0_x}} \frac{l_0}{w_0} \frac{\partial \overline{U}_y}{\partial Y} + \frac{U_{0_z}}{U_{0_x}} \frac{l_0}{h_0} \frac{\partial \overline{U}_z}{\partial Z} \right) \right]
$$

$$
+ 2 \frac{\mu_0}{\rho_0 U_{0_x} l_0} \frac{1}{\overline{\rho}} \frac{\partial}{\partial X} \left(\overline{\mu} \frac{\partial \overline{U}_x}{\partial X} \right)
$$

$$
+ \frac{\mu_0}{\rho_0 U_{0_x} l_0} \left(\frac{l_0}{w_0} \right)^2 \frac{1}{\overline{\rho}} \frac{\partial}{\partial Y} \left[\overline{\mu} \left(\frac{\partial \overline{U}_x}{\partial Y} + \frac{U_{0_y}}{U_{0_x}} \frac{w_0}{l_0} \frac{\partial \overline{U}_y}{\partial X} \right) \right]
$$

$$
+ \frac{\mu_0}{\rho_0 U_{0_x} l_0} \left(\frac{l_0}{h_0} \right)^2 \frac{1}{\overline{\rho}} \frac{\partial}{\partial Z} \left[\overline{\mu} \left(\frac{\partial \overline{U}_x}{\partial Z} + \frac{U_{0_z}}{U_{0_x}} \frac{h_0}{l_0} \frac{\partial \overline{U}_z}{\partial X} \right) \right],
$$

(2.18)

$$
\frac{w_0}{U_{0_y} t_0} \frac{\partial \overline{U}_y}{\partial T} + \left(\frac{w_0}{l_0} \frac{U_{0_x}}{U_{0_y}} \overline{U}_x \frac{\partial \overline{U}_y}{\partial X} + \overline{U}_y \frac{\partial \overline{U}_y}{\partial Y} + \frac{w_0}{h_0} \frac{U_{0_z}}{U_{0_y}} \overline{U}_z \frac{\partial \overline{U}_y}{\partial Z} \right) =
$$

$$
\frac{w_0 g_y}{U_{0_y}^2} - \frac{\mu_0}{\rho_0 U_{0_y} w_0} \frac{U_{0_x}}{U_{0_y}} \frac{l_0}{w_0} \left(\frac{w_0}{h_0} \right)^2 \frac{1}{\overline{\rho}} \frac{\partial P}{\partial Y}
$$

$$
- \frac{2}{3} \frac{\mu_0}{\rho_0 U_{0_y} w_0} \frac{1}{\overline{\rho}} \frac{\partial}{\partial Y} \left[\overline{\mu} \left(\frac{U_{0_x}}{U_{0_y}} \frac{w_0}{l_0} \frac{\partial \overline{U}_x}{\partial X} + \frac{\partial \overline{U}_y}{\partial Y} + \frac{U_{0_z}}{U_{0_y}} \frac{w_0}{h_0} \frac{\partial \overline{U}_z}{\partial Z} \right) \right]
$$

$$
+ \frac{\mu_0}{\rho_0 U_{0_y} w_0} \left(\frac{w_0}{l_0} \right)^2 \frac{1}{\overline{\rho}} \frac{\partial}{\partial X} \left[\overline{\mu} \left(\frac{\partial \overline{U}_y}{\partial X} + \frac{U_{0_x}}{U_{0_y}} \frac{l_0}{w_0} \frac{\partial \overline{U}_x}{\partial Y} \right) \right]
$$

$$
+ 2 \frac{\mu_0}{\rho_0 U_{0_y} w_0} \frac{1}{\overline{\rho}} \frac{\partial}{\partial Y} \left(\overline{\mu} \frac{\partial \overline{U}_y}{\partial Y} \right)
$$

$$
+ \frac{\mu_0}{\rho_0 U_{0_y} w_0} \left(\frac{w_0}{h_0} \right)^2 \frac{1}{\overline{\rho}} \frac{\partial}{\partial Z} \left[\overline{\mu} \left(\frac{\partial \overline{U}_y}{\partial Z} + \frac{U_{0_z}}{U_{0_y}} \frac{h_0}{w_0} \frac{\partial \overline{U}_z}{\partial Y} \right) \right],
$$

(2.19)

$$\frac{h_0}{U_{0_z}t_0}\frac{\partial \overline{U}_z}{\partial T} + \left(\frac{h_0}{l_0}\frac{U_{0_x}}{U_{0_z}}\overline{U}_x\frac{\partial \overline{U}_z}{\partial X} + \frac{h_0}{w_0}\frac{U_{0_y}}{U_{0_z}}\overline{U}_y\frac{\partial \overline{U}_z}{\partial Y} + \overline{U}_z\frac{\partial \overline{U}_z}{\partial Z}\right) =$$

$$\frac{h_0 g_z}{U_{0_z}^2} - \frac{\mu_0}{\rho_0 U_{0_x}l_0}\left(\frac{U_{0_x}}{U_{0_z}}\right)^2\left(\frac{l_0}{h_0}\right)^2\frac{1}{\overline{\rho}}\frac{\partial P}{\partial Z}$$

$$-\frac{2}{3}\frac{\mu_0}{\rho_0 U_{0_z}h_0}\frac{1}{\overline{\rho}}\frac{\partial}{\partial Z}\left[\overline{\mu}\left(\frac{U_{0_x}}{U_{0_z}}\frac{h_0}{l_0}\frac{\partial \overline{U}_x}{\partial X} + \frac{U_{0_y}}{U_{0_z}}\frac{h_0}{w_0}\frac{\partial \overline{U}_y}{\partial Y} + \frac{\partial \overline{U}_z}{\partial Z}\right)\right]$$

$$+\frac{\mu_0}{\rho_0 U_{0_z}h_0}\left(\frac{h_0}{l_0}\right)^2\frac{1}{\overline{\rho}}\frac{\partial}{\partial X}\left[\overline{\mu}\left(\frac{\partial \overline{U}_z}{\partial X} + \frac{U_{0_x}}{U_{0_z}}\frac{l_0}{h_0}\frac{\partial \overline{U}_x}{\partial Z}\right)\right]$$

$$+\frac{\mu_0}{\rho_0 U_{0_z}h_0}\left(\frac{h_0}{w_0}\right)^2\frac{1}{\overline{\rho}}\frac{\partial}{\partial Y}\left[\overline{\mu}\left(\frac{\partial \overline{U}_z}{\partial Y} + \frac{U_{0_y}}{U_{0_z}}\frac{w_0}{h_0}\frac{\partial \overline{U}_y}{\partial Z}\right)\right]$$

$$+2\frac{\mu_0}{\rho_0 U_{0_z}h_0}\frac{1}{\overline{\rho}}\frac{\partial}{\partial Z}\left(\overline{\mu}\frac{\partial \overline{U}_z}{\partial Z}\right). \tag{2.20}$$

Due to the presumed dominance of viscous terms ($\partial^2\overline{U}_x/\partial Z$ and $\partial^2\overline{U}_y/\partial Z$) in fluid film lubrication, the modified Reynolds numbers are used for determining the ratio between inertia and viscous forces:

$$\mathrm{Re}_x = \frac{\text{inertia}}{\text{viscous}} = \frac{\rho_0 U_{0_x}h_0^2}{\mu_0 l_0} \tag{2.21}$$

$$\mathrm{Re}_y = \frac{\rho_0 U_{0_y}h_0^2}{\mu_0 w_0} \tag{2.22}$$

$$\mathrm{Re}_z = \frac{\rho_0 U_{0_z}h_0}{\mu_0} \tag{2.23}$$

Hamrock et al. [48] analysed the values of dimensionless numbers for typical cases of journal bearing and thrust bearing pads, and concluded that all three modified Reynolds numbers, together with the squeeze number σ_{s}, are considerably smaller than unity and of the order of h_0/l_0. For a typical thrust bearing pad the ratio between lubricant thickness and length h_0/l_0 is of the order of 10^{-3}, while for a typical journal bearing $h_0/l_0 = \mathcal{O}(10^{-4})$. The width and length of the lubricant film is of the same order for both cases, thus $\mathcal{O}(h_0/w_0) = \mathcal{O}(h_0/l_0)$.

Substituting Eqs. 2.21 to 2.23 into Eqs. 2.18 to 2.20 results in the Navier–

Stokes momentum equations in the following dimensionless form:

$$
\sigma_{\mathrm{s}}\frac{\partial \overline{U}_x}{\partial T} + \left(\mathrm{Re}_x \overline{U}_x \frac{\partial \overline{U}_x}{\partial X} + \mathrm{Re}_y \overline{U}_y \frac{\partial \overline{U}_x}{\partial Y} + \mathrm{Re}_z \overline{U}_z \frac{\partial \overline{U}_x}{\partial Z} \right) =
$$

$$
g_x \frac{l_0}{U_{0_x}^2}\mathrm{Re}_x - \frac{1}{\overline{\rho}}\frac{\partial P}{\partial X} + \frac{1}{\overline{\rho}}\frac{\partial}{\partial Z}\left(\overline{\mu}\frac{\partial \overline{U}_x}{\partial Z} \right)
$$

$$
-\frac{2}{3}\left(\frac{h_0}{l_0}\right)^2 \frac{1}{\overline{\rho}}\frac{\partial}{\partial X}\left[\overline{\mu}\left(\frac{\partial \overline{U}_x}{\partial X} + \frac{U_{0_y}}{U_{0_x}}\frac{l_0}{w_0}\frac{\partial \overline{U}_y}{\partial Y} + \frac{U_{0_z}}{U_{0_x}}\frac{l_0}{h_0}\frac{\partial \overline{U}_z}{\partial Z} \right) \right]
$$

$$
+\frac{2}{\overline{\rho}}\left(\frac{h_0}{l_0}\right)^2 \frac{\partial}{\partial X}\left(\overline{\mu}\frac{\partial \overline{U}_x}{\partial X} \right)
$$

$$
+\frac{1}{\overline{\rho}}\left(\frac{h_0}{w_0}\right)^2 \frac{\partial}{\partial Y}\left[\overline{\mu}\left(\frac{\partial \overline{U}_x}{\partial Y} + \frac{U_{0_y}}{U_{0_x}}\frac{w_0}{l_0}\frac{\partial \overline{U}_y}{\partial X} \right) \right]
$$

$$
+\frac{1}{\overline{\rho}}\frac{\partial}{\partial Z}\left(\overline{\mu}\frac{U_{0_z}}{U_{0_x}}\frac{h_0}{l_0}\frac{\partial \overline{U}_z}{\partial X} \right),
$$

$$(2.24)$$

$$
\sigma_{\mathrm{s}}\frac{\partial \overline{U}_y}{\partial T} + \left(\mathrm{Re}_x \overline{U}_x \frac{\partial \overline{U}_y}{\partial X} + \mathrm{Re}_y \overline{U}_y \frac{\partial \overline{U}_y}{\partial Y} + \mathrm{Re}_z \overline{U}_z \frac{\partial \overline{U}_y}{\partial Z} \right) =
$$

$$
g_y \frac{w_0}{U_{0_y}^2}\mathrm{Re}_y - \frac{1}{\overline{\rho}}\frac{U_{0_x}}{U_{0_y}}\frac{l_0}{w_0}\frac{\partial P}{\partial Y} + \frac{1}{\overline{\rho}}\frac{\partial}{\partial Z}\left(\overline{\mu}\frac{\partial \overline{U}_y}{\partial Z} \right)
$$

$$
-\frac{2}{3}\left(\frac{h_0}{w_0}\right)^2 \frac{1}{\overline{\rho}}\frac{\partial}{\partial Y}\left[\overline{\mu}\left(\frac{U_{0_x}}{U_{0_y}}\frac{w_0}{l_0}\frac{\partial \overline{U}_x}{\partial X} + \frac{\partial \overline{U}_y}{\partial Y} + \frac{U_{0_z}}{U_{0_y}}\frac{w_0}{h_0}\frac{\partial \overline{U}_z}{\partial Z} \right) \right]
$$

$$
+\frac{1}{\overline{\rho}}\left(\frac{h_0}{l_0}\right)^2 \frac{\partial}{\partial X}\left[\overline{\mu}\left(\frac{\partial \overline{U}_y}{\partial X} + \frac{U_{0_x}}{U_{0_y}}\frac{l_0}{w_0}\frac{\partial \overline{U}_x}{\partial Y} \right) \right]
$$

$$
+\frac{2}{\overline{\rho}}\left(\frac{h_0}{w_0}\right)^2 \frac{\partial}{\partial Y}\left(\overline{\mu}\frac{\partial \overline{U}_y}{\partial Y} \right)
$$

$$
+\frac{1}{\overline{\rho}}\frac{\partial}{\partial Z}\left(\overline{\mu}\frac{U_{0_z}}{U_{0_y}}\frac{h_0}{w_0}\frac{\partial \overline{U}_z}{\partial Y} \right),
$$

$$(2.25)$$

$$\sigma_{\mathrm{s}}\frac{U_{0_z}}{U_{0_x}}\frac{h_0}{l_0}\frac{\partial\overline{U}_z}{\partial T}+\left(\mathrm{Re}_z\left(\frac{h_0}{l_0}\right)^2\overline{U}_x\frac{\partial\overline{U}_z}{\partial X}+\mathrm{Re}_y\frac{U_{0_z}}{U_{0_x}}\frac{h_0}{l_0}\overline{U}_y\frac{\partial\overline{U}_z}{\partial Y}\right.$$

$$\left.+\mathrm{Re}_x\left(\frac{U_{0_z}}{U_{0_x}}\right)^2\overline{U}_z\frac{\partial\overline{U}_z}{\partial Z}\right)=$$

$$g_z\frac{h}{U_{0_x}U_{0_z}}\frac{h_0}{l_0}\mathrm{Re}_z-\frac{1}{\rho}\frac{\partial P}{\partial Z}+\frac{2}{\rho}\frac{\partial}{\partial Z}\frac{U_{0_z}}{U_{0_x}}\frac{h_0}{l_0}\left(\overline{\mu}\frac{\partial\overline{U}_z}{\partial Z}\right)$$

$$-\frac{2}{3}\frac{U_{0_z}}{U_{0_x}}\frac{h_0}{l_0}\frac{1}{\rho}\frac{\partial}{\partial Z}\left[\overline{\mu}\left(\frac{U_{0_x}}{U_{0_z}}\frac{h_0}{l_0}\frac{\partial\overline{U}_x}{\partial X}+\frac{U_{0_y}}{U_{0_z}}\frac{h_0}{w_0}\frac{\partial\overline{U}_y}{\partial Y}+\frac{\partial\overline{U}_z}{\partial Z}\right)\right]$$

$$+\frac{1}{\rho}\frac{U_{0_z}}{U_{0_x}}\frac{h_0}{l_0}\left(\frac{h_0}{l_0}\right)^2\frac{\partial}{\partial X}\left[\overline{\mu}\left(\frac{\partial\overline{U}_z}{\partial X}+\frac{U_{0_x}}{U_{0_z}}\frac{l_0}{h_0}\frac{\partial\overline{U}_x}{\partial Z}\right)\right]$$

$$+\frac{1}{\rho}\frac{U_{0_z}}{U_{0_x}}\frac{h_0}{l_0}\left(\frac{h_0}{w_0}\right)^2\frac{\partial}{\partial Y}\left[\overline{\mu}\left(\frac{\partial\overline{U}_z}{\partial Y}+\frac{U_{0_y}}{U_{0_z}}\frac{w_0}{h_0}\frac{\partial\overline{U}_y}{\partial Z}\right)\right].$$

$$(2.26)$$

In Eqs. 2.24 and 2.25 the inertia terms and the gravity term are of the order of h_0/l_0, while the pressure gradient term and the first viscous term are of the order of 1. Term U_{0_z}/U_{0_x} is considered to be of the order of h_0/l_0, while term U_{0_z}/U_{0_y} is of the order of h_0/w_0. The remaining viscous terms in Eqs. 2.24 and 2.25 are of the order of $(h_0/l_0)^2$ or $(h_0/w_0)^2$. In Eq. 2.26 the pressure gradient term is of the order of 1, while all the other terms are of the order of $(h_0/l_0)^2$, $(h_0/w_0)^2$ or even lower, e.g. $(h_0/l_0)^3$.

As stated before, the defined dimensionless numbers (Re_x, Re_y, Re_z and σ_{s}) are of the order of $h_0/l_0=\mathcal{O}\left(10^{-3}\right)$. Therefore, a reasonable next step would be to disregard terms which are of the lower order. By neglecting terms of the order of $(h_0/l_0)^2$, $(h_0/w_0)^2$ or lower, the Navier–Stokes momentum equations take the following form:

$$\sigma_{\mathrm{s}}\frac{\partial\overline{U}_x}{\partial T}+\left(\mathrm{Re}_x\overline{U}_x\frac{\partial\overline{U}_x}{\partial X}+\mathrm{Re}_y\overline{U}_y\frac{\partial\overline{U}_x}{\partial Y}+\mathrm{Re}_z\overline{U}_z\frac{\partial\overline{U}_x}{\partial Z}\right)=$$

$$g_x\frac{l_0}{U_{0_x}^2}\mathrm{Re}_x-\frac{1}{\rho}\frac{\partial P}{\partial X}+\frac{1}{\rho}\frac{\partial}{\partial Z}\left(\overline{\mu}\frac{\partial\overline{U}_x}{\partial Z}\right),$$

$$(2.27)$$

$$\sigma_{\mathrm{s}}\frac{\partial\overline{U}_y}{\partial T}+\left(\mathrm{Re}_x\overline{U}_x\frac{\partial\overline{U}_y}{\partial X}+\mathrm{Re}_y\overline{U}_y\frac{\partial\overline{U}_y}{\partial Y}+\mathrm{Re}_z\overline{U}_z\frac{\partial\overline{U}_y}{\partial Z}\right)=$$

$$g_y\frac{w_0}{U_{0_y}^2}\mathrm{Re}_y-\frac{1}{\rho}\frac{U_{0_x}}{U_{0_y}}\frac{l_0}{w_0}\frac{\partial P}{\partial Y}+\frac{1}{\rho}\frac{\partial}{\partial Z}\left(\overline{\mu}\frac{\partial\overline{U}_y}{\partial Z}\right),$$

$$(2.28)$$

$$\frac{\partial P}{\partial Z} = 0 \qquad \longrightarrow \qquad P = f(X, Y, T). \qquad (2.29)$$

The continuity equation, Eq. 2.17, expressed in a similar way states:

$$\sigma_{\mathrm{s}} \frac{\partial \overline{\rho}}{\partial T} + \mathrm{Re}_x \frac{\partial}{\partial X} \left(\overline{\rho} \overline{U}_x \right) + \mathrm{Re}_y \frac{\partial}{\partial X} \left(\overline{\rho} \overline{U}_y \right) + \mathrm{Re}_z \frac{\partial}{\partial X} \left(\overline{\rho} \overline{U}_z \right) = 0. \qquad (2.30)$$

Derivation of the Reynolds Equation

The order–of–magnitude analysis, presented in the previous section, results in the reduction of general Navier–Stokes momentum equations, Eqs. 2.14 to 2.16, into Eqs. 2.27 to 2.29 by neglecting terms of the order of $(h_0/l_0)^2$, $(h_0/w_0)^2$ or lower. Therefore, the starting point for the derivation of the Reynolds equation are Eqs. 2.27 to 2.29.

Neglecting the terms of the order of h_0/l_0 or h_0/w_0, and keeping only the terms of the order of 1, further reduces Eqs. 2.27 and 2.28 into:

$$\frac{1}{\overline{\rho}} \frac{\partial P}{\partial X} = \frac{1}{\overline{\rho}} \frac{\partial}{\partial Z} \left(\overline{\mu} \frac{\partial \overline{U}_x}{\partial Z} \right), \qquad (2.31)$$

$$\frac{1}{\overline{\rho}} \frac{U_{0_x}}{U_{0_y}} \frac{l_0}{w_0} \frac{\partial P}{\partial Y} = \frac{1}{\overline{\rho}} \frac{\partial}{\partial Z} \left(\overline{\mu} \frac{\partial \overline{U}_y}{\partial Z} \right). \qquad (2.32)$$

Expanding Eqs. 2.31 and 2.32 into dimensional forms results in:

$$\frac{\partial p}{\partial x} = \frac{\partial}{\partial z} \left(\mu \frac{\partial U_x}{\partial z} \right), \qquad (2.33)$$

$$\frac{\partial p}{\partial y} = \frac{\partial}{\partial z} \left(\mu \frac{\partial U_y}{\partial z} \right). \qquad (2.34)$$

For the steady–state conditions, pressure p is a function of x and y, shown by Eq. 2.29. By directly integrating Eqs. 2.33 and 2.34 the general expressions for velocity gradients are attained:

$$\frac{\partial U_x}{\partial z} = \frac{z}{\mu} \frac{\partial p}{\partial x} + \frac{\tilde{C}_1}{\mu}, \qquad (2.35)$$

$$\frac{\partial U_y}{\partial z} = \frac{z}{\mu} \frac{\partial p}{\partial y} + \frac{\tilde{C}_3}{\mu}, \qquad (2.36)$$

19

where $\tilde{C}_1$ and $\tilde{C}_3$ are integration constants. While viscosity μ can change considerably across the thin film (z–direction) due to temperature variations, an average value of viscosity across the film can be taken as constant in most fluid film applications [48]. A strong argument for using this approximation is the fact that the rheological properties of the lubricant in the industrial applications, e.g. metal forming, are usually unknown or incomplete [11]. Therefore, temperature, pressure and shear rate dependence of viscosity is, in most cases, only partially known. While this approximation limits the value of viscosity across the film to a single averaged value, it does not restrict its variation in the directions parallel to the flow, i.e. x– and y–direction. Integrating Eqs. 2.35 and 2.36 and using the cross–film averaged viscosity assumption results in the following velocity components:

$$U_x = \frac{z^2}{2\mu}\frac{\partial p}{\partial x} + \tilde{C}_1\frac{z}{\mu} + \tilde{C}_2, \tag{2.37}$$

$$U_y = \frac{z^2}{2\mu}\frac{\partial p}{\partial y} + \tilde{C}_3\frac{z}{\mu} + \tilde{C}_4. \tag{2.38}$$

Assuming zero slip condition between the fluid and solid interface, the velocity boundary conditions state:

$$z = 0 \qquad \longrightarrow \qquad U_x = U_{a_x},\ U_y = U_{a_y},\ U_z = U_{a_z}$$

$$z = h \qquad \longrightarrow \qquad U_x = U_{b_x},\ U_y = U_{b_y},\ U_z = U_{b_z}$$

where subscript a denotes the lower flat surface while b denotes the upper curved surface. Applying the boundary conditions to Eqs. 2.37 and 2.38 velocity components and their gradients are expressed as:

$$U_x = -z\left(\frac{h-z}{2\mu}\right)\frac{\partial p}{\partial x} + U_{a_x}\frac{h-z}{h} + U_{b_x}\frac{z}{h}, \tag{2.39}$$

$$U_y = -z\left(\frac{h-z}{2\mu}\right)\frac{\partial p}{\partial y} + U_{a_y}\frac{h-z}{h} + U_{b_y}\frac{z}{h}, \tag{2.40}$$

$$\frac{\partial U_x}{\partial z} = \left(\frac{2z-h}{2\mu}\right)\frac{\partial p}{\partial x} - \frac{U_{a_x} - U_{b_x}}{h}, \tag{2.41}$$

$$\frac{\partial U_y}{\partial z} = \left(\frac{2z - h}{2\mu}\right)\frac{\partial p}{\partial y} - \frac{U_{a_y} - U_{b_y}}{h}, \tag{2.42}$$

Expressing the continuity equation, Eq. 2.17, in its integral form gives:

$$\int_0^h \left(\frac{\partial \rho}{\partial t} + \frac{\partial}{\partial x}(\rho U_x) + \frac{\partial}{\partial y}(\rho U_y) + \frac{\partial}{\partial z}(\rho U_z)\right)\mathrm{d}z = 0. \tag{2.43}$$

The Leibniz rule for differentiation under the integral sign states [50]:

$$\frac{\mathrm{d}}{\mathrm{d}x}\left(\int_{a(x)}^{b(x)} f(x,t)\,\mathrm{d}t\right) = f(x,b(x))\frac{\mathrm{d}}{\mathrm{d}x}b(x) - f(x,a(x))\frac{\mathrm{d}}{\mathrm{d}x}a(x) \\ + \int_{a(x)}^{b(x)} \frac{\partial}{\partial x}f(x,t)\,\mathrm{d}t. \tag{2.44}$$

Assuming constant mean density ρ across the film (the same principle as for viscosity) together with the Leibniz rule, the velocity component terms in their integrated forms are expressed as:

$$\int_0^h \frac{\partial}{\partial x}(\rho U_x)\,\mathrm{d}z = -\rho U_{b_x}\frac{\partial h}{\partial x} + \frac{\partial}{\partial x}\left(\rho \int_0^h U_x\,\mathrm{d}z\right), \tag{2.45}$$

$$\int_0^h \frac{\partial}{\partial y}(\rho U_y)\,\mathrm{d}z = -\rho U_{b_y}\frac{\partial h}{\partial y} + \frac{\partial}{\partial y}\left(\rho \int_0^h U_y\,\mathrm{d}z\right), \tag{2.46}$$

$$\int_0^h \frac{\partial}{\partial z}(\rho U_z)\,\mathrm{d}z = \frac{\partial}{\partial z}\left(\rho \int_0^h U_z\,\mathrm{d}z\right) = \rho\left(U_{b_z} - U_{a_z}\right). \tag{2.47}$$

Now, the integrated continuity equation takes the following form:

$$h\frac{\partial \rho}{\partial t} - \rho U_{b_x}\frac{\partial h}{\partial x} + \frac{\partial}{\partial x}\left(\rho \int_0^h U_x\,\mathrm{d}z\right) - \rho U_{b_y}\frac{\partial h}{\partial y} + \frac{\partial}{\partial y}\left(\rho \int_0^h U_y\,\mathrm{d}z\right) \\ + \rho\left(U_{b_z} - U_{a_z}\right) = 0. \tag{2.48}$$

The two integrals in Eq. 2.48 represent the volume flow rates per unit width:

$$q_x' = \int_0^h U_x\,\mathrm{d}z, \tag{2.49}$$

$$q_y' = \int_0^h U_y\,\mathrm{d}z. \tag{2.50}$$

Substituting Eqs. 2.37 and 2.38 into Eqs. 2.49 and 2.50 results in:

$$q_x' = \int_0^h U_x\,\mathrm{d}z = -\frac{h^3}{12\mu}\frac{\partial p}{\partial x} + \frac{U_{a_x} + U_{b_x}}{2}, \tag{2.51}$$

$$q'_y = \int_0^h U_y \, \mathrm{d}z = -\frac{h^3}{12\mu} \frac{\partial p}{\partial y} + \frac{U_{a_y} + U_{b_y}}{2}. \tag{2.52}$$

Finally, introducing the flowrates into Eq. 2.48 yields the general Reynolds equation:

$$\frac{\partial}{\partial x}\left(\frac{\rho h^3}{12\mu}\frac{\partial p}{\partial x}\right) + \frac{\partial}{\partial y}\left(\frac{\rho h^3}{12\mu}\frac{\partial p}{\partial y}\right) =$$
$$\frac{\partial}{\partial x}\left(\frac{\rho h \left(U_{a_x} + U_{b_x}\right)}{2}\right) + \frac{\partial}{\partial y}\left(\frac{\rho h \left(U_{a_y} + U_{b_y}\right)}{2}\right)$$
$$-\rho U_{b_x}\frac{\partial h}{\partial x} - \rho U_{b_y}\frac{\partial h}{\partial y} + \rho\left(U_{b_z} - U_{a_z}\right) + h\frac{\partial \rho}{\partial t}, \tag{2.53}$$

The form in which the Reynolds equation is usually represented in the literature states [48]:

$$\frac{\partial}{\partial x}\left(\frac{\rho h^3}{12\mu}\frac{\partial p}{\partial x}\right) + \frac{\partial}{\partial y}\left(\frac{\rho h^3}{12\mu}\frac{\partial p}{\partial y}\right) =$$
$$\frac{\partial}{\partial x}\left(\frac{\rho h \left(U_{a_x} + U_{b_x}\right)}{2}\right) + \frac{\partial}{\partial y}\left(\frac{\rho h \left(U_{a_y} + U_{b_y}\right)}{2}\right) + \frac{\partial(\rho h)}{\partial t}.$$
$$\tag{2.54}$$

Comparing equations 2.53 and 2.54 results in the implication that the following expression is valid:

$$\frac{\partial h}{\partial t} = U_{b_z} - U_{a_z} - U_{b_x}\frac{\partial h}{\partial x} - U_{b_y}\frac{\partial h}{\partial y}. \tag{2.55}$$

In order to prove this statement a total derivative of film thickness $h = f(x, y, t)$ is analysed:

$$\mathrm{D}h = \frac{\partial h}{\partial t}\,\mathrm{d}t + \frac{\partial h}{\partial x}\,\mathrm{d}x + \frac{\partial h}{\partial y}\,\mathrm{d}y,$$

together with the temporal total derivative:

$$\frac{\mathrm{D}h}{\mathrm{D}t} = \frac{\partial h}{\partial t} + \frac{\partial h}{\partial x}\frac{\mathrm{d}x}{\mathrm{d}t} + \frac{\partial h}{\partial y}\frac{\mathrm{d}y}{\mathrm{d}t}.$$

Substituting

$$U_{b_x} = \frac{\mathrm{d}x}{\mathrm{d}t}, \qquad U_{b_y} = \frac{\mathrm{d}y}{\mathrm{d}t} \qquad \text{and} \qquad \frac{\mathrm{D}h}{\mathrm{D}t} = U_{b_z} - U_{a_z}$$

into the temporal total derivative results in:

$$U_{b_z} - U_{a_z} = \frac{\partial h}{\partial t} + U_{b_x}\frac{\partial h}{\partial x} + U_{b_y}\frac{\partial h}{\partial y}$$

$$\longrightarrow \quad \frac{\partial h}{\partial t} = U_{b_z} - U_{a_z} - U_{b_x}\frac{\partial h}{\partial x} - U_{b_y}\frac{\partial h}{\partial y},$$

thus proving that Eq. 2.55 is valid, and that the two forms of the Reynolds equation, Eqs. 2.53 and 2.54, are indeed the same equation. Finally, the Reynolds equation can be written using the vector notation:

$$\underbrace{\nabla_s\bullet\left(\frac{\rho h^3}{12\mu}\nabla_s p\right)}_{\text{Poiseuille}} = \underbrace{\nabla_s\bullet\left[\frac{\rho h\left(\mathbf{U}_a + \mathbf{U}_b\right)}{2}\right]}_{\text{Couette}} \quad + \quad \underbrace{\rho\frac{\partial h}{\partial t} \quad + \quad h\frac{\partial \rho}{\partial t}}_{\text{Squeeze and local expansion}} \quad ,$$

(2.56)

where ∇_s and $\nabla_s\bullet$ are two–dimensional surface gradient and divergence operators, respectively. For more information regarding the physical meaning of specific terms comprising the Reynolds equation one can refer to [48].

2.2.2. Cavitation

When considering thin film flows one must take into account the possibility of cavitation. Cavitation may occur locally, between the asperities, and globally in divergent parts of the contact [37]. Since cavitation may occur multiple times inside a single contact, the mass conservation of fluid passing through rupture and reformation boundaries needs to be accounted for properly.

One of the first cavitation models for the Reynolds equation, the Swift-Stieber model [51, 52], considered a zero pressure gradient at the rupture boundary. However, the model did not take into account mass conservation in the cavitation zone, thus the correct location of the reformation was not unknown. The mass–conserving cavitation models are usually based on the Jakobsson–Floberg–Olson (JFO) boundary conditions proposed by Jakobsson and Floberg [53] and Olsson [54]. The JFO boundary conditions satisfy the mass conservation between the full–film (non–cavitating) and cavitating regions, Fig. 2.2. At the rupture boundary B_{rup} the zero pressure gradient condition applies with a constant cavitation pressure [55]:

$$\nabla_s p = 0 \qquad p = p_{\text{cav}},$$

(2.57)

23
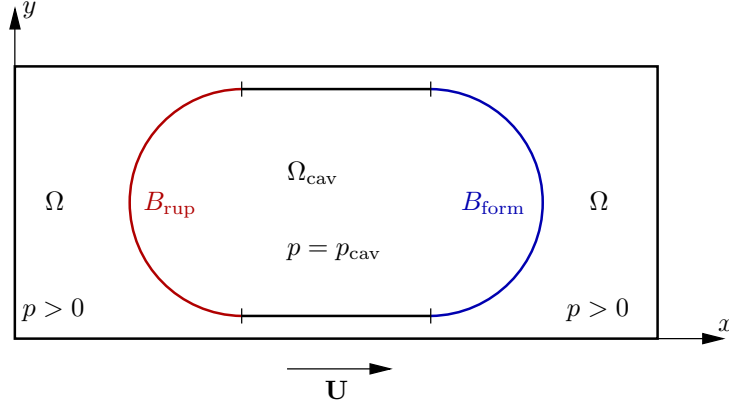
Figure 2.2: Full–film and cavitating regions.

where p_{cav} is the cavitation pressure of the fluid. At the formation boundary B_{form} the non–zero pressure gradient represents feeding of the full film zone, Fig. 2.3, by the cavitating region [55]:

$$\frac{h^2}{12\mu}\nabla_{\text{s}}p = \frac{\mathbf{U}_{\text{a}} + \mathbf{U}_{\text{b}}}{2}\left(1 - \theta_{\text{form}}\right),\qquad(2.58)$$

where $\theta_{\text{form}} = \rho_{\text{form}}/\rho_{\text{cav}}$ is the fractional film content in the cavitating region and ρ_{form} is the density of gas–liquid mixture next to the formation boundary in the upwind direction.
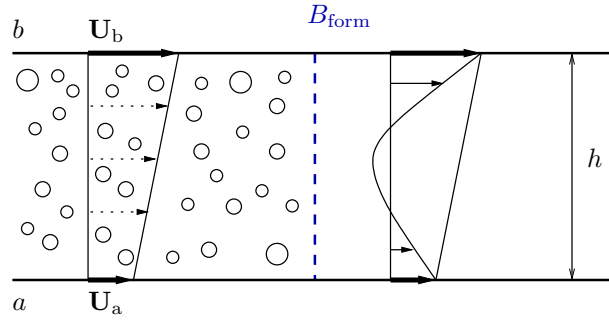
Figure 2.3: Feeding of the full–film zone through the formation boundary.

The first efficient algorithm for calculating cavitation was developed by Elrod and Adams [56]. Their algorithm is based on the Finite Difference Method and implicitly incorporates JFO boundary conditions by iteratively dividing the computational domain into full–film and cavitating regions. Elrod and Adams

introduced a switch function g defined as:

$$\begin{aligned}\theta \geq 1 &\quad\longrightarrow\quad \text{full-film} &\longrightarrow&\quad g = 1 \\ \theta < 1 &\quad\longrightarrow\quad \text{cavitating} &\longrightarrow&\quad g = 0,\end{aligned}$$
(2.59)

which terminates the pressure term of the Reynolds equation inside the cavitating zone, thus only leaving the Couette flow. They also incorporated the fractional film content θ into the Reynolds equation treating the lubricant flow inside the cavitating region as a two–phase flow of liquid lubricant and gas with a homogeneous density, while the flow inside the full–film region was treated as a compressible flow of liquid lubricant with a constant bulk modulus. The Reynolds equation derived by Elrod and Adams has the following form:

$$\nabla_{\mathrm{s}}\bullet\left(g\frac{\beta h^3}{12\mu}\nabla_{\mathrm{s}}\,\theta \right) = \nabla_{\mathrm{s}}\bullet\left[\frac{\theta h\left(\mathbf{U}_{\mathrm{a}} + \mathbf{U}_{\mathrm{b}}\right)}{2} \right],$$
(2.60)

where $\beta = \rho\left(\partial p/\partial\rho\right)$ is the fluid bulk modulus. While the Elrod–Adams algorithm has been successfully applied in the lubrication theory [37], the nature of Eq. 2.60 changes from elliptic in full–film region to hyperbolic in cavitating region which, together with the abrupt changes in switch function g, often leads to instabilities and convergence problems. Therefore, many improvements to the Elrod–Adams algorithm have been proposed over the years.

One of the more significant improvements to the Elrod cavitation algorithm was introduced by Vijayaraghavan and Keith [57]. Their modified version automatically predicts film rupture and formation boundaries for grooved bearing calculations. They used an implicit numerical finite difference scheme, based on the approximate factorisation technique, in both orthogonal and non-orthogonal grids, which significantly improved numerical stability of the cavitation algorithm. Their algorithm was also suitable for unsteady calculations, where time accurate solutions were achieved using Newton iterations. In 2007 Sahlin et al. [58] developed a general cavitation algorithm which considers arbitrary density–pressure relation of the fluid. Their finite difference algorithm is similar to that of Elrod, also using a switch function which terminates the pressure gradient inside the cavitating region. Qiu and Khonsari [4] used the algorithm developed by Vijayaraghavan and Keith [57] together with the Multigrid method and the iterative Gauss–Seidel relaxation scheme within the finite difference framework, resulting

in the improvement of convergence. They tested their algorithm on a dimple–enhanced seal/thrust bearing structure. Fesanghary and Khonsari [59] proposed another enhancement to the Elrod algorithm by using a continuous switch function g instead of a binary one. They reported that the proposed algorithm used together with the successive over–relaxation technique significantly improves the solution convergence compared to the original algorithm using a binary switch function. Bayada and Chupin [38] presented a homogeneous mixture model employing a void fraction variable to quantify the intensity of cavitation, allowing the value of pressure to fall below the cavitation pressure in the cavitating area. Their model accounts for compressibility effects and viscosity changes both in the full–film and cavitating regions, and is considered to be an approximation of the Elrod model by using a smooth compressibility law over the whole lubricated contact. They compared their results to the Elrod cavitation model showing discrepancies in light load situations where the effects of sub–cavitation pressures are noticeable.

Giacopini et al. [60] used the concept of complementarity for resolving cavitation problems where the reformation of liquid film occurs. They discretised the Reynolds equation using the Finite Element Method and constructed a linear complementarity problem (LCP) for which solution techniques already existed. By formulating a linear complementarity problem the need for using a single differential equation with a switch function g valid through both regions was eliminated. Bertocchi et al. [3] extended the one–dimensional incompressible model from Giacopini et al. [60] to two–dimensional model including fluid compressibility, piezoviscosity, and non–Newtonian effects. Almqvist et al. [61] derived a Reynolds equation LCP model based on the constant bulk modulus compressibility formulation. It was derived from an expression for the mass flow, thus leading directly to a linear complementarity formulation. This approach in contrast to the model by Giacopini et al. [60] where the pressure–density relation is inserted into the Reynolds equation, leading to a discussion which terms should be cancelled out before reaching the complementarity formulation. Almqvist et al. [61] introduced a change of variables into the derivation, thus eliminating the iterative solution process. Later, Almqvist and Wall [62] extended the mathematical model from [61] to include more general pressure–density relationships and en-

abling viscosity and film thickness to depend on the pressure. These extensions allowed the authors to employ the implemented model on elastohydrodynamic (EHL) lubrication problems.

Woloszynski et al. [63] developed their own efficient cavitation algorithm called Fischer–Burmeister–Newton–Schur (FBNS) by reformulating the Elrod–Adams algorithm. The algorithm was implemented using the Finite Volume Method. Their system of equations arising from the reformulation is continuously differentiable and unconstrained which enables the use of gradient–based solvers. Also, when considering cavitational effects the computational cost of solving their system of equations does not increase significantly compared to the computational cost when cavitation is neglected. The authors compared the efficiency of their own model to the previous algorithms by Ausas et al. [64], Bertocchi et al. [3] and Fesanghary and Khonsari [59]. According to the report, the model developed by Woloszynski et al. [63] is significantly faster than the other models, up to two orders of magnitude.

In conclusion, there is a significant number of different approaches to modelling cavitation in thin film flows. Some of them are developed for specific types of problems, while others are more general. However, there is no single universal method which is easy to implement and computationally efficient at the same time. The rule of thumb is that for more complex problems with dense computational grids efficient algorithms should be used, despite the complexity of their implementation.

2.3. Flow Factors and Averaged Reynolds Equation

In the previous section the Reynolds equation, Eq. 2.56, was presented, allowing the calculation of lubricant hydrodynamic flow between two smooth surfaces in contact. Real surfaces, seemingly smooth, have a large number of micro–asperities (roughness) which can have significant effect on the lubricant flow as their size may be comparable with film thickness in the lubricated contact. Depending on the lubricant thickness between two real surfaces in contact, the lubricant flow can

be divided into four regimes [13]: **hydrodynamic thick** film, **hydrodynamic thin** film, **mixed** and **boundary** lubrication regime, Fig. 2.4. In the hydrodynamic regime two surface are completely separated by the fluid [8]. In the **thick film** hydrodynamic regime, two surfaces are separated enough that the roughness does not influence the fluid flow. Therefore surfaces can be considered smooth during the flow calculations. In the **thin film** hydrodynamic regime surfaces are still completely separated, however surface roughness significantly influences the lubricant flow. In the **mixed** regime surfaces are partially in contact, thus the contact pressure is shared between the asperities and the fluid. In the **boundary** regime nearly the whole contact pressure is carried by the asperities, while the fluid is found in traces inside asperity valleys.

Hydrodynamic thick film regime

Hydrodynamic thin film regime

Mixed regime

Boundary regime
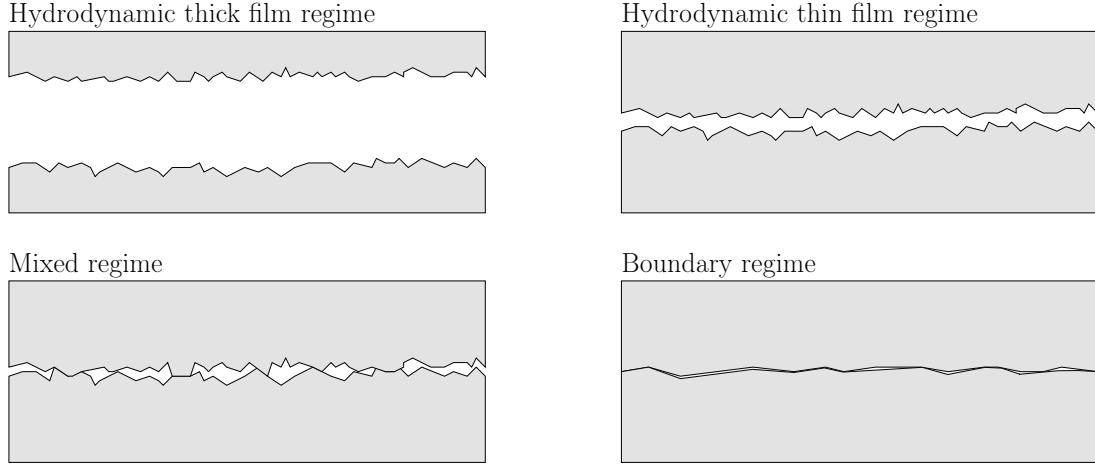
Figure 2.4: Lubrication regimes.

One approach for capturing the effects of surface roughness on fluid flow is to utilise the Reynolds equation, Eq. 2.56, and increase the computational mesh density up to the point where the surface texture is deterministically represented. However, this approach is not applicable for calculating film flow in geometries significantly larger than the texture of their surfaces (e.g. journal bearings, cylinder liners, wires) due to the significant memory consumption and excessive computational efforts [65].

The other approach is to introduce a modification to the Reynolds equation allowing the surface roughness to effect the thin film pressure, while maintaining the calculation on the macroscopic level. In this approach surface topography

is represented statistically, inevitably losing some local asperity information [65]. This approach, however, is negligibly more computationally expensive than the calculation of smooth surface hydrodynamic flow. Using the stochastic theory in describing surface roughness Christensen [66] derived two forms of averaged Reynolds equation for calculating hydrodynamic lubrication of journal bearings with rough surfaces. His equations were limited to one–dimensional longitudinal or transversal roughness. Patir and Cheng [67, 9] developed an approach enabling the calculation of thin film flow between two rough surfaces by introducing correction factors, called flow factors, into the Reynolds equation, Eq. 2.56. The form of the Reynolds equation containing flow factors was named averaged Reynolds equation by the authors, and can be expressed as:

$$
\nabla_{s}\bullet\left(\phi_{xy}\frac{\rho h^3}{12\mu}\nabla_s p\right) = \nabla_{s}\bullet\left[\frac{\rho h\left(\mathbf{U}_a + \mathbf{U}_b\right)}{2}\right] - \nabla_{s}\bullet\left[\frac{\phi_s\rho\left(\mathbf{U}_a - \mathbf{U}_b\right)}{2}\right]R_q + \frac{\partial(\rho h)}{\partial t},
$$

(2.61)

where ϕ_{xy} is the pressure flow factor, ϕ_s is the shear flow factor and $R_q = \sqrt{R_{q_a}^2 + R_{q_b}^2}$ is the combined root mean squared (RMS) surface roughness of surfaces a and b.

The assumption of this approach is that the distance between two calculation points is large enough to include a considerable number of asperities, allowing the use of statistical representation, but still small compared to the geometry for which the calculation is being performed. The use of flow factors does not restrict the calculations to longitudinal or transversal cases, thus enabling the application to real three–dimensional surfaces. Another advantage is the ability to calculate thick film hydrodynamic, thin film hydrodynamic and mixed lubrication regimes continuously, using a single equation. However, the flow factors derived by Patir and Cheng [67, 9] are not suited for contacts with large fractional areas, i.e. small film thicknesses $h/R_q < 1$. In order to expand the application of averaged Reynolds equation to the near–boundary regime Wilson and Marsault [2] derived semi–empirical equations for flow factors which cover the full range of contact conditions.

The flow factors are determined by carrying out a significant number of deterministic film flow calculations. Once obtained, the use of flow factors inside the Reynolds equation has negligible effect on computational performance compared

to the hydrodynamic cases, as mentioned before. The only extra computation is the calculation of flow factors via analytical equations depending on the value of film thickness at the computational point. The disadvantages of this approach are: the lack of theoretical explanation on how many times the deterministic calculation needs to be conducted in order to acquire statistically relevant results and uncertainty about how to truncate the solution in order to reduce the influence of the boundary conditions.

2.4. Contact Models

Depending on the type and application of a lubricated machine element it can operate in different lubrication regimes. In case of a journal bearing and cylinder liner the mixed lubrication regime can significantly reduce their operational lives due to increased wear, while the appearance of boundary lubrication regime usually results in their immediate failure.

In case of metal forming processes the appropriate lubrication regime is essential in producing satisfactory surface quality of the product. In wire manufacturing, e.g. drawing and rolling, the mixed lubrication regime is the main operating regime [68], with parts of the contact operating in the boundary regime. It was shown in the previous section that the contact pressure is shared between the lubricant and asperities during the mixed and boundary lubrication regimes, Fig. 2.4. Hence, the algorithm for calculating lubricated contact in metal forming needs to consider solid to solid contact between asperities, which are being deformed (flattened) under the influence of contact pressure. Depending on the amount of applied force, asperities will undergo elastic or even plastic deformations.

In order to calculate dry contact between two surfaces, their topographies need to be modelled or characterised appropriately. This is usually done in two ways [65]:

- statistical modelling,

- deterministic characterisation.

2.4.1. Statistical Contact Models

Due to random characteristics of real surfaces, their topographies are quite complex and cannot be easily described and modelled. Greenwood and Williamson (GW) [69] derived an analytical model based on the Hertzian contact theory for elastic deformation of hemispherical asperities under normal contact force. They assumed constant asperity radius and Gaussian distribution of asperities' heights around the mean surface plane. Due to the assumption of Gaussian distribution function the integrals of the GW model were calculated numerically until Jackson [70] derived the closed–form solutions to the GW model. This model was later extended to include curved surfaces [71], two misaligned rough surfaces [72], non–uniform radii of asperities [73], anisotropic surfaces [74], etc. In his work McCool [74] showed that the anisotropic model with varying radii gives very good agreement to the original isotropic GW model with constant asperity radii, thus confirming that the original assumptions, which greatly simplifies the calculation, do not limit the applicability of the model.

In order to take plasticity into account Chang, Etsion and Bogy [75] (CEB) developed an analytical elastic–perfectly–plastic asperity contact model applicable to small asperity deformations, near the asperity tip, using a fixed relation between the hardness and yield strength of the material. Green [76] derived a closed–form solution for the plastic deformation part of the CEB model. Jackson and Green (JG) [77] performed the finite element simulations of elastic–perfectly–plastic contact between deformable hemisphere and a rigid flat. The authors used their results to derive a statistical model of elastic–perfectly–plastic rough surface contact [78] which alleviates the assumption of a fixed hardness–yield strength relation. They adopted the GW model for elastic deformation, and derived new analytical equations for plastic deformation using the calculated contact area and force values from the finite element simulations. Their model was derived for smaller deformations where the ratio of contact radius and undeformed asperity radius is less than 0.41. Wadwalkar et al. [79] expanded the JG model to include large plastic deformations. The authors conducted finite element simulations and used the results to derive the analytical model. Peng et al. [80] performed finite element simulations of contact between a rigid flat and a single

hemisphere with substrate. The authors used simulation results for deriving their own elastic–perfectly–plastic rough surface contact model.

All these models require inputs regarding the properties of surfaces for which the calculation is performed. The usual inputs are mean asperity curvature, asperity density, RMS surface roughness and material properties, mainly Young's modulus, Poisson's ratio and yield strength. The surface parameters are commonly calculated using spectral moments acquired by analysing surface roughness measurements [70, 81]. One of the disadvantages of these models is the characterisation of surface topography using only a few parameters, where the same parameters can be calculated for quite different topographies. The other disadvantage is the use of a mean value of asperity curvature which can vary considerably between individual asperities [65]. The main advantages are straightforward implementation and computational efficiency which is of great importance in metal forming simulations.

2.4.2. Deterministic Contact Models

Using a well–implemented statistical contact model does provide computational efficiency, however, due to the simplifications presented in the previous section, they can give uncertain results. On the other hand, using a deterministic approach to normal contact modelling enables the direct usage of measured surface topographies while being computationally more expensive. Using the Finite Element Method to calculate the normal contact between realistic surfaces is possible [82], however, if the surface topography encompasses high frequencies the density of a computational grid (mesh) significantly increases, especially in case of three–dimensional simulations, resulting in high memory consumption and high computational efforts. The advantage of the finite element approach is the choice of material models and operating conditions (friction, tangential motion, etc.). The other approach is to use either closed–form analytical solutions for specific surface topographies, or models based on the Fast Fourier Transformation (FFT). Westergaard [83] derived an exact closed–form solution for the two–dimensional case of normal contact between a rigid plane and a single period sinusoidal surface. Johnson et al. [84] combined the two solutions from Westergaard and derived

simple analogous three–dimensional equations. Stanley and Kato [85] introduced a three–dimensional elastic contact model between a rigid plane and a half–space with arbitrary surface heights. Their model uses an exact result in linear elasticity and the FFT method to calculate surface normal displacements and contact pressures. The method implicitly incorporates the multiscale nature of surface topography, and naturally allows for asperity interaction and contact agglomeration. Almqvist et al. [86] modified the Stanley–Kato algorithm and expanded it to include elastic–perfectly–plastic deformations. For more details regarding their implementation the reader is referred to [87]. Using a deterministic normal contact model based on the FFT method allows relatively fast calculations of pressure, deformation and contact area of measured surfaces. These calculations can be performed during the runtime of the macroscopic simulation (e.g. journal bearing, wire rolling), or as a pre–processing step where a database of required values (e.g. contact pressure, film thickness) is created.

2.5. Thermal Modelling of a Thin Film

In highly loaded hydrodynamic contacts where two surfaces are slipping, i.e. have different velocities, shearing of the lubricant can cause significant heat dissipation. In the mixed and boundary lubrication regimes, aside from the lubricant shearing, the friction between sliding asperities generates substantial heat. Changes of the lubricant temperature lead to variations in its properties, mainly density and viscosity, which can significantly influence both film thickness and traction characteristics of the contact [41].

Lai and Cheng [88] analysed simple sliding contacts between rough surfaces under lubricated conditions. They assumed a linear distribution of temperature across the lubricant film and used the well known approach of Carslaw and Jaeger [89] for calculating temperature increase of the moving surfaces. Zhu and Hu [90] presented a numerical framework for calculating lubricated point contact using a measured three–dimensional surface roughness. Their framework was capable of capturing the entire transition from hydrodynamic to boundary lubrication regime, where they used the reduced form of the Reynolds equation. The thermal analysis was conducted by calculating surface flash temperatures using the

approach developed by Zhu and Chu [91]. Gao et al. [92] and Zhao et al. [93] were one of the first authors to employ the FFT method in order to accelerate the calculation of surface temperatures. The principle of surface flash temperature combined with the Reynolds equation for analysing point contact under mixed lubricated was used by different authors, e.g. Liu and Wang [94], Wang and Hu [95], Deolalikar et al. [96].

While the surface flash temperature was regularly used in lubricated contact analysis, more information is required regarding the temperature distribution inside the lubricant in order to gain better reflection on rheological properties, and consequently traction characteristics of the contact. Solving the energy equation of the lubricant [41] is necessary in order to obtain its temperature distribution. The common approach to solving the energy equation of thin film flow is to assume a particular shape of the temperature profile across the film thickness, reducing the three–dimensional analysis to two dimensions. This approach avoids the discretisation of the computational domain across the film thickness, which in return reduces computational time and is in accordance with the calculation of the Reynolds equation, also being two–dimensional. Salehizadeh and Saka [97] analysed a pure rolling line contact problem with the assumption of parabolic temperature profile of the lubricant using the one–dimensional energy equation with the Reynolds equation. Kazama et al. [98] also analysed the line contact comparing the temperature profile approach to the full two–dimensional model. The results showed that the two approaches give different results in the inlet region of the contact, mainly due to the effects of reverse flow, where the profile assumption model gives higher temperatures. However, in the high pressure region both methods gave the same mean temperature. Sui and Sadeghi [99] performed a finite element analysis of a thermal line contact and confirmed the parabolic shape of the temperature profile in the high–pressure region. Lee et al. [100], Ehret et al. [101] and Kim et al. [41] used the same temperature profile method for analysing elliptical and point contacts. In their first paper Kim et al. [41] used a parabolic temperature profile together with their elastohydrodynamic model for analysing circular contact with a Newtonian lubricant. In their second paper Kim et al. [42] expanded their model to consider non-Newtonian effects. Kim and Sadeghi [102] performed a thermal three–dimensional analysis of point

contact and showed that the film temperature profile in the high–pressure region was close to the parabolic shape. Recently Yan et al. [44] examined the effect of surface texture orientation on the thermal mixed lubrication using the same parabolic temperature profile as Kim et al. [42].

When considering metal forming analyses, especially wire rolling, a wide range of approaches have been developed for modelling heat transfer through the contacting interface [103]. Tseng [103, 104] gave a detailed review of frequently used heat transfer methods in rolling processes. The three major approaches were specifically discussed: prescribed heat flux on the contact boundary, prescribed convective heat transfer coefficient on the contact boundary and prescribed thermal contact conductance along the interface. After examining different approaches, the author concluded that the prescribed thermal contact conductance approach is closest to the actual physical process taking place and is the most dependable to be used to simulate thermal interface phenomena in rolling processes.

2.6. Lubricant Properties

When calculating lubricated contact the use of appropriate lubricant properties is necessary in order to capture proper film pressure, thickness and traction characteristics. Considering the Reynolds equation the important properties are density and viscosity of the lubricant film. When dealing with thermal analysis of a contact the information regarding specific heat and thermal conductivity of the lubricant is necessary. All of the mentioned properties are pressure and temperature dependent [105, 106], where viscosity is a property most sensitive to changes.

2.6.1. Viscosity

Fluid viscosity can vary several orders of magnitude with pressure changes [107]. Beside the pressure and temperature dependence, viscosity also depends on the shear stress in case of a non-Newtonian lubricant.

Pressure and Temperature Dependence

One of the commonly used pressure–viscosity relations is the Barus law:

$$\mu_{\mathrm{B}} = \mu_0 \exp\left(\alpha p\right), \tag{2.62}$$

where α is the pressure–viscosity coefficient and μ_0 is the viscosity at ambient pressure. Barus law gives satisfactory results below 0.5 GPa [108], compared to the experimental results. Above the 0.5 GPa the inaccuracy of Eq. 2.62 significantly increases, especially under high ambient temperatures. The main reason behind the low accuracy under the specified conditions is the dependence of the pressure–viscosity coefficient on pressure and temperature, whereas in Eq. 2.62 it is considered constant.

Following Barus' work Roelands [109] and Houpert [110] derived a more detailed expression for calculating viscosity [108, 105]:

$$\mu_{\mathrm{H}} = \mu_{\mathrm{R}} \exp\left(-\beta^*(T - T_0)\right), \tag{2.63}$$

where H and R stand for Houpert and Roelands respectively, β^* is the temperature–viscosity coefficient and T_0 is the ambient temperature. The Roelands viscosity μ_{R} is expressed as:

$$\mu_{\mathrm{R}} = \mu_0 \exp\left(\alpha^* p\right), \tag{2.64}$$

where α^* is the pressure–viscosity coefficient. Both coefficients, α^* and β^*, are pressure– and temperature–dependent. Roelands–Houpert equations are widely used equations for calculating pressure and temperature dependence of viscosity. However, Bair [111, 112] examined the accuracy of Eq. 2.63, and showed that it does not correctly capture pressure–viscosity behaviour at very high pressures and gives debatable temperature–viscosity results compared to the experimental data [106].

Yet another approach is to use Doolittle's free volume model [113], based on the assumption that the relative volume of molecules per unit free volume dictates the fluid's resistance to flow [3]. The Doolittle relation is defined as [107]:

$$\mu(p,T) = \mu_{\mathrm{R}} \exp\left[BR_0 \left(\frac{\dfrac{V_\infty}{V_{\infty\mathrm{R}}}}{\dfrac{V}{V_{\mathrm{R}}} - R_0 \dfrac{V_\infty}{V_{\infty\mathrm{R}}}} - \frac{1}{1 - R_0} \right) \right], \tag{2.65}$$

where B and R_0 are lubricant–dependent constants, $V_\infty/V_{\infty\mathrm{R}}$ is the relative occupied volume [107], and V/V_R is defined by a chosen equation of state. This viscosity model is often used with Tait's equation of state, Eq. 2.77.

While more accurate than the Roelands–Houpert model at high pressures, the Tait–Doolittle model is still rarely used due to its mathematical complexity and additional input parameters, which require more sophisticated experimental measurements. In the recent years researchers started conducting detailed experiments and analyses of lubricant properties (e.g. [10, 11]), especially viscosity. It provides more insight into the lubricant behaviour, enables the use of complex rheological models and even derivation of lubricant–specific expressions [10].

Shear Stress Dependence

Under high shear rates, above the Newtonian limit, fluids lose their linear shear stress–strain relationship. Lubricants often operate under extreme conditions (e.g. in journal bearings), where pressure can go up to 3 GPa, and entrainment speeds may reach 100 m/s [107]. Further complications of the lubricant behaviour is brought by their complex chemical compositions used more often today. Different constitutive laws have been derived over the years in order to capture the non-Newtonian behaviour under high shear rates. Models describing the non-Newtonian behaviour are usually divided into two groups [106]: shear–thinning models and limiting–shear–stress models.

If the fluid is viscoelastic, the total shear strain rate is the sum of elastic strain rate and viscous shear strain rate [105]:

$$\dot{\gamma} = \dot{\gamma}_\mathrm{e} + \dot{\gamma}_\mathrm{v}. \tag{2.66}$$

Johnson and Tevaarwerk [114] introduced the Ree–Eyring model based on the sinh–law, which uses a hyperbolic sine function in order to represent the shear–thinning behaviour of the lubricant. The viscous shear strain rate is expressed as:

$$\dot{\gamma}_\mathrm{v} = \frac{\tau_\mathrm{E}}{\mu} \sinh\left(\frac{\tau}{\tau_\mathrm{E}}\right), \tag{2.67}$$

where τ_E is the Eyring stress, $\dot{\gamma}$ is the shear rate, τ is the shear stress, and μ is the low–shear viscosity presented in the previous subsection. Sharif et al. [115]

expanded the Ree–Eyring model, a shear–thinning model, to include the limiting shear stress:

$$\dot{\gamma}_{\mathrm{v}} = \frac{\tau_{\mathrm{E}}}{\mu} \sinh\left(\frac{\tau}{\tau_{\mathrm{E}}}\right) \left[\frac{1}{1 - \left(\frac{\tau}{\tau_{\mathrm{L}}}\right)^{2\nu}}\right], \tag{2.68}$$

where τ_{L} is the limiting shear stress and ν is the parameter for controlling the rapidness with which the limiting shear stress is approached. Bair et al. [112] conducted acoustic, capillary and impact measurements for timescales shorter than the elastohydrodynamic timescale. They concluded that the viscous response for an EHL contact is unlikely, thus the elastic strain rate can be dropped from Eq. 2.66. If the total fluid shear stress is expressed as [105]:

$$\tau = \eta\dot{\gamma}, \tag{2.69}$$

inserting Eq. 2.69 into Eq. 2.67 results in the Ree–Eyring shear–thinning viscosity of the fluid:

$$\eta_{\mathrm{RE}} = \frac{\tau_{\mathrm{E}}}{\dot{\gamma}} \sinh^{-1}\left(\frac{\mu\dot{\gamma}}{\tau_{\mathrm{E}}}\right), \tag{2.70}$$

Another well known shear–thinning model is the Carreau [116] model, based on the power law equation:

$$\eta_{\mathrm{C}} = \mu \left[1 + (\lambda\dot{\gamma})^2\right]^{(n-1)/2}, \tag{2.71}$$

where n is the power law exponent and λ is the characteristic time. In case where the shear stress distribution is known, a modification of the Eq. 2.71 is used [117], where the characteristic time λ is written as a relaxation time $\lambda = \mu/G$ [118]:

$$\eta_{\mathrm{C}} = \mu \left[1 + \left(\frac{\tau}{G}\right)^2\right]^{\frac{n-1}{2n}}, \tag{2.72}$$

where G is the effective shear modulus. A more general form of the Carreau equation is the Carreau–Yasuda equation [119]:

$$\eta_{\mathrm{CY}} = \mu \left[1 + \left(\frac{\tau}{G}\right)^a\right]^{\frac{n-1}{an}}, \tag{2.73}$$

where a is the Yasuda parameter. The Carreau–Yasuda equation usually achieves a better fit to the experimentally measured viscosity compared to the original Carreau equation, e.g. [10, 119].

While there are other models available in the literature [107], the models presented above are commonly used for numerical analysis of lubricated contact. Depending on the known properties of the lubricant the appropriate shear–thinning model should be used.

2.6.2. Density

For the same pressure change the lubricant experiences significantly lower density variation compared to the viscosity. Consequently, less research was directed towards predicting lubricant compressibility and far more towards determining its rheological properties, i.e. viscosity and shearing [106]. Dowson and Higginson [120] presented a widely used isothermal density–pressure relation:

$$\frac{\rho}{\rho_{\text{ref}}} = \frac{C_1 + C_2(p - p_{\text{ref}})}{C_1 + (p - p_{\text{ref}})}, \tag{2.74}$$

where C_1 and C_2 are constant coefficient whose values depend on the observed lubricant, and ρ_{ref} is the reference density at the pressure p_{ref}. Dowson and Higginson [120] proposed the following values in case of a mineral lubricant: $C_1 = 0.59 \times 10^9$ and $C_2 = 1.34$. The proposed coefficients have been extensively applied for mineral oils because of their good agreement with the experimental results for pressures up to 400 MPa. For pressures over 400 MPa Eq. 2.74 together with the proposed C_1 and C_2 coefficients significantly overestimates the density. In order to use Eq. 2.74 with higher pressures Sahlin et al. [58] derived new coefficients, $C_1 = 2.22 \times 10^9$ and $C_2 = 1.66$, using the experimental data for mineral oil by Tuomas and Isaksson [121] for pressures up to 3 GPa. In Fig. 2.5 a comparison between these two sets of coefficients is presented.

One of the more accurate compressibility expressions is the one proposed by Jacobson and Vinet [122, 3]:

$$p = 3B_0 \left(\frac{\rho}{\rho_{\text{ref}}}\right)^{-2/3} \left[1 - \frac{\left(\frac{\rho}{\rho_{\text{ref}}}\right)^{-1}}{3}\right] \exp\left[\eta' \left(1 - (\rho/\rho_{\text{ref}})^{-1/3}\right)\right], \tag{2.75}$$
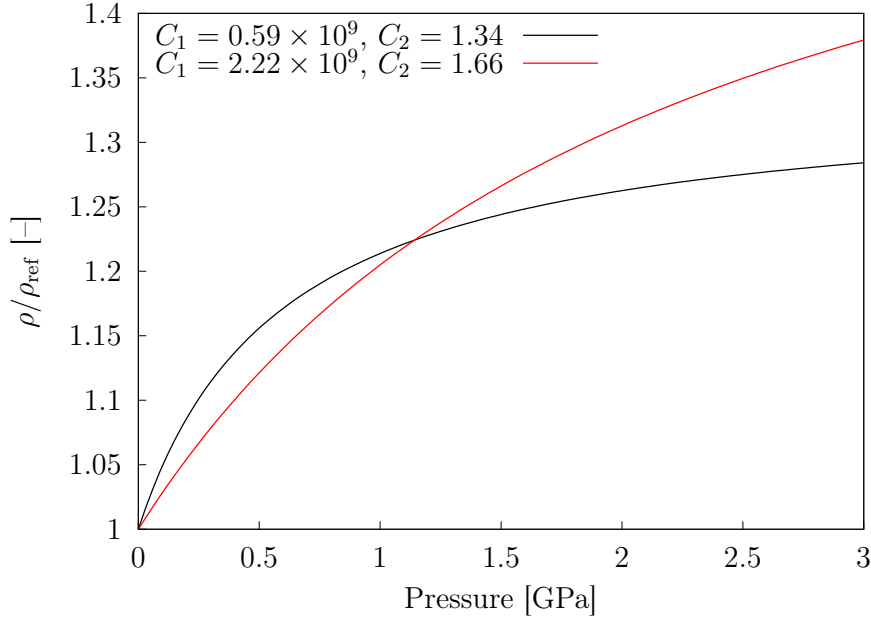
Figure 2.5: Comparison of pressure–density relations for two sets of Dowson–Higginson coefficients.

where B_0 and η' are constant parameters depending on the particular lubricant. Common values for mineral oil are $B_0 = 1.7 \times 10^9$ and $\eta' = 10$. Eq. 2.75 is not analytically invertible, therefore, one must use an iterative method (e.g. Newton–Raphson) to calculate density ρ for a given pressure p.

Another popular density–pressure relation is the Murnaghan model [123, 10]:

$$\frac{\rho_0}{\rho} = \left(1 + \frac{K_0'}{K_0}p\right)^{(-1/K_0')}, \tag{2.76}$$

where K_0' is the initial pressure rate of change of the bulk modulus, and K_0 is the bulk modulus at ambient pressure. Similarly, a density–pressure relation called Tait equation of state is expressed as [107]:

$$\frac{\rho_0}{\rho} = 1 - \frac{1}{1 + K_0'} \ln\left[1 + \frac{p}{K_0}\left(1 + K_0'\right)\right]. \tag{2.77}$$

Murnaghan and Tait models are more physically relevant compared to the Dowson and Higginson model. However, they are much more complicated and require specific experimental data as input [107].

When lubricant experiences temperature variations compressibility is also affected. Zhu [124], Yang [125] and later Yan et al. [44] modified the Dowson and

Higginson equation, Eq. 2.74, by adding a linear temperature correction. Habchi et al. [10] used Murnaghan's equation of state, Eq. 2.76, with the similar linear temperature correction. The same approach can be used for the Tait equation of state [107], Eq. 2.77. Wong et al. [126] derived a theoretical model describing the influence of temperature and pressure on the density of liquid lubricants, based on the molecular interaction theory, which showed good correlations with the experimentally measured data.

2.7. Conclusion

An overview of numerical models necessary for calculating lubricated rough surface contact was presented.

Reynolds equation, a partial differential equation governing the pressure distribution in thin film flow, was derived from Navier–Stokes and continuity equations. In order to address cavitational effects and non–physical negative pressures when calculating Reynolds equation an overview of boundary conditions and available algorithms used with Reynolds equation was given. In commonly used algorithms the computational domain is divided into full–film and cavitating regions, with rupture and formation boundaries between them. In the cavitating region a fixed value of pressure equal to cavitation pressure of the lubricant is assumed. In order to satisfy mass conservation between the two regions the zero–gradient pressure boundary condition is assumed, Eq. 2.57, and the non–zero pressure gradient at the formation boundary, Eq. 2.58.

In order to take into account surface roughness effects during on the lubricant flow, the averaged Reynolds equation and flow factors were introduced. Flow factors are coefficients calculated analytically for a specific surface roughness and surface separation. By inserting flow factors into Reynolds equation, Eq. 2.56, the averaged Reynolds equation is created, Eq. 2.61. The pressure flow factor, added to the Poiseuille coefficient, represents the influence of surface roughness on the pressure gradient. The shear flow factor is added inside the additional convective term, taking into account the mutual effects of surface roughness and sliding.

During mixed and boundary lubrication regimes there is significant contact

between asperities of neighbouring surfaces. In order to calculate contact area, contact pressure and film thickness contact models were introduced. There are two approaches to contact modelling: statistical and deterministic. An overview of both approaches was given.

In highly loaded hydrodynamic contacts where two surfaces are slipping, i.e. have different velocities, shearing of the lubricant can cause significant heat dissipation. In the mixed and boundary lubrication regimes, aside from the lubricant shearing, the friction between sliding asperities generates substantial heat. Since temperature increase can have significant influence on lubricant properties, an overview of different approaches to thin film thermal modelling is given.

A detailed characterisation of lubricant transport properties is important in order to achieve satisfying lubricant flow results. Two most important properties are density and viscosity. Detailed models give more realistic representation of lubricant behaviour under high pressures, temperatures and shear stress, however they require serious experimental measurements. The most commonly used viscosity models and pressure–temperature–density relations were given.

3. Finite Area Method

3.1. Introduction

In this chapter an overview of the Finite Area Method (FAM) is given. The FAM is considered to be a two–dimensional counterpart of the Finite Volume Method enabling the discretisation of the surface integral transport equations. The computational mesh is created by discretising spatial curved surfaces using finite areas of arbitrary polygonal shape. The computational point is located at the face centroid. The transport equation is discretised in accordance with the finite volume principles. The method was developed and implemented within the `foam-extend` framework by Tuković [1]. The author validated the method using orthogonal and non–orthogonal meshes discretised over a surface of sphere against analytical solutions. In the same work the author applied the method for calculating multiphase flows by free surface tracking. The FAM was successfully applied on different problems: free–rising bubbles with soluble surfactants [127], thin liquid film flows [128], interface tracking and surface tension with moving meshes [129], linear elasticity [130], shallow granular flows [131]. In this study the FAM is used for discretising the Reynolds and thin film energy equations.

   In the following sections an overview of the Finite Area Method is given. First, the discretisation of the spatial domain is presented. Next, the discretisation of the transport equation is presented. Finally, the basic treatment of boundary conditions is shown. The following sections are based exclusively on the work done by Tuković in [1], and are given here for the purpose of an overview of the method.

3.2. Discretisation of the Spatial Domain

Computational domain is a curved surface with time-dependent shape and position, Fig. 3.1.
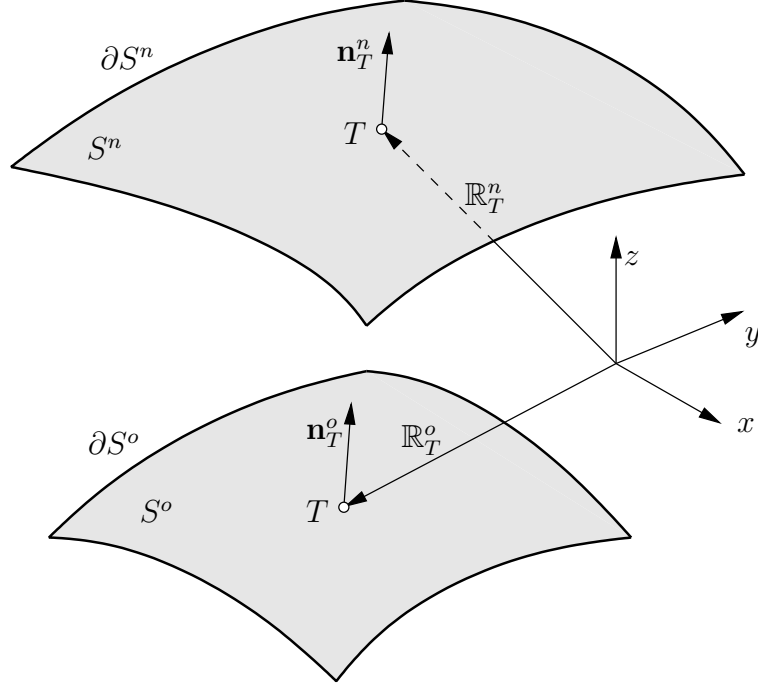
Figure 3.1: Curved smooth surface with time-dependent shape [1].

When a domain is spatially discretised, a computational area mesh with a finite number of non–overlapping finite area faces is created. A single finite area face is a convex polygon with an arbitrary number of straight edges. Computational point of a finite area face coincides with its centroid.

Fig. 3.2 depicts two neighbouring finite area faces, P and N, with e as their connecting edge. S_P represents the surface area of finite area face P with $\mathbf{n}_P$ as the unit normal vector located in its centroid. L_e is the length of edge e, while $\mathbf{n}_e$ is the unit normal vector located in the centroid of edge e and calculated as the mean value between unit normal vectors located in marginal points (i and j) of edge e:

$$\mathbf{n}_e = \frac{\mathbf{n}_i + \mathbf{n}_j}{|\mathbf{n}_i + \mathbf{n}_j|} \tag{3.1}$$

The unit binormal vector $\mathbf{m}_e$ of edge e is perpendicular to unit normal vector $\mathbf{n}_e$ and edge e, while pointing to neighbour face N:

$$\mathbf{m}_e = \hat{\mathbf{e}} \times \mathbf{n}_e, \tag{3.2}$$

where $\hat{e}$ is the unit vector parallel to edge e. Calculation of the unit normal vector
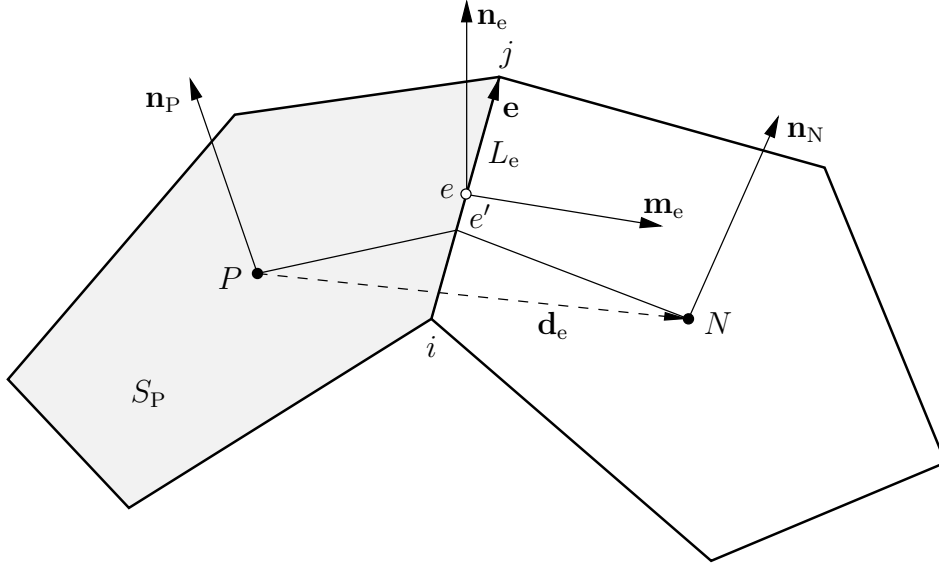
Figure 3.2: Finite area faces P and N [1].

located at an arbitrary point of finite area mesh is explained in details in [1].

Geodesic line $Pe'N$ connects two finite area face centres P and N while intersecting edge e at point e'. In case of a zero–skewness between faces P and N at edge e point e' is located at the centroid of the edge. In case of an existing skewness the position of point e' is calculated by:

$$\mathbf{r}'_e = \mathbf{r}_i + \beta_e \mathbf{e}, \tag{3.3}$$

where $e = r_j - r_i$ is the vector parallel to and equal in length with edge e, while r_i and r_j are position vectors of points i and j respectively. Coefficient β_e is calculated in a way that the triangle defined by vectors $\overline{PN}$, $\overline{Pe'}$ and $\overline{e'N}$ has minimal surface area:

$$\beta_e = \frac{[\mathbf{d}_e \times (\mathbf{r}_i - \mathbf{r}_P)] \bullet (\mathbf{d}_e \times \mathbf{e})}{|\mathbf{d}_e \times \mathbf{e}|^2}, \tag{3.4}$$

where $\mathbf{d}_e = \overline{PN}$ and $\mathbf{r}_P$ is the position vector of point P.

The geometric properties of finite area faces are calculated in the same way as the properties of finite volume cells. Edge addressing is used for the definition of finite area faces and contains the following: list of points, list of edges, list of faces and list of boundaries. Criteria for the topological and geometrical validity of the finite area mesh is the same as in the case of the finite volume mesh [49].

3.3. Discretisation of the Transport Equation

In this section a summary of the finite area discretisation of a scalar transport equation is presented. For more details one should refer to [1].

The surface transport of a scalar property ρ along a curved deformable surface can be expressed using the following differential equation in its integral form [1]:

$$\frac{\mathrm{d}}{\mathrm{d}t} \int_S \rho \, \mathrm{d}S + \oint_{\partial S} \mathbf{m} \cdot (\mathbf{v}_t - \mathbf{b}_t) \rho \, \mathrm{d}L = \oint_{\partial S} \mathbf{m} \cdot (\Gamma_\rho \nabla_s \rho) \, \mathrm{d}L + \int_S s_\rho \, \mathrm{d}S, \qquad (3.5)$$

where S is an arbitrary movable surface bounded by curve ∂S, $\mathbf{m}$ is a unit binormal vector, $\mathbf{v}_t$ and $\mathbf{b}_t$ are tangential components of a material surface velocity vector and arbitrary surface S velocity vector, respectively. The movement of these two surfaces is constricted by the following expression [1]:

$$\mathbf{n} \cdot \mathbf{b} = \mathbf{n} \cdot \mathbf{v}.$$

The finite area discretisation of Eq. 3.5 is performed with the assumption of normal movement of finite area faces, i.e. $\mathbf{b}_t = 0$. Integrating Eq. 3.5 over finite area S_P, while taking into account the previous assumption, results in:

$$\underbrace{\frac{\mathrm{d}}{\mathrm{d}t} \int_{S_P} \rho \, \mathrm{d}S}_{\text{Temporal term}} + \underbrace{\oint_{\partial S_P} \mathbf{m} \cdot \mathbf{v}_t \rho \, \mathrm{d}L}_{\text{Convection term}} = \underbrace{\oint_{\partial S_P} \mathbf{m} \cdot (\Gamma_\rho \nabla_s \rho) \, \mathrm{d}L}_{\text{Diffusion term}} + \underbrace{\int_S s_\rho \, \mathrm{d}S}_{\text{Source term}}, \quad (3.6)$$

where ∂S_P is the boundary of finite area S_P, containing a finite number of straight lines.

Discretisation of the spatial terms (convection and diffusion) in Eq. 3.6 assumes the linear distribution of variable ρ over finite area P:

$$\rho(\mathbf{r}) = \rho_P + (\mathbf{r} - \mathbf{r}_P) \cdot (\nabla_s \rho)_P, \qquad (3.7)$$

where $(\nabla_s \rho)_P$ is the surface gradient of variable ρ at the centroid of finite area face P, and $\mathbf{r}_P$ is the position vector of point P. The temporal distribution of variable ρ on interval $[t^o, t^n]$ is defined by:

$$\rho(t^o + \Delta t) = \rho(t^o) + \Delta t \left(\frac{\partial \rho}{\partial t} \right)^o. \qquad (3.8)$$

The discretisation of the spatial terms assumes that all tensor variables located in computational points (area and edge centres) are defined in global Cartesian coordinate system.

3.3.1. Spatial Terms

The finite area discretisation of surface integrals is performed using the central point rule [1]:

$$\int_{S_P} \rho(\mathbf{r})\,\mathrm{d}S = \rho_P S_P. \tag{3.9}$$

Since a finite area is bounded by the finite number of straight edges, the line integral over the surface boundary can be expressed as the sum of line integrals per every edge (central point rule):

$$\oint_{\partial S_P} \rho(\mathbf{r})\,\mathrm{d}L = \sum_e \int_{L_e} \rho(\mathbf{r})\,\mathrm{d}L = \sum_e \rho_e L_e, \tag{3.10}$$

where $\rho_e = \rho(\mathbf{r}_e)$ is the value of variable ρ at the edge centroid e, while L_e is the length of edge e.

Convection Term

Discretisation of the convection term, using Eq. 3.10, states:

$$
\begin{aligned}
\oint_{\partial S_P} \mathbf{m}{\bullet}\mathbf{v}_t \rho \,\mathrm{d}L &= \sum_e \mathbf{m}_{e}{\bullet}(\mathbf{v}_t)_e L_e \rho_e \\
&= \sum_e \dot{s}_e \rho_e,
\end{aligned}
\tag{3.11}
$$

where $\dot{s}_e = \mathbf{m}_{e}{\bullet}(\mathbf{v}_t)_e L_e$ is the edge flux of the material surface.

The value of variable ρ on edge e is calculated from values in neighbouring area centroids using the appropriate convection discretisation scheme. In case of a scalar variable typical finite volume schemes (e.g. central, upwind, ...) may be used [1], substituting Euclidean distance between two neighbouring finite volumes with geodesic distance between two neighbouring finite areas. In case of a central differencing scheme the value of scalar variable ρ on edge e is calculate by [1]:

$$\rho_e = e_x \rho_P + (1 - e_x)\rho_N, \tag{3.12}$$

where the interpolation factor e_x is defined as a ratio of geodesic distances (Fig. 3.2):

$$e_x = \frac{\overline{eN}}{\overline{PN}}.$$

In case of a vector variable $\mathbf{V}$, written in global Cartesian coordinate system, using the central differencing scheme the edge value is interpolated as follows [1]:

$$\mathbf{V}_e = (\mathbf{C}_e)^T \bullet [e_x \mathbf{C}_P \bullet \mathbf{V}_P + (1 - e_x) \mathbf{C}_N \bullet \mathbf{V}_N], \tag{3.13}$$

while in the case of a tensor variable $\mathbf{T}_e$ (second rank tensor):

$$\mathbf{T}_e = (\mathbf{C}_e)^T \bullet [e_x \mathbf{C}_P \bullet \mathbf{T}_P \bullet (\mathbf{C}_P)^T + (1 - e_x) \mathbf{C}_N \bullet \mathbf{T}_N \bullet (\mathbf{C}_N)^T] \bullet \mathbf{C}_e, \tag{3.14}$$

where $\mathbf{C}_P$, $\mathbf{C}_N$ and $\mathbf{C}_e$ are transformation tensors used for transforming $\mathbf{T}_P$, $\mathbf{T}_N$ and $\mathbf{T}_e$ from global Cartesian to local orthogonal curvilinear coordinate system. For the detailed derivation of Eqs. 3.13 and 3.14 one should refer to [1].

Diffusion Term

Discretisation of the diffusion term, using Eq. 3.10, states:

$$\oint_{\partial S_P} \mathbf{m} \bullet (\Gamma_\rho \nabla_s \rho) \, dL = \sum_e \mathbf{m}_e \bullet (\Gamma_\rho \nabla_s \rho)_e L_e$$
$$= \sum_e (\Gamma_\rho)_e L_e \mathbf{m}_e \bullet (\nabla_s \rho)_e, \tag{3.15}$$

where $\mathbf{m}_e \bullet (\nabla_s \rho)_e$ is the normal surface gradient of variable ρ on edge e.

Discretisation of the normal surface gradient depends on the mesh orthogonality. The non–orthogonality angle α_e is defined for every edge on a non–structured finite area mesh 3.3 as follows [1]:

$$\alpha_e = \arccos(\mathbf{t}_e \bullet \mathbf{m}_e). \tag{3.16}$$

Following the definition above, mesh is orthogonal at edge e when $\alpha_e = 0$, i.e. when:

$$\mathbf{t}_e \bullet \mathbf{m}_e = 1.$$

The normal surface gradient of variable ρ on edge e in case of an orthogonal finite area mesh is calculated using the following expression:

$$\mathbf{m}_e \bullet (\nabla_s \rho)_e = \frac{\rho_N - \rho_P}{L_{PN}}, \tag{3.17}$$
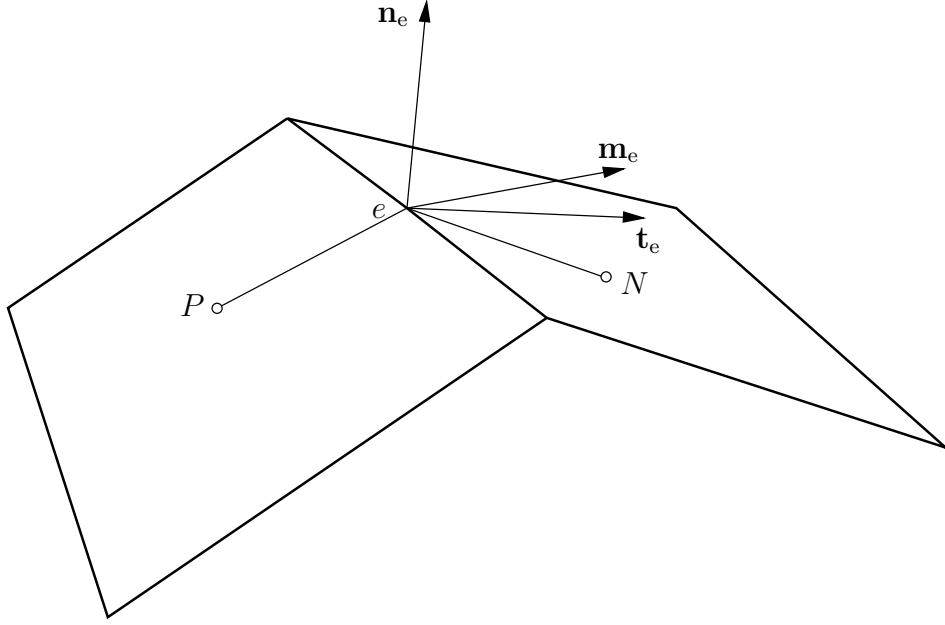
Figure 3.3: With the definition of non–orthogonality of a finite area mesh [1].

where L_{PN} is the geodesic distance between the centroids of two neighbouring finite area faces P and N. For calculating the normal surface gradient on non–orthogonal meshes a correction is introduced:

$$\mathbf{m}_e\bullet(\nabla_{\mathrm{s}}\rho)_e = \underbrace{|\mathbf{\Delta}_e|\frac{\rho_N - \rho_P}{L_{PN}}}_{\text{Orthogonal contr.}} + \underbrace{\mathbf{k}_e\bullet(\nabla_{\mathrm{s}}\rho)_e}_{\text{Non-orthogonal corr.}}, \tag{3.18}$$

where vectors $\mathbf{\Delta}_e$ and $\mathbf{k}_e$ are calculated in accordance with the over–relaxed non–orthogonal correction [1, 49]:

$$\mathbf{\Delta}_e = \frac{\mathbf{t}_e}{\mathbf{t}_e\bullet\mathbf{m}_e}, \tag{3.19}$$

$$\mathbf{k}_e = \mathbf{m}_e - \mathbf{\Delta}_e. \tag{3.20}$$

The non–orthogonal correction in Eq. 3.18 is treated explicitly, where the edge surface gradient $(\nabla_{\mathrm{s}}\rho)_e$ is calculated by interpolating from surface gradients in neighbouring finite area centroids using the central differencing scheme, Eq. 3.13. Surface gradient in a finite area centroid is calculated using the Gauss's theorem for a curved surface [1]:

$$(\nabla_{\mathrm{s}}\rho)_P = \frac{1}{S_P}(\mathbf{I} - \mathbf{n}_P\mathbf{n}_P)\bullet\sum_e \mathbf{m}_e\rho_e L_e, \tag{3.21}$$

where ρ_e is the value of variable ρ on a finite area edge from the previous iteration.

Due to the discretisation of a real curved surface using finite area faces, bounded by straight lines, the geodesic distance between two neighbouring areas is shorter compared to the geodesic line between two corresponding points on a real curved surface. In order to account for this difference when calculating normal surface gradients an explicit correction [49, 1] is added to the right hand side of Eq. 3.18:

$$D_k = \frac{1}{15}\left[|\boldsymbol{\Delta}_e|\frac{\rho_N - \rho_P}{L_{PN}} - \boldsymbol{\Delta}_e \bullet (\nabla_s\rho)_e\right]. \tag{3.22}$$

3.3.2. Temporal Discretisation

By discretising spatial integrals Eq. 3.6 takes the following form [1]:

$$\frac{\mathrm{d}}{\mathrm{d}t}(\rho_P S_P) = -\sum_e \dot{s}_e\rho_e + \sum_e (\Gamma_\rho)_e L_e \mathbf{m}_e \bullet (\nabla_s\rho)_e + s_{\rho u}S_P + s_{\rho p}S_P\rho_P, \tag{3.23}$$

where $s_{\rho u}S_P$ is the explicit part and $s_{\rho p}S_P\rho_P$ is the implicit part of the source term specified in Eq. 3.6.

Depending on the selected temporal discretisation scheme, the completely discretised transport equation for finite area face S_P takes the following forms:

- Implicit Euler method,

$$\frac{\rho_P^n S_P^n - \rho_P^o S_P^o}{\Delta t} + \sum_e \dot{s}_e^n\rho_e^n$$
$$= \sum_e (\Gamma_\rho)_e^n L_e^n \mathbf{m}_e^n \bullet (\nabla_s\rho)_e^n + s_{\rho u}^n S_P^n + s_{\rho p}^n S_P^n\rho_P^n, \tag{3.24}$$

- Second order backward implicit method,

$$\frac{3\rho_P^n S_P^n - 4\rho_P^o S_P^o + \rho_P^{oo} S_P^{oo}}{2\Delta t} + \sum_e \dot{s}_e^n\rho_e^n$$
$$= \sum_e (\Gamma_\rho)_e^n L_e^n \mathbf{m}_e^n \bullet (\nabla_s\rho)_e^n + s_{\rho u}^n S_P^n + s_{\rho p}^n S_P^n\rho_P^n, \tag{3.25}$$

- Crank-Nicolson method,

$$
\begin{aligned}
\frac{\rho_P^n S_P^n - \rho_P^o S_P^o}{\Delta t} &+ \frac{1}{2}\sum_e \dot{s}_e^n \rho_e^n + \frac{1}{2}\sum_e \dot{s}_e^o \rho_e^o \\
&= \frac{1}{2}\sum_e (\Gamma_\rho)_e^n L_e^n \mathbf{m}_e^n \boldsymbol{\cdot} (\nabla_s \rho)_e^n + \frac{1}{2}\sum_e (\Gamma_\rho)_e^o L_e^o \mathbf{m}_e^o \boldsymbol{\cdot} (\nabla_s \rho)_e^o \\
&+ \frac{1}{2}\left(s_{\rho u}^n S_P^n + s_{\rho p}^n S_P^n \rho_P^n\right) + \frac{1}{2}\left(s_{\rho u}^o S_P^o + s_{\rho p}^o S_P^o \rho_P^o\right).
\end{aligned} \tag{3.26}
$$

The above time discretisation procedure considers mesh motion in the surface normal direction where finite area face S_P, binormal $\mathbf{m}_e$ and edge length L_e are changing with time.

3.3.3. Boundary Conditions

Finite area face P with edge b positioned at the edge of spatial domain is depicted in Fig. 3.4. The starting point of vector $\mathbf{d}_b$ is the centroid of finite area P, while the end point is the centroid of edge $\mathbf{b}$. The length of vector $\mathbf{d}_m$ is calculated in the following way:

$$
|\mathbf{d}_m| = \frac{(\mathbf{I} - \mathbf{n}_P \mathbf{n}_P) \boldsymbol{\cdot} \mathbf{m}_b}{|(\mathbf{I} - \mathbf{n}_P \mathbf{n}_P) \boldsymbol{\cdot} \mathbf{m}_b|} \boldsymbol{\cdot} \mathbf{d}_b. \tag{3.27}
$$

With the defined geometrical parameters of boundary edges, values for ρ_e and $\mathbf{m}_e \boldsymbol{\cdot} (\nabla_s \rho)_e$ are calculated in the same manner as in the Finite Volume Method [1].

3.4. Conclusion

In this chapter an overview of the Finite Area Method, based on the work done by Tuković, was given. The spatial discretisation is performed over a curved surface using a finite number of non–overlapping finite area faces, where a single finite area face is a convex polygon with an arbitrary number of straight edges. The spatial terms of a transport equation are discretised using the same principles as in the Finite Volume Method, considering face instead of volume integrals and edge instead of face fluxes. Temporal discretisation using three temporal
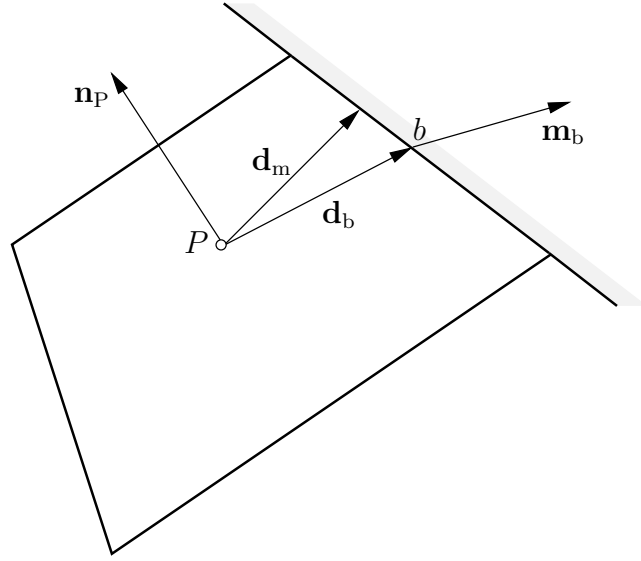
Figure 3.4: With the definition of geometrical parameters of boundary edge [1].

schemes is given: implicit Euler, second order backward and Crank–Nicolson method. Geometrical parameters of boundary edges are given at the end.

4. Numerical Modelling and Implementation

4.1. Introduction

In this chapter an overview of implemented numerical models is given. First, the finite area discretisation of Reynolds equation is given, considering active region, cavitating region and boundaries between them. Analytical equations used for calculating flow factors are presented next. Flow factor equations given by Wilson and Marsault [2] are used for contacts with large fractional contact areas, while flow factors given by Patir and Cheng [9] are used under mixed and thin film lubrication regimes. Implemented models describing lubricant density and viscosity dependence on pressure and temperature are given next. In order to consider effects of lubricant shear thinning on viscosity two models were implemented: Ree–Eyring and Carreau–Yasuda. A two–dimensional thin film energy equation is given, used for calculating changes of lubricant temperature due to convective, compressive and shearing effects. In order to calculate temperatures of two surfaces in contact during ball–on–disc simulations, a deterministic surface temperature model based on the moving heat source equation is presented. A thermal boundary condition for rough surface contact used in metal forming simulations is given next. Finally, three statistical and one deterministic contact model, implemented in the current study, are presented.

4.2. Reynolds Equation

In Chapter 2., the Reynolds equation was presented and derived. In this section the Reynolds equation is given in specific forms in which it was implemented in the code. In addition, the cavitation algorithm and flow factor equations are given.

In order to use a unified Reynolds equation both in the active and in the

cavitation region (see Chapter 2., section 2.2.2.), the form of the Reynolds similar to the one suggested by Bayada and Chopin [38] was implemented:

$$\nabla_{\mathrm{s}}\bullet\left(\alpha\frac{\beta h^3}{12\eta}\nabla_{\mathrm{s}}\rho\right) = \nabla_{\mathrm{s}}\bullet\left[\frac{\rho h\left(\mathbf{U}_{\mathrm{a}}+\mathbf{U}_{\mathrm{b}}\right)}{2}\right] + \frac{\partial(\rho h)}{\partial t}, \tag{4.1}$$

where α is the cavitation switch function, $\beta = \rho\frac{\mathrm{d}p}{\mathrm{d}\rho}$ is the fluid bulk modulus, and η is the non–Newtonian viscosity calculated via Eq. 2.70, 2.72 or 2.73. The equation is solved numerically for density ρ.

In Eq. 4.1 both viscosity and bulk modulus are pressure–dependent. Therefore, a density–pressure relation is used in order to calculate lubricant pressure from known density values. In case of the Dowson–Higginson relation, Eq. 2.74, the pressure is expressed as:

$$p = \frac{(\rho_{\mathrm{ref}} - \rho)C_1}{\rho - \rho_{\mathrm{ref}}C_2}. \tag{4.2}$$

The bulk modulus β using the same density–pressure relation states:

$$\beta = \rho\frac{\mathrm{d}p}{\mathrm{d}\rho} = \rho\frac{C_1(C_2 - 1)\rho_{\mathrm{ref}}}{(\rho - \rho_{\mathrm{ref}}C_2)^2}. \tag{4.3}$$

The cavitation switch function is calculated explicitly using the similar principle as in the Elrod–Adams algorithm:

$$\begin{aligned}
\rho^o > \rho_{\mathrm{cav}} \quad &\rightarrow \quad \alpha^n = 1, \\
\rho^o \leq \rho_{\mathrm{cav}} \quad &\rightarrow \quad \alpha^n = 0.
\end{aligned} \tag{4.4}$$

where superscripts ^{o} and ^{n} denote values in the previous time step (outer iteration), and in the current one, respectively. In order to consider cavitational effects conservatively, specific boundary conditions between the active and cavitating regions are required. These boundary conditions are presented in the next section.

Similarly, the averaged Reynolds equation, Eq. 2.61, is implemented as:

$$\begin{aligned}
\nabla_{\mathrm{s}}\bullet\left(\alpha\phi_{xy}\frac{\beta h^3}{12\mu}\nabla_{\mathrm{s}}\rho\right) = &\nabla_{\mathrm{s}}\bullet\left[\frac{\rho h\left(\mathbf{U}_{\mathrm{a}}+\mathbf{U}_{\mathrm{b}}\right)}{2}\right] \\
&- \nabla_{\mathrm{s}}\bullet\left[\frac{\phi_{\mathrm{s}}\rho\left(\mathbf{U}_{\mathrm{a}}-\mathbf{U}_{\mathrm{b}}\right)}{2}\right]R_{\mathrm{q}} + \frac{\partial(\rho h)}{\partial t},
\end{aligned} \tag{4.5}$$

where ϕ_x and ϕ_{s} are pressure and shear flow factor, respectively. The expressions for the flow factors are given in section 4.2.2..

4.2.1. Finite Area Discretisation with Cavitation Boundaries

Both forms of the Reynolds equation, Eqs. 4.1 and 4.5, presented above are implemented within the `foam-extend` framework [132] using the Finite Area Method described in Chapter 3. In this section the discretisation of Eq. 4.1 on an orthogonal finite area mesh is given, taking into account cavitation boundaries. The discretisation is written for finite area face P with four neighbouring faces E, N, W and S, Fig. 4.1. Two regions are distinguished, active and cavitating, with the rupture or the formation boundary between them. The values obtained by solving the Reynolds equation represent the density values of the liquid lubricant in the active region, while in the cavitating region they describe the density values of the liquid–gas mixture. In the cavitating region the Poiseuille coefficient becomes zero, due to the assumption of a constant cavitation pressure. A special treatment between the two regions is required in order to satisfy cavitation boundary conditions specified in Eqs. 2.57 and 2.58. The cavitation switch function α is equal to unity in the active region, and equal to zero in the cavitating region. Finite area faces inside the active region are represented by red colour, while faces inside cavitating region by blue, Fig. 4.1.
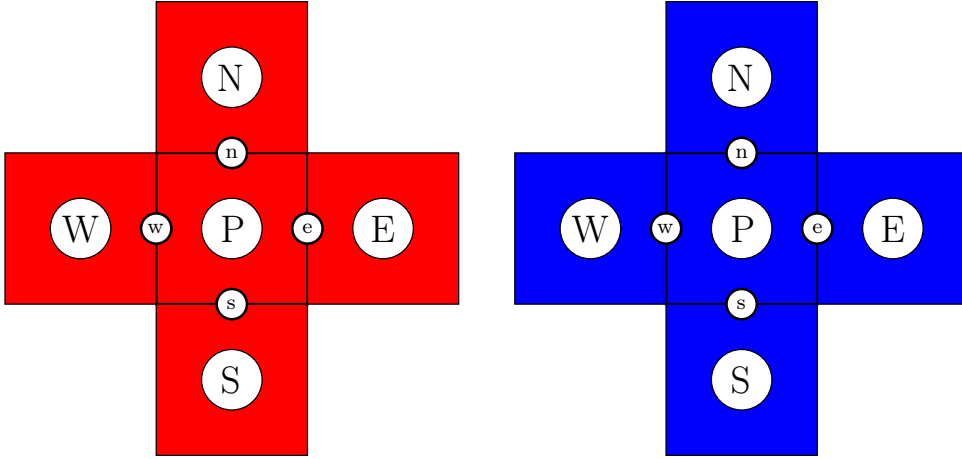
Figure 4.1: Active (left) and cavitating regions (right).

Active region

If finite area face P is non–cavitating and is surrounded by non–cavitating faces (E, W, N, S), face P is considered to be completely inside the active region, Fig. 4.1. Poiseuille coefficient is the diffusion term discretised using Eqs. 3.15 and 3.17 in the following way:

$$\oint_{\partial S_P} \nabla_{\mathrm{s}}\bullet(\Gamma\nabla_{\mathrm{s}}\rho)\,\mathrm{d}L = \oint_{\partial S_P} \mathbf{m}\bullet(\Gamma\nabla_{\mathrm{s}}\rho)\,\mathrm{d}L$$
$$= \Gamma_e L_e \frac{\rho_E - \rho_P}{L_{PE}} + \Gamma_w L_w \frac{\rho_W - \rho_P}{L_{PW}} \qquad (4.6)$$
$$+ \Gamma_n L_n \frac{\rho_N - \rho_P}{L_{PN}} + \Gamma_{\mathrm{s}} L_{\mathrm{s}} \frac{\rho_S - \rho_P}{L_{PS}},$$

where $\Gamma = \frac{\alpha\beta h^3}{12\eta}$ and $\alpha = 1$.

Couette coefficient is the convection term discretised using Eqs. 3.11 and 3.12 in the following way:

$$\oint_{\partial S_P} \nabla_{\mathrm{s}}\bullet(h\overline{\mathbf{U}})\rho\,\mathrm{d}L = \oint_{\partial S_P} \mathbf{m}\bullet(h\overline{\mathbf{U}})\rho\,\mathrm{d}L$$
$$= \mathbf{m}_e\bullet(h\overline{\mathbf{U}})_e L_e \rho_e + \mathbf{m}_w\bullet(h\overline{\mathbf{U}})_w L_w \rho_w \qquad (4.7)$$
$$+ \mathbf{m}_n\bullet(h\overline{\mathbf{U}})_n L_n \rho_n + \mathbf{m}_{\mathrm{s}}\bullet(h\overline{\mathbf{U}})_{\mathrm{s}} L_{\mathrm{s}} \rho_{\mathrm{s}}$$
$$= \dot{s}_e \rho_e + \dot{s}_w \rho_w + \dot{s}_n \rho_n + \dot{s}_{\mathrm{s}} \rho_{\mathrm{s}},$$

where $\overline{\mathbf{U}} = \frac{\mathbf{U}_{\mathrm{a}}+\mathbf{U}_{\mathrm{b}}}{2}$ is the mean velocity of two surfaces a and b in contact. The edge values of density ρ are calculated using the central differencing scheme, Eq. 3.12.

The temporal derivative, i.e. squeeze and local expansion, is discretised using the implicit Euler method, Eq. 3.24:

$$\frac{\partial(h\rho)}{\partial t} = \frac{\mathrm{d}(h\rho)}{\mathrm{d}t} = \frac{h_P^n \rho_P^n S_P^n - h_P^o \rho_P^o S_P^o}{\Delta t}. \qquad (4.8)$$

When considering the steady–state case, the temporal derivative is equal to zero.

Cavitating region

If finite area face P is cavitating and is surrounded by cavitating faces (E, W, N, S), face P is considered to be completely inside the cavitating region, Fig. 4.1.

Following the Elrod–Adams principle, Eqs. 2.59 and 2.60, the switch function α is equal to zero. Thus, Poiseuille coefficient is equal to zero:

$$\oint_{\partial S_P} \nabla_{\mathrm{s}}{\scriptstyle\bullet}(\Gamma\nabla_{\mathrm{s}}\rho)\,\mathrm{d}L = \oint_{\partial S_P} \mathbf{m}{\scriptstyle\bullet}(\Gamma\nabla_{\mathrm{s}}\rho)\,\mathrm{d}L = 0, \qquad (4.9)$$

where $\Gamma = \frac{\alpha\beta h^3}{12\eta}$ and $\alpha = 0$.

Couette coefficient is discretised using Eq. 4.7, the only difference being the calculation of the edge values of density ρ, which is done by the upwind differencing scheme [49]. The temporal derivative is calculated in the same way as in the active region, Eq. 4.8.

Rupture and formation boundary

In order to satisfy cavitation boundary conditions specified in Eqs. 2.57 and 2.58 the following treatment is required. If finite area face P is an active face (Fig. 4.2 left) while face E (located downwind from face P) is a cavitating face, Poiseuille coefficient is modified:

$$\begin{aligned}
\oint_{\partial S_P} \nabla_{\mathrm{s}}{\scriptstyle\bullet}(\Gamma\nabla_{\mathrm{s}}\rho)\,\mathrm{d}L = {} & \oint_{\partial S_P} \mathbf{m}{\scriptstyle\bullet}(\Gamma\nabla_{\mathrm{s}}\rho)\,\mathrm{d}L \\
= {} & \Gamma_e L_e \frac{\rho_{\mathrm{cav}} - \rho_P}{L_{PE}} + \Gamma_w L_w \frac{\rho_W - \rho_P}{L_{PW}} \\
& + \Gamma_n L_n \frac{\rho_N - \rho_P}{L_{PN}} + \Gamma_{\mathrm{s}} L_{\mathrm{s}} \frac{\rho_S - \rho_P}{L_{PS}},
\end{aligned} \qquad (4.10)$$

where $\Gamma = \frac{\alpha\beta h^3}{12\eta}$ and $\alpha_e = 1$.

If finite area face P is a cavitating face (Fig. 4.2 right) while face W (located upwind from face P) is an active face, an additional source term is added to face P:

$$S_P = \Gamma_w L_w \frac{\rho_{\mathrm{cav}} - \rho_P}{L_{PW}}, \qquad (4.11)$$

where $\Gamma_w = \left(\frac{\alpha\beta h^3}{12\eta}\right)_w$ and $\alpha_w = 1$.

The discretisation of the averaged Reynolds equation, Eq. 4.5, is analogous to the discretisation of the main Reynolds equation, Eq. 4.1.
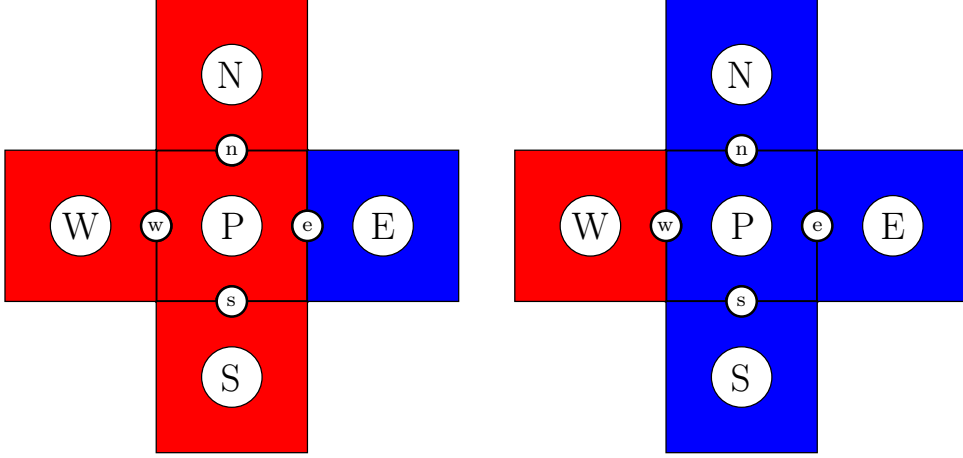
Figure 4.2: With discretisation of cavitation boundaries.

4.2.2. Flow Factors

In order to utilise the implemented averaged Reynolds equation, Eq. 4.5, the flow factors by Wilson and Marsault [2], and Patir and Chang [9] were implemented.

Wilson and Marsault

Wilson and Marsault [2] derived analytical equations for flow factors under the conditions of large fractional contact area. The analytical equation for the pressure flow factor for non–dimensional film thickness $H < 3$ is expressed as:

$$\phi_x = \left[a_2(H - H_\mathrm{c})^2 + a_3(H - H_\mathrm{c})^3\right]/H^3, \tag{4.12}$$

where $H = h/R_\mathrm{q}$ is the non–dimensional film thickness, H_c is the value of H corresponding to the percolation threshold, and a_2 and a_3 are functions of correlation length ratio γ, also known as Peklenik surface parameter [133]. The film thickness percolation threshold is calculated by:

$$H_\mathrm{c} = 3\left[1 - (0.47476/\gamma + 1)^{-0.25007}\right]. \tag{4.13}$$

Functions a_2 and a_3 in Eq. 4.12 are calculated using the following semi–empirical expressions [2]:

$$a_2 = 0.051375\ln^3(9\gamma) - 0.0071901\ln^4(9\gamma), \tag{4.14}$$

$$a_3 = 1.0019 - 0.17927 \ln(\gamma) + 0.047583 \ln^2 -0.016417 \ln^3(\gamma). \tag{4.15}$$

The Peklenik surface parameter is the ratio of two half–correlation lengths calculated in two orthogonal directions for a desired rough surface measurement [9]:

$$\gamma = \frac{\lambda_{0.5x}}{\lambda_{0.5y}}, \tag{4.16}$$

where x and y denote two orthogonal directions. The correlation length is the length over which the autocorrelation function [134] drops to a specific fraction of its value [135]. Therefore, the half–correlation length $\lambda_{0.5}$ is the length over which the calculated autocorrelation function drops to 50% of its original value. When considering two rough surfaces a and b in contact the combined correlation length λ_{ab} is calculated as [135]:

$$\frac{1}{\lambda_{ab}} = \frac{1}{\lambda_a} + \frac{1}{\lambda_b}. \tag{4.17}$$

For the shear flow factor ϕ_s Wilson and Marsault [2] derived an analytical equation for non–dimensional film thickness $H < 5$:

$$\phi_s = b_0 + b_1 H + b_2 H^2 + b_3 H^3 + b_4 H^4 + b_5 H^5, \tag{4.18}$$

where coefficients b_0, b_1, b_2, b_3, b_4 and b_5 are given by:

$b_0 = 0.12667 \gamma^{-0.6508},$
$b_1 = \exp\left(-0.38768 - 0.44160 \ln(\gamma) - 0.12679 \ln^2(\gamma) + 0.042414 \ln^3(\gamma)\right),$
$b_2 = -\exp\left(-1.1748 - 0.39916 \ln(\gamma) - 0.11041 \ln^2(\gamma) + 0.031775 \ln^3(\gamma)\right),$
$b_3 = \exp\left(-2.8843 - 0.36712 \ln(\gamma) - 0.10676 \ln^2(\gamma) + 0.028039 \ln^3(\gamma)\right),$
$b_4 = -0.004706 + 0.0014493 \ln(\gamma) + 0.00033124 \ln^2(\gamma) - 0.00017147 \ln^3(\gamma),$
$b_5 = 0.00014734 - 4.255 \times 10^{-5} \ln(\gamma) - 1.057 \times 10^{-5} \ln^2(\gamma) + 5.0292 \times 10^{-6} \ln^3(\gamma).$

$$\tag{4.19}$$

The comparison between shear flow factors given in [2] and calculated by Eq. 4.18 is given in Fig. 4.3. By examining Fig. 4.3, it can be noticed that Eq. 4.18 gives significant under–prediction of shear flow factor values in case of $\gamma = 1/9$, and over–prediction in case of $\gamma = 1/3$, while for $\gamma = 1/6$ there are noticeable

discrepancies compared to [2]. For the rest of Peklenik parameters, the values of shear flow factors calculated via Eq. 4.18 are in agreement with [2]. In order to achieve a better agreement between shear flow factors, a new analytical equation was derived by curve–fitting to values given in [2]. The curve–fitting done via Matlab® Curve Fitting Toolbox [136] resulted in the following expression:

$$
\begin{aligned}
\phi_{\mathrm{s}} = & p_{00} + H \left\{ p_{10} + H \left[p_{20} + H \left(p_{30} + H \left(p_{40} + p_{50} H \right) \right) \right] \right\} \\
& + H\gamma \{ \\
& \qquad p_{11} + H \left[p_{21} + H \left(p_{31} + p_{41} H \right) \right] + \gamma \left[p_{12} + \gamma \left(p_{13} + p_{14}\gamma \right) \right] \\
& \qquad + H\gamma \left(p_{22} + p_{32} H + p_{23}\gamma \right) \\
& \qquad \} \\
& + \gamma \left\{ p_{01} + \gamma \left[p_{02} + \gamma \left(p_{03} + \gamma \left(p_{04} + p_{05}\gamma \right) \right) \right] \right\},
\end{aligned}
\tag{4.20}
$$

where p_{xy} are constants defined for $\gamma < 1$ as:

$$
\begin{aligned}
p_{00} &= 1.0360000 \\
p_{10} &= 0.3781000 & p_{01} &= -4.05000 \\
p_{20} &= -0.1298000 & p_{02} &= 9.71100 \\
p_{30} &= -0.0147700 & p_{03} &= -13.49000 \\
p_{40} &= 0.0073650 & p_{04} &= 10.21000 \\
p_{50} &= -0.0005668 & p_{05} &= -3.19400 \\
p_{11} &= 0.6817000 \\
p_{21} &= 0.0030600 & p_{12} &= -1.20400 \\
p_{31} &= -0.0128900 & p_{13} &= 0.66320 \\
p_{41} &= 0.0005116 & p_{14} &= -0.10980 \\
p_{22} &= 0.0900800 \\
p_{32} &= 0.0033670 & p_{23} &= -0.04641,
\end{aligned}
\tag{4.21}
$$

and for $\gamma \geq 1$ as

$$
\begin{aligned}
p_{00} &= 0.14030000 \\
p_{10} &= 0.74480000 & p_{01} &= 0.10980000 \\
p_{20} &= -0.27440000 & p_{02} &= -0.10420000 \\
p_{30} &= 0.03141000 & p_{03} &= 0.02828000 \\
p_{40} &= -0.00059320 & p_{04} &= -0.00310500 \\
p_{50} &= -0.00007039 & p_{05} &= 0.00012030 \\
p_{11} &= -0.20300000 \\
p_{21} &= 0.05916000 & p_{12} &= 0.02689000 \\
p_{31} &= -0.00483300 & p_{13} &= -0.00141300 \\
p_{41} &= 0.00010060 & p_{14} &= 0.00002183 \\
p_{22} &= -0.00596800 \\
p_{32} &= 0.00026560 & p_{23} &= 0.00019160.
\end{aligned}
\tag{4.22}
$$

Fig. 4.4 depicts the comparison of shear flow factors calculated by Wilson and Marsault [2] and by Eq. 4.20, which was derived using a curve–fitting procedure. Comparing Figs. 4.3 and 4.4, Eq. 4.20 shows significantly better agreement to Wilson and Marsault data than Eq. 4.18 for Peklenik parameters $\gamma < 1$, and slightly better agreement for $\gamma \geq 1$. Both equations were implemented in the code.

Following Wilson and Marsault [2], for larger non–dimensional film thicknesses, $H \geq 3$ in case of ϕ_x and $H \geq 5$ in case of ϕ_s, the flow factor expressions derived by Patir and Cheng [9] were implemented and used.

Patir and Cheng

Patir and Cheng [67, 9] derived empirical relations for calculating flow factors under thin film hydrodynamic lubrication and mixed lubrication conditions with small fractional contact areas. The pressure flow factors are calculated using the following expressions [9]:

$$
\phi_x = 1 - C \exp(-rH) \qquad \text{for} \qquad \gamma \leq 1, \tag{4.23}
$$
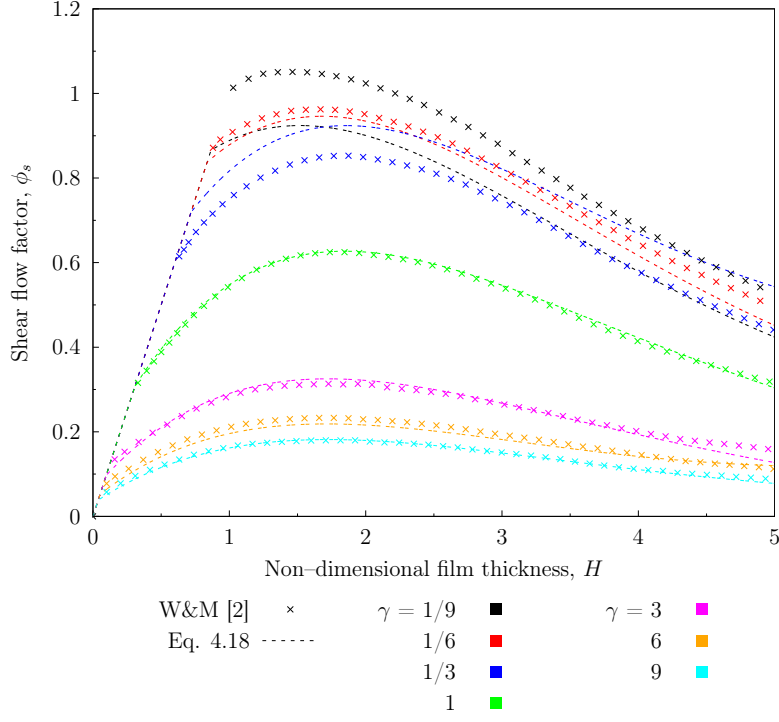
Figure 4.3: Shear flow factors – comparison between Wilson and Marsault [2] and Eq. 4.18.
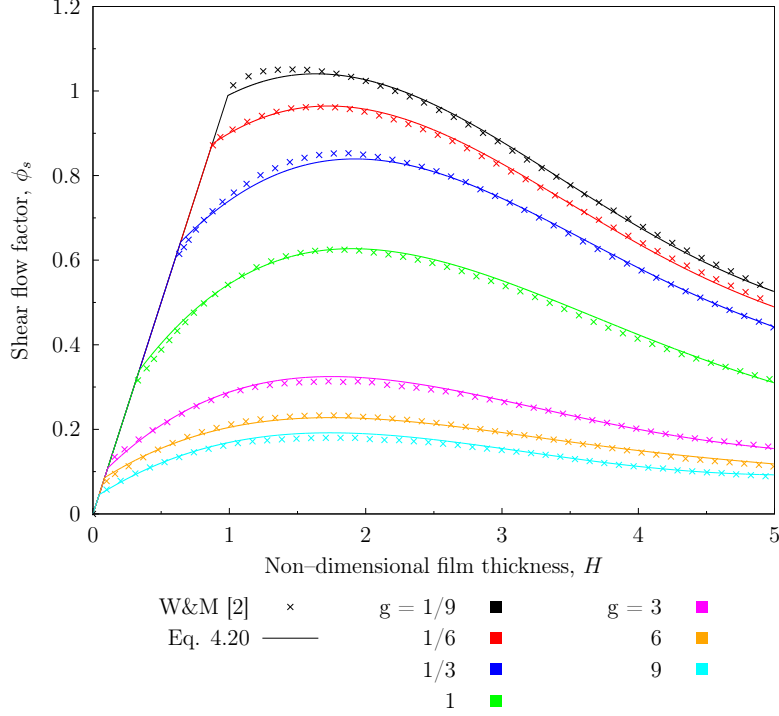
Figure 4.4: Shear flow factors – comparison between Wilson and Marsault [2] and Eq. 4.20.

$$\phi_x = 1 - CH \exp(-r) \qquad \text{for} \qquad \gamma > 1, \tag{4.24}$$

where constants C and r are given in Table 4.1 for different values of Peklenik parameter γ.

Table 4.1: C and r coefficients of pressure flow factor Eqs. 4.22 and 4.23 [9].

γ	C	r	Range
1/9	1.480	0.42	$H > 1$
1/6	1.380	0.42	$H > 1$
1/3	1.180	0.42	$H > 0.75$
1	0.900	0.56	$H > 0.5$
3	0.225	1.50	$H > 0.5$
6	0.520	1.50	$H > 0.5$
9	0.870	1.50	$H > 0.5$

For the calculation of shear flow factor ϕ_s, Patir and Cheng [9] presented the following form:

$$\phi_s = V_{r_a} \Phi_s \left(H, \gamma_a\right) - V_{r_b} \Phi_s \left(H, \gamma_b\right), \tag{4.25}$$

where V_{r_a} and V_{r_b} are the variance ratios of surfaces a and b given by:

$$V_{r_a} = \left(\frac{R_{q_a}}{R_q}\right)^2$$
$$V_{r_b} = \left(\frac{R_{q_b}}{R_q}\right)^2 = 1 - V_{r_a}. \tag{4.26}$$

Factor Φ_s is calculated using the following expression:

$$\Phi_s = A_1 H^{\alpha_1} \exp\left(-\alpha_2 H + \alpha_3 H^2\right) \qquad \text{for} \qquad H \leq 5, \tag{4.27}$$

$$\Phi_s = A_2 \exp\left(-0.25H\right) \qquad \text{for} \qquad H > 5. \tag{4.28}$$

Coefficients A_1, A_2, α_1, α_2, α_3 are functions of Peklenik parameter γ defined in Table 4.2.

To summarise, the flow factors introduced by Wilson and Marsault [2] and Patir and Cheng [9] were implemented. In case of the pressure flow factor ϕ_x Eq. 4.12 is used for non–dimensional film thickness $H < 3$, while Eqs. 4.23 and 4.24 for $H \geq 3$. In case of the shear flow factor ϕ_s Eq. 4.20 is used for $H < 5$, while Eqs. 4.25 and 4.28 for $H \geq 5$.

Table 4.2: Coefficients of shear flow factor Eqs. 4.26 and 4.27 [9].

γ	A_1	α_1	α_2	α_3	A_2
1/9	2.046	1.12	0.78	0.03	1.856
1/6	1.962	1.08	0.77	0.03	1.754
1/3	1.858	1.01	0.76	0.03	1.561
1	1.899	0.98	0.92	0.05	1.126
3	1.560	0.85	1.13	0.08	0.556
6	1.290	0.62	1.09	0.08	0.388
9	1.011	0.54	1.07	0.08	0.295

4.3. Lubricant Properties

In the following section the implemented models describing lubricant properties are given, i.e. pressure–temperature–density relations, low–shear and high–shear viscosity equations. Certain equations have already been specified in Chapter 2., however they are repeated here for the sake of completeness.

4.3.1. Density

Dowson–Higginson

The Dowson–Higginson [120] pressure–density relation, derived primarily for mineral oils, was implemented. Dependence of pressure on density, according to the Dowson–Higginson relation, can be expressed as:

$$p = \frac{(\rho_{\text{ref}} - \rho)C_1}{\rho - \rho_{\text{ref}}C_2}. \tag{4.29}$$

The bulk modulus β using the same density–pressure relation is calculated as:

$$\beta = \rho\frac{\mathrm{d}p}{\mathrm{d}\rho} = \rho\frac{C_1(C_2 - 1)\rho_{\text{ref}}}{(\rho - \rho_{\text{ref}}C_2)^2}. \tag{4.30}$$

The values of coefficients C_1 and C_2, and reference density ρ_{ref} are case–specific.

Murnaghan equation of state

In order to describe the pressure–temperature–density relation of Turbo T9 oil, used in the point contact analysis, the Murnaghan equation of state [123, 10] was

implemented, where the pressure depends both on density and temperature:

$$p = \frac{K_0}{K_0'} \left\{ \left[\frac{\rho}{\rho_{\text{ref}}} \left(1 + \alpha_{\text{v}}(T - T_{\text{ref}}) \right) \right]^{K_0'} - 1 \right\}, \tag{4.31}$$

where K_0' is the pressure rate of change of isothermal bulk modulus at $p = 0$, α_{v} is the thermal volume expansivity coefficient. K_0 is the isothermal bulk modulus defined at $p = 0$ and expressed as [10]:

$$K_0 = K_{00} \exp\left(\beta_{\text{K}} T \right), \tag{4.32}$$

where K_{00} is the isothermal bulk modulus defined at $p = 0$ and at zero absolute temperature. Murnaghan model is more physically relevant compared to the Dowson and Higginson model. However, it is much more complicated and requires specific experimental data as input [107]. In case of T9 oil the coefficients specified in Table 4.3 are proposed by Habchi et al. [10]. They defined the reference state as $p_{\text{ref}} = 0$ Pa, $T_{\text{ref}} = 25\,°\text{C}$.

Table 4.3: Murnaghan EOS coefficients for T9 oil [10].

K_0'	10.545	-
α_{V}	7.734×10^{-4}	K^{-1}
K_{00}	9.234	GPa
ρ_0	872	kg/m^3
β_{K}	6.090×10^{-3}	K^{-1}

4.3.2. Viscosity – Pressure and Temperature Dependence

In this section, several rheology models implemented in the code are presented. These include temperature–, pressure– and shear–dependent formulations.

Barus law

The simple law of Barus says:

$$\mu_{\text{B}} = \mu_0 \exp\left(\alpha p \right), \tag{4.33}$$

where μ_0 is the viscosity at ambient pressure and α is the pressure–viscosity coefficient.

Roelands and Houpert

The pressure– and temperature–dependent viscosity by Roelands [109] and Houpert [110] is expressed as [108]:

$$\mu_{\mathrm{H}} = \mu_0 \exp\left(\alpha^* p - \beta^*(T - T_0)\right), \tag{4.34}$$

where μ_0 is the viscosity at ambient pressure, α^* is the pressure–viscosity coefficient, β^* is the temperature–viscosity coefficient and T_0 is the ambient temperature in K. Pressure– and temperature–viscosity coefficients are defined as [108]:

$$\alpha^* p = [\ln(\mu_0) + 9.67] \left\{ \left(\frac{T - 138}{T_0 - 138}\right)^{-S_0} \left[\left(1 + \frac{1}{1.98 \times 10^8}\right)^Z - 1 \right] \right\},$$
$$\beta^* = [\ln(\mu_0) + 9.67] \left[1 + 5.1 \times 10^{-9} p\right]^Z \left[\frac{S_0}{(T_0 - 138)} \right]. \tag{4.35}$$

Exponents Z and S_0 are calculated using the following expressions [108]:

$$Z = \frac{\alpha}{5.1 \times 10^9 \left[\ln(\mu_0) + 9.67\right]},$$
$$S_0 = \frac{\beta(T_0 - 138)}{\ln(\mu_0) + 9.67}. \tag{4.36}$$

where α and β are pressure and temperature exponents, respectively, given for a specific oil.

Improved Yasutomi model

The improved Yasutomi model [11] developed by Bair et al. [137] is written as follows:

$$\mu = \mu_{\mathrm{g}} \exp\left[\frac{-2.303 C_1 (T - T_{\mathrm{g}})(1 + b_1 p)^{b_2}}{C_2 + (T - T_{\mathrm{g}})(1 + b_1 p)^{b_2}} \right], \tag{4.37}$$

where μ_{g} is the glass viscosity, and T_{g} is the glass transition temperature defined as:

$$T_{\mathrm{g}} = T_{\mathrm{g}0} + A_1 \ln(1 + A_2 p). \tag{4.38}$$

Yasutomi parameters (A_1, A_2), improved Yasutomi parameters (b_1, b_2), WLF parameters (C_1, C_2) and glass viscosity μ_{g} are lubricant specific. In case of Shell Turbo T68 oil the improved Yasutomi parameters proposed by Bair [11] are used, Table 4.4.

Table 4.4: Improved Yasutomi parameters for T68 oil [11].

μ_{g}	10^{12}	Pa s
T_{g_0}	-127.88	°C
A_1	1180.0	°C
A_2	0.1362	GPa^{-1}
b_1	17.26	GPa^{-1}
b_2	-0.1453	-
C_1	17.75	-
C_2	56.98	°C

Viscosity model – Shell Turbo T9 oil

Habchi et al. [10] derived a Vogel–like form of a viscosity model for Shell Turbo T9 oil using a least–squares regression on the viscosity measurement data. Their measurements include both pressure and temperature dependence of viscosity. The viscosity for T9 oil is, therefore, expressed as:

$$\mu = \mu_\infty \exp\left(\frac{B_{\mathrm{F}}\phi_\infty}{\phi - \phi_\infty}\right), \qquad (4.39)$$

where a scaling parameter ϕ is defined as:

$$\phi = \left(\frac{T}{T_{\mathrm{ref}}}\right)\left(\frac{\rho_{\mathrm{ref}}}{\rho}\right)^g. \qquad (4.40)$$

The reference temperature is defined as $T_{\mathrm{ref}} = 25$ °C, while the ratio ρ_{ref}/ρ is calculated using Eq. 4.31. The coefficients ϕ_∞, B_{F} and μ_∞ are specified in Table 4.5.

Table 4.5: Viscosity parameters for T9 oil [10].

ϕ_∞	0.26844	-
B_{F}	12.898	-
μ_∞	1.489×10^{-4}	Pa s
g	5.0348	–

4.3.3. Viscosity – Shear Dependence

In order to calculate shear–dependent viscosity, a viscosity flow factor ϕ_η is introduced:

$$\eta = \frac{\mu}{\phi_\eta}, \tag{4.41}$$

where η is the shear–dependent viscosity and μ is the low–shear viscosity. The approach adopted here for calculating viscosity flow factors was given by Ehret et al. [138], which uses a linear approximation of viscosity flow factors [10, 139]:

$$\begin{aligned} \phi_{\eta_x} &= f(\tau) + \tau f'(\tau), \\ \phi_{\eta_y} &= f(\tau), \end{aligned} \tag{4.42}$$

where ϕ_{η_x} is the viscosity flow factor in the direction of the shear stress τ, while ϕ_{η_y} is in the direction orthogonal to the shear stress. $f(\tau)$ is the shear–thinning function, depending on the selected shear–thinning model. Here, two models were implemented with the following shear–thinning functions:

- Ree–Eyring [114, 139]

$$f(\tau)_{\mathrm{RE}} = \frac{\tau_{\mathrm{E}}}{\tau} \sinh\left(\frac{\tau}{\tau_{\mathrm{E}}}\right), \tag{4.43}$$

- Carreau–Yasuda [119, 10]

$$f(\tau)_{\mathrm{CY}} = \left[1 + \left(\frac{\tau}{G}\right)^a\right]^{\frac{1-n}{an}}, \tag{4.44}$$

where τ_{E} is the Eyring stress, G is the critical stress, a and n are lubricant specific exponents. The shear rate $\dot{\gamma}$ can be expressed as:

$$\dot{\gamma} = \frac{\tau}{\mu} f(\tau). \tag{4.45}$$

Substituting shear–thinning functions into Eq. 4.42 results in the following expressions for viscosity flow factors:

- Ree–Eyring

$$\begin{aligned} \phi_{\eta_x} &= \cosh\left(\frac{\tau}{\tau_{\mathrm{E}}}\right), \\ \phi_{\eta_y} &= \frac{\tau_{\mathrm{E}}}{\tau} \sinh\left(\frac{\tau}{\tau_{\mathrm{E}}}\right), \end{aligned} \tag{4.46}$$

- Carreau–Yasuda

$$\phi_{\eta_x} = \left[1 + \left(\frac{\tau}{G}\right)^a\right]^{\frac{1-n}{an}} + \frac{1-n}{n}\left(\frac{\tau}{G}\right)^a\left[1 + \left(\frac{\tau}{G}\right)^a\right]^{\frac{1-n-an}{an}},$$

$$\phi_{\eta_y} = \left[1 + \left(\frac{\tau}{G}\right)^a\right]^{\frac{1-n}{an}}. \tag{4.47}$$

Following the linear approximation approach, the shear stress τ is calculated using the following expression [39]:

$$\frac{U_s\mu}{h} = \tau f(\tau), \tag{4.48}$$

where U_s is the magnitude of slip velocity.

Parameters needed for calculating shear–dependent viscosity is listed in Table 4.6 for Shell Turbo T9 and T68 oils.

Table 4.6: Ree–Eyring and Carreau–Yasuda parameters for T68 [12] and T9 oil [10].

Shell Turbo T68			
	τ_E	4.7	MPa
Shell Turbo T9			
	G	7	GPa
	a	5	-
	n	0.35	-

4.4. Thermal Contact Models

In this section, a review of the implemented heat transfer models used during the lubricated analysis is given. First, a two–dimensional thin film energy equation is given. Then, a model for calculating surface temperature increase based on the equation by Carslaw and Jaeger [89] is described. Finally, a lubricated contact boundary condition for the heat transfer model used in metal forming simulations is given.

4.4.1. Thin Film Energy Equation

In this section an energy equation is presented, used for calculating fluid temperature during hydrodynamic lubrication regime. Assuming thin film flow, Fig.

2.1, while neglecting the heat convection across the film (z–direction) and heat conduction along the film (x– and y–direction), the general expression of the energy equation states [41, 140]:

$$
\rho C_p \left(\frac{\partial T}{\partial t} + U_x \frac{\partial T}{\partial x} + U_y \frac{\partial T}{\partial y} \right) = \quad \frac{\partial}{\partial z} \left(k_{\mathrm{f}} \frac{\partial T}{\partial z} \right)
$$
$$
+ \beta_{\mathrm{f}} T \left(\frac{\partial p}{\partial t} + U_x \frac{\partial p}{\partial x} + U_y \frac{\partial p}{\partial y} \right) \tag{4.49}
$$
$$
+ \left(\tau_x \dot{\gamma}_x + \tau_y \dot{\gamma}_y \right),
$$

where C_p is the lubricant specific heat capacity, k_{f} is the lubricant conductivity, β_{f} is the thermal expansion coefficient, and velocity components U_x and U_y are defined as:

$$
U_x = -z \frac{h-z}{2\eta} \frac{\partial p}{\partial x} + U_{\mathrm{a}_x} \frac{h-z}{h} + U_{\mathrm{b}_x} \frac{z}{h},
$$
$$
U_y = -z \frac{h-z}{2\eta} \frac{\partial p}{\partial y} + U_{\mathrm{a}_y} \frac{h-z}{h} + U_{\mathrm{b}_y} \frac{z}{h}.
$$

In order to avoid the three–dimensional analysis, Eq. 4.49 is integrated across the film thickness (z–direction):

$$
\frac{1}{h} \int_0^h \rho C_p \left(\frac{\partial T}{\partial t} + U_x \frac{\partial T}{\partial x} + U_y \frac{\partial T}{\partial y} \right) = \quad \frac{1}{h} \int_0^h \frac{\partial}{\partial z} \left(k_{\mathrm{f}} \frac{\partial T}{\partial z} \right)
$$
$$
+ \frac{1}{h} \int_0^h \beta_{\mathrm{f}} T \left(\frac{\partial p}{\partial t} + U_x \frac{\partial p}{\partial x} + U_y \frac{\partial p}{\partial y} \right)
$$
$$
+ \frac{1}{h} \int_0^h \tau_x \dot{\gamma}_x + \tau_y \dot{\gamma}_y.
$$

$$\tag{4.50}$$

During the integration a parabolic temperature profile is assumed [41]:

$$
T(x,y,z) = (3T_{\mathrm{a}} + 3T_{\mathrm{b}} - 6T_{\mathrm{m}}) \left(\frac{z}{h} \right)^2 + (6T_{\mathrm{m}} - 4T_{\mathrm{a}} - 2T_{\mathrm{b}}) \frac{z}{h} + T_{\mathrm{a}}, \tag{4.51}
$$

where T_{a} and T_{b} are temperatures of surfaces a and b, while T_{m} represents the mean temperature across the film. After integration, the energy equation takes

the following two–dimensional form:

$$
\begin{aligned}
\rho C_p \Bigg[&\frac{\partial T_{\mathrm{m}}}{\partial t} + \frac{h^2}{120\eta_x}\frac{\partial p}{\partial x}\left(\frac{\partial T_{\mathrm{a}}}{\partial x} + \frac{\partial T_{\mathrm{b}}}{\partial x} - 12\frac{\partial T_{\mathrm{m}}}{\partial x}\right) \\
&+ \frac{h^2}{120\eta_y}\frac{\partial p}{\partial y}\left(\frac{\partial T_{\mathrm{a}}}{\partial y} + \frac{\partial T_{\mathrm{b}}}{\partial y} - 12\frac{\partial T_{\mathrm{m}}}{\partial y}\right) \\
&+ \frac{1}{2}\left(U_{\mathrm{a}_x} + U_{\mathrm{b}_x}\right)\frac{\partial T_{\mathrm{m}}}{\partial x} + \frac{1}{12}\left(U_{\mathrm{a}_x} - U_{\mathrm{b}_x}\right)\left(\frac{\partial T_{\mathrm{a}}}{\partial x} - \frac{\partial T_{\mathrm{b}}}{\partial x}\right) \\
&+ \frac{1}{2}\left(U_{\mathrm{a}_y} + U_{\mathrm{b}_y}\right)\frac{\partial T_{\mathrm{m}}}{\partial y} + \frac{1}{12}\left(U_{\mathrm{a}_y} - U_{\mathrm{b}_y}\right)\left(\frac{\partial T_{\mathrm{a}}}{\partial y} - \frac{\partial T_{\mathrm{b}}}{\partial y}\right)\Bigg] \\
= \quad &\frac{6k_{\mathrm{f}}}{h^2}(T_{\mathrm{a}} + T_{\mathrm{b}} - 2T_{\mathrm{m}}) \\
&+ \beta\Bigg\{ T_{\mathrm{m}}\frac{\partial p}{\partial t} + \frac{h^2}{120\eta}\left[\left(\frac{\partial p}{\partial x}\right)^2 + \left(\frac{\partial p}{\partial y}\right)^2\right](T_{\mathrm{a}} + T_{\mathrm{b}} - 12T_{\mathrm{m}}) \\
&\qquad + \frac{1}{2}T_{\mathrm{m}}\left(U_{\mathrm{a}_x} + U_{\mathrm{b}_x}\right)\frac{\partial p}{\partial x} + \frac{1}{12}\left(T_{\mathrm{a}} - T_{\mathrm{b}}\right)\left(U_{\mathrm{a}_x} - U_{\mathrm{b}_x}\right)\frac{\partial p}{\partial x} \\
&\qquad + \frac{1}{2}T_{\mathrm{m}}\left(U_{\mathrm{a}_y} + U_{\mathrm{b}_y}\right)\frac{\partial p}{\partial y} + \frac{1}{12}\left(T_{\mathrm{a}} - T_{\mathrm{b}}\right)\left(U_{\mathrm{a}_y} - U_{\mathrm{b}_y}\right)\frac{\partial p}{\partial y}\Bigg\} \\
&+ \left(\tau_{\mathrm{m}_x}\dot{\gamma}_x + \tau_{\mathrm{m}_y}\dot{\gamma}_y\right).
\end{aligned}
\tag{4.52}
$$

Eq. 4.52 written in vector notation says:

$$
\begin{aligned}
\rho C_p \Bigg[&\frac{\partial T_{\mathrm{m}}}{\partial t} + \frac{h^2}{120\eta}\nabla_{\mathrm{s}}p\bullet\left(\nabla_{\mathrm{s}}T_{\mathrm{a}} + \nabla_{\mathrm{s}}T_{\mathrm{b}} - 12\nabla_{\mathrm{s}}T_{\mathrm{m}}\right) \\
&+ \frac{1}{2}\left(\mathbf{U}_{\mathrm{a}} + \mathbf{U}_b\right)\bullet\left(\nabla_{\mathrm{s}}T_{\mathrm{m}}\right) + \frac{1}{12}\left(\mathbf{U}_{\mathrm{a}} - \mathbf{U}_b\right)\bullet\left(\nabla_{\mathrm{s}}T_{\mathrm{a}} - \nabla_{\mathrm{s}}T_{\mathrm{b}}\right)\Bigg] \\
= \quad &\frac{6k_{\mathrm{f}}}{h^2}(T_{\mathrm{a}} + T_{\mathrm{b}} - 2T_{\mathrm{m}}) \\
&+ \beta\Bigg[T_{\mathrm{m}}\frac{\partial p}{\partial t} + \frac{h^2}{120\eta}(\nabla_{\mathrm{s}}p)\bullet(\nabla_{\mathrm{s}}p)\left(T_{\mathrm{a}} + T_{\mathrm{b}} - 12T_{\mathrm{m}}\right) \\
&\qquad + \frac{1}{2}T_{\mathrm{m}}\left(\mathbf{U}_{\mathrm{a}} + \mathbf{U}_b\right)\bullet\nabla_{\mathrm{s}}p + \frac{1}{12}\left(T_{\mathrm{a}} - T_{\mathrm{b}}\right)\left(\mathbf{U}_{\mathrm{a}} - \mathbf{U}_b\right)\bullet\nabla_{\mathrm{s}}p\Bigg] \\
&+ \boldsymbol{\tau}_{\mathrm{m}}\bullet\dot{\boldsymbol{\gamma}},
\end{aligned}
\tag{4.53}
$$

where $\boldsymbol{\tau}_{\mathrm{m}}$ is the mean shear stress across the film thickness and $\dot{\boldsymbol{\gamma}}$ is the shear rate vector. In this two–dimensional form Eq. 4.53 is discretised using the Finite Area Method, on the same computational surface mesh as the Reynolds equation, Eq. 4.1. The energy equation is solved for the mean film temperature T_{m}, given

thermophysical properties, surface velocities and lubricant pressure p, calculated via Reynolds equation.

4.4.2. Deterministic Surface Temperature Model for Lubricated Point Contact

In this section a deterministic surface temperature model for lubricated point contact is presented. The model is based on the moving heat source equation by Carslaw and Jaeger [89], and is used in conjuction with the thin film energy equation, Eq. 4.53, for analysing point contacts.

The energy equation, Eq. 4.53, requires surface temperatures T_a and T_b as inputs, in order to calculate the mean film temperature T_m. When considering steady–state point contact [41, 44] between two semi–infinite bodies, the moving heat source equation by Carslaw and Jaeger [89] is used:

$$
\begin{aligned}
\Delta T(x, y) = \frac{1}{2\pi k_s} \int \int_\Omega q(x_1, y_1) \\
\times \frac{\exp\left(-\frac{|\mathbf{U}|}{2\kappa_s}\left[\sqrt{(x-x_1)^2 + (y-y_1)^2} - (x-x_1)\right]\right)}{\sqrt{(x-x_1)^2 + (y-y_1)^2}} \\
\times \mathrm{d}x_1 \, \mathrm{d}y_1,
\end{aligned}
$$

$$(4.54)$$

where $q(x_1, y_1)$ represents the heat flux to the surface at position (x_1, y_1), Ω is the boundary of the computational element located at (x_1, y_1), $\mathbf{U}$ is the velocity vector of considered surface, $\kappa_s = k_s/(\rho_s c_s)$ is the thermal diffusivity, k_s is the thermal conductivity, ρ_s is the density and c_s is the specific heat of a solid in consideration.

If a surface is spatially discretised using $N \times M$ square–shaped finite area faces, Fig. 4.5, and heat flux q has a constant value inside face Q, Eq. 4.54 takes the following form:

$$
\Delta T_P^Q = \frac{1}{2\pi k_s} q_Q \times I_Q^P,
\tag{4.55}
$$

where ΔT_P^Q is the temperature increase of face P due to heat flux q_Q of face Q. The centroids of faces P and Q are located at (x, y) and (x_1, y_1), respectively. I_Q^P

is the temperature coefficient surface integral defined by:

$$I_N^P = \int_{-d}^{d} \int_{-c}^{c} \frac{\exp\left(-\frac{|\mathbf{U}|}{2\kappa_\mathrm{s}}\left[\sqrt{(x-x_1)^2+(y-y_1)^2}-(x-x_1)\right]\right)}{\sqrt{(x-x_1)^2+(y-y_1)^2}}\,\mathrm{d}x_1\,\mathrm{d}y_1, \quad (4.56)$$

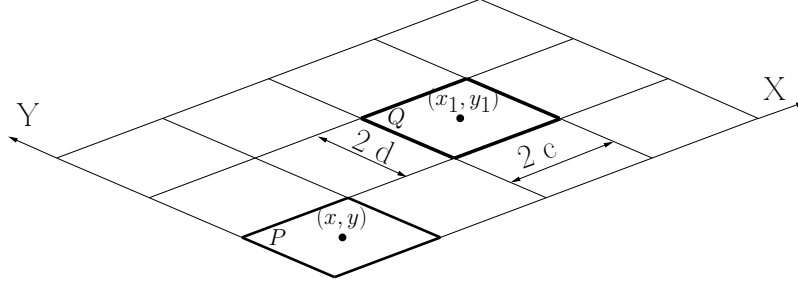where c and d are half–width and half–length of finite area face Q, Fig. 4.5.

Figure 4.5: With the definition of Eq. 4.55.

The surface integral form of Eq. 4.56 is inconvenient for numerical calculation. Following Bos [141], the Eq. 4.56 can be written in line integral form:

$$
\begin{aligned}
I_Q^P = \quad & \mathrm{E}_1\left(\frac{|\mathbf{U}|}{2\kappa_\mathrm{s}}\left[\sqrt{c^2+d^2}-c\right]\right) \times d \\
& - \mathrm{E}_1\left(\frac{|\mathbf{U}|}{2\kappa_\mathrm{s}}\left[\sqrt{c^2+(-d)^2}-c\right]\right) \times (-d) \\
& - \mathrm{E}_1\left(\frac{|\mathbf{U}|}{2\kappa_\mathrm{s}}\left[\sqrt{(-c)^2+d^2}-(-c)\right]\right) \times d \\
& + \mathrm{E}_1\left(\frac{|\mathbf{U}|}{2\kappa_\mathrm{s}}\left[\sqrt{(-c)^2+(-d)^2}-(-c)\right]\right) \times (-d) \\
& - \int_{-d}^{d} \frac{(y-y_1)^2}{\sqrt{(-c)^2+(y-y_1)^2)}} \frac{\exp\left(\frac{|\mathbf{U}|}{2\kappa_\mathrm{s}}\left[\sqrt{(-c)^2+(y-y_1)^2}-(-c)\right]\right)}{\sqrt{(-c)^2+(y-y_1)^2}-(-c)} \\
& + \int_{-d}^{d} \frac{(y-y_1)^2}{\sqrt{c^2+(y-y_1)^2)}} \frac{\exp\left(\frac{|\mathbf{U}|}{2\kappa_\mathrm{s}}\left[\sqrt{c^2+(y-y_1)^2}-c\right]\right)}{\sqrt{c^2+(y-y_1)^2}-c)},
\end{aligned}
$$
$$(4.57)$$

where $\mathrm{E}_1(\cdot)$ is the exponential integral function.

In order to account for the influence of heat fluxes of all finite area faces on temperature increase in face P, the following expression is used:

$$\Delta T_P = \sum_{i=0}^{i=n-1} \frac{1}{2\pi k_\mathrm{s}} q_i \times I_i^P, \quad (4.58)$$

where i is the index of finite area face, while n is the total number of faces. The heat flux q_i is considered constant inside a single finite area face, while its value variates between faces. Eq. 4.58 represents a linear convolution between the heat fluxes q_i and temperature coefficient integrals I_i, and can be written as:

$$\Delta T_P = c_1 \left(q * I^P \right),$$
(4.59)

where $c_1 = 1/(2\pi k_s)$. Calculating Eq. 4.59 by direct discrete integration is computationally expensive. If computational grid consists of $M \times N$ finite area faces, a two–dimensional convolution calculated by direct integration requires $(M \times N)^2$ multiplications and additions [50]. In order to reduce the number of operations required for calculating convolution, the Fast Fourier Transformation (FFT) can be applied. The FFT theory states that the convolution in the spatial domain corresponds to multiplication in the frequency domain [33]. In order to perform convolution using the FFT method, heat fluxes and temperature coefficient integrals for every finite area face need to be calculated and written in a form of two–dimensional matrices. Both matrices are transformed into the frequency domain, multiplied point–by-point, and the resulting matrix is transformed back to the spatial domain. That matrix is then multiplied with $1/(2\pi k_s)$ and the resulting values correspond to temperature increase of each finite area face. The FFT approach requires $(M \times N) \log (M \times N)$ operations, which is significantly less compared to the direct integration.

The FFT in this work is conducted numerically using the Discrete Fourier Transformation (DFT). The DFT can only be applied for the circular convolution, so the linear convolution has to be calculated using a circular convolution in order to utilise the FFT method. This can be done via two approaches [30]:

- By extending the heat flux matrix and temperature coefficient matrix using zero padding,

- By reordering the temperature coefficient matrix according to the rule of circular convolution [142].

If the size of the two–dimensional heat flux matrix is $M \times N$, the size of the temperature coefficient matrix, in both approaches, has to be $(2M-1) \times (2N-1)$.

In the first approach (zero padding), both matrices have to be extended to the equal size of

$$[M + (2M - 1) - 1] \times [N + (2N - 1) - 1],$$

i.e.

$$(3M - 2) \times (3N - 2).$$

In the second approach (coefficient reordering) only the heat flux matrix needs to be extended by zero padding to the size of temperature coefficient matrix, i.e. $(2M-1) \times (2N-1)$. Size of the temperature coefficient matrix remains unchanged, however the coefficients need to be shifted according to the [142]. Thus, the second approach offers significant matrix size reduction compared to the zero padding approach, which results in less memory consumption and computational time. Also, if the finite area mesh does not change and the thermal diffusivity κ_s is considered to be constant the temperature coefficient matrix can be calculated only once, at the beginning of a simulation. In this study, the second approach is adopted. The complete overview of both approaches was given by Liu et al. [30].

4.4.3. Thermal Boundary Condition for Rough Lubricated Contact

In this section a thermal boundary condition for rough lubricated contact is presented. The boundary condition is used with the hyperelastoplastic finite volume deformation solver described in [22]. The existing thermal contact boundary condition used for calculating heat transfer between two rough surfaces in dry contact is expanded to include the effects of lubricant conductance.

When two surfaces, a and b, are in contact the thermal equilibrium between them can be written as:

$$q_\mathrm{a} + q_\mathrm{b} - q_\mathrm{f} = 0, \tag{4.60}$$

where q_a and q_b are heat fluxes of surfaces a and b, while q_f is the friction generated heat flux. The surface heat fluxes are defined as:

$$
\begin{aligned}
q_\mathrm{a} &= h_\mathrm{c} \left(T_\mathrm{a} - T_\mathrm{b} \right) + q_{\mathrm{f_a}} \\
q_\mathrm{b} &= h_\mathrm{c} \left(T_\mathrm{b} - T_\mathrm{a} \right) + q_{\mathrm{f_b}},
\end{aligned}
\tag{4.61}
$$

where h_c is the thermal contact conductance, T_a and T_b are surface temperatures, while q_{f_a} and q_{f_b} are friction heat fluxes conducted by surfaces a and b respectively. The total heat flux generated by the surface friction q_f is expressed as:

$$q_f = \boldsymbol{\tau} \bullet (\mathbf{U}_a - \mathbf{U}_b), \tag{4.62}$$

where τ is the tangential surface traction vector, while $\mathbf{U}_a$ and $\mathbf{U}_b$ are velocity vectors of surfaces a and b, respectively. The total friction heat flux is divided between two contacting surfaces in the following manner [143]:

$$
\begin{aligned}
q_{f_a} &= q_f \frac{K_a}{\xi_a}, \\
q_{f_b} &= q_f \frac{K_b}{\xi_b},
\end{aligned}
\tag{4.63}
$$

where K_a and K_b are conductivities, while ξ_a and ξ_b are heat partition coefficients of surfaces a and b, respectively. Heat partition coefficients are calculated via:

$$
\begin{aligned}
\xi_a &= \sqrt{\frac{\rho_b C_b}{\rho_a C_a} K_a K_b} + K_a, \\
\xi_b &= \sqrt{\frac{\rho_a C_a}{\rho_b C_b} K_b K_a} + K_b,
\end{aligned}
\tag{4.64}
$$

where C_a and C_b are specific heat capacities of surfaces a and b.

In rough surface contact heat is conducted through a finite number of contact spots, i.e. asperities [103]. Between asperities there are gaps which are, in case of lubricated contact, filled with a liquid. Therefore, aside from the conduction, heat convection and radiation can occur across the gap. The non–ideal contact and existence of liquid between the two surfaces constrain the heat flow, thus causing temperature drop across the interface. Generally, there are three heat transfer modes involved [103]:

- solid conduction through contacting asperities,

- convection and conduction through the lubricant,

- thermal radiation between neighbouring non–contacting asperities.

The three modes of heat transfer may influence each other. However, the assumption that each mode acts in parallel to another is accepted for engineering analysis, as it usually introduces a small error [103]. In the metal forming applications, mainly wire drawing and rolling, the temperature rarely exceeds 900 K (steel and aluminium hot rolling) if the appropriate cooling is applied [144, 145]. The contribution of radiation in total heat transfer is around 2% for metallic contacts at temperatures up to 900 K [146]. Therefore, for these applications the radiative heat transfer component can be neglected.

Considering stated assumptions, the total thermal conductance for wire rolling and drawing cases can be expressed as:

$$h_c = h_{cs} + h_{cf}, \qquad (4.65)$$

where h_{cs} is the solid contact conductance and h_{cf} is the fluid conductance. In this study, a simplified model for pressure–dependent heat conduction through a dry rough surface contact interface is used [143]:

$$h_{cs} = h_{cs_0} \left(\frac{P_a}{H_v} \right)^w, \qquad (4.66)$$

where h_{cs_0} is the thermal resistance coefficient, H_v is the Vickers hardness, w is the exponent, while P_a is the asperity contact pressure. The three parameters (h_{cs_0}, H_v, w) are experimentally measured. For heat transfer through the lubricant, the following expression for fluid conductance is used [103]:

$$h_{cf} = (k_f/h) \times (1 - A_r), \qquad (4.67)$$

where k_f is the thermal conductivity of the fluid, h is the mean film thickness and A_r is the ratio of asperity contact area over the nominal area. Eqs. 4.66 and 4.67 are calculated for every boundary face under contact.

In case of non–contacting boundary faces, the surface heat flux due to heat convection is assumed:

$$\begin{aligned} q_{a_{conv}} &= \alpha_a \left(T_a - T_\infty \right), \\ q_{b_{conv}} &= \alpha_b \left(T_b - T_\infty \right), \end{aligned} \qquad (4.68)$$

where α_a and α_b are heat transfer coefficients of surfaces a and b outside the contact region, and T_∞ is the ambient temperature.

Finally, the thermal boundary condition used with the hyperelastoplastic finite volume deformation solver is the fixed temperature gradient (Neumann) boundary condition [49] expressed as:

$$\left(\frac{\mathbf{S}}{|\mathbf{S}|}\bullet\nabla T\right)_{\mathrm{a,b}} = -q_{\mathrm{a,b}}/K_{\mathrm{a,b}}, \tag{4.69}$$

where surface heat fluxes $q_{\mathrm{a,b}}$ are calculated using Eqs. 4.61 to 4.68, while $\mathbf{S}$ is the boundary face area vector.

4.5. Asperity Contact Models

In the following section the implemented asperity contact models are given. Three statistical single asperity models were implemented and one deterministic elastic–perfectly–plastic contact model. The literature overview of the models was presented in Chapter 2., section 2.4., while the equations and implementation are given here.

4.5.1. Statistical Contact Models

Three statistical contact models were implemented: Greenwood–Williamson (GW) [70], Wadwalkar–Jackson (WJ) [79] and Peng–Liu (PL) [80]. The GW model is a single asperity contact model based on the Hertzian theory where the deformation of hemispherical asperity is considered to be purely elastic. WJ and PL models are elastic–perfectly–plastic single asperity models, using Hertzian theory for the elastic and analytical relations for the plastic contact. The analytical relations were derived by authors based on the results of finite elements simulations of contact between a deformable hemisphere and a rigid plate. Single asperity models were derived using the following assumptions [8]:

- Rough surface contact is calculated by integrating analytical single–asperity equations for contact force and area;

- The tip of the asperity is hemispherical;

- All asperities have the same average radius R, but different heights z_y;

- One contacting surface is considered to be smooth, while the other surface has a large number asperities.

Two variables of the rough surface contact are calculated: the asperity contact pressure and the contact area ratio. The contact area ratio is a ratio between asperity contact area and nominal contact area defined by [8]:

$$A_{\mathrm{r}}(d) = \eta \int_{d_y}^{\infty} A_{\mathrm{s}}(\omega)\, \varphi(z_y)\, \mathrm{d}z_y, \tag{4.70}$$

where η is the asperity density (number of asperities per unit area), $\omega = z_y - d_y$ is the asperity interference, z_y is the single asperity height measured from the mean asperity height plane [75] (Fig. 4.6), $d_y = d - y_{\mathrm{s}}$ is the distance between the smooth surface and mean asperity height plane, d is the distance between the smooth surface and mean surface height plane, $A_{\mathrm{s}}(\omega)$ is the single asperity contact area function, and $\varphi(z_y)$ is the asperity height distribution function. The asperity contact pressure is calculated using the following expression:

$$P_{\mathrm{a}}(d) = \eta \int_{d_y}^{\infty} F_{\mathrm{s}}(\omega)\, \varphi(z_y)\, \mathrm{d}z_y, \tag{4.71}$$

where F_{s} is the single asperity contact force function. Note that the asperity contact pressure P_{a} is equal to the asperity contact force per **nominal** contact area. The distance between the mean surface and mean asperity height planes y_{s}, Fig. 4.6, is calculated using the following expression [75]:

$$y_{\mathrm{s}} = \frac{0.25}{\sqrt{3\pi\, \eta\, R}}, \tag{4.72}$$

in case of GW and WJ models, while in the case of PL contact model the following expression is used [80]:

$$y_{\mathrm{s}} = 1.5\sqrt{\frac{R_{\mathrm{q}}}{108\pi\, \eta\, R}}, \tag{4.73}$$

where R_{q} is the combined RMS surface roughness of two surface in contact. For the implemented statistical contact models a Gaussian asperity height distribution is assumed:

$$\varphi(z_y) = \frac{1}{\sigma_{\mathrm{s}}\sqrt{2\pi}} \exp\left(-0.5\left(\frac{z}{\sigma_{\mathrm{s}}}\right)^2\right), \tag{4.74}$$

where σ_s is the standard deviation of asperity heights calculated by [75]:

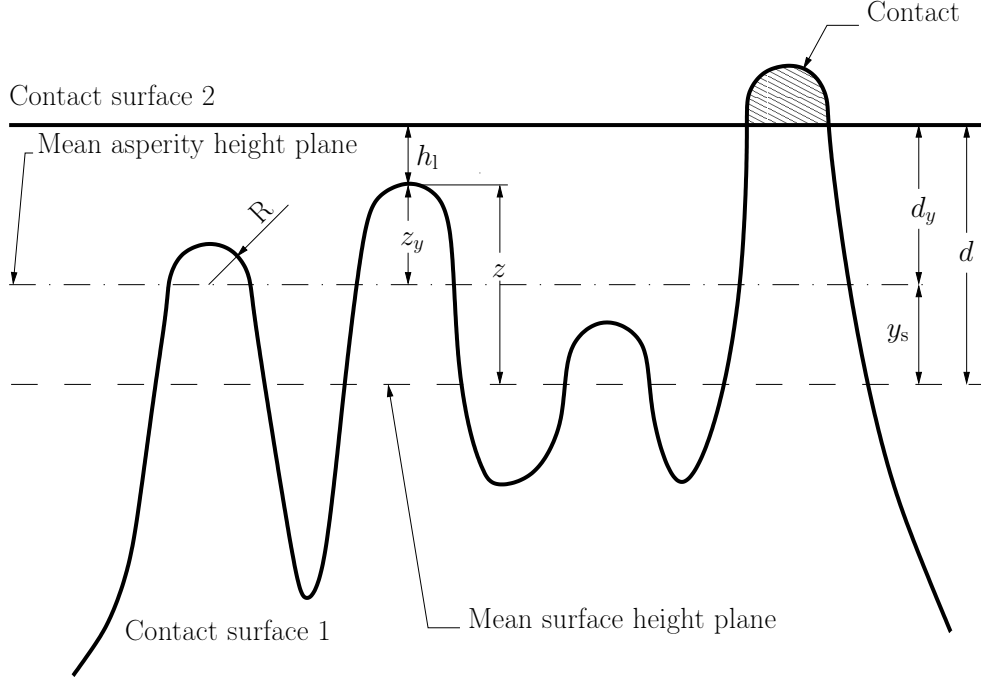$$\sigma_\mathrm{s} = \sqrt{R_\mathrm{q}^2 - \frac{3.7169 \times 10^{-4}}{(\eta\,R)^2}}. \tag{4.75}$$

Figure 4.6: Rough contact schematics.

The required rough surface parameters η, R and R_q can be expressed as [81]:

$$\eta = \frac{m_4}{6\pi\sqrt{3}\,m_2}, \tag{4.76}$$

$$R = 0.375\sqrt{\frac{\pi}{m_4}}, \tag{4.77}$$

$$R_\mathrm{q} = \sqrt{m_0}, \tag{4.78}$$

where spectral moments m_0, m_2 and m_4 are calculated from a measured surface roughness profile or a three–dimensional surface scan as follows:

$$
\begin{aligned}
m_0 &= \frac{1}{n}\sum_{i=1}^{n} z_{y_i}^2, \\
m_2 &= \frac{1}{n}\sum_{i=1}^{n} \left(\frac{\mathrm{d}z_{y_i}}{\mathrm{d}x}\right)^2, \\
m_4 &= \frac{1}{n}\sum_{i=1}^{n} \left(\frac{\mathrm{d}z_{y_i}^2}{\mathrm{d}^2 x}\right)^2.
\end{aligned}
\tag{4.79}
$$

In case where both contacting surfaces are rough, equivalent surface roughness is considered in which the spectral moments are summed for the two rough surfaces a and b:

$$m_0 = m_{0_\mathrm{a}} + m_{0_\mathrm{b}},$$
$$m_2 = m_{2_\mathrm{a}} + m_{2_\mathrm{b}}, \qquad (4.80)$$
$$m_4 = m_{4_\mathrm{a}} + m_{4_\mathrm{b}}.$$

In case of a three–dimensional surface scan, spectral moments can be calculated for a number of different directions, and for a number of profiles parallel to the selected direction. Usually, two main directions are chosen; one orthogonal to the other, with multiple parallel profiles for each direction [81]. In case of two orthogonal directions x and y the equivalent spectral moments are calculated as [81]:

$$m_{0\mathrm{e}} = \frac{m_{0x} + m_{0y}}{2},$$
$$m_{2\mathrm{e}} = \sqrt{m_{2x} \times m_{2y}}, \qquad (4.81)$$
$$m_{4\mathrm{e}} = \sqrt{m_{4x} \times m_{4y}}.$$

When n_p profiles are examined along a single direction, e.g. x–direction, the average spectral moments are calculated as follows [135]:

$$m_{0x} = \frac{1}{n_p} \sum_{i=1}^{n_p} m_{0x_i},$$
$$m_{2x} = \frac{1}{n_p} \sum_{i=1}^{n_p} m_{2x_i}, \qquad (4.82)$$
$$m_{4x} = \frac{1}{n_p} \sum_{i=1}^{n_p} m_{4x_i}.$$

The mean film thickness h, required by Eqs. 4.1 and 4.5, between two rough surfaces in contact is calculated by integrating the local film thickness h_l, Fig. 4.6:

$$h = \int_{-\infty}^{h} (h_\mathrm{l} - z)\, \varphi(z)\, \mathrm{d}z, \qquad (4.83)$$

where z is the asperity height measured from the mean surface height plane, h_l is the local film thickness, and $\varphi(z)$ is the surface height distribution function defined by Eq. 4.74.

The numerical integration of Eqs. 4.70, 4.71 and 4.83 is conducted using the fixed–order Gauss–Legendre integration function [147].

The Greenwood–Williamson (GW) Contact Model

The Greenwood–Williamson (GW) model [69] for a single asperity contact is based on the Hertzian theory where the deformation of hemispherical asperity is considered to be purely elastic. The asperity contact area and force functions are defined by:

$$A_{\mathrm{s}}(\omega) = \pi \, R \, \omega, \tag{4.84}$$

$$F_{\mathrm{s}}(\omega) = \frac{4}{3} E' \sqrt{R \, \omega^3}, \tag{4.85}$$

where E' is the equivalent elastic modulus of two surfaces a and b in contact defined by [70]:

$$\frac{1}{E'} = \frac{1 - \nu_{\mathrm{a}}^2}{E_{\mathrm{a}}} + \frac{1 - \nu_{\mathrm{b}}^2}{E_{\mathrm{b}}}. \tag{4.86}$$

In Eq. 4.86 variables E_{a} and E_{b} are moduli of elasticity of materials a and b, while ν_{a} and ν_{b} are Poisson's ratios.

In order to avoid the numerical integration of Eqs. 4.70 and 4.71, the closed–form equations given by Jackson and Green [70] were implemented. The contact area ratio $A_{\mathrm{r}}(d)$ is expressed as:

$$A_{\mathrm{r}}(d) = \eta \, \pi \, R \, I_{\mathrm{ae}}(d), \tag{4.87}$$

where $I_{\mathrm{ae}}(d)$ is the asperity contact area integral defined as:

$$I_{\mathrm{ae}}(d) = \frac{\sigma_{\mathrm{s}}}{\sqrt{2\pi}} \exp\left(-0.5 d_*^2\right) + 0.5 d_y \left[\mathrm{erf}\left(\frac{d_*}{\sqrt{2}}\right) - 1 \right], \tag{4.88}$$

where $d_* = d_y / \sigma_{\mathrm{s}}$ and $\mathrm{erf}(\cdot)$ is the error function. The asperity contact pressure $P_{\mathrm{a}}(d)$ is calculated as:

$$P_{\mathrm{a}}(d) = \frac{4}{3} \eta \, E' \, \sqrt{R} \, I_{\mathrm{pe}}(d), \tag{4.89}$$

where $I_{\mathrm{pe}}(d)$ is the asperity contact pressure integral defined by:

$$I_{\mathrm{pe}}(d) = \begin{cases} \dfrac{\Gamma(1.25)(\sigma_{\mathrm{s}})^{1.5}}{2^{0.25}\sqrt{\pi}} & d_y = 0, \\[2em] \dfrac{\sigma_{\mathrm{s}}}{4\exp(d_{**})}\sqrt{\dfrac{d_y}{\pi}}\left[\left(1+d_*^2\right)\mathrm{K}_{0.25}(d_{**}) - d_*^2\,\mathrm{K}_{0.75}(d_{**})\right] & d_y > 0, \\[2em] \dfrac{\sigma_{\mathrm{s}}}{4\exp(d_{**})}\sqrt{\dfrac{-d_y\pi}{2}} & \\ \quad \left\{\left(1+d_*^2\right)\left[\mathrm{I}_{0.25}(d_{**}) + \dfrac{2}{\pi}\sin(0.25\pi)\,\mathrm{K}_{0.25}(d_{**})\right]\right. & \\ \quad + \left(3+d_*^2\right)\mathrm{I}_{0.25}(d_{**}) & d_y < 0, \\ \quad \left.+\, d_*^2\left[\mathrm{I}_{0.75}(d_{**}) + \mathrm{I}_{1.25}(d_{**})\right]\right\} & \end{cases}$$

$$(4.90)$$

where $d_{**} = d_*^2/4$, $\Gamma(\cdot)$ is the gamma function, $\mathrm{I}_\nu(\cdot)$ and $\mathrm{K}_\nu(\cdot)$ are the modified Bessel functions of the first and second kinds.

The Wadwalkar–Jackson (WJ) Contact Model

The Wadwalkar–Jackson (WJ) [79] model is an elastic–perfectly–plastic single asperity contact model. The elastic part of the model uses the GW model, Eqs. 4.70, 4.71, 4.84 and 4.85, while the plastic deformation is calculated via analytical equations derived based on the results of the finite element simulations of contact between a deformable hemisphere and a rigid plate [79]. This model represents an extension to the Jackson–Green model [78] allowing larger asperity deformations, in which the ratio of the asperity contact radius a and initial asperity radius R is greater than 0.412. The contact area ratio and pressure are calculated using expressions similar to Eqs. 4.70 and 4.71, with the difference of splitting the integrals into elastic and plastic integration boundaries:

$$A_{\mathrm{r}}(d) = \eta\left(\int_{d_y}^{d_y+1.9\omega_{\mathrm{c}}} A_{\mathrm{se}}(\omega)\,\varphi(z_y)\,\mathrm{d}z_y + \int_{d_y+1.9\omega_{\mathrm{c}}}^{\infty} A_{\mathrm{sp}}(\omega)\,\varphi(z_y)\,\mathrm{d}z_y\right), \quad (4.91)$$

$$P_{\mathrm{a}}(d) = \eta\left(\int_{d_y}^{d_y+1.9\omega_{\mathrm{c}}} F_{\mathrm{se}}(\omega)\,\varphi(z_y)\,\mathrm{d}z_y + \int_{d_y+1.9\omega_{\mathrm{c}}}^{\infty} F_{\mathrm{sp}}(\omega)\,\varphi(z_y)\,\mathrm{d}z_y\right), \quad (4.92)$$

where $A_{\text{se}}(\omega)$ is the elastic contact area function defined by Eq. 4.84, $A_{\text{sp}}(\omega)$ is the plastic contact area function, F_{se} is the elastic contact force function defined by Eq. 4.85, F_{sp} is the plastic contact force function and ω_{c} is the critical interference. The critical interference is given by [78]:

$$\omega_{\text{c}} = \left(\frac{\pi\,C\,Y}{2E'}\right)^2 R, \tag{4.93}$$

where Y is the yield strength of the material, and the critical yield coefficient C is defined as:

$$C = 1.295 \exp(0.736\nu).$$

Since two surfaces $(a,\ b)$ in contact can have different material properties, the yield strength and critical yield coefficient to be used in the model are of the material which yields first, i.e. which has a lower CY product:

$$CY = \min\left(C_{\text{a}}\,Y_{\text{a}}, C_{\text{b}}\,Y_{\text{b}}\right).$$

The elastic upper integration limit of $d_y + 1.9\omega_{\text{c}}$ was determined by Jackson and Green [78] through their finite element simulations. The plastic contact area function $A_{\text{sp}}(\omega)$ is calculated as:

$$A_{\text{sp}}(\omega) = a_{\text{new}}^2\pi, \tag{4.94}$$

where a is the asperity contact radius. If the considered hemispherical asperity has a **deformable** base, its contact radius is calculated via:

$$a_{\text{new}} = a_{\text{JG}} + \left[A_1\left(\frac{\omega}{\omega_{\text{c}}}\right)^2 - A_2\left(\frac{\omega}{\omega_{\text{c}}}\right)\right]R, \tag{4.95}$$

where a_{JG} is the contact radius derived by Jackson and Green [78], while A_1 and A_2 are coefficients defined as:

$$A_1 = 0.0826\left(\frac{Y}{E'}\right)^{3.148},$$

$$A_2 = 0.3805\left(\frac{Y}{E'}\right)^{1.545}.$$

The contact radius a_{JG} is calculated by:

$$a_{\text{JG}} = \sqrt{\omega R\left(\frac{\omega}{1.9\omega_{\text{c}}}\right)^B}, \tag{4.96}$$

where $B = 0.14 \exp\left(23Y/E'\right)$ is the material dependent exponent.

In case of a **rigid** asperity base the contact radius is determined using the following expression:

$$a_{\text{new}} = a_{\text{JG}} - \left[A_3 \left(\frac{\omega}{\omega_{\text{c}}}\right)^2 + A_4 \left(\frac{\omega}{\omega_{\text{c}}}\right)\right] R, \tag{4.97}$$

where A_3 and A_3 are defined as:

$$A_3 = 158393 \left(\frac{Y}{E'}\right)^{5.605},$$

$$A_4 = 0.0034 \left(\frac{Y}{E'}\right)^{0.8939}.$$

The plastic contact force function F_{sp} used in Eq. 4.92 is expressed as:

$$\begin{aligned}
F_{\text{sp}} = &\exp\left(-\frac{1}{4}\left(\frac{\omega}{\omega_{\text{c}}}\right)^{5/12}\right)\left(\frac{\omega}{\omega_{\text{c}}}\right)^{3/2} \\
&+ \frac{P_{\text{m}}}{F_{\text{c}}}\pi a^2 \left[1 - \exp\left(-\frac{1}{25}\left(\frac{\omega}{\omega_{\text{c}}}\right)^{5/9}\right)\right],
\end{aligned} \tag{4.98}$$

where P_{m} is the mean contact pressure and F_{c} is the critical contact force defined by:

$$F_c = \frac{4}{3}\left(\frac{R}{E'}\right)^2 \left(\frac{\pi C Y}{2}\right)^3. \tag{4.99}$$

The expression for the mean pressure P_{m} is given as [79]:

$$P_{\text{m}} = \left\{2.84 - 0.92\left[1 - \cos\left(\pi\frac{a_{\text{new}}}{R_{\text{new}}}\right)\right]\right\} Y, \tag{4.100}$$

where R_{new} is the radius of curvature of the deformed hemispherical asperity defined for asperities with:

- Deformable base

$$R_{\text{new}} = \sqrt{\frac{R^3}{0.76(R - \omega)} - \frac{a_{\text{new}}^2}{2}};$$

- Rigid base

$$R_{\text{new}} = \sqrt{\frac{4R^3}{3(R - \omega)} - \frac{(R - \omega)^2}{3} - a_{\text{new}}^2}.$$

The Peng–Liu (PL) Contact Model

Peng et al. [80] derived their own set of equations for calculating rough surface contact from the results of finite element simulations of contact between a rigid flat and a single asperity on a deformable substrate. The authors defined separate contact area and force functions for five integration intervals:

$$
\begin{aligned}
A_{\mathrm{r}}(d) = \eta\,R^2\pi\Bigg(&\int_{d_y}^{d_y+\omega_{\mathrm{c}}'R} A_{\mathrm{s1}}'(\omega')\,\varphi(z_y)\,\mathrm{d}z_y \\
&+ \int_{d_y+\omega_{\mathrm{c}}'R}^{d_y+6\omega_{\mathrm{c}}'R} A_{\mathrm{s2}}'(\omega')\,\varphi(z_y)\,\mathrm{d}z_y \\
&+ \int_{d_y+6\omega_{\mathrm{c}}'R}^{d_y+110\omega_{\mathrm{c}}'R} A_{\mathrm{s3}}'(\omega')\,\varphi(z_y)\,\mathrm{d}z_y \\
&+ \int_{d_y+110\omega_{\mathrm{c}}'R}^{d_y+(2\omega_{\mathrm{c}}'RE'/Y)} A_{\mathrm{s4}}'(\omega')\,\varphi(z_y)\,\mathrm{d}z_y \\
&+ \int_{d_y+(2\omega_{\mathrm{c}}'RE'/Y)}^{d_y+0.15R} A_{\mathrm{s5}}'(\omega')\,\varphi(z_y)\,\mathrm{d}z_y\Bigg),
\end{aligned}
\tag{4.101}
$$

where $\omega' = \omega/R$ is the dimensionless asperity interference, $\omega_{\mathrm{c}}' = \omega_{\mathrm{c}}/R$ is the dimensionless critical interference, and A_{s1}' to A_{s5}' are dimensionless contact area functions defined by:

$$
\begin{aligned}
A_{\mathrm{s1}}'(\omega') &= \omega', \\
A_{\mathrm{s2}}'(\omega') &= 0.93\omega_{\mathrm{c}}'\left(\frac{\omega'}{\omega_{\mathrm{c}}'}\right)^{1.136}, \\
A_{\mathrm{s3}}'(\omega') &= 0.94\omega_{\mathrm{c}}'\left(\frac{\omega'}{\omega_{\mathrm{c}}'}\right)^{1.146}, \\
A_{\mathrm{s4}}'(\omega') &= C_{\mathrm{a1}}\omega'^{C_{\mathrm{a2}}}, \\
A_{\mathrm{s5}}'(\omega') &= C_{\mathrm{a3}} + C_{\mathrm{a4}}\omega' + C_{\mathrm{a5}}\omega'^2 + C_{\mathrm{a6}}\omega'^3.
\end{aligned}
\tag{4.102}
$$

The calculation of the contact pressure is also divided into the same five intervals:

$$
\begin{aligned}
P_{\mathrm{a}}(d) = \eta\, R^2 \pi Y \Bigg(& \int_{d_y}^{d_y+\omega_c'R} F_{\mathrm{s1}}'(\omega')\, \varphi(z_y)\; \mathrm{d}z_y \\
& + \int_{d_y+\omega_c'R}^{d_y+6\omega_c'R} F_{\mathrm{s2}}'(\omega')\, \varphi(z_y)\; \mathrm{d}z_y \\
& + \int_{d_y+6\omega_c'R}^{d_y+110\omega_c'R} F_{\mathrm{s3}}'(\omega')\, \varphi(z_y)\; \mathrm{d}z_y \\
& + \int_{d_y+110\omega_c'R}^{d_y+(2\omega_c'RE'/Y)} F_{\mathrm{s4}}'(\omega')\, \varphi(z_y)\; \mathrm{d}z_y \\
& + \int_{d_y+(2\omega_c'RE'/Y)}^{d_y+0.15R} F_{\mathrm{s5}}'(\omega')\, \varphi(z_y)\; \mathrm{d}z_y \Bigg),
\end{aligned}
\tag{4.103}
$$

where F_{s1}' to F_{s5}' are dimensionless contact force functions defined by:

$$
\begin{aligned}
F_{\mathrm{s1}}'(\omega') &= \frac{4E'\omega'^{1.5}}{3\pi Y}, \\
F_{\mathrm{s2}}'(\omega') &= \frac{4.12E'\omega_c'^{0.075}}{3\pi Y}\omega'^{1.425}, \\
F_{\mathrm{s3}}'(\omega') &= C_{l1}\omega'^{C_{l2}} + C_{l3}, \\
F_{\mathrm{s4}}'(\omega') &= C_{l4} + C_{l5}\omega' + C_{l6}\omega'^2 + C_{l7}\omega'^3, \\
F_{\mathrm{s5}}'(\omega') &= C_{l8} + C_{l9}\omega' + C_{l10}\omega'^2 + C_{l11}\omega'^3.
\end{aligned}
\tag{4.104}
$$

Coefficients C_{a1} to C_{a6} and C_{l1} to C_{l11} are given in [80].

4.5.2. Deterministic Contact Model

In the previous section statistical contact models were presented. These models are single asperity models which do not account for asperity interaction, the asperity shape is assumed to be hemispherical with a single average radius and the distribution of asperity heights is Gaussian. Moreover, characterising surface topography using only a few parameters, which is the case with the implemented statistical models, is ambiguous since the same parameters can be calculated for quite different topographies, as was already mentioned in Chapter 2. In this section a linear elastic–perfectly–plastic deterministic contact model is presented. The algorithm is based on the calculation procedure by Stanley and Kato [85], using the FFT method for calculating elastic deflection of a rough surface. The

method for calculating plastic part of the contact was adopted from Sahlin et al. [45, 46].

The elastic deflection δ at point (x, y) due to pressure p acting on element E_Q, Fig. 4.7, using the Boussinesq–Cerruti theory [148] can be expressed as [108]:

$$\delta(x, y) = \frac{1}{E_r} \int_{-d}^{d} \int_{-c}^{c} \frac{p \, dx_1 \, dy_1}{\sqrt{(x - x_1)^2 + (y - y_1)^2}}, \tag{4.105}$$

where $E_r = \pi E'$ is the reduced elastic modulus. The centroid of rectangular base Q of element E_q is located at (x_1, y_1). If element E_Q is flat–roofed and pressure p is constant over the whole element, Eq. 4.105 can be integrated [108]:

$$\delta(x, y) = \frac{p}{E_r} D(x', y'), \tag{4.106}$$

where $x' = x - x_1$, $y' = y - y_1$ and $D(x', y')$ is the flexibility coefficient defined as:

$$\begin{aligned}
D(x', y') = \quad & (y' - d) \ln \left[\frac{(x' - c) + \sqrt{(y' - d)^2 + (x' - c)^2}}{(x' + c) + \sqrt{(y' - d)^2 + (x' + c)^2}} \right] \\
& + (y' + d) \ln \left[\frac{(x' + c) + \sqrt{(y' + d)^2 + (x' + c)^2}}{(x' - c) + \sqrt{(y' + d)^2 + (x' - c)^2}} \right] \\
& + (x' + c) \ln \left[\frac{(y' + d) + \sqrt{(y' + d)^2 + (x' + c)^2}}{(y' - d) + \sqrt{(y' - d)^2 + (x' + c)^2}} \right] \\
& + (x' - c) \ln \left[\frac{(y' - d) + \sqrt{(y' - d)^2 + (x' - c)^2}}{(y' + d) + \sqrt{(y' + d)^2 + (x' - c)^2}} \right] .
\end{aligned} \tag{4.107}$$

Examining Eq. 4.106 in the sense of the Finite Area Method means that the value of deflection of finite area face P in its centre (x, y) is equal to $\delta(x, y)$, due to pressure p acting on finite area face Q. In order to account for the influence of pressure of every finite area face on face P, the circular convolution is performed:

$$\delta_P = \frac{1}{E_r} \sum_{i=0}^{i=n-1} p_i \times D_i^P = \frac{1}{E_r} \left(p \otimes D^P \right). \tag{4.108}$$

where i is the index of a finite area face, while n is the total number of faces. In order to perform the circular convolution efficiently for all finite area faces the FFT method is utilised, similar to how it was described in Section 4.4.2.

The difference, however, is that in order to re–introduce the periodicity of the pressure (the calculation domain is just a small, periodically–repeating part of a larger domain) the pressure matrix is not zero–padded, but the values are mirrored following the procedure by Chen et al. [149].

The calculation of the elastic–perfectly–plastic deformations and contact pressures of a rough surface follows the procedure similar to [45, 46]:

1. Set target contact plane Z_T and set (guess) the initial contact pressure p;

2. Calculate the initial RMS surface roughness R_{q0} and the initial gap between the undeformed surface and the contact plane:

$$G_0 = Z_T - z_0;$$
(4.109)

3. Based on the current gap, calculate new contact pressure:

$$p = \left(\frac{p}{E'} - \frac{G}{R_{q0}} \right) E';$$
(4.110)

4. Truncate negative pressures: $p = \max(p, 0)$;

5. Identify faces with plastic deformation, i.e. where pressure p is greater than the material hardness H;

6. Truncate pressures greater than the hardness: $p = \min(p, H)$;

7. Calculate surface deformations δ_e using the FFT method, Eq. 4.108 and pressure p. The calculated deformations are as if the surface material is purely elastic;

8. Calculate elastically deformed surface heights by subtracting the elastic deformation from initial surface heights:

$$z = z_0 - \delta_e;$$
(4.111)

9. Calculate elastic surface gap G between z and the target plane:

$$G = Z_T - z;$$
(4.112)

10. Considering only faces in which the non–truncated pressure was below hardness determine the maximum surface height $\mathbf{max(z(p < H))}$, the minimum surface height $\mathbf{min(z(p < H))}$ and the maximum contact gap $\mathbf{max(G(p < H))}$;

11. Calculate new surface heights while taking into account both elastic and perfectly–plastic deformations:

$$z = \min(z, \, \max(z(p < H)));\tag{4.113}$$

12. Calculate new surface gap:

$$G = Z_{\mathrm{T}} - z;\tag{4.114}$$

13. Calculate the maximum contact gap residual:

$$\max(R_G) = \left| \frac{\max(G(p < H))}{\max(z(p < H)) - \min(z(p < H))} \right|;\tag{4.115}$$

14. If the maximum contact gap residual is below the desired threshold then exit, otherwise go back to step 3.

Using the described procedure the mean asperity contact pressure and film thickness can be calculated for an arbitrary distance between the mean of surface heights and the contact plane, which is required for the analysis of mixed lubrication.

4.6. Conclusion

An overview of implemented numerical models necessary for calculating lubricated rough surface contact was presented.

A finite area discretisation of Reynolds equation was presented. In order to account for cavitational effects the computational domain was divided into active and cavitating region, following the principle given by Elrod and Adams. The Poiseuille coefficient becomes zero in the cavitating region, since pressure is constant and equal to cavitating pressure specific to each lubricant. At the boundary
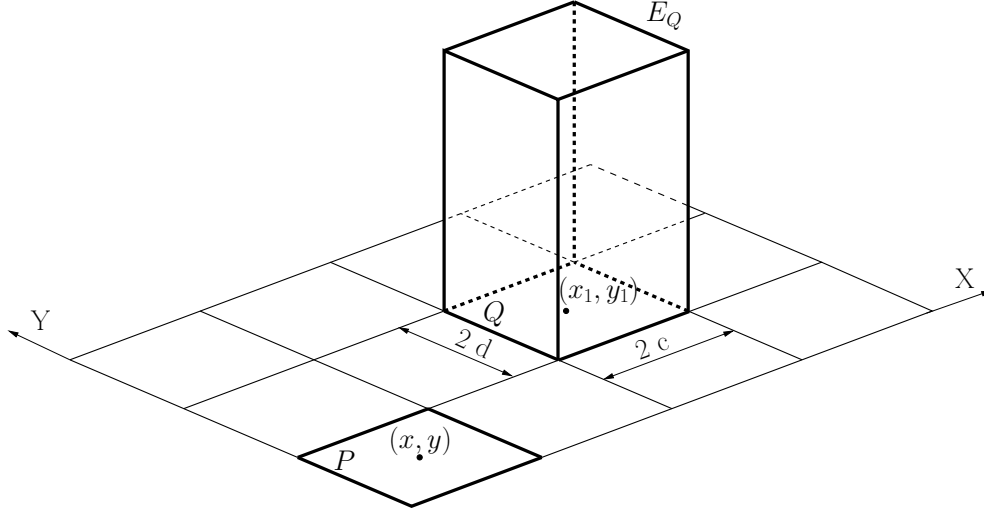
Figure 4.7: With the definition of elastic deflection.

between active and cavitating region, special conditions were implemented. In the active region, close to the rupture boundary, lubricant pressure asymptotically reaches cavitation pressure, thus a zero–gradient condition was imposed. In the cavitating region, close to the formation boundary, the amount of liquid inside the mixture feeds the active region on the other side of the formation boundary. Thus, an additional source is added to the to the cavitating face next to the formation boundary.

Two types of flow factor equations were implemented: Wilson and Marsault [2] equations for lubricated contacts with large fractional areas, and Patir and Cheng [9] equations for light mixed regime and thin hydrodynamic regime. In the implemented code Patir and Cheng equations are used for film thickness values above $3R_q$ in case of the pressure flow factor, and above $5R_q$ in case of the shear flow factor. A new shear flow factor polynomial was derived for large fractional contact areas in order to achieve better agreement with the data provided by Wilson and Marsault.

Two pressure–density relations were implemented: Dowson–Higginson and Murnaghan EOS. Dowson–Higginson relation is a simple relation, with only two coefficients, usually used for mineral oils, while the Murnaghan EOS is a more complex relation requiring five coefficients. In Chapter 5. the Dowson-Higginson relation is used in the validation of the Reynolds equation and cavitation algo-

rithm, and also for performing ball–on–disc simulations with Turbo T68 oil. The Murnaghan EOS is used for characterising Turbo T9 oil in ball–on–disc validation cases under hydrodynamic lubrication regime. Viscosity of the lubricant depends on pressure, temperature and shearing. First, the pressure–temperature–viscosity relation by Roelands and Houpert was implemented, requiring only two inputs: pressure and temperature exponents. Next, a more complex Yasutomi model was implemented, which requires eight parameters, usually calculated via curve fitting to the experimentally measured viscosity values for a range of pressures and temperatures. This model is used for characterising viscosity behaviour of Turbo T68 oil. Finally, a special Vogel–like form of a viscosity model, derived by Habchi et al. [10], was implemented for calculating viscosity of Turbo T9 oil. In order to characterise the shear dependence of viscosity two models were implemented: Ree–Eyring and Carreau–Yasuda. The Ree–Eyring model is used more often in the literature, even though the Carreau–Yasuda model is nowadays considered significantly more accurate. In Chapter 5. the Ree–Eyring model is used for calculating high–shear viscosity of Turbo T68 oil, while the Carreau–Yasuda model is used for Turbo T9 oil.

In order to calculate temperature increase of the lubricant a two–dimensional thin film energy equation was implemented, assuming a parabolic temperature profile across the film thickness. The energy equation is discretised over the contact surface using the Finite Area Method. In order to calculate surface temperature increase in ball–on–disc analysis a deterministic surface temperature model for lubricated point contact was implemented. The model is based on the moving heat source equation by Carslaw and Jaeger [89] and uses FFT method due to computational efficiency. A thermal contact boundary condition for the finite volume displacement solver is also presented, considering rough surface conductance and thermal resistance due to the existence of lubricant between two surfaces in contact.

Implementation of the contact models is presented next. Three statistical single asperity contact models were implemented: Greenwood–Williamson, Wadwalkar–Jackson and Peng–Liu model. Greenwood–Williamson is a Hertzian–based elastic model, while the other two are elastic–perfectly–plastic contact models with analytical equations derived from the results of finite element simulations.

Statistical single asperity models do not account for asperity interaction, the asperity shape is assumed to be hemispherical with a single average radius and the distribution of asperity heights is Gaussian. These models use only a few parameters for characterising surface topography, while the same parameters can be calculated for quite different surfaces. In order to circumvent these simplifications a deterministic elastic–perfectly–plastic contact model is derived and implemented, enabling a direct use of measured surface topography for calculating contact pressures, area ratios and film thicknesses between two surfaces in contact.

5. Validation and Verification

5.1. Introduction

In this chapter, the previously presented models are verified and validated against the available analytical, numerical or experimental data from the literature.

First, the implementation of the Reynolds equation including the cavitation algorithm is validated using five test cases. The first three cases are one–dimensional, where the verification is achieved by performing mesh refinement studies, while the validation is carried out against the analytical and other numerical solutions. The last two cases are two–dimensional and they are validated against the available data from the literature.

The implemented deterministic contact model is validated next. Elastic contact is validated against the results of similar numerical implementation by Yastrebov et al. [150] and experimental measurements done by Johnson et al. [84]. Elastic–perfectly–plastic contact is validated against three–dimensional simulations of the same wavy surface geometry, which were performed using the equivalent three–dimensional finite volume deformation solver. Next, the simulations of elastic–perfectly–plastic contact between a rough deformable surface and a smooth rigid plane are presented, where the results of statistical contact models are compared to the results of implemented deterministic model for three rough surfaces. Next, the deterministic surface temperature model is validated against the exact analytical solutions of square and parabolic moving heat sources.

Finally, a cumulative validation of the implemented models is carried out using numerical simulations of lubricated point contacts. The results are compared with the ball–on–disc experimental measurements performed by Habchi et al. [10] and Guegan et al. [12]. The analysis takes into account lubricant flow and cavitation (Reynolds equation), asperity contact (deterministic contact model), changes of lubricant transport properties (density and viscosity relations), non–Newtonian effects (high–shear viscosity) and temperature variations (thin film energy equation and surface temperature model). Two cases are considered, dis-

tinguished by the type of oil used in the experiments:

- Turbo T9 oil (hydrodynamic lubrication),

- Turbo T68 oil (hydrodynamic and mixed lubrication).

5.2. Reynolds Equation

In this section the implemented hydrodynamic lubrication solver named `lubri-cationFoam` is validated. The solver is based on models presented in Chapter 4. and implemented inside the `foam-extend` framework using the finite area discretisation. The validation is carried out against five test cases:

- pocket slider bearing,

- single parabolic slider bearing,

- twin parabolic slider bearing,

- microtexture pocket bearing,

- dimple seal bearing.

5.2.1. Pocket Slider Bearing

A one–dimensional pocket slider bearing case [61] is considered here, Fig. 5.1.
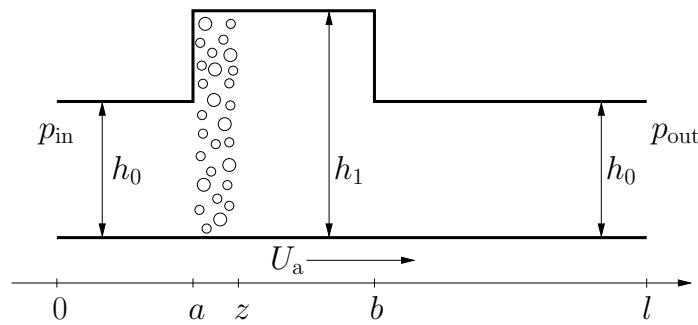
Figure 5.1: Pocket slider bearing geometry.

The bottom surface a is completely flat, while the top surface b is flat and contains a pocket. The length of the bearing is $l = 20$ mm, while the pocket is located between longitudinal positions $a = 2$ mm and $b = 5$ mm. The film thickness

outside the pocket area is $h_0 = 1~\mu$m, while inside the pocket the film thickness is equal to $h_1 = 11~\mu$m. The bottom surface of the bearing is sliding with constant velocity U_a, while the top surface is stationary. Boundary conditions and lubricant properties of the case are specified in Table 5.1. A constant bulk modulus β is assumed with the following pressure–density relation:

$$p = p_\mathrm{cav} + \beta \log \left(\frac{\rho}{\rho_\mathrm{cav}} \right), \tag{5.1}$$

where ρ_cav is the lubricant density at the cavitation pressure p_cav. For the current case the lubricant viscosity μ is also considered to be constant.

Table 5.1: Boundary conditions and lubricant properties of the pocket slider bearing case

Description	Symbol	Value	Unit
Surface a velocity	U_a	1	m/s
Cavitation pressure	p_cav	0	MPa
Inlet pressure	p_in	0.1	MPa
Outlet pressure	p_out	0.1	MPa
Bulk modulus	β	0.5	GPa
Viscosity	μ	0.01	Pa s

For this test case an analytical solution was derived by Almqvist et al. [61]. The derivation is in accordance with the terminology of the authors' LCP solver, where they introduced solution variables u and η. The analytical solution is calculated using the following expressions:

$$
\begin{aligned}
u &= C_1 + C_2 \exp \left(\frac{6\mu U_\mathrm{a}}{\beta h_0^2} x \right), & \eta &= 0, & 0 \leq x \leq a, \\
u &= 0, & \eta &= C, & a \leq x \leq z; \\
u &= C_3 + C_4 \exp \left(\frac{6\mu U_\mathrm{a}}{\beta h_1^2} x \right), & \eta &= 0, & z \leq x \leq b, \\
u &= C_5 + C_6 \exp \left(\frac{6\mu U_\mathrm{a}}{\beta h_0^2} x \right), & \eta &= 0, & b \leq x \leq l,
\end{aligned}
\tag{5.2}
$$

where z is the expected location of the film reformation and C to C_6 are coefficients defined by Eq. 5.3. Note that coefficients C to C_6 are written in the order

of calculation, and are reformatted compared to [61] due to discrepancies.

$$
\begin{aligned}
C_2 &= -\frac{1 - \exp\left(\frac{p_{\text{in}} - p_{\text{cav}}}{\beta}\right)}{1 - \exp\left(\frac{6\mu U_{\text{a}} a}{\beta h_0^2}\right)}, \\[2mm]
C_1 &= \exp\left(\frac{p_{\text{in}} - p_{\text{cav}}}{\beta}\right) - 1 - C_2, \\[2mm]
C &= 1 - \frac{h_0}{h_1}\left(1 + C_1\right), \\[2mm]
C_3 &= -C, \\[2mm]
C_6 &= \frac{h_0 \exp\left(\frac{p_{\text{out}} - p_{\text{cav}}}{\beta}\right) - h_1\left(1 - C\right)}{h_0 \exp\left(\frac{6\mu U_{\text{a}} l}{\beta h_0^2}\right)}, \\[2mm]
C_5 &= \exp\left(\frac{p_{\text{out}} - p_{\text{cav}}}{\beta}\right) - 1 - C_6 \exp\left(\frac{6\mu U_{\text{a}} l}{\beta h_0^2}\right), \\[2mm]
C_4 &= \frac{-C_3 + C_5 + C_6 \exp\left(\frac{6\mu U_{\text{a}} b}{\beta h_0^2}\right)}{\exp\left(\frac{6\mu U_{\text{a}} b}{\beta h_1^2}\right)},
\end{aligned}
\tag{5.3}
$$

The point of reformation is calculated as:

$$
z = \frac{\beta h_1^2}{6\mu U_{\text{a}}} \log\left(-\frac{C_3}{C_4}\right). \tag{5.4}
$$

The fluid pressure and density are calculated using solution variables u and η in the following manner:

$$
\begin{aligned}
p &= p_{\text{cav}} + \beta \log\left(u + 1\right), \\
\rho &= \rho_{\text{cav}}\left(u + 1\right) & u > 0, \\
\rho &= \rho_{\text{cav}}\left(1 - \eta\right) & u = 0.
\end{aligned}
\tag{5.5}
$$

Eight simulations were performed using `lubricationFoam` solver with different mesh sizes: 32, 64, 128, 256, 512, 1024, 2048 and 4096 structured finite area faces. Also, a simulation was performed using the LCP finite difference solver [61] implemented in Matlab® [151] using 4096 computational nodes. Comparisons between simulations and the analytical solution are given in Fig. 5.2 for the pressure field and in Fig. 5.3 for the density field. Note that the density ratio ρ/ρ_{cav} in the cavitating region represents the fraction of the lubricant inside the cavitating liquid–gas mixture. Results of only three mesh densities (64, 128 and
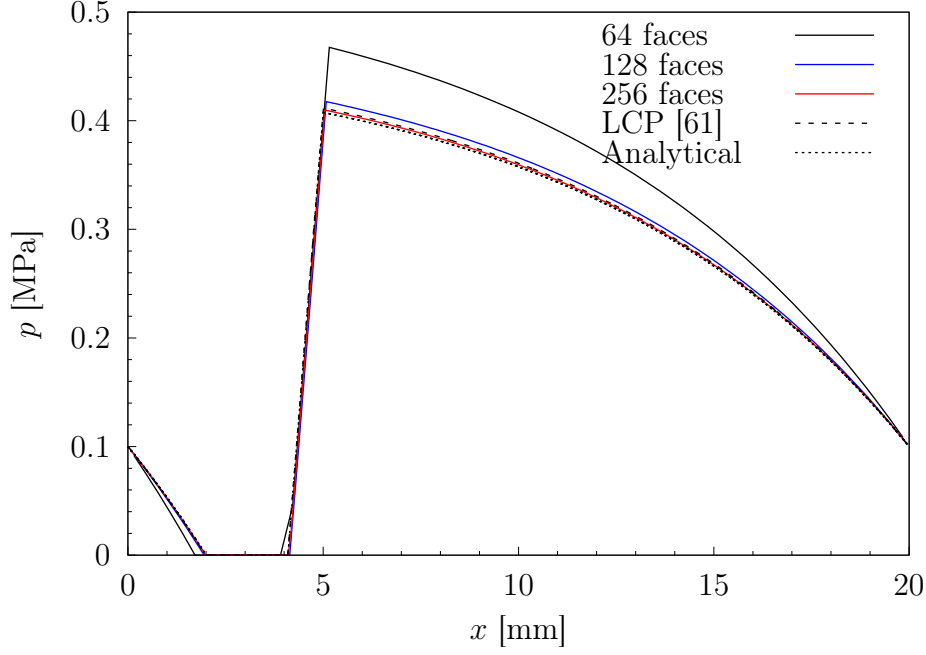
Figure 5.2: Comparison of pressure results for the pocket slider bearing case.

256 faces) are presented in Figs. 5.2 and 5.3 due to the clarity of results. The case with 64 faces significantly deviates from the analytical solution inside and outside the cavitating region. The spatial discrepancy of the cavitating region is apparent between the analytical solution and the solution of the coarsest mesh. For cases with 128 and 256 faces and the LCP case, the position of the cavitating region is indistinguishable from the analytical solution. The case with 128 faces has a visible overshoot of pressure values after the film reformation, while the case with 256 faces is closer to the analytical solution compared to the LCP case, with small overshoot of pressure values. The values of density follow the same trend in the active region ($p > p_{\text{cav}}$), which is expected since pressure is calculated directly from the density. The minimum values of density in the cavitating region are equal for all cases, where the case with 64 faces has the most significant spatial difference of the cavitating region compared to the rest, which is the same when comparing solutions of the pressure.

In order to quantify the difference between cases the relative error is estimated
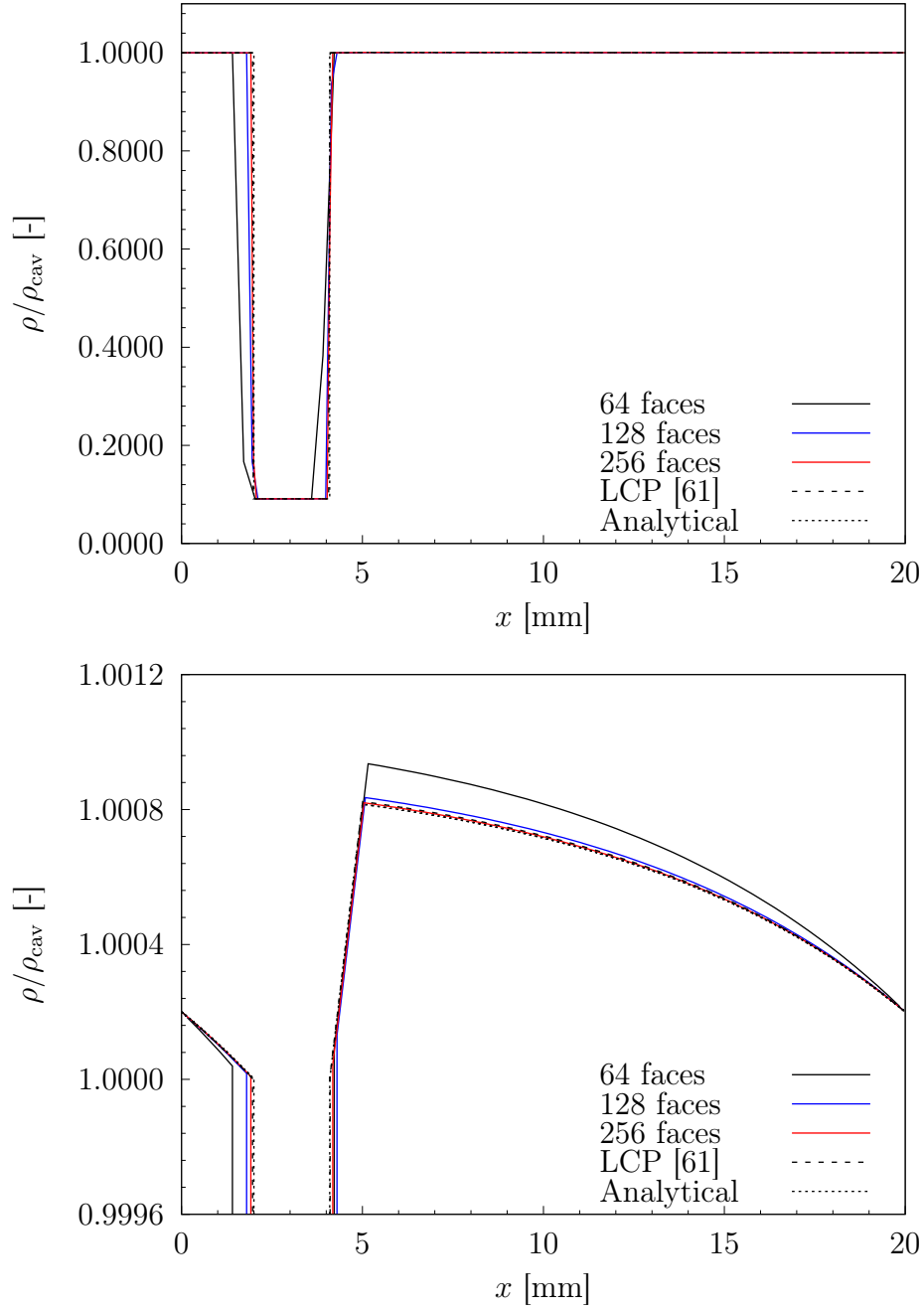
Figure 5.3: Comparison of density results for the pocket slider bearing case.

using the following expression [61]:

$$E_\psi = \sum_{i=0}^{n-1} \left| \psi_i^{\text{ref}} - \psi_i \right| \Bigg/ \sum_{i=0}^{n-1} \psi_i^{\text{ref}}, \tag{5.6}$$

where ψ is the calculated property for which the error is estimated, ψ^{ref} is the reference ("correct") value of the property, i is the index of a computational point and n is the total number of computational points.
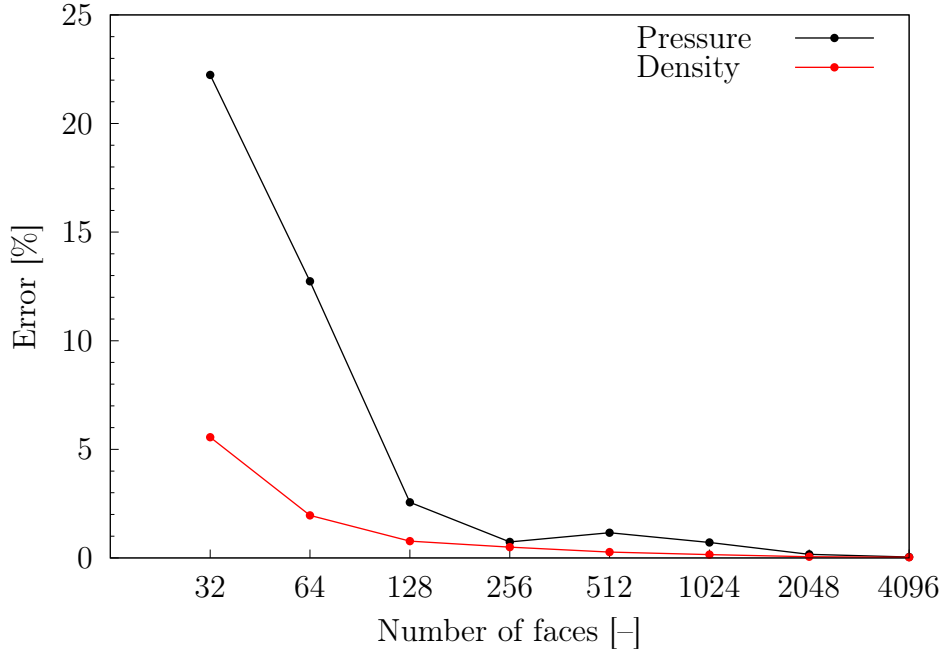
Figure 5.4: The measure of pressure and density error against the number of finite area faces for the pocket slider bearing case.

The error is calculated for all the cases, including the LCP, with the analytical solution as the reference. Errors of pressure and density solutions are depicted in Fig. 5.4. By increasing the mesh density the relative error decreases both for the pressure and for the density, which is expected. For the coarsest mesh, 32 faces, the error is 22.23% for the pressure and 5.56% for the density, while the case with 4096 faces has the 0.04% pressure error and 0.03% density error. For the reference, the error of pressure falls bellow 1% in the case of 1024 faces and is equal to 0.71%, while the error of pressure in the LCP case, with 4096 nodes, is equal to 0.85%. One interesting point of this analysis is the relative pressure error

of case with 256 faces (0.74%) being lower than the pressure error of case with 512 faces (1.16%). This is due to the "fortunate" combination of number of faces, domain and cavitation region length which results in the solution of both pressure and density closer to the analytical solution, in the regions before the rupture boundary and after the point of the pressure peak, compared to the case with 512 faces case. The case with 512 faces has a better agreement with the analytical solution when considering length of the cavitating region and values of pressure and density from the point of reformation to the point of pressure peak, which, due to small variation of density (order of 10^{-4}) in the active region, results in lower density error (0.27%) compared to the 256 faces case (0.50%) in the active region.

5.2.2. Single Parabolic Slider Bearing

A one–dimensional single parabolic slider bearing case [58] is considered here, Fig. 5.5.
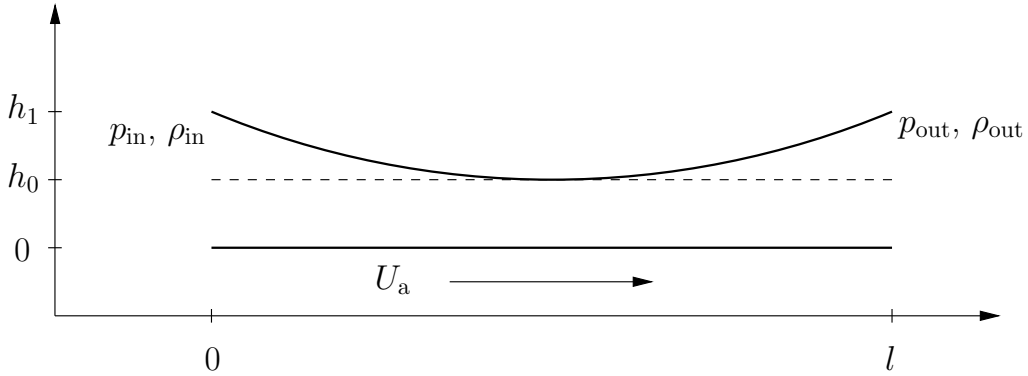
Figure 5.5: Single parabolic slider bearing geometry.

The bottom surface a is completely flat, while the top surface b has a parabolic shape defined by the following expression:

$$h = 4 \left(h_1 - h_0 \right) \left(\frac{x - 0.5l}{l} \right)^2 + h_0,$$

where $l = 100$ mm, $h_0 = 2 \ \mu$m and $h_1 = 4 \ \mu$m. The bottom surface of the bearing is sliding with constant velocity U_a, while the top parabolic surface is stationary. Boundary conditions and lubricant properties of the case are specified in Table

5.2. Viscosity is considered constant, while the bulk modulus and the pressure–density relation are calculated using the Dowson–Higginson model (Eqs. 4.29 and 4.30) with the specified C_1 and C_2 coefficients.

Two cases are considered, A and B, with different inlet conditions. Case A has a full film lubricant at the inlet with pressure of $p_{in} = 0.1$ MPa, while case B has a liquid–gas lubricant mixture at the inlet with density ratio of $\rho_{in}/\rho_{cav} = 0.55$.

Table 5.2: Boundary conditions and lubricant properties of the single parabolic slider bearing case

Description	Symbol	Value	Unit
Surface a velocity	U_a	0.25	m/s
Cavitation pressure	p_{cav}	0	MPa
Outlet pressure	p_{out}	zero–gradient	MPa
Outlet density ratio	ρ_{out}/ρ_{cav}	zero–gradient	-
Dowson–Higginson coefficient	C_1	2.22×10^9	-
	C_2	1.66	-
Viscosity	μ	0.04	Pa s
Case A			
Inlet density ratio	ρ_{in}/ρ_{cav}	1.00003	-
Inlet pressure	p_{in}	0.1	MPa
Case B			
Inlet density ratio	ρ_{in}/ρ_{cav}	0.55	-
Inlet pressure	p_{in}	0	MPa

Eight simulations were performed using `lubricationFoam` solver for case A inlet conditions with different mesh sizes: 8, 16, 32, 64, 128, 256, 512 and 1024 faces. For case B inlet conditions five different meshes were used: 256, 512, 1024, 2048, 4096. As a reference result the LCP solver [61] was used with 4096 computational nodes for case A and 8192 nodes for case B. The relative errors were calculated using Eq. 5.6.

Comparisons between case A simulations and the LCP solution are given in Fig. 5.6 for the pressure field and in Fig. 5.7 for the density field. Results for three meshes are presented: 8, 32 and 128 faces. Pressure and density values of

the case with 8 faces are only rough estimates of the LCP solution. The mesh of 32 faces shows good agreement with the LCP result, however pressure differences can be noticed in the high pressure region, while a discrepancy of density values is visible in the cavitating region. The case with 128 faces visually shows excellent agreement with the LCP solution. The relative errors for case A are depicted in Fig. 5.8. Both pressure and density errors decrease monotonically with the increase of mesh density. Relative errors of the coarsest mesh (8 faces) is 3.39% for the pressure and 2.45% for the density, while for the largest mesh (1024 faces) the pressure error is 0.01% and the density error is 0.02%. For the simulation with 256 faces both errors are below 0.1%.
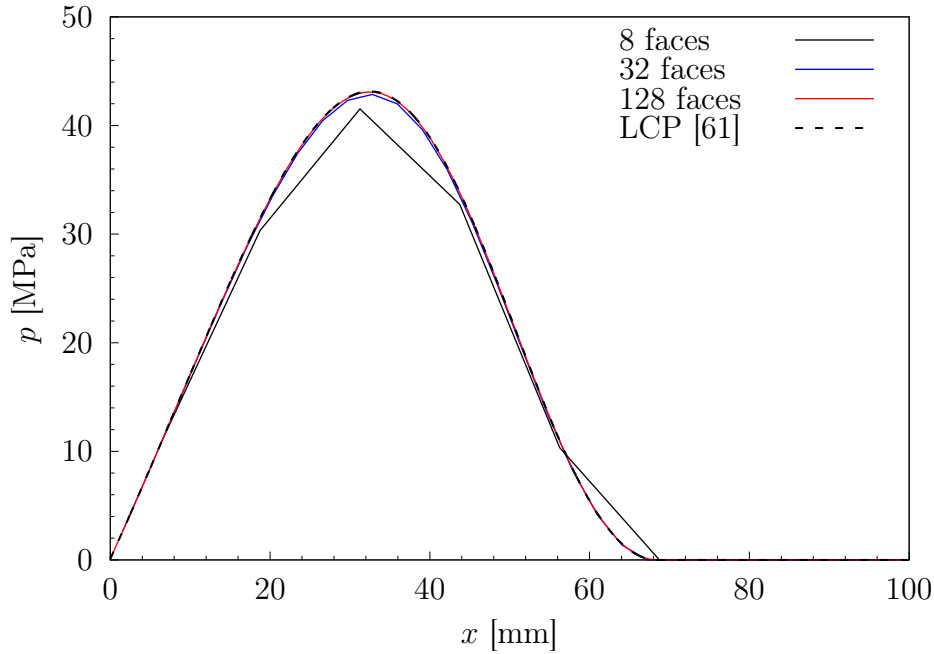
Figure 5.6: Comparison of pressure results for single parabolic slider bearing case A.

Pressure and density results of simulations with case B inlet conditions are given in Figs. 5.9 and 5.10. All three mesh densities capture the shape of pressure and density profiles, with coarser meshes resulting in underprediction of the solution in the high pressure region. In Fig. 5.11 pressure and density errors are shown, where a pressure error of 8.29% for case with 256 faces can be noticed. This error is large even comparing to the coarsest mesh (8 faces) of case A, Fig. 5.8. The mesh with 1024 faces results in the pressure error of 1.73% in contrast
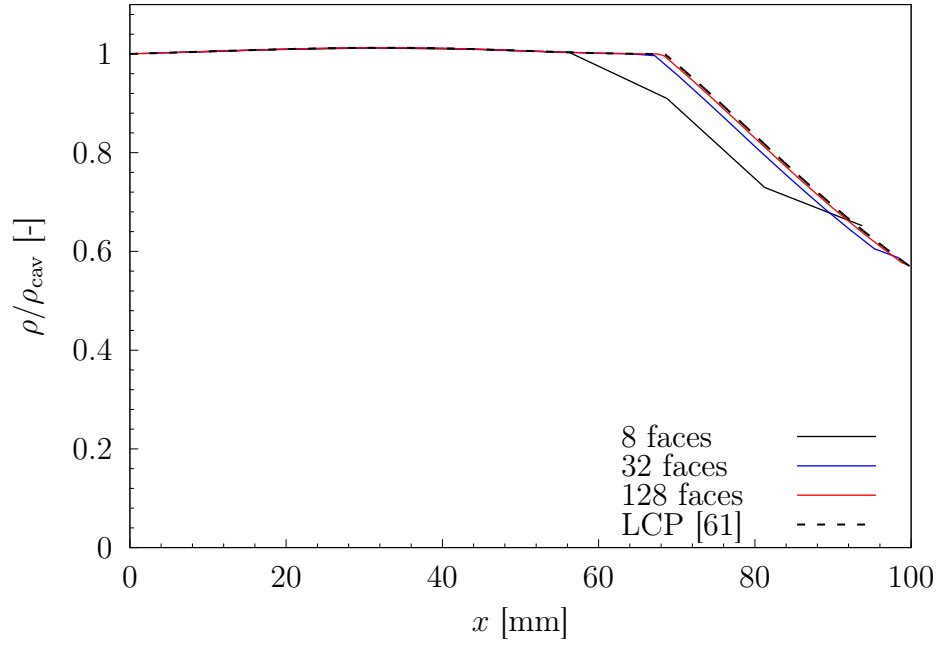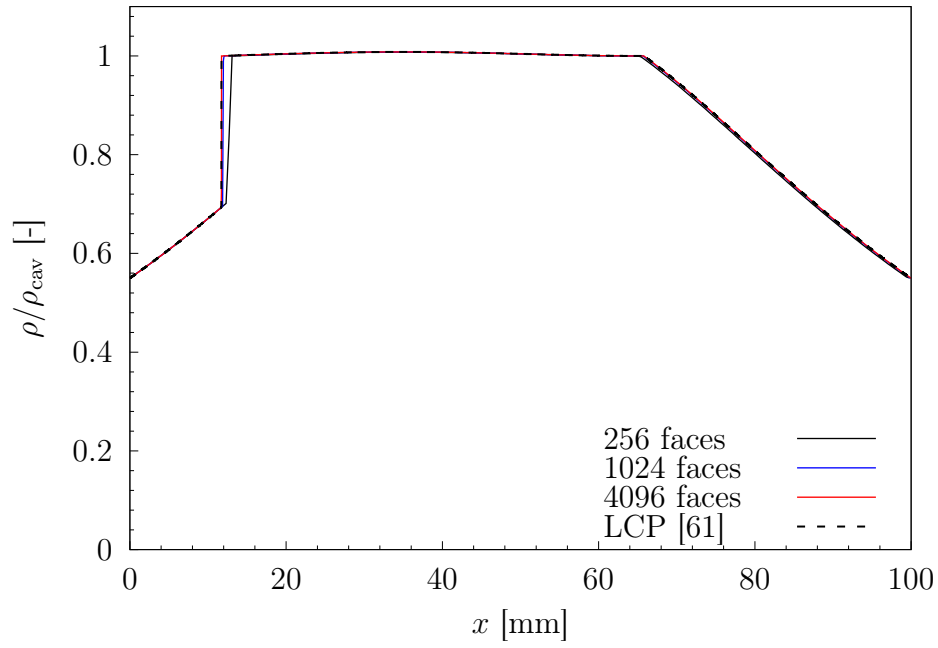
Figure 5.7: Comparison of density results for single parabolic slider bearing case A.
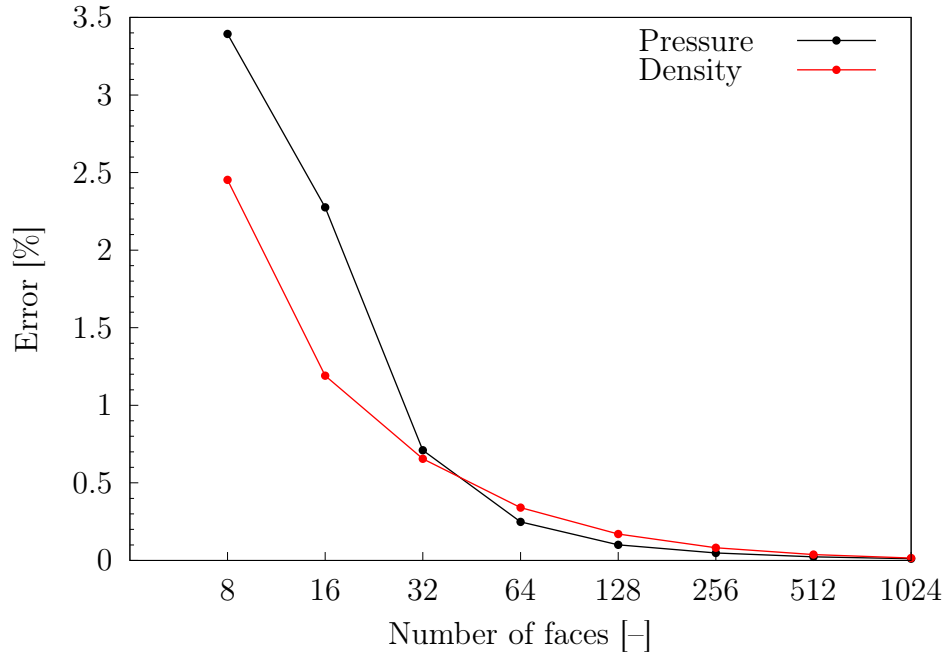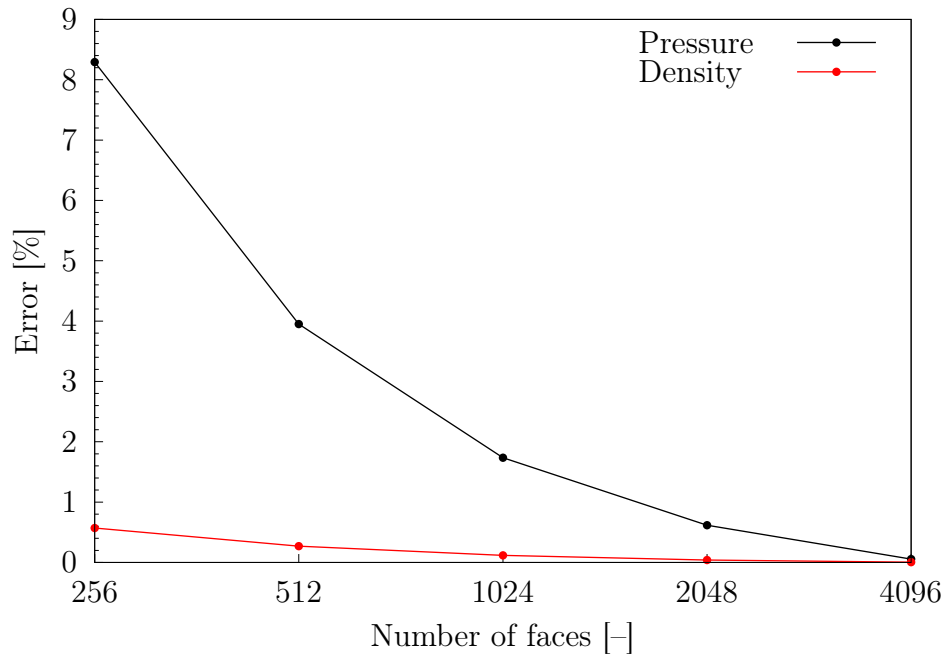

Figure 5.8: The measure of pressure and density error against the number of finite area faces for single parabolic slider bearing case A.

to the case A mesh with the same number of faces resulting in an error of only 0.01%. Even the case A mesh with 32 faces has a low pressure error of 0.71%. Comparing density errors of the two cases with 1024 faces, case B has an error of 0.12%, while the case A has an error of 0.015%. The largest case B mesh (4096 faces) has the error of pressure of 0.06% and 0.004% of density error.

Due to significantly different inlet conditions between A and B, only the rupture boundary appears in case A while in case B both the rupture and the formation boundaries are present. A more complex phenomena occurring in case B requires meshes with a larger number of faces in order to achieve as low pressure errors as in case A. Specifically, a mesh with 32 face in case A without a formation boundary has a pressure error of 0.71%, while the mesh with 2048 faces in case B where both types of the cavitation boundaries are present achieves a pressure error of 0.61%. Therefore, when considering inlet conditions A, the mesh with 64 times less number of finite area faces faces, compared to the inlet conditions B, achieves similar pressure error.
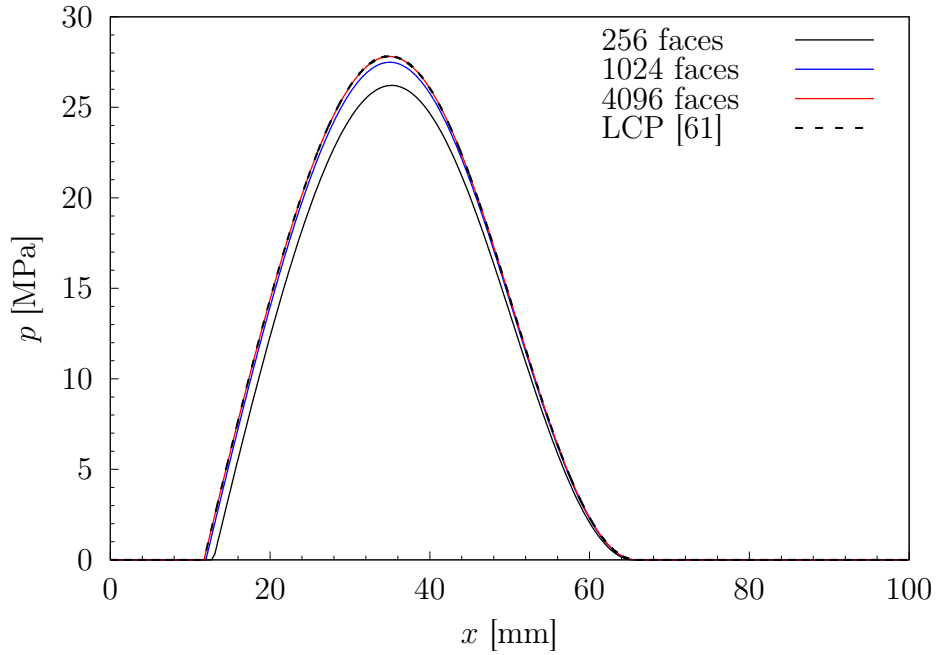
Figure 5.9: Comparison of pressure results for single parabolic slider bearing case B.

Figure 5.10: Comparison of density results for single parabolic slider bearing case B.

Figure 5.11: The measure of pressure and density error against the number of finite area faces for single parabolic slider bearing case B.

5.2.3. Twin Parabolic Slider Bearing

A one–dimensional twin parabolic slider bearing case [58] is considered here, Fig. 5.12.
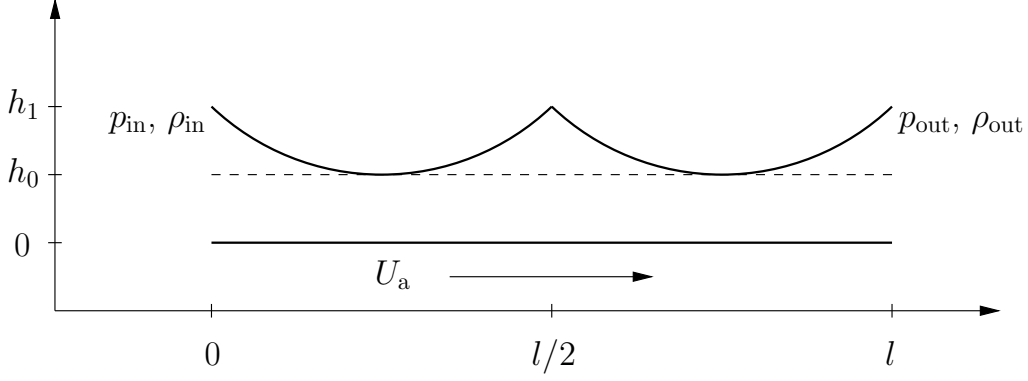

Figure 5.12: Twin parabolic slider bearing geometry.

Similar to the single parabolic slider bearing, the bottom surface a of the twin parabolic slider bearing is flat, while the top surface b has a twin parabolic shape defined by the following expression:

$$h = 16\,(h_1 - h_0)\left(\frac{x - 0.5l}{l}\right)^2 + 8\,(h_1 - h_0)\left(\frac{x - 0.5l}{l}\right) + h_1 \qquad x < 0.5l$$

$$h = 16\,(h_1 - h_0)\left(\frac{x - l}{l}\right)^2 + 8\,(h_1 - h_0)\left(\frac{x - l}{l}\right) + h_1 \qquad x > 0.5l$$

where $h_0 = 25.4\ \mu$m, $h_1 = 50.8\ \mu$m and $l = 76.2$ mm. The bottom surface of the bearing is sliding with constant velocity U_a, while the top parabolic surface is stationary. Boundary conditions and lubricant properties of the case are specified in Table 5.3. Viscosity is considered constant, while the bulk modulus and the pressure–density relation are calculated using the Dowson–Higginson model (Eqs. 4.29 and 4.30) with the specified C_1 and C_2 coefficients.

Eight simulations were performed using `lubricationFoam` solver with different mesh sizes: 16, 32, 64, 128, 256, 512, 1024, 2048 finite area faces. As a reference result the same case was calculated using the LCP solver [61] and computational grid of 8192 nodes. The relative errors were calculated using Eq. 5.6.

Results of simulations are presented in Figs. 5.13 and 5.14. By examining the shape of the pressure distribution, there are two rupture boundaries and one

Table 5.3: Boundary conditions and lubricant properties of the twin parabolic slider bearing case

Description	Symbol	Value	Unit
Surface a velocity	U_a	4.57	m/s
Cavitation pressure	p_cav	0	MPa
Inlet pressure	p_in	0.3364	MPa
Outlet pressure	p_out	zero–gradient	MPa
Inlet density ratio	$\rho_\mathrm{in}/\rho_\mathrm{cav}$	1.0001	-
Outlet density ratio	$\rho_\mathrm{out}/\rho_\mathrm{cav}$	zero–gradient	-
Dowson–Higginson coefficient	C_1	2.22×10^9	-
	C_2	1.66	-
Viscosity	μ	0.039	Pa s

formation boundary with two pressure peaks. Regarding the pressure solution, the case with 32 faces does show discrepancies compared to the LCP case, while cases with 128 and 512 faces are visually almost indistinguishable from the LCP case. The differences are more apparent when analysing the density solution, Fig. 5.14, where density values of cases with 32 and 128 faces clearly differ from the LCP solution in the cavitating region, while maintaining similar shape of the density profile. Density values of the case with 512 faces are very close to the LCP solution.

The error comparison is given in Fig. 5.15. The case with the coarsest mesh (16 faces) gives the solution of pressure with a 1.84% relative error and the solution of density with an error of 4.51%. The pressure error is lower than the density error for every mesh size except the mesh with 32 faces. The pressure error drops to 0.1% at 128 faces, while its value is near zero (0.0007%) in the case of mesh with 2048 faces. While physical phenomena (one formation and two rupture boundaries) are more complex compared to the single parabolic slider case B, inlet and operating conditions of this test case enable the use of significantly coarser meshes for the similar values of pressure errors (64 faces - 0.40%).
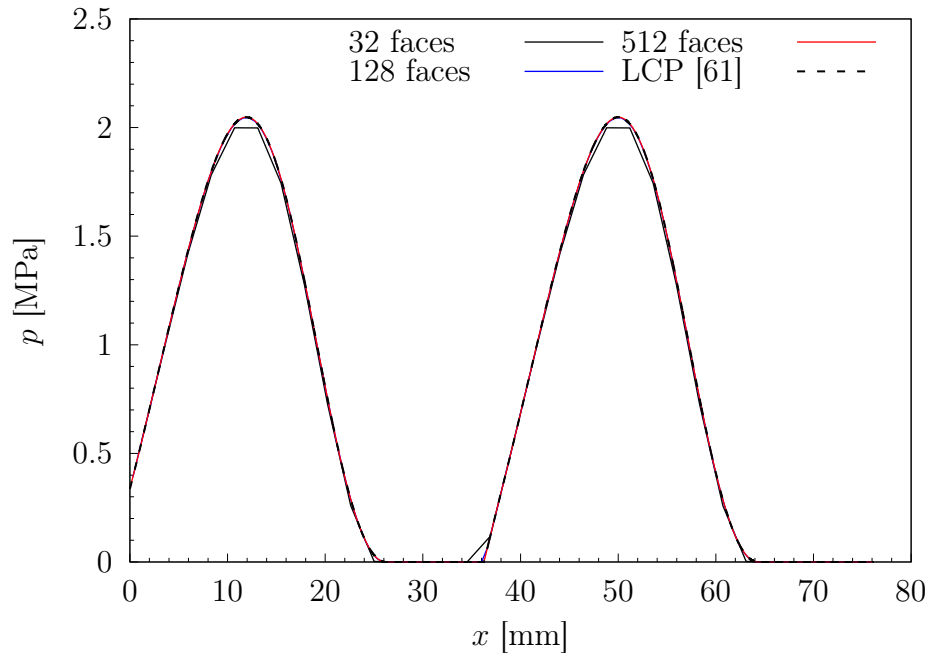
Figure 5.13: Comparison of pressure results for the twin parabolic slider bearing case.
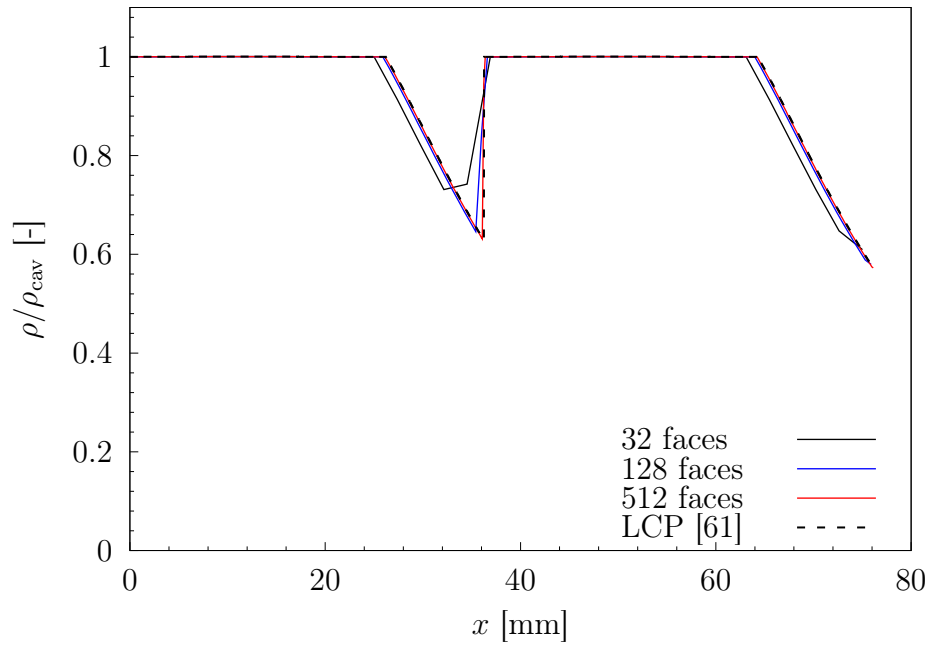

Figure 5.14: Comparison of density results for the twin parabolic slider bearing case.
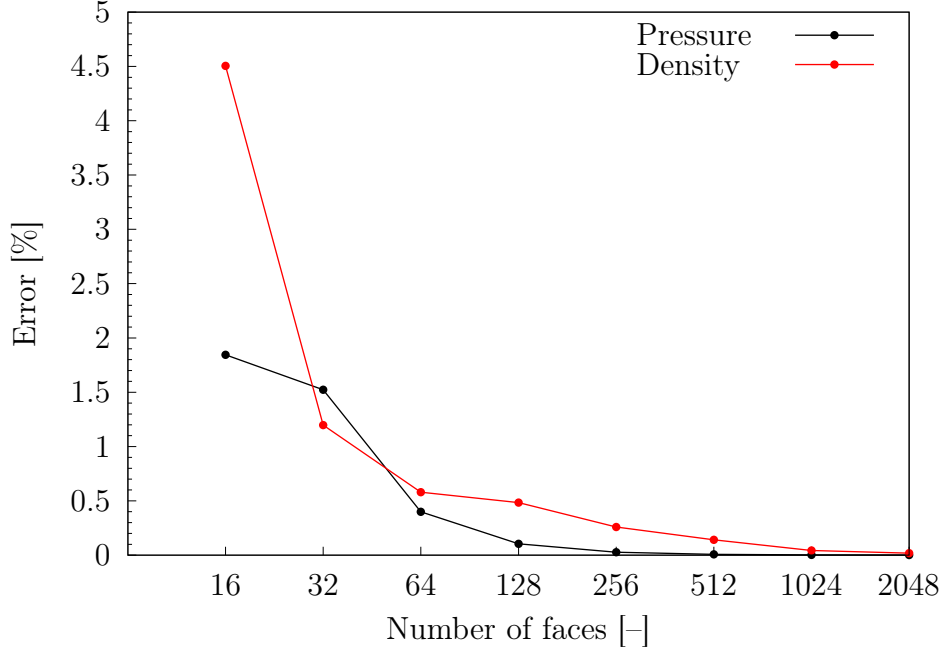
Figure 5.15: The measure of pressure and density error against the number of finite area faces for the twin parabolic slider bearing case.

5.2.4. Microtexture Pocket Bearing

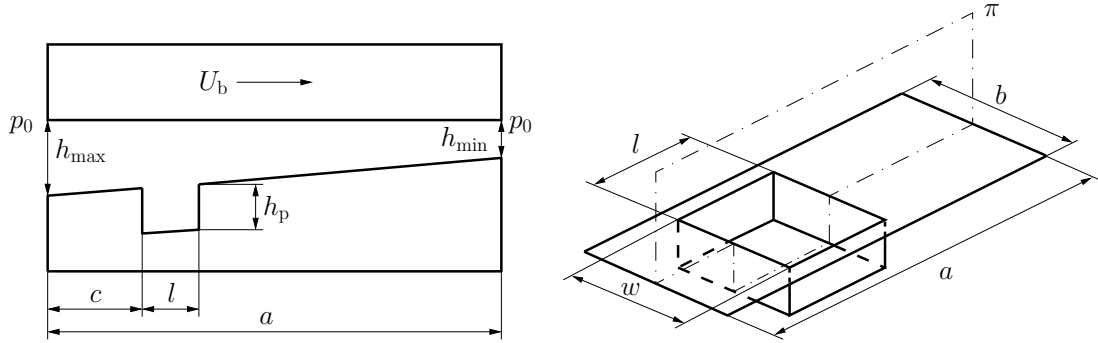A two–dimensional microtexture pocket bearing case [3] is considered here, Fig. 5.16.

Figure 5.16: Microtexture pocket bearing geometry.

The top surface b of the bearing is flat, while the bottom surface a is inclined, with the film thickness decreasing from $h_{\max} = 1.1$ μm at the inlet to $h_{\min} = 1$ μm at the outlet. At the distance $c = 4$ mm from the inlet a pocket is located.

Pocket dimensions are: length $l = 6$ mm, width $w_1 = 7$ mm, and depth $h_p = 0.4$ μm. The bottom of the pocket has the same inclination as the rest of the bearing. The bearing is $a = 20$ mm long and $b_1 = 10$ mm wide. A geometry variation is also considered where the width of the bearing is $b_2 = 300$ mm and the width of the pocket is $w_2 = 210$ mm. The top surface of the bearing is sliding with constant velocity U_b, while the bottom surface is stationary. Boundary conditions and lubricant properties of the case are specified in Table 5.4. Viscosity is calculated using Barus' exponential law (Eq. 4.33) combined with Ree–Eyring shear thinning model (Eq. 4.43).

Table 5.4: Boundary conditions and lubricant properties of the twin parabolic slider bearing case

Description	Symbol	Value	Unit
Surface a velocity	U_a	1	m/s
Cavitation pressure	p_{cav}	0	MPa
Inlet pressure	p_{in}	0.1	MPa
Outlet pressure	p_{out}	0.1	MPa
Side pressure	p_{side}	0.1	MPa
Dowson–Higginson coefficient	C_1	2.22×10^9	-
	C_2	1.66	-
Barus' viscosity law with Ree–Eyring shear–thinning			
Reference viscosity	μ_0	0.01	Pa s
Pressure–viscosity coefficient	α	1.2×10^{-8}	Pa^{-1}
Eyring stress	τ_E	5	MPa

Six simulations were performed using `lubricationFoam` solver with different mesh sizes: 20×10, 40×20, 80×40, 160×80, 320×160, and 640×320 faces. Cavitation switch function and pressure fields are shown in Fig. 5.17. The cavitation region is located inside the pocket with the gas–liquid mixture forming back into the full film near the exit. The high pressure zone is located outside the pocket, but close to its exit, with maximum value located at middle plane π, Fig. 5.16. The pressure decrease towards outlet and side boundaries due to exposure to the ambient pressure. Due to higher pressure in the middle of the bearing the

length of the cavitating region decreases while moving closer to the middle plane π. Pressure increase, although small compared to the maximum values, can also be seen in the region before lubricant enters the pocket.
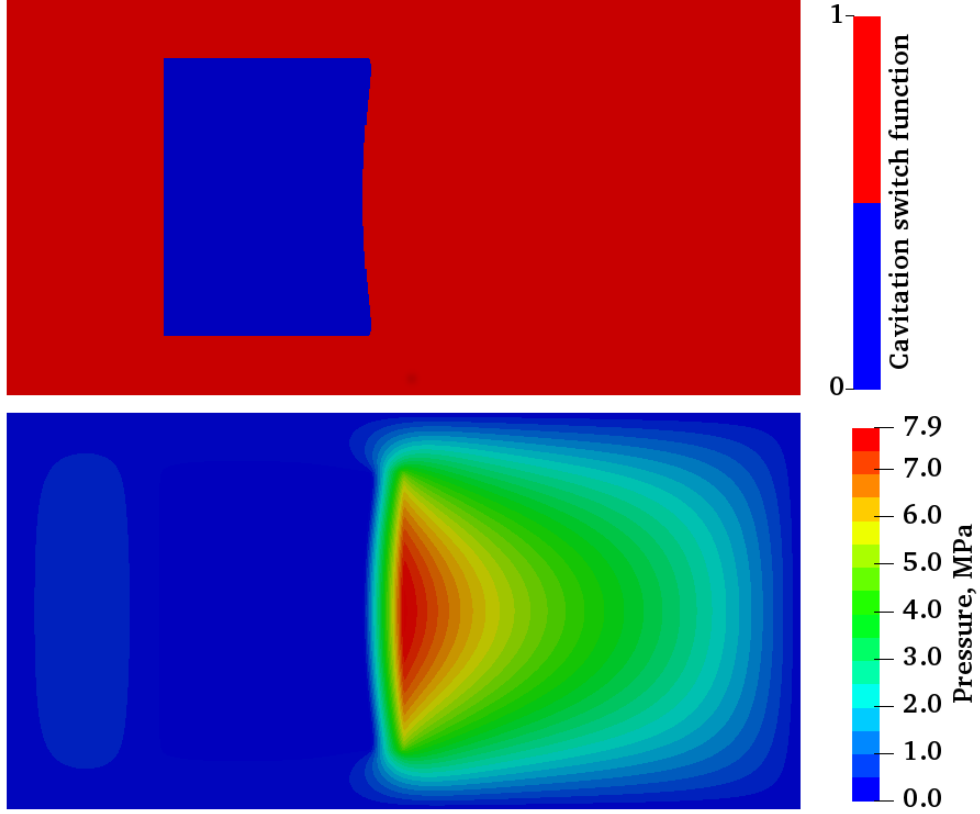

Figure 5.17: Cavitation switch function and pressure field for the microtexture pocket bearing case with 640×320 faces.

As a reference, result pressure profiles at middle plane π, Fig. 5.16, given by Bertocchi et al. [3] are used. A comparison between simulation results and [3] for both bearing configurations ($w = 10$ mm and $w = 300$ mm) are presented in Fig. 5.18. Results of the case with the largest mesh (640×320 faces) is shown. The pressure solution is in a moderate agreement with [3] for the narrow configuration ($w = 10$ mm) with visible discrepancies in the high pressure region. The relative pressure error for the narrow configuration is 7.07%. In their work Bertocchi et al. [3] used a single computational mesh (84×42 elements) and did not perform a grid convergence study, therefore an insufficient grid density might be a reason for relatively large pressure error. For the wide configuration ($w = 300$ mm),

the pressure solution is in a very good agreement with [3] with a pressure error of 1.06%. The possible reason behind the better agreement between the results of the wide configuration is the fact that by increasing the bearing width the solution at the middle plane is closer to the one–dimensional case and further away from the influence of boundaries.
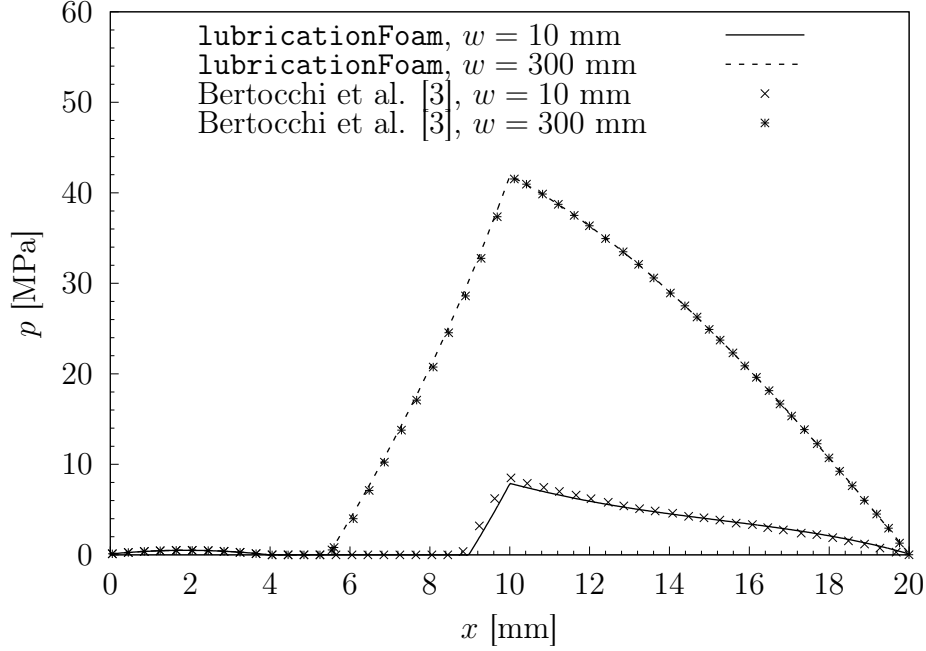

Figure 5.18: Comparison of pressure results (mesh 640×320) for the microtexture pocket bearing case against Bertocchi et al. [3].

In Fig. 5.19 a comparison of pressure errors for two bearing configurations is presented. The number of faces in the longitudinal direction is depicted on the x–axis, where at the same time the number of faces in the transverse direction is equal to a half of that, i.e. 20×10, 40×20, etc. As a reference result, pressure solution from the case with the largest mesh (640×320 faces) is used. The narrow configuration shows significantly larger errors for the first two coarse meshes, 11.26% and 5.35%, compared to the wide configuration where errors for the same mesh densities are 2.92% and 1.54%. Errors become comparable at the mesh density of 320×160 faces, where the narrow configuration produces the pressure error of 0.23%, while the wide configuration 0.11%.
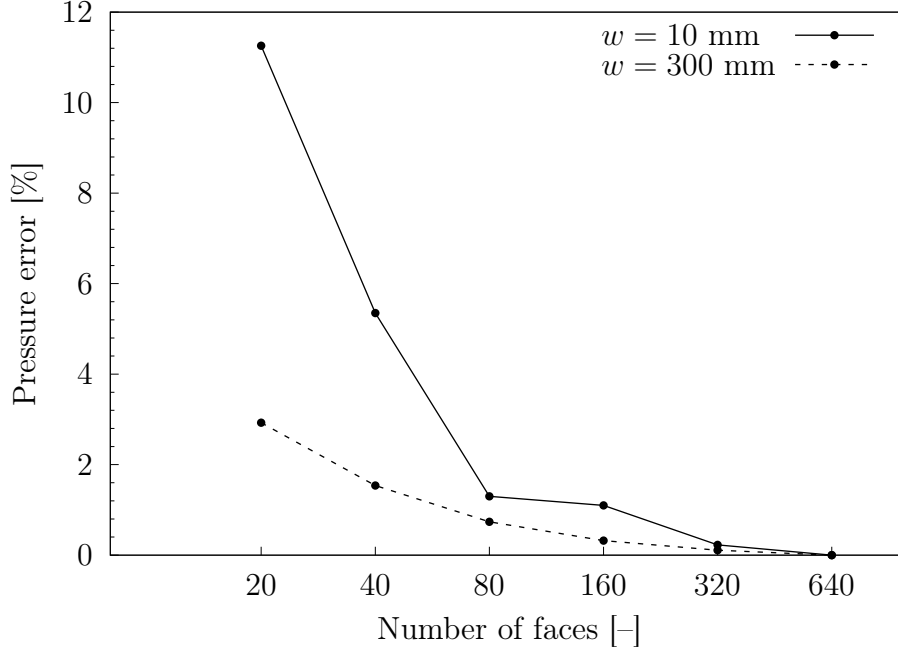
Figure 5.19: The measure of pressure error against the number of finite area faces in the longitudinal direction for both microtexture pocket bearing configurations.

5.2.5.   Dimple Seal Bearing

A two–dimensional dimple seal bearing case [4] is considered here, Fig. 5.20. The bearing consists of two discs, where surface a (the bottom disc) is flat, while surface b (the top disc) has four rows of dimples in the radial direction from radius R_i to R_o with 48 dimples in every row. Three cases are considered, denoted as A, B and C, where thin film flow over a single dimple is analysed. In case A, a cyclic (top–bottom) domain is considered, Fig. 5.20, while in cases B and C a rectangular domain with a single dimple, Fig. 5.21, and periodicity from left to right. The geometrical properties of cases A, B and C are defined in Table 5.5. Boundary conditions and lubricant properties are given in Table 5.6. Viscosity is considered constant, while the bulk modulus and the pressure–density relation are calculated using the Dowson–Higginson model (Eqs. 4.29 and 4.30) with the specified C_1 and C_2 coefficients.

A single simulation was performed for each case using a mesh with 128×128 faces. The comparison of pressure fields between `lubricationFoam` results and Qiu et al. [4] is given in Fig. 5.22 for case A, in Fig. 5.23 for case B and in Fig.
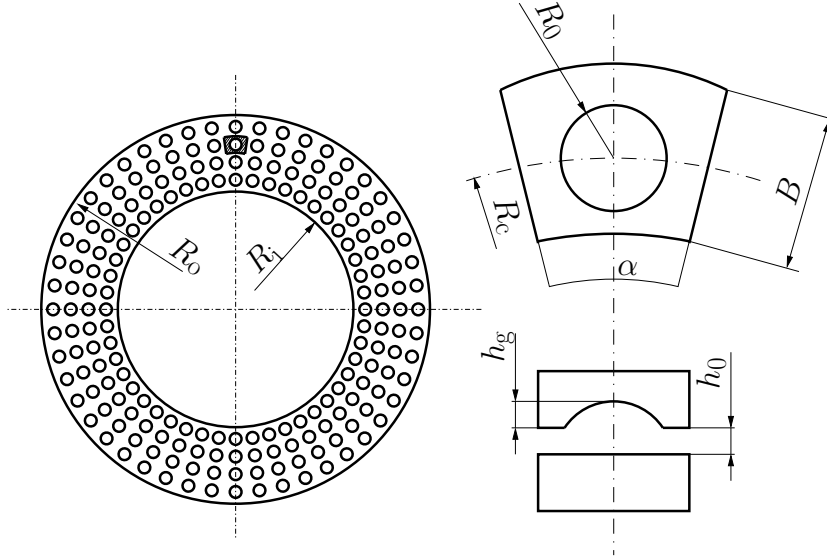
114

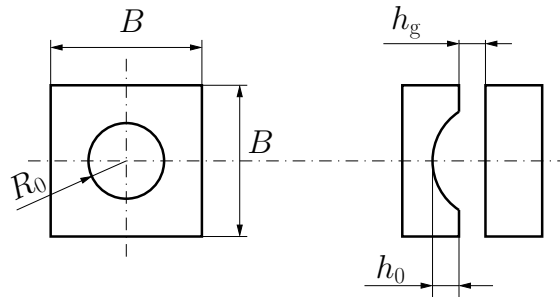Figure 5.20: Dimple seal bearing geometry - case A.

Figure 5.21: Dimple seal bearing geometry - cases B and C.

Table 5.5: Geometric properties of seal bearing cases.

	α [°]	B [mm]	h_0 [μm]	h_g [μm]	R_0 [mm]	R_c [mm]
Case A	7.5	3	4	10	0.75	23
Case B	–	3	4	10	0.75	–
Case C	–	0.3	4	10	0.075	–

Table 5.6: Boundary conditions and lubricant properties of the dimple seal bearing case.

Description	Symbol	Value	Unit
Top and bottom pressure	p_{tb}	0.1	MPa
Cavitation pressure	p_{cav}	0.09	MPa
Dowson–Higginson coefficient	C_1	2.22×10^9	-
	C_2	1.66	-
Viscosity	μ	0.0035	Pa s
Case A			
Surface b angular velocity	ω_{b}	600	rpm
Cases B and C			
Surface b velocity	U_{b}	10	m/s

5.24 for case C.

For all three cases results are in a very good agreement with the literature. In Fig. 5.22 the film ruptures (cavitates) before entering the dimple and reforms into full film before exiting the dimple. In Figs. 5.23 and 5.24 the situation is similar, however the cavitating region in case B is noticeably larger compared to cases A and C. The periodicity of the flow can be observed in all three cases.
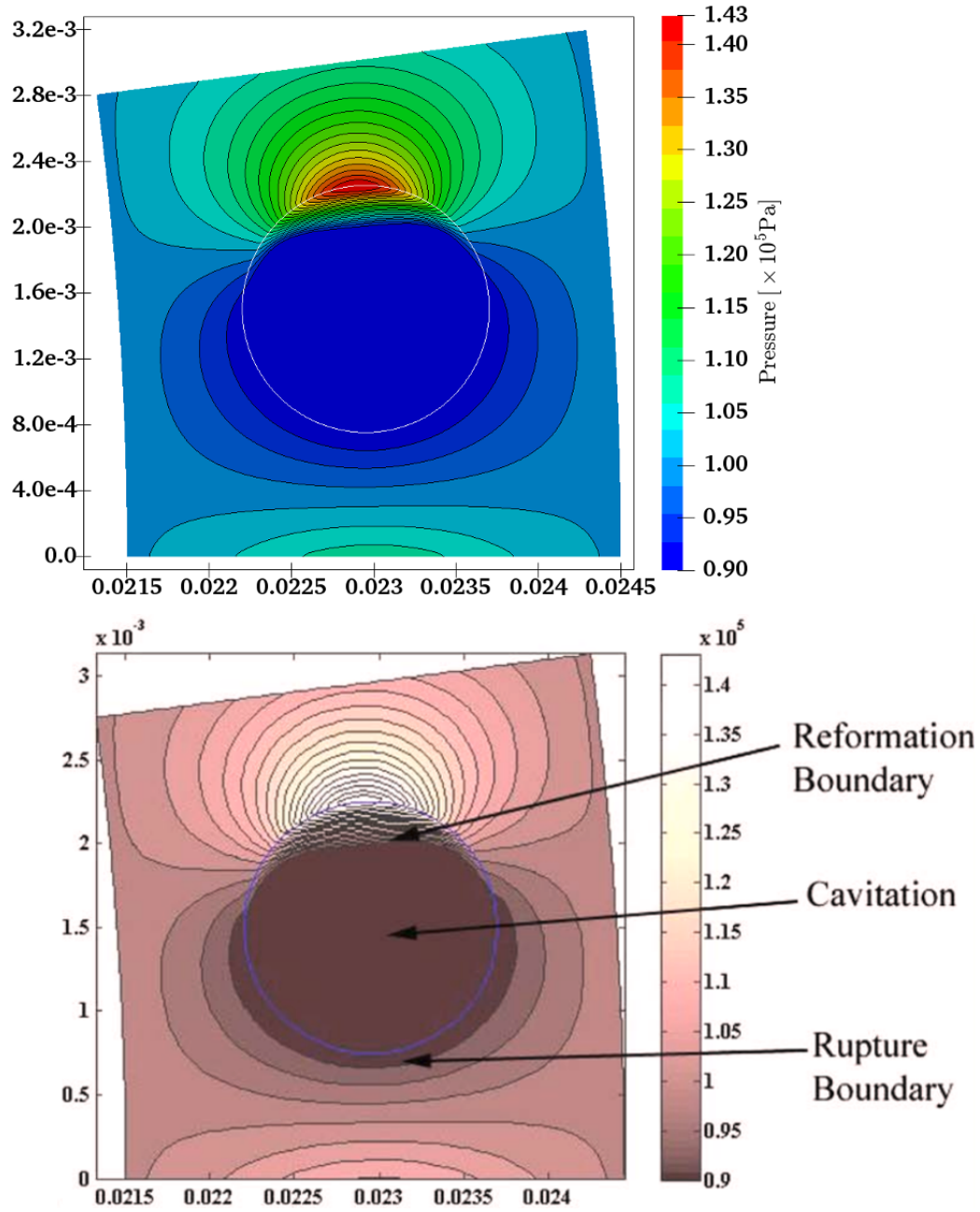
Figure 5.22: Comparison of pressure fields between `lubricationFoam` and Qiu et al. [4] - **case A**.
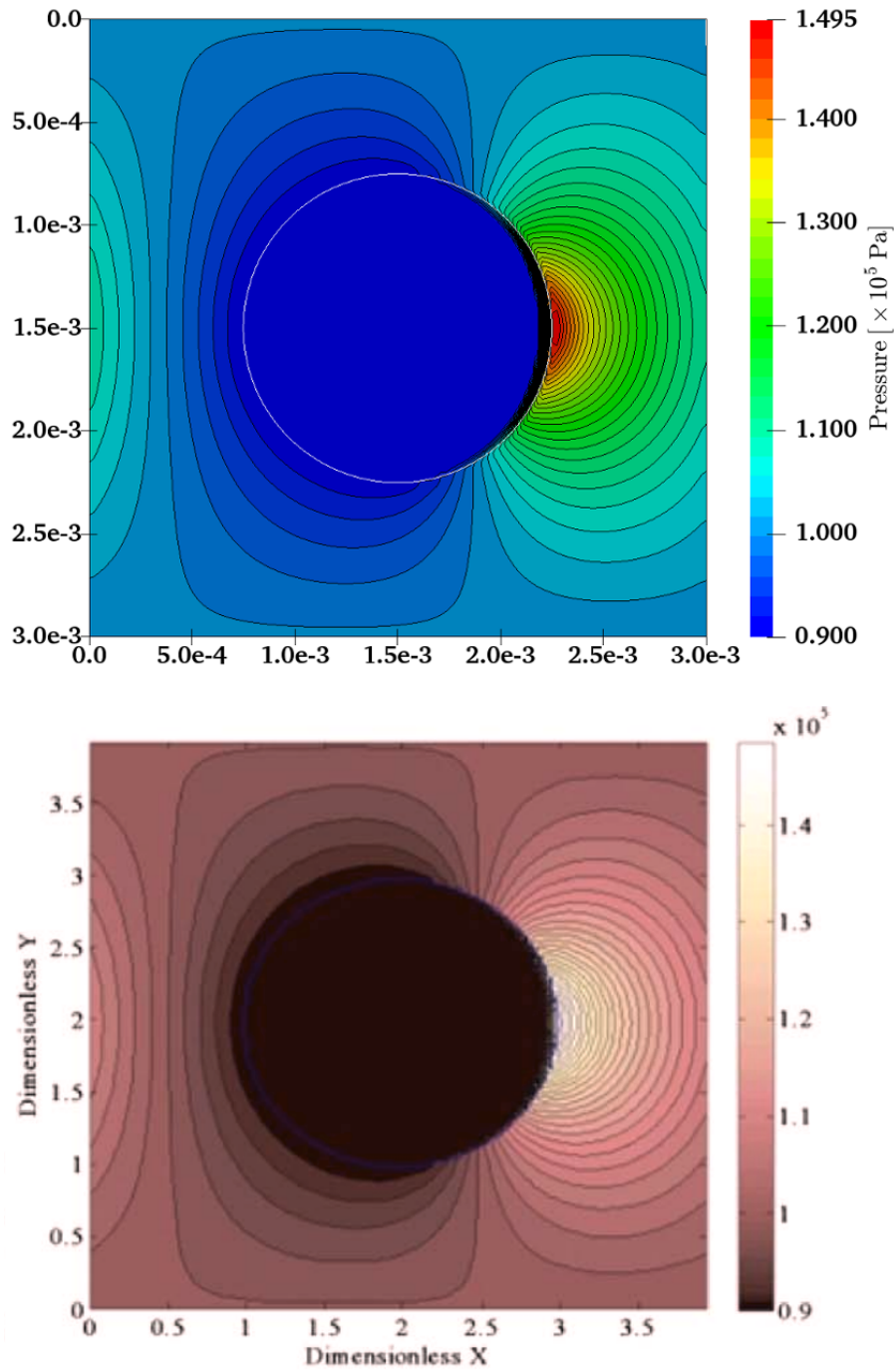
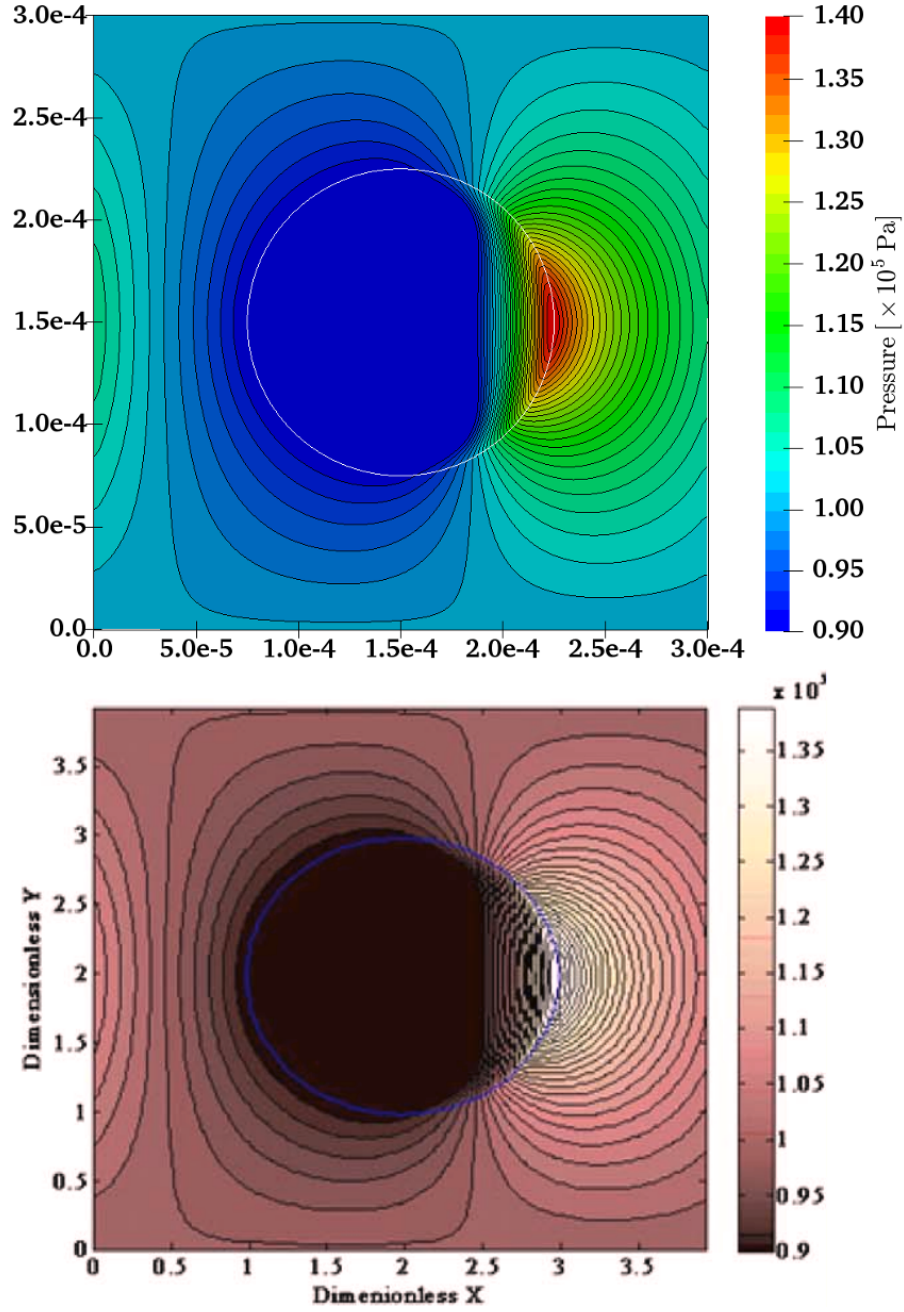Figure 5.23: Comparison of pressure fields between `lubricationFoam` and Qiu et al. [4] - **case B**.

Figure 5.24: Comparison of pressure fields between `lubricationFoam` and Qiu et al. [4] - **case C**.

5.3. Contact Models

In this section deterministic and statistical contact models implemented in this study are validated. Deterministic elastic contact model is validated against the experimental data [84] and numerical results [150] available from the literature. Deterministic elastic–perfectly–plastic contact model is validated against large strain hyperelastoplastic finite volume deformation solver developed by Cardiff et al. [22]. The results of the implemented statistical contact models are compared with the results of deterministic model for three different rough surfaces.

5.3.1. Deterministic Contact Model

In this section the deterministic contact solver named `stanleyKatoPlasticFoam` is validated. The solver is based on the linearly elastic–perfectly–plastic contact procedure presented in Chapter 4. The validation is presented in two parts, where the first part considers only elastic contact, while the second part takes into account both elastic and perfectly–plastic contacts. Validation is carried out on a normal contact test case between a rigid flat and a three–dimensional wavy surface profile [84] shown of Fig. 5.25 and defined by the following equation:

$$z = \Delta \left[1 - \cos\left(\frac{2\pi x}{\lambda}\right) \cos\left(\frac{2\pi y}{\lambda}\right) \right],$$

where $\Delta = 0.48$ mm is the amplitude and $\lambda = 40\sqrt{2}$ mm is the wavelength of the surface profile. Domain length and width are equal to one surface wavelength, i.e. $l_x = l_y = 40\sqrt{2}$ mm.

In case of the purely elastic contact the equivalent elastic modulus E' of the contact is equal to 2.64 N/mm^2 (silicone rubber in contact with a rigid flat surface). The contact simulation is performed by gradually lowering the rigid plane from the point of initial contact up to the complete contact with the deformable wavy surface. During the simulation contact area ratio and average contact pressure are calculated for each step. Calculations were conducted using three mesh densities: 128×128, 256×256 and 512×512 uniformly spaced finite area faces. Simulation results are presented in Fig. 5.26, where they are compared with experimentally measured values by Johnson et al. [84] and numerical calculations by
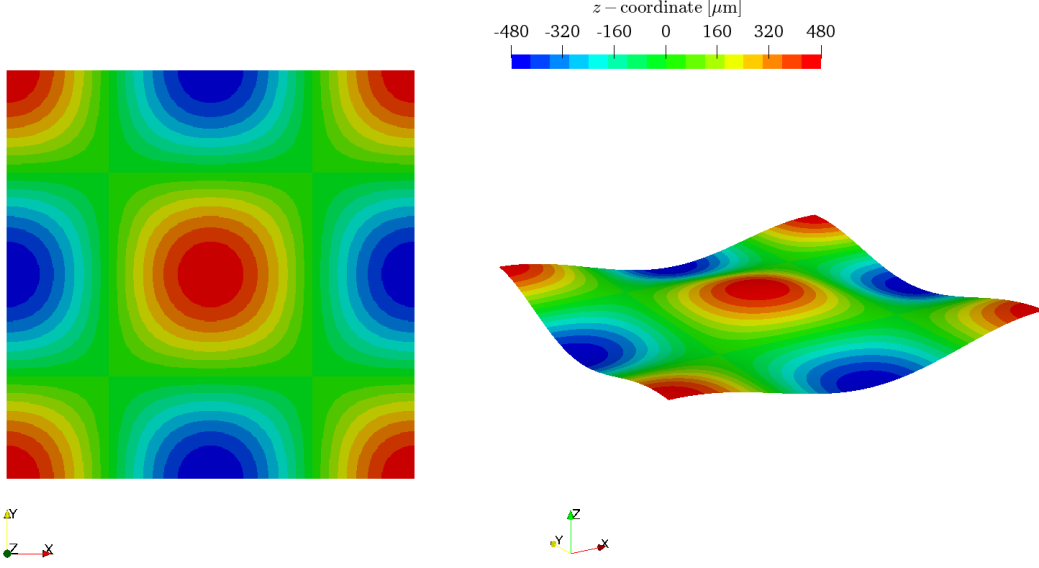
Figure 5.25: Wavy surface profile used for deterministic contact model validation. Waviness of the surface in the left figure is increased five times for visual effect.

Yastrebov et al. [150]. The normalised pressure (x–axis on Fig. 5.26) represents the ratio of normal contact pressure and contact pressure at the point of complete contact ($p^* = \sqrt{2}E'\Delta/\lambda$). The results show a good agreement with experimental data [84] and excellent agreement with numerical calculations done by Yastrebov et al. [150] for all three mesh densities. The error, calculated by Eq. 5.6, of simulation results (mesh with 512×512 faces) compared to the experimental measurements is 4.27%, while the error compared to numerical calculations [150] is 0.22%. In Figs. 5.27 and 5.28 a comparison between experimentally acquired [84] and numerically calculated (via `stanleyKatoPlasticFoam`) contact areas is presented. The comparison is given for six normalised contact pressures where the surface in contact is represented with a bright grey colour. Three bright spots located at the centre of every experimentally acquired photograph represent small holes drilled in the rigid block to release trapped air [84]. The comparison shows a very good agreement between the experiment and simulation. Discrepancies can be observed at higher contact pressures at contact edges. The reason behind these discrepancies lies in the fact that the deformable rubber block had a finite width and length of 80×80 mm, thus the periodicity of the wavy surface was lost near the edges, whereas in the simulation the infinite periodicity of the surface is

assumed. Note that the figures of the contact areas are at the 45° angle compared to the wavy surface profile shown in Fig. 5.25.
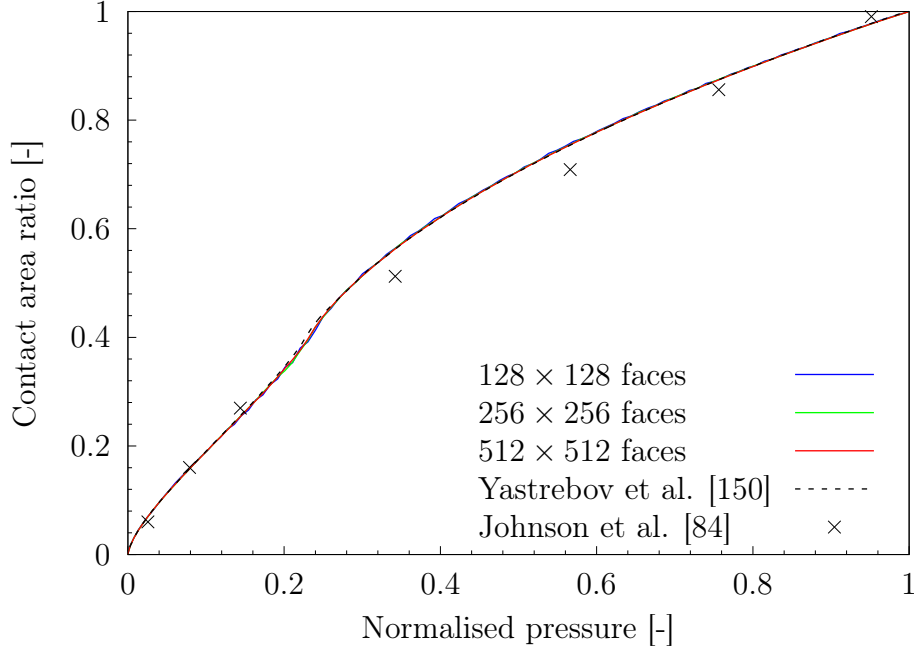

Figure 5.26: Comparison of contact area ratio versus contact pressure between `stanleyKatoPlasticFoam` and literature.

The same wavy surface profile was used to validate linearly elastic–perfectly–plastic contact. The equivalent elastic modulus E' of the contact is equal to 205.16 GPa (steel in contact with a rigid flat), Poisson's ratio is 0.3, while the yield strength of the wavy surface is equal to 0.85 GPa. Simulations performed using `stanleyKatoPlasticFoam` solver were carried out on the same finite area meshes as in the purely elastic case. The results are compared with a three–dimensional simulation of contact between the wavy surface and a rigid flat. The three–dimensional simulation was carried out using the hyperelastoplastic finite volume deformation solver developed by Cardiff et al. [22] and implemented within the `foam-extend` framework. The material model used in the simulation was neo–Hookean elastic–perfectly–plastic. The neo–Hookean solid [152] is a hyperelastic material model, similar to Hooke's law, with a non–linear stress–strain curve. For small deformations the stress–strain curve is linear, and at a certain point the curve plateaus. Three meshes of the wavy surface were considered: $32 \times 32 \times$

$$p/p^* = 0.024$$
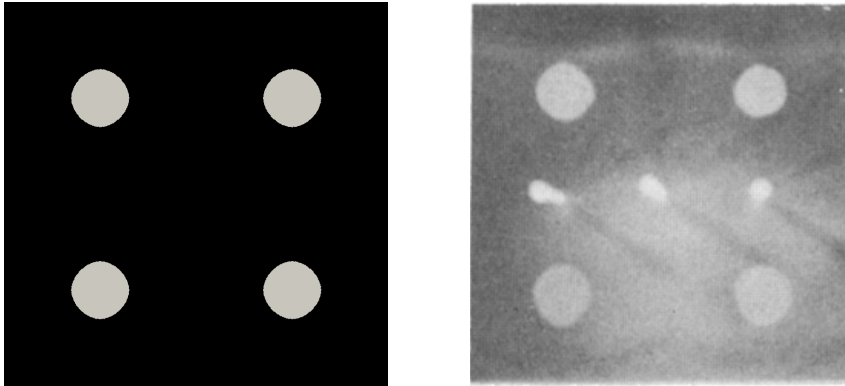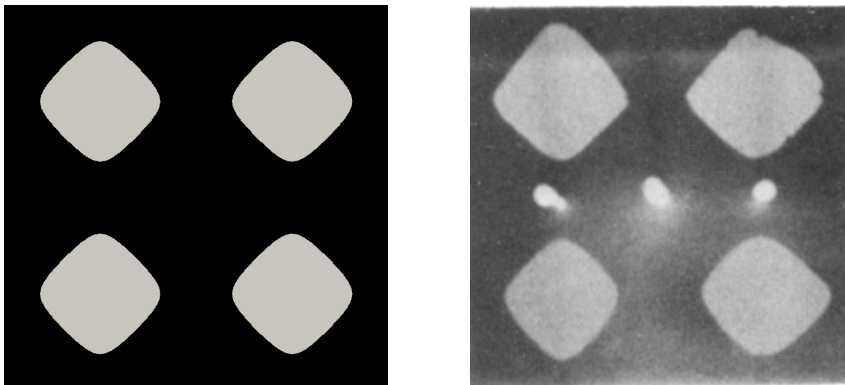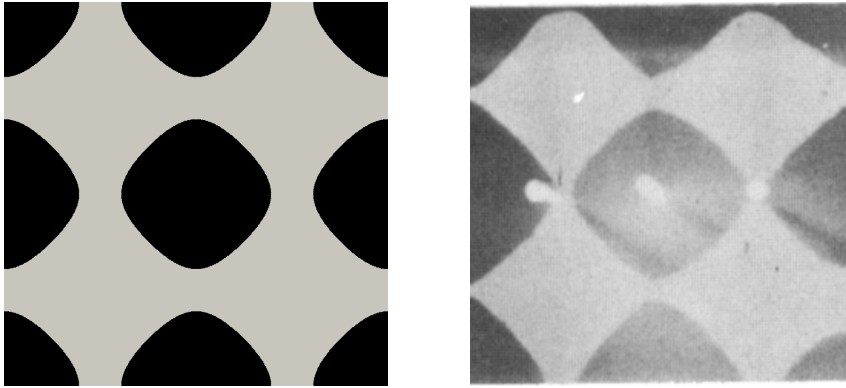

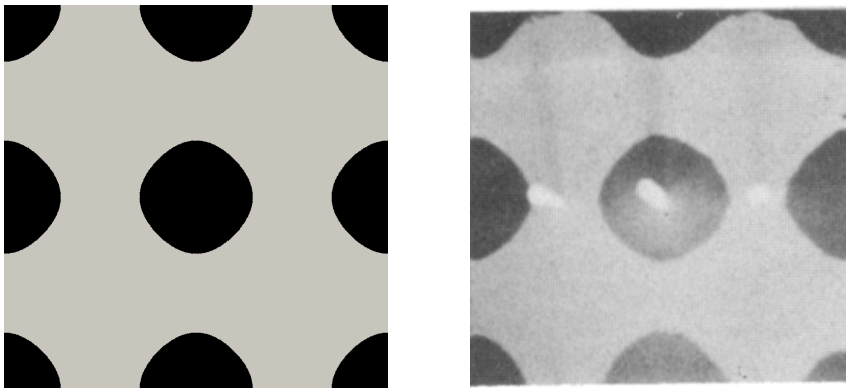$$p/p^* = 0.08$$
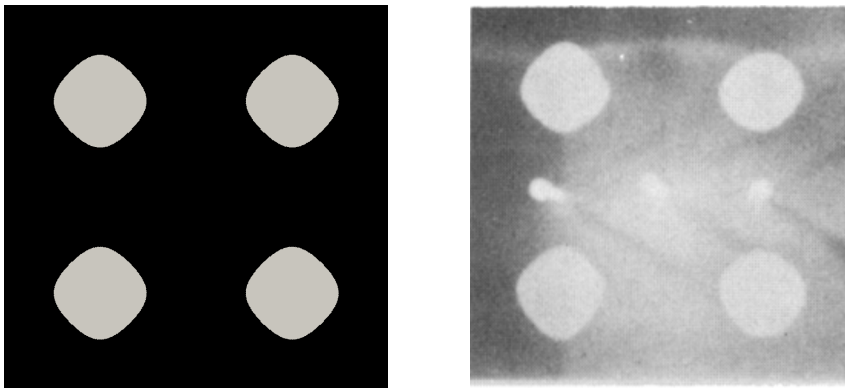
$$p/p^* = 0.14$$

Figure 5.27: Simulation (left) versus experimental (right) contact areas.

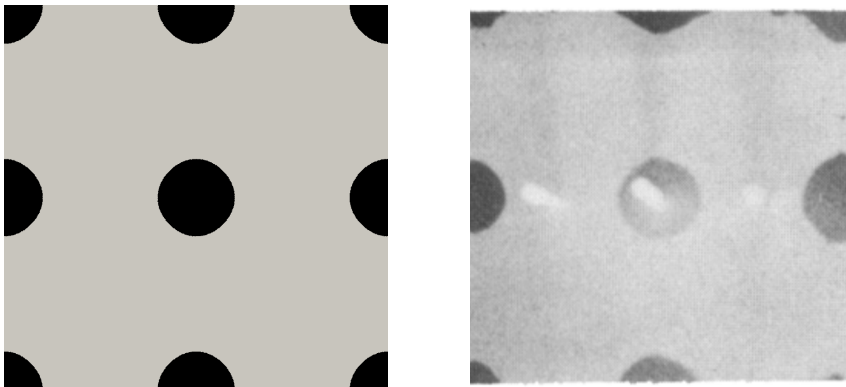$$p/p^* = 0.35$$

$$p/p^* = 0.55$$

$$p/p^* = 0.76$$

Figure 5.28: Simulation (left) versus experimental (right) contact areas.

16, $64 \times 64 \times 16$, $128 \times 128 \times 16$ cells. The number of cells in the z–direction (normal contact direction) was intentionally kept small in order to achieve small cell deformations, in order to remain in the linear stress–strain zone as much as possible. Results from all three meshes are presented in Fig. 5.29.
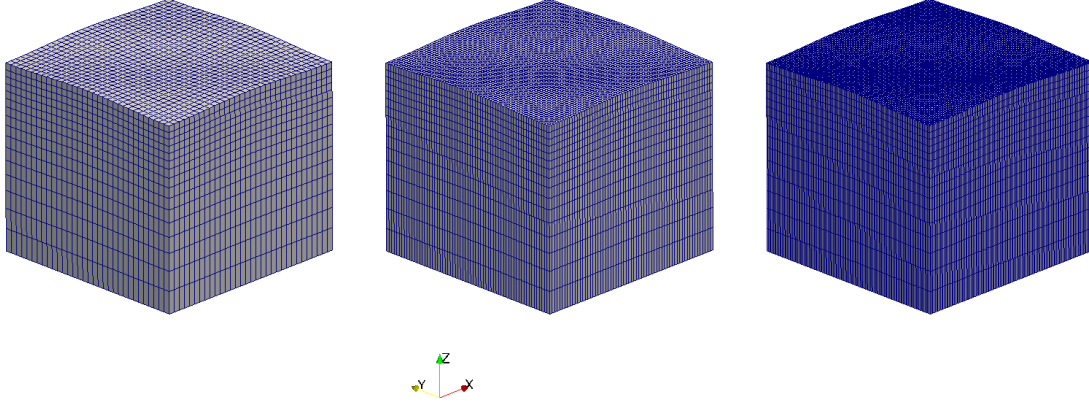

Figure 5.29: Three meshes used with the finite volume deformation solver.

A single–cell rigid plate was used for crushing the deformable wavy surface via penalty–based contact model [20]. The simulations were steady state with gradually lowering rigid plate. The total of ten contact situations were calculated.

The comparison between results of the two–dimensional `stanleyKatoPlasticFoam` solver and the three–dimensional finite volume solver is given in Fig. 5.31. In this case the normalised pressure is the contact pressure divided by the yield strength. The comparison shows a good agreement between results of the two solvers. The error of `stanleyKatoPlasticFoam` results is 3.98% compared to the results of the finite volume solver, considering the densest meshes in both cases. The discrepancy between the results is expected, since the material deformation models are not the same.

In Fig. 5.30 elastic and plastic deformations of the surface are presented for twelve different values of normalised pressure. As the contact pressure increaeses, so does the amount of elastic and plastic deformation of the wavy surface. In case of unloading, the surface will regain its shape only for the amount elastic deformation.

Taking into account the presented results, both for the elastic and elastic–perfectly–plastic contact, the deterministic contact solver is considered validated.
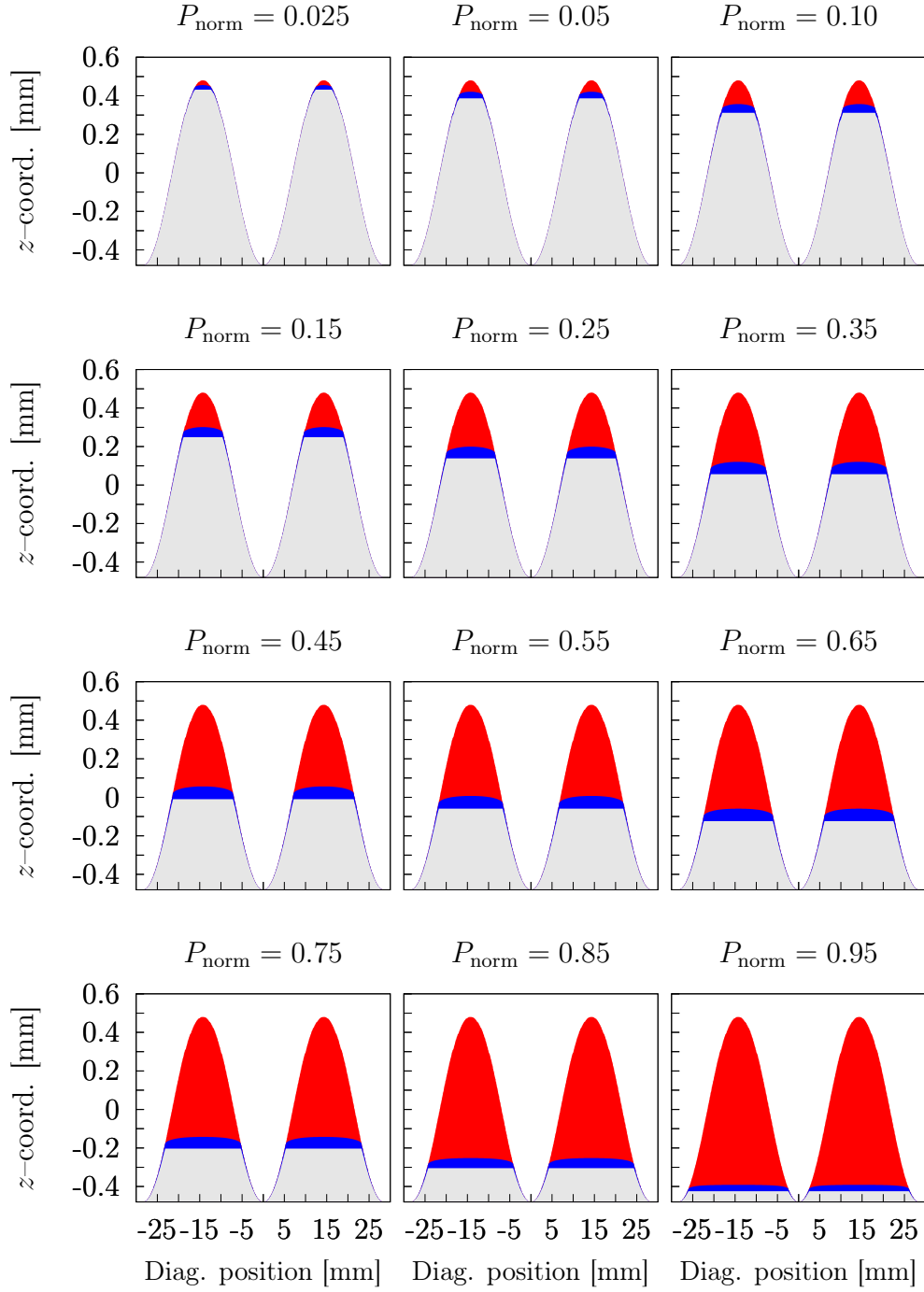
Figure 5.30: Elastic and plastic deformation of the wavy surface profile calculated using `stanleyKatoPlasticFoam` for different contact pressures. P_{norm} – contact pressure normalised with yield strength.
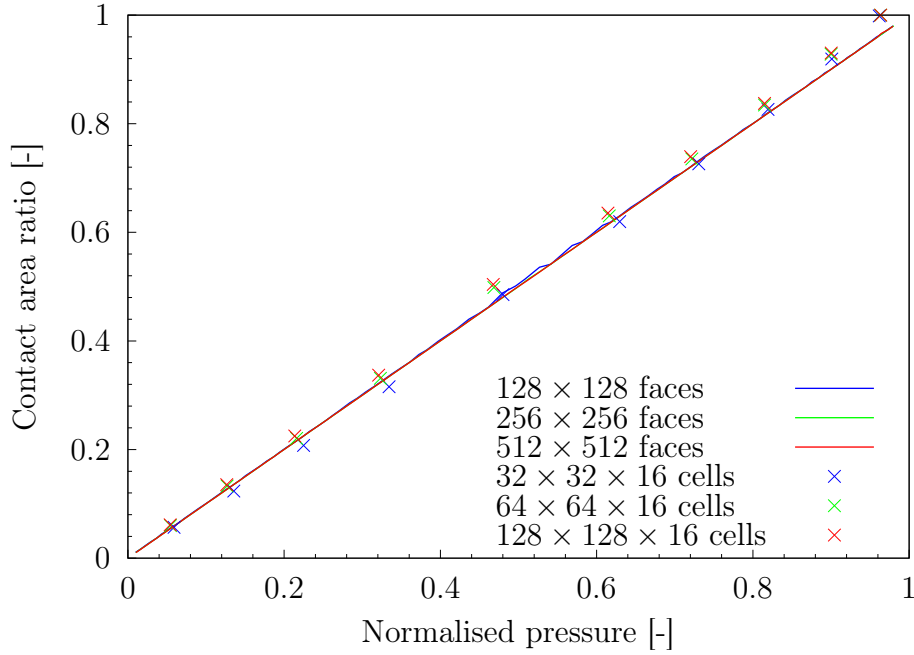
Figure 5.31: Comparison of contact area ratio versus contact pressure between `stanleyKatoPlasticFoam` and finite volume deformation solver.

5.3.2. Statistical Contact Models

In this section a comparison between the deterministic and statistical contact models is given. The implemented statistical models under consideration are:

- Greenwood–Williamson (GW) [69],

- Peng–Liu (PL) [80],

- Wadwalkar–Jackson [79] with deformable (WJ–D) and rigid (WJ–R) spherical asperity base.

Implemented statistical contact models are tested against the deterministic model on three numerically generated surfaces, Fig. 5.32. Surfaces 1, 2 and 3 have the following RMS roughnesses: 1 μm, 5 μm and 10 μm. All three surfaces have the correlation length equal to 10 μm with the Peklenik parameter (Eq. 4.16) equal to 1. Surfaces were generated using `Random Surface Generator` [153] utility for Matlab®. The size of the domain is 1 mm × 1 mm. For calculating deterministic contact between a rough surface and a rigid flat

`stanleyKatoPlasticFoam` solver is used. The computational mesh used in these simulations consists of 512×512 finite area faces. Surface material properties properties used here are the same as in the previous section: equivalent elastic modulus $E' = 205.16$ GPa, Poisson's ratio $\nu = 0.3$ and yield strength $Y = 0.85$ GPa.
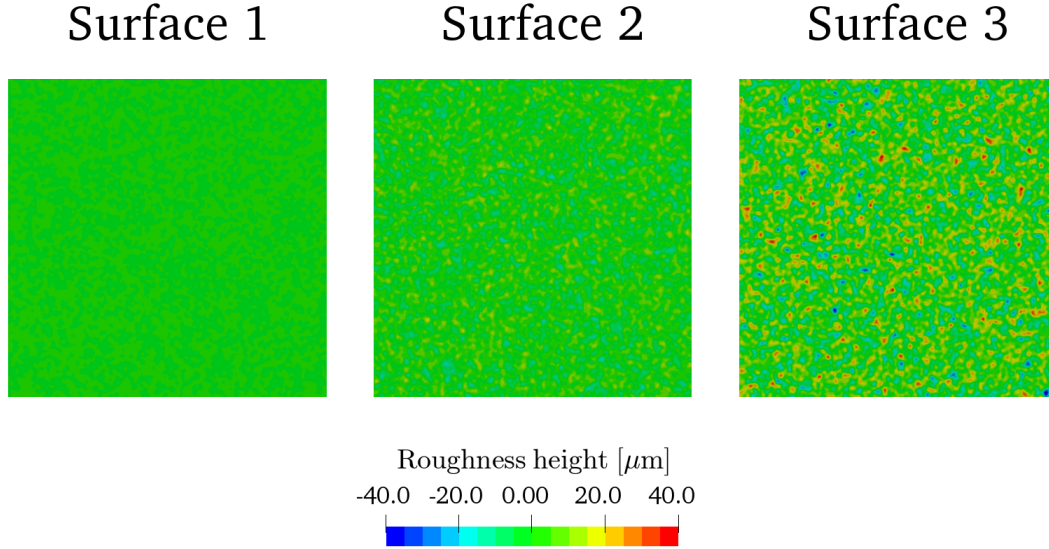

Figure 5.32: Numerically generated rough surfaces.

In Fig. 5.33 the comparison between the deterministic and statistical models is given for elastic contact and all three surfaces. When compared mutually statistical models give exactly the same contact area ratios. This is expected since all four of them are based on the same single asperity Hertzian contact model given by Greenwood and Williamson [69]. When compared to the deterministic model, statistical models significantly underestimate contact area ratios (up to 30%) for all three rough surfaces. Statistical models give fairly good prediction of the contact pressure at which the complete elastic contact is achieved, however they do not asymptotically approach this value, while the deterministic model does. In Fig. 5.34 comparisons between deterministic and statistical contact models are given for elastic–perfectly–plastic contact for all three surfaces. Statistical models underestimate contact area ratios (up to 50%) for the whole range of contact pressures for all three surfaces. Mutually compared Wadwalkar–Jackson models

give very similar results for all cases. Peng–Liu model gives similar results to WJ models for surface 1, i.e. surface with the smallest surface roughness, while deviates from the WJ models for rougher surfaces. Vertical grey line in Fig. 5.34 denotes point at which the material yields. Only the deterministic contact model accurately predicts the full contact at that point, while statistical models underestimate the contact area ratio even up to one order of magnitude in case of Peng–Liu model. In Fig. 5.35 comparison of film thicknesses versus contact pressure between deterministic and statistical models is given. The average film thickness is equal to the total empty volume between the rigid plane and rough surface divided by the nominal contact area. In the case of deterministic model film thickness converges to zero at the material yielding point (grey vertical line) for all three surfaces, which is expected since at that point complete contact is reached.

Statistical models do not describe this phenomena accurately, which was already noticed in Fig. 5.34. Film thicknesses calculated via statistical models follow deterministic values in case of surface 1 (the smoothest surfaces), while in cases of surfaces 2 and 3 film thicknesses significantly deviate from the deterministic values especially at higher contact pressures.

Based on the presented results, a conclusion can be made that in order to achieve accurate predictions of contact area and film thickness during the elastic or elastic–perfectly–plastic normal contact a deterministic calculation of the rough surface contact should be conducted.

Figure 5.33: Comparison of contact area ratio versus contact pressure between deterministic and statistical models for purely elastic contact. Det. – deterministic; GW – Greenwood–Williamson; PL – Peng–Liu; WJ-D – Wadwalkar–Jackson deformable; WJ-R – Wadwalkar–Jackson rigid.
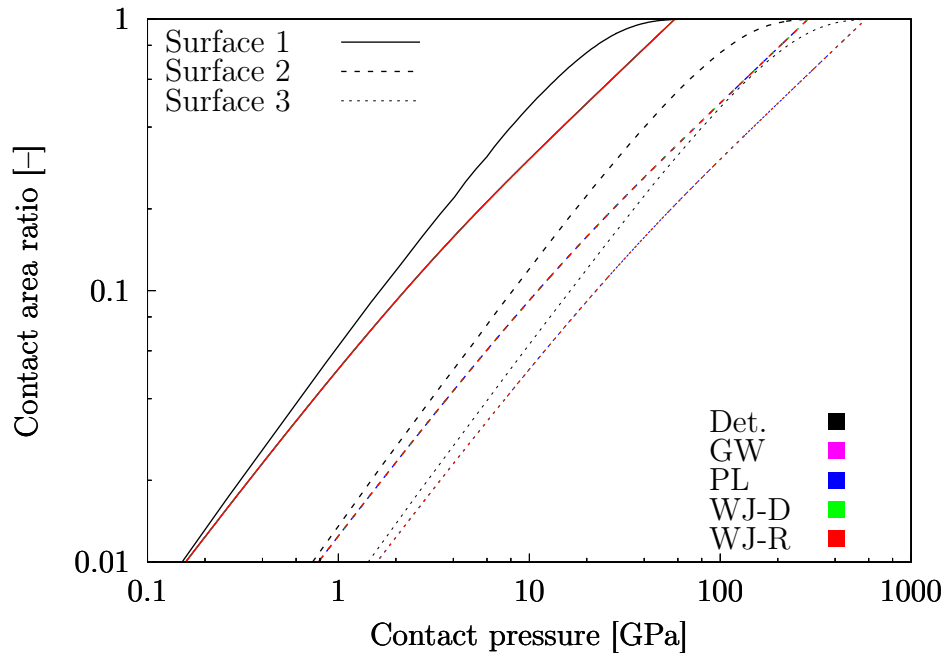
Figure 5.34: Comparison of contact area ratio versus contact pressure between deterministic and statistical models for elastic–perfectly–plastic contact. Det. – deterministic; PL – Peng–Liu; WJ-D – Wadwalkar–Jackson deformable; WJ-R – Wadwalkar–Jackson rigid.

Figure 5.35: Comparison of film thickness versus contact pressure between deterministic and statistical models for elastic–perfectly–plastic contact. Det. – deterministic; PL – Peng–Liu; WJ-D – Wadwalkar–Jackson deformable; WJ-R – Wadwalkar–Jackson rigid.

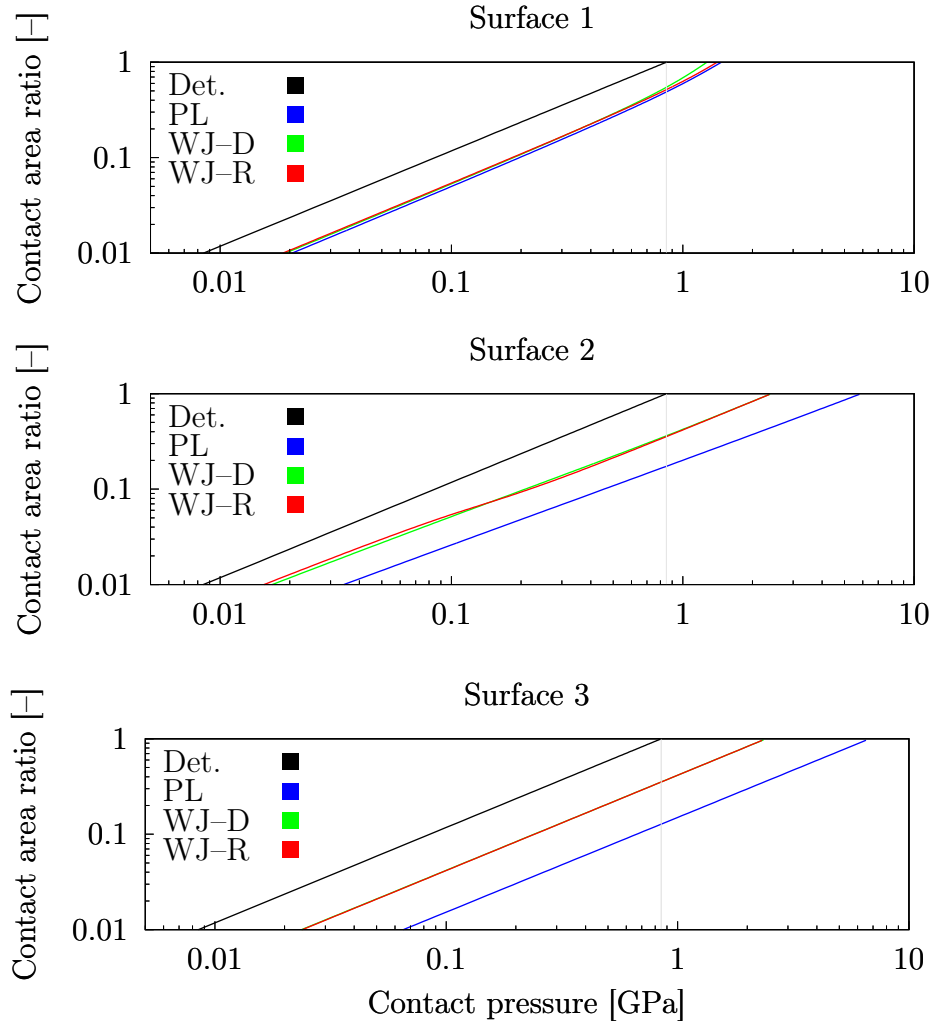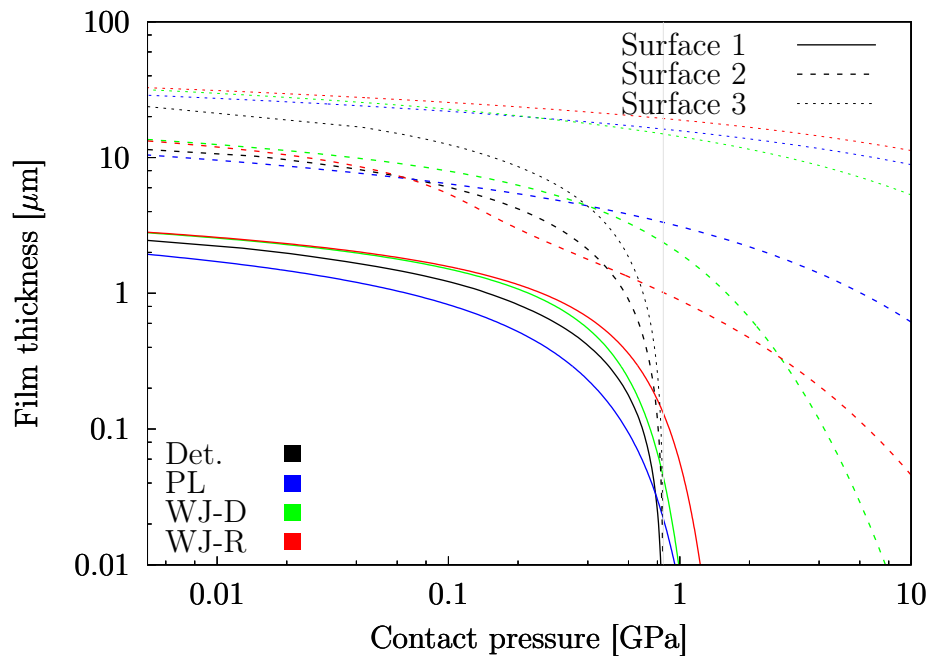## 5.4. Deterministic Surface Temperature Model for Lubricated Point Contact

In this section the thermal model used for calculating surface temperature increase in ball–on–disc test cases is validated. The model is implemented inside the `foam-extend` framework as a solver called `surfaceHeatFoam`. The implementation of the solver was described in Chapter 4.

Validation is carried out using two steady–state cases for which the exact solution can be calculated:

- smooth surface with a square heat source,

- smooth surface with a parabolic heat source.

The exact solution of the two cases was given by Tian and Kennedy [5]:

$$\Delta T(x,y) = \int_{-l}^{l} \int_{-l}^{l} \frac{q(x',y')}{2\pi K s} \exp\left(-\frac{|\mathbf{U}|}{2\kappa}\left[s - (x - x')\right]\right) \mathrm{d}x' \, \mathrm{d}y',$$

where $s = \sqrt{(x - x')^2 + (y - y')^2}$, $q(x,y)$ is the heat flux, K is the surface material thermal conductivity, U is the surface velocity vector, $\kappa = K/(\rho c)$ is the surface material thermal diffusivity, c is the material specific heat capacity, $l = L/2$ is the half–width and length of the heat source, and L is the half–width and length of the computational domain. The assumption is that the velocity vector points in the positive x–direction. The centre of the computational domain is located at position $(0,0)$. The heat flux for the square heat source case is defined by:

$$q_{\mathrm{square}} = \frac{Q}{L^2} = \mathrm{const.},$$

where Q is the heat power, while the heat flux for the parabolic heat source case is defined by:

$$q_{\mathrm{parabolic}}(x,y) = \frac{3Q}{2R^2\pi} \sqrt{\max\left(1 - \frac{x^2 + y^2}{R^2}, \ 0.0\right)},$$

where R is the radius of the parabolic heat source.

In both cases the half–width and length of the domain is $L = 10$ mm while the heat power is equal to $Q = 1$ W. The material surface properties used in simulations are: density $\rho = 7860$ kg/m^3, specific heat capacity $c = 420$ J/kgK and thermal conductivity $K = 46$ W/mK. The radius of the parabolic heat source is equal to $R = L/2$. Each case was calculated for three Peclet numbers (1, 10 and 100) and for five mesh densities (16×16, 32×32, 64×64, 128×128, 256×256). In Fig. 5.36 computational domains and heat fluxes are shown.
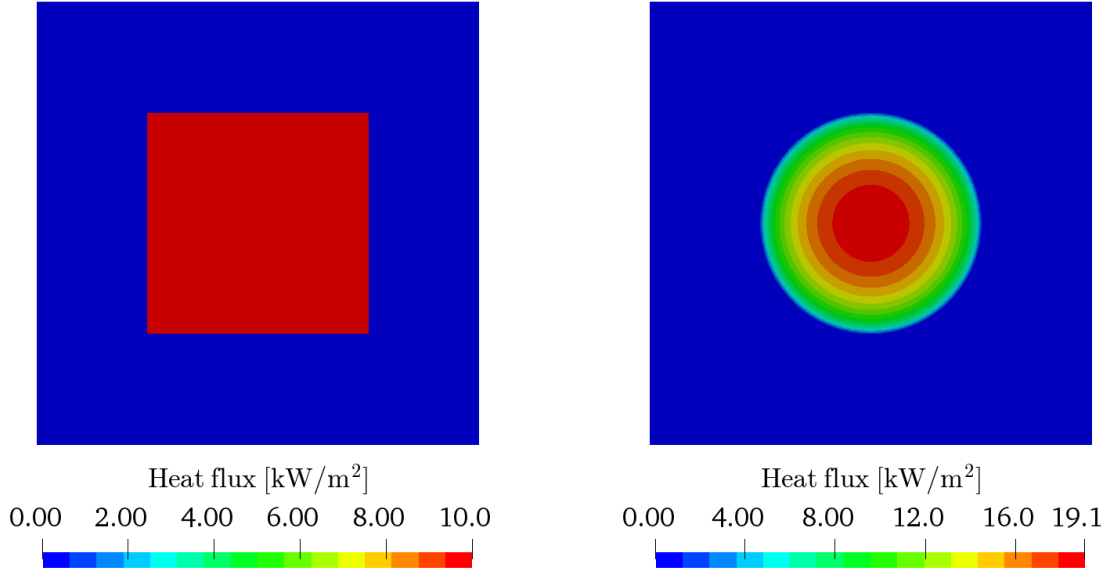

Figure 5.36: Computational domain and surface heat flux in case of square (left) and parabolic (right) heat flux.

In Fig. 5.38 a comparison between the `surfaceHeatFoam` results and exact solutions by Tian and Kennedy [5] is given for square heat flux cases with 256×256 finite area faces. The results are in a perfect agreement with exact solutions for all three Peclet numbers. In Fig. 5.37 the error of temperature increase between the results and the exact solution for different mesh densities is given. The error is calculated using Eq. 5.6. For the square heat source the solution is mesh–independent even for the coarsest mesh with 16×16 finite area faces, with the error below 0.0001%. In Fig. 5.39 a comparison between the `surfaceHeatFoam` results and exact solutions is given for parabolic heat flux cases with 256×256 finite area faces. Again, the results are in a perfect agreement with exact solutions for all three Peclet numbers. In Fig. 5.37 the error of temperature increase for

different mesh densities is given. The temperature error is around 2.5% for the coarsest mesh and falls bellow 0.1% for mesh with 256×256 faces for all three Peclet numbers. The temperature increase field for both the square and the parabolic heat source cases is given in Fig. 5.40 for Peclet number equal to 10.

Taking into account presented results, the thermal model used for calculating surface temperature increase is considered validated.
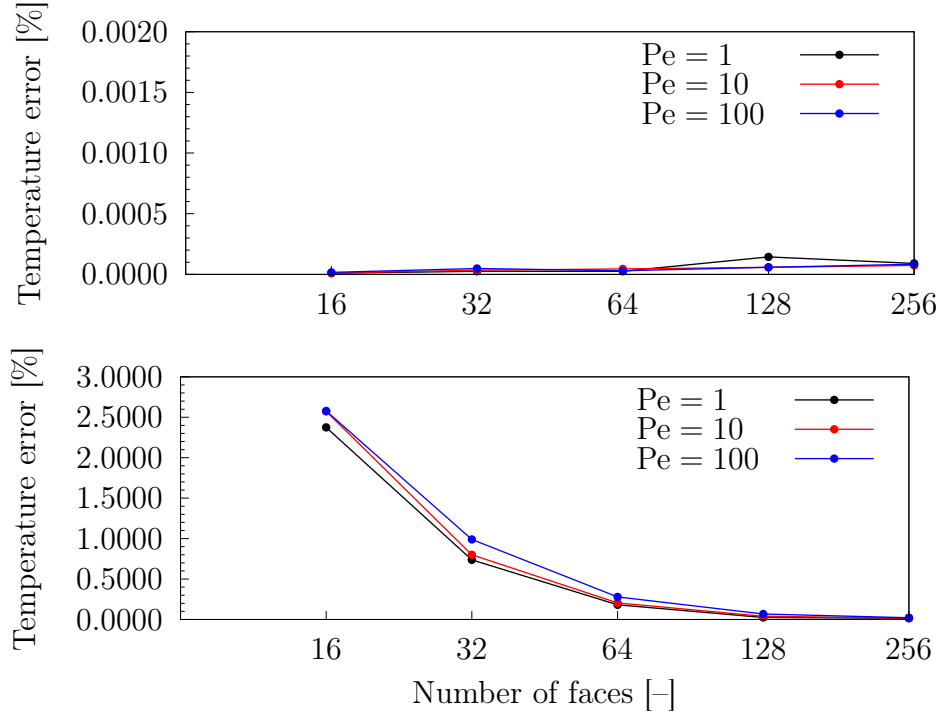
Figure 5.37: Temperature increase error for the square (top) and parabolic (bottom) heat sources.

135
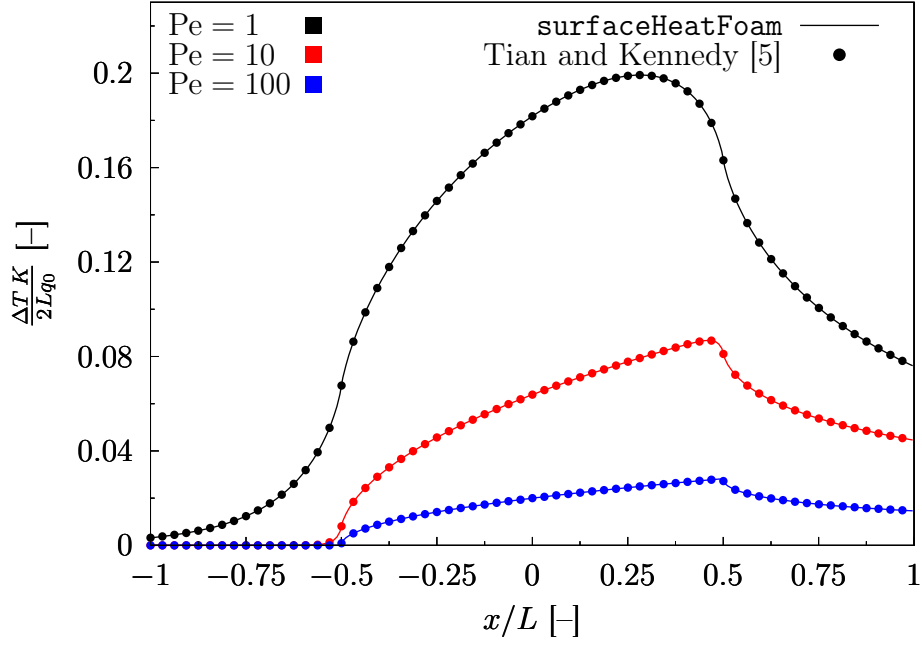
Figure 5.38: Comparison of temperature increase between `surfaceHeatFoam` and exact solution [5] at the longitudinal centreline for the square heat source. Note: $q_0 = Q/L^2$.
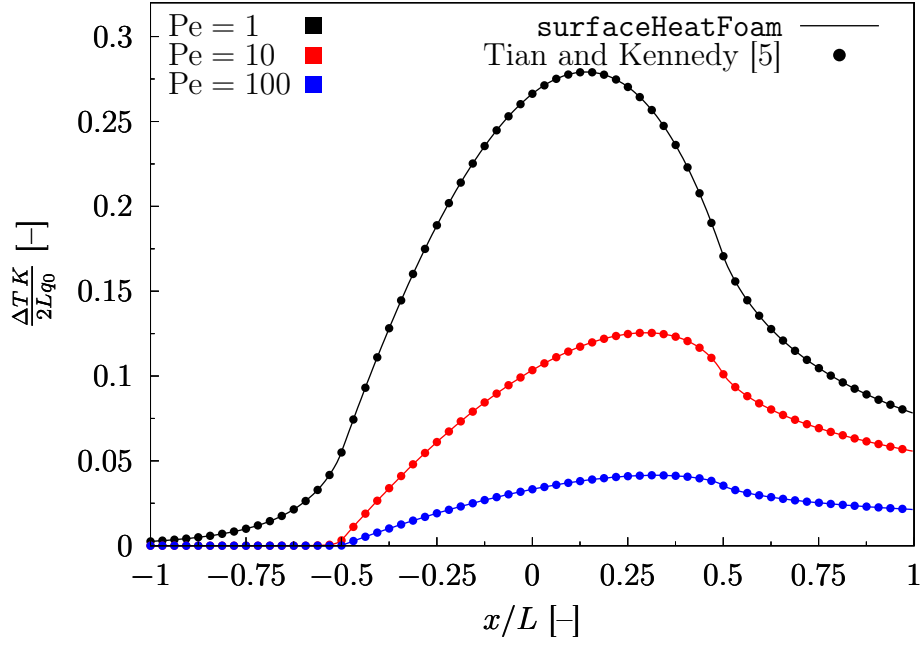
Figure 5.39: Comparison of temperature increase between `surfaceHeatFoam` and exact solution [5] at the longitudinal centreline for the parabolic heat source. Note: $q_0 = Q/(R^2\pi)$.

Figure 5.40: Temperature increase in case of square (left) and parabolic (right) heat flux for Peclet number 10.

5.5. Point Contact Analysis

In this section implemented models described in Chapter 4. and validated in previous sections are utilised for the analysis of lubricated point contacts. Analysis is conducted for hydrodynamic and mixed lubrication conditions, for the following lubricant oils:

- Turbo T9 oil (hydrodynamic) [10],

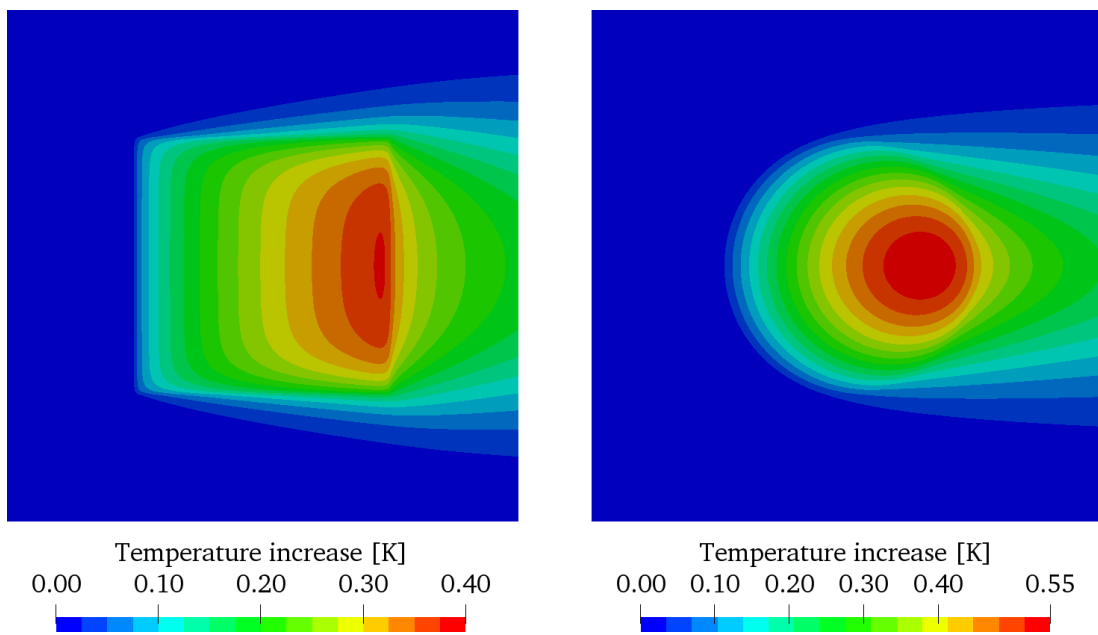- Turbo T68 oil (hydrodynamic and mixed) [12].

Simulation results are compared to the available numerical and experimental data from the literature. Habchi et al. [10] performed measurements of film thickness and friction coefficients during hydrodynamic lubrication using a ball–on–disc tribometer. They also performed thermal elastohydrodynamic simulations and compared their results to the experimental data. Guegan et al. [6, 12] performed experimental measurements of friction coefficients during mixed lubrication between a smooth glass disc and a rough steel ball, also using a ball–on–disc tribometer. Habchi et al. [10] utilised Turbo T9 mineral oil for which they provided detailed transport properties, while Guegan et al. [6, 12] used Turbo T68 mineral oil for which only the following transport properties are available: the low–shear viscosity [11], density for three pressure values [154] and thermophysical properties (conductivity, specific heat capacity and thermal expansion coefficient) for a single temperature and pressure value [155]. The main parts of ball–on-disc apparatus are a disc and a ball, Fig. 5.41. Bottom half of the ball is submerged inside a lubricant bath with a constant temperature. The disc and the ball are rotating with their respective speeds, while the ball is pressed against the disc with a desired normal load. The friction force is measured using a torque meter connected to the ball's shaft. The film thickness is measured using a camera positioned above the disc at the location of the contact. For more details regarding the apparatus and the measuring process one should refer to [7].
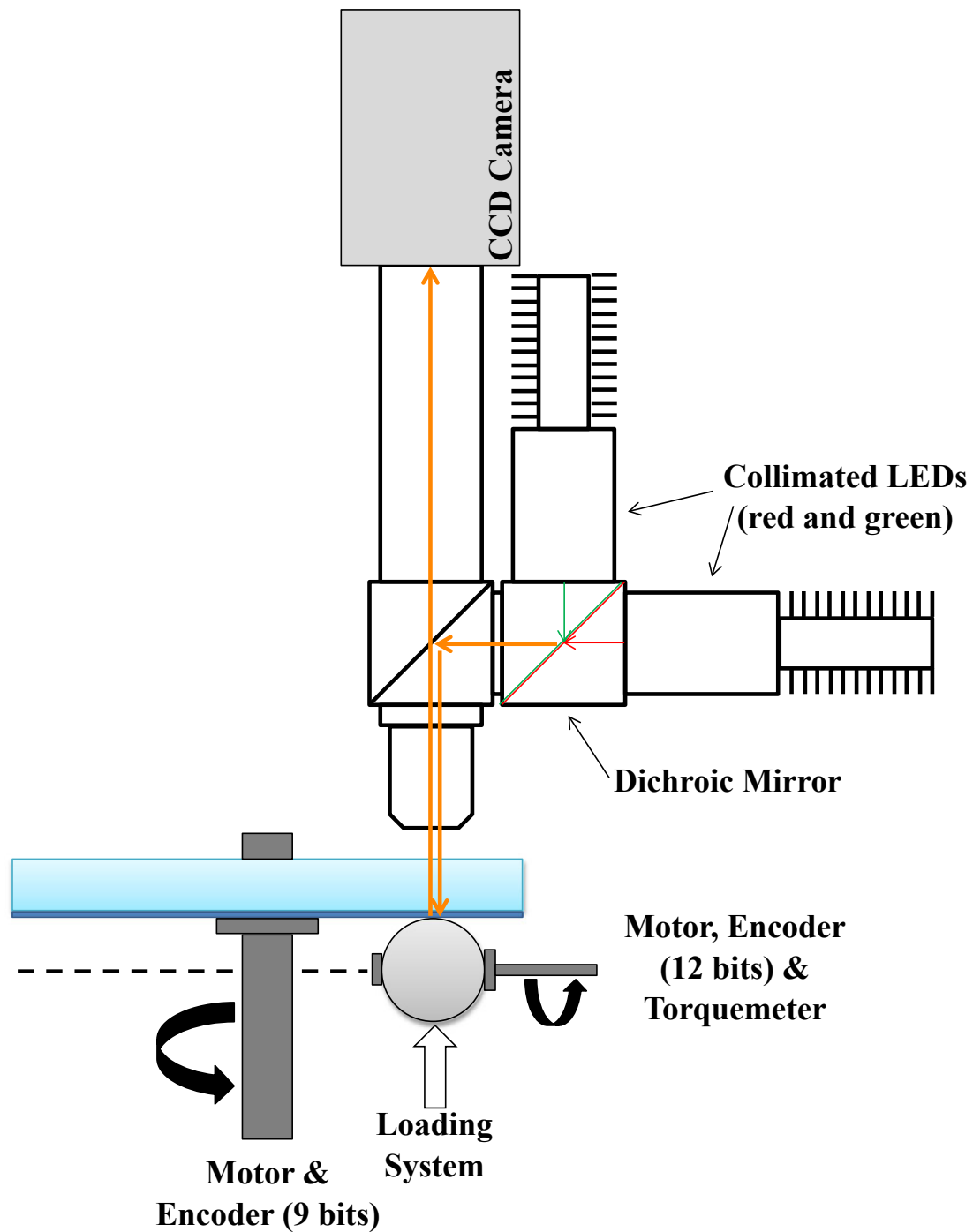
Figure 5.41: Schematic of the ball–on–disc apparatus [6].

5.5.1. Turbo T9 Oil

Results of ball–on–disc simulations using Turbo T9 lubricant oil are presented in this section. Habchi et al. [10] performed experimental measurements of the film thickness for pure rolling conditions and measurements of friction coefficients for sliding conditions. The ball was made of bearing steel in all cases, while two discs made out of different materials were used. The sapphire disc was used for pure rolling conditions and film thickness measurements, while a bearing steel disc was used for friction measurements. Material properties are specified in Table 5.7. The ball diameter is 25.4 mm.

Table 5.7: Material properties used in ball–on–disc simulations with Turbo T9 oil.

Description	Sapphire	Bearing steel	Unit
Young's modulus	360	210	GPa
Poisson's ratio	0.34	0.3	–
Density	4000	7850	kg/m^3
Thermal conductivity	40	50	W/mK
Specific heat	750	470	J/kgK

Pressure–density relation used in calculations is the Murnaghan equation of state [10], Eqs. 4.31 and 4.32, with required coefficients specified in Table 4.3. Pressure and temperature dependence of viscosity is calculated using Eqs. 4.39 and 4.40 with coefficients specified in Table 4.5, while the shear dependence is calculated using the Carreau–Yasuda model, Eq. 4.47 and Table 4.6. Further details regarding thermophysical and other transport properties are specified in [10].

Size of the computational domain depends on the prescribed load, i.e. length and width of the domain is twice the size of the Hertzian contact diameter, as recommended by Wu et al. [33]. The centre of the contact is located in the centre of the computational domain.

Several simulations were conducted for different rolling and loading conditions. Pure rolling conditions were calculated considering loads of 23 and 95 N for entrainment speeds ranging from 0.5 to 7 m/s. Sliding conditions were calculated considering loads of 38 and 154 N, with entrainment speeds set at 0.8 and 2 m/s

respectively, for slide–to–roll ratios ranging from 0 to 1.

In Fig. 5.42 the calculated minimum and central film thickness is compared with the experimental data [10] for two pure rolling cases with loads of 23 N and 95 N. The presented numerical results were calculated using a mesh with 128×128 finite area faces. For the case with a load of 23 N, both minimum and central film thickness values are in a very good agreement with experimental data. The maximum relative deviation from the experimental results is 4.7% for minimum film thickness and 5.1% for central film thickness, while the mean relative deviations are 2.3% and 3.0%. It should be noted that the original experimental data was not available, therefore values were extracted from publication [10]. For the case with a load of 95 N calculated values are in a good agreement with the experiment for higher entrainment speeds. The relative deviation of minimum film thickness compared to the experimental results for the smallest entrainment speed of 0.5 m/s is 41.7% while the relative deviation of central film thickness is 1%. For the largest entrainment speed of 7 m/s relative deviations for the minimum and central film thickness are around 13.6% and 11%, respectively. The mean relative deviation is 13.6% for the minimum film thickness, and 7.8% for the central film thickness. The simulation results given by Habchi et al. [10] are very similar to the ones presented here.

In Fig. 5.43 calculated friction coefficients for four different cases are compared to experimental measurements and numerical solutions given in [10]. For all cases simulation results show a good agreement both with the numerical and experimental data. For the first case (38 N load, 0.8 m/s entrainment speed) the average relative deviation of friction coefficients from the numerical results given by Habchi et al. [10] is 0.9%, and 7.4% from the experimental measurements. For the second case (38 N load, 2 m/s entrainment speed) the average relative deviations are 5.9% and 11.2% from numerical results and experimental data, respectively. For the third case (154 N load, 0.8 m/s entrainment speed) relative deviations are 1.8% and 5.7%, while for the fourth case (154 N load, 2 m/s entrainment speed) they are 3.1% and 5.0%.

Larger relative deviations from numerical results [10] for cases with higher entrainment speeds are expected since in the current work average values of density and viscosity across the film and parabolic temperature profile are assumed,

23 N, pure rolling
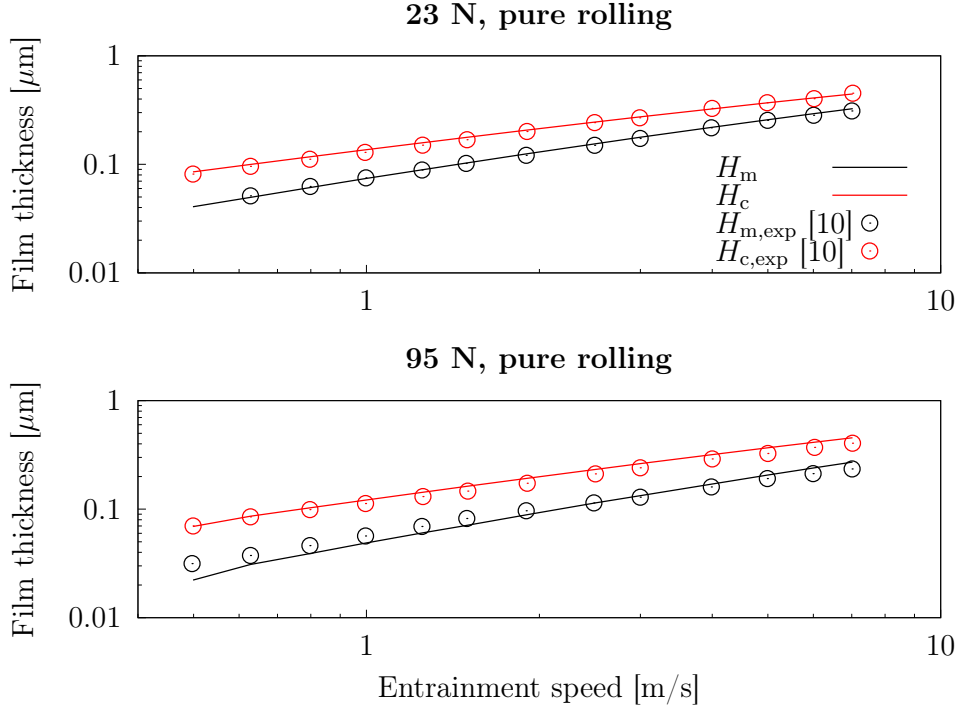
95 N, pure rolling

Figure 5.42: Film thickness versus entrainment speed for pure rolling ball–on–disc simulations with T9 oil.

38 N, 0.8 m/s   **38 N, 2 m/s**
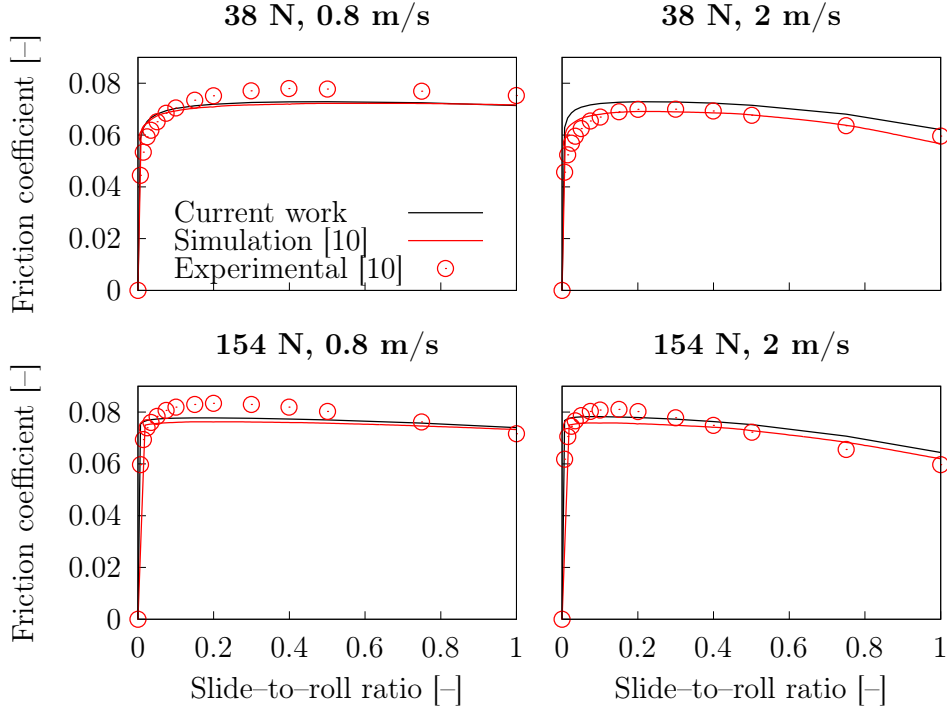
154 N, 0.8 m/s   **154 N, 2 m/s**

Figure 5.43: Friction coefficient versus entrainment speed for ball–on–disc simulations with T9 oil.

while in [10] authors numerically integrate density and viscosity values across the film, and they discretise computational domain across the film thickness in order to solve the three–dimensional temperature equation. Since average relative deviations of friction coefficients between the current approach and the approach from [10] are relatively small (5.9% and 3.1%), the current approach is justified since no additional numerical integration is needed and the temperature equation is solved in only two dimensions, thus enabling the use of Finite Area Method, which reduces computational time. Another argument for using the simplified approach is the fact that the authors [10] gave extremely detailed information regarding the lubricant transport properties of Turbo T9 oil, which is rarely the case in industrial applications.

In order to calculate the achieved accuracy in space a mesh convergence study was performed for the case with a load of 38 N and entrainment speed 0.8 m/s, for three slide–to–roll ratios (SRR): 0.1, 0.5 and 1. The study was performed with respect to the friction coefficient value. The study was performed systematically using four mesh densities: 64×64, 96×96, 128×128, 256×256 finite area faces. The test matrix is shown in Table 5.8. Uncertainty and error estimation was performed using the freely available code [156] based on the procedures suggested by Eça and Hoekstra [157]. Results of the analysis are presented in Fig. 5.44 and Table 5.9, where ϕ_0 is the extrapolated exact solution, ϕ_1 is the finest level solution, U_ϕ is the estimated uncertainty and p is the achieved accuracy in space. For all three slide–to–roll ratios the theoretical second–order accuracy is achieved, with the largest uncertainty of 0.17% for 0.1 slide–to–roll ratio.

Table 5.8: Test matrix for the ball–on–disc T9 case uncertainty analysis.

No. of faces SRR	4096	9216	16384	65536
0.1	0.0714	0.0706	0.0702	0.0700
0.5	0.0737	0.0731	0.0728	0.0726
1.0	0.0723	0.0717	0.0714	0.0712

In Fig. 5.45 hydrodynamic pressure fields for pure rolling cases with a 23 N load are presented. By increasing the entrainment speed U_e, the high pressure

143
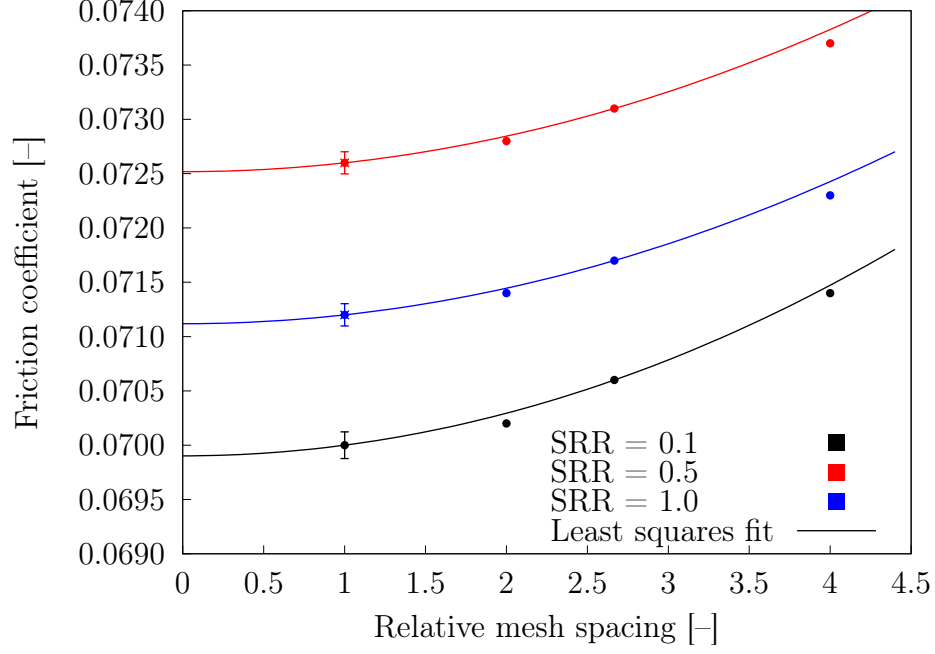
Figure 5.44: Friction coefficients calculated for different mesh spacings for the ball–on–disc T9 case. Uncertainty estimate U_ϕ (Table 5.9) is depicted for the finest mesh result.

Table 5.9: Results of the uncertainty analysis for the ball–on–disc T9 case.

SRR	ϕ_0 [–]	ϕ_1 [–]	U_ϕ [%]	p [–]
0.1	0.0699	0.0700	0.17	2.00
0.5	0.0725	0.0726	0.14	2.00
1.0	0.0711	0.0712	0.14	2.00

region becomes elongated in the direction of the flow (left to right). Pressure contours near the centre of the contact retain approximately the same shapes and values, close to the Hertzian pressure of 0.84 GPa. Also, by increasing entrainment speed, the high pressure front becomes more noticeable with the maximum value reaching 1.1 GPa for the entrainment speed of 7 m/s.

In Fig. 5.46 film temperature fields for cases with a 38 N load are presented. Two entrainment speeds are compared, 0.8 and 2 m/s, and three slide–to-roll ratios, 0.1, 0.5 and 1.0. Higher entrainment speed, 2 m/s, results in higher film temperatures and a longer high temperature trail after film exits the contact. The high temperature front located at the exit of the contact is more noticeable for the higher entrainment speed, which is actually the consequence of the high pressure front presented in Fig. 5.45. By increasing slide–to–roll ratio the high temperature region becomes wider and higher film temperatures are achieved, which is expected. For the entrainment speed of 2 m/s and slide–to–roll ratio of 1 the maximum film temperature increase is 54 °C.

$U_\mathrm{e} = 0.8$ m/s $U_\mathrm{e} = 1.25$ m/s

$U_\mathrm{e} = 1.9$ m/s $U_\mathrm{e} = 3.0$ m/s

$U_\mathrm{e} = 5.0$ m/s $U_\mathrm{e} = 7.0$ m/s

Hydrodynamic pressure [GPa]

0.0   0.2   0.4   0.6   0.8   1.1
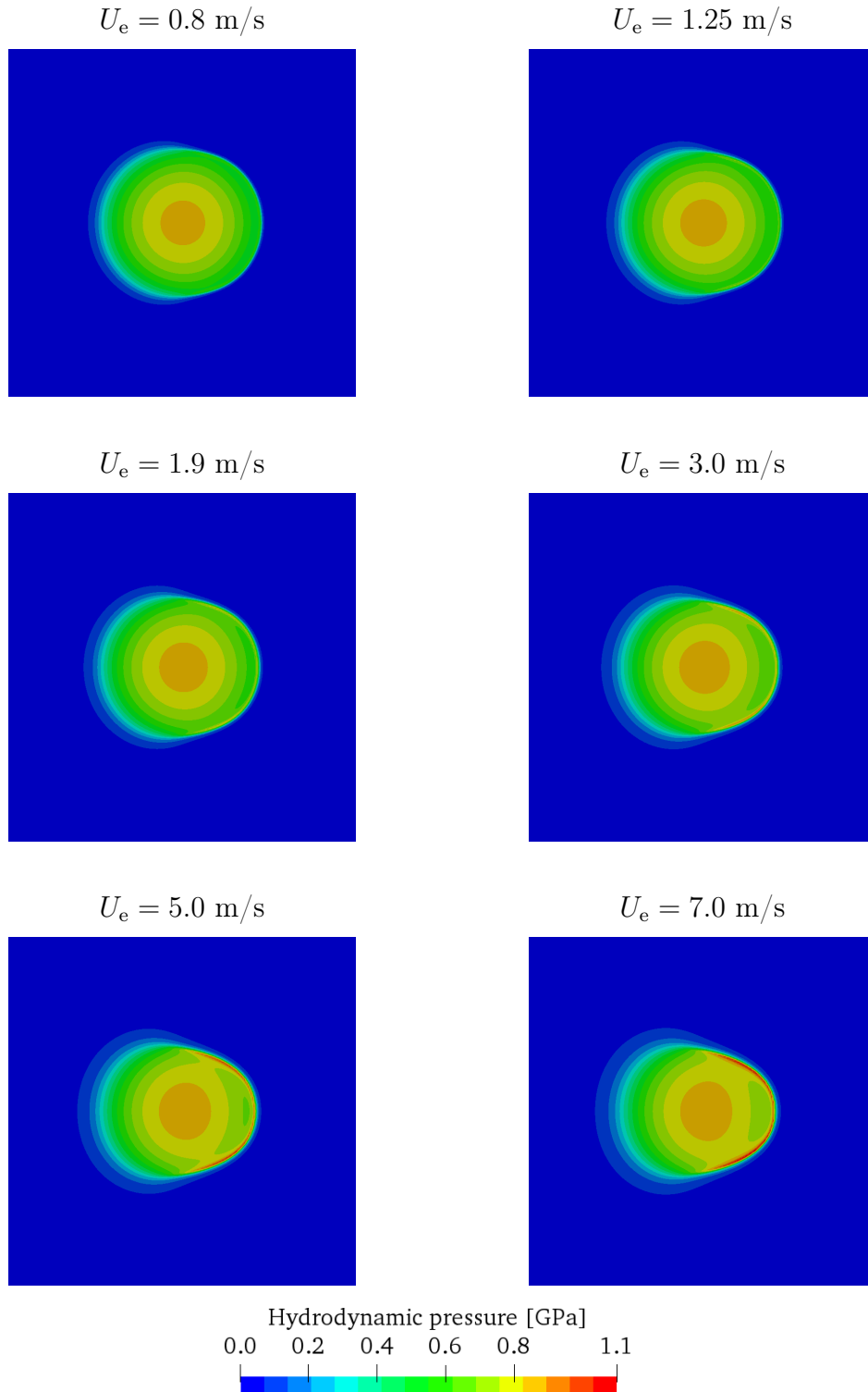
Figure 5.45: Hydrodynamic pressure fields for T9 ball–on–disc pure rolling cases with a load of 23 N.

$U_\mathrm{e} = 0.8$ m/s $\qquad\qquad$ $U_\mathrm{e} = 2$ m/s

SRR = 0.1

SRR = 0.5

SRR = 1.0

Temperature [$^\circ$C]

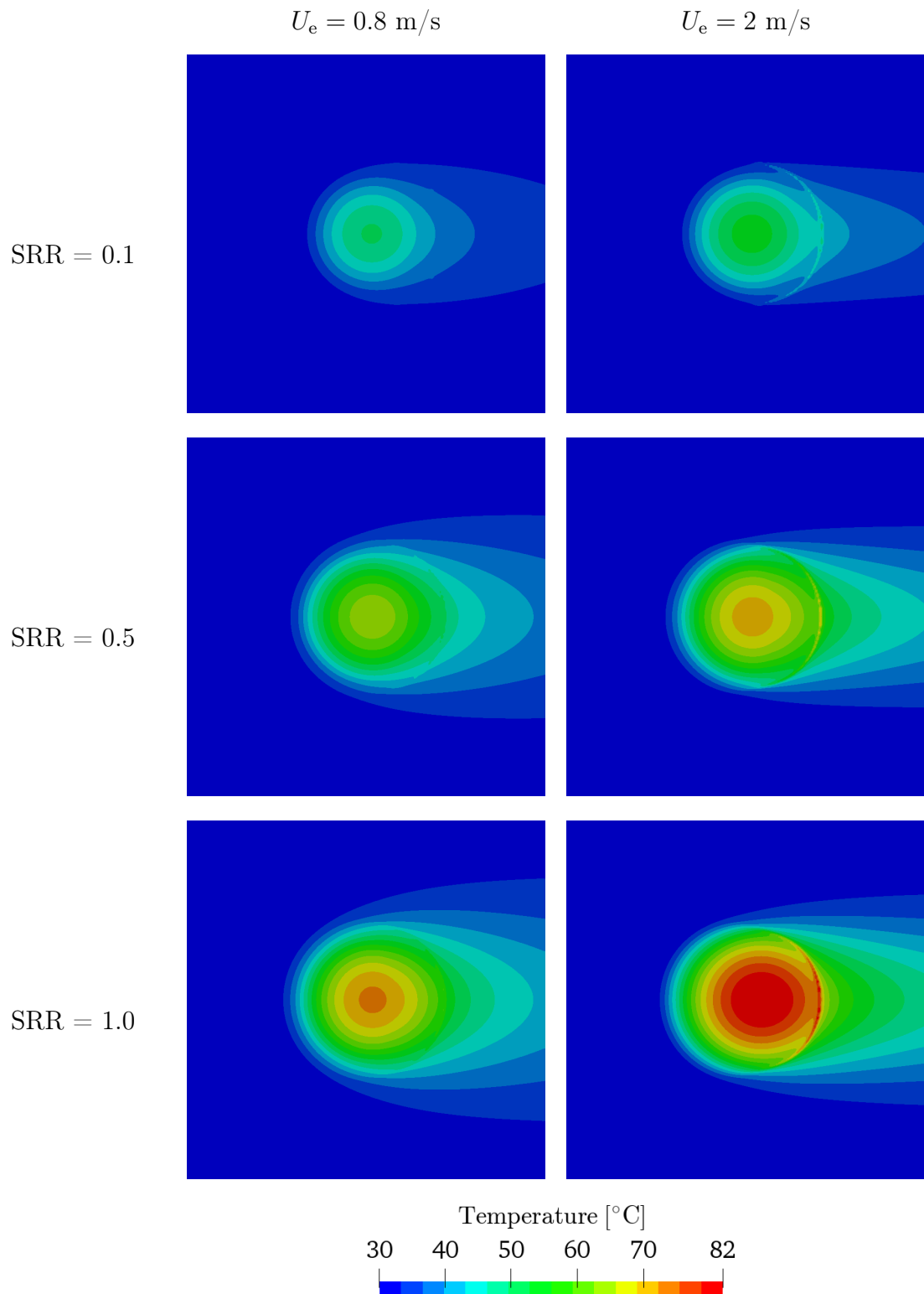30 $\quad$ 40 $\quad$ 50 $\quad$ 60 $\quad$ 70 $\quad$ 82

Figure 5.46: Temperature fields for T9 ball–on–disc cases with a load of 38 N.

147

5.5.2. Turbo T68 Oil

Results of ball–on–disc simulations using Turbo T68 lubricant oil are presented in this section. Guegan et al. [12] performed experimental measurements of friction coefficients with which simulation results are compared. Three balls with different longitudinal roughnesses were used and one smooth disc. Balls were made of AISI 52100 steel, while the disc was made of glass. Material properties are specified in Table 5.10. The ball diameter is 19.05 mm.

Table 5.10: Material properties used in ball–on–disc simulations with Turbo T68 oil.

Description	Glass	Steel	Unit
Young's modulus	75	207	GPa
Poisson's ratio	0.22	0.3	–
Density	2600	7860	kg/m^3
Thermal conductivity	0.8	46	W/mK
Specific heat	800	420	J/kgK

Pressure–density relation used in calculations is Dowson–Higginson relation with coefficients $C_1 = 0.9228$ GPa and $C_2 = 1.31$. Coefficients were calculated using Curve Fitting Toolbox [136] based on pressure and density values given by Dwyer–Joyce et al. [154]. Pressure and temperature dependence of viscosity is calculated using Eqs. 4.37 and 4.38 with coefficients specified in Table 4.4, while the shear dependence is calculated using Ree–Eyring model, Eq. 4.46 and Table 4.6. Thermophysical properties of Turbo T68 oil given by Napel et al. [155] are specified in Table 5.11.

Table 5.11: Thermophysical properties of Turbo T68 oil.

Description	Value	Unit
Density (at 15 °C)	876	kg/m^3
Thermal expansion coeff.	7.6×10^{-4}	1/K
Thermal conductivity	0.14	W/mK
Specific heat	2035	J/kgK

Several simulations were conducted for three longitudinal surface roughnesses

under hydrodynamic and mixed lubrication regimes. Two slide–to-roll ratios were considered, 50% and 100%, with entrainment speeds ranging from 0.02 to 2.2 m/s. Normal contact load is set to 20 N for all cases. Lubricant is kept warm at 40 °C inside the lubricant bath. Width and length of the computational domain is 0.54 mm which is equal to twice the size of the Hertzian contact diameter.

The measured roughness specimens are presented in Fig. 5.47, alongside their sine function approximations. Roughness parameters of surface specimens calculated by Guegan et al. [6] using FFT are given in Table 5.12. Simulations were performed using a dense finite area mesh with 640×640 faces, which is equal to the resolution of measured surface roughness profiles.

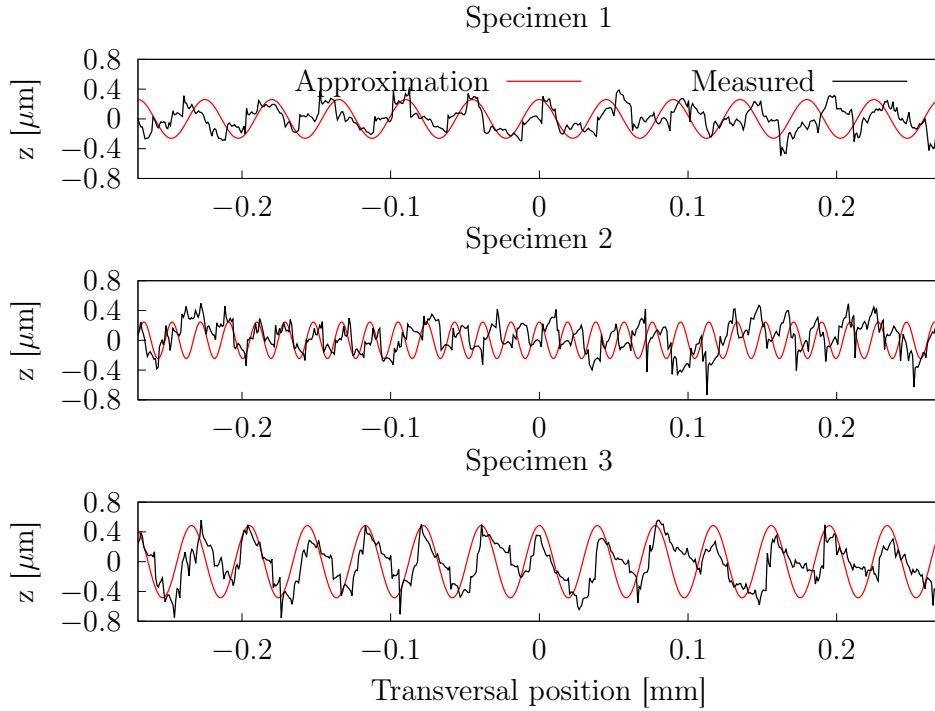Figure 5.47: Three roughness specimens [7] used in ball–on–disc simulations with Turbo T68 oil.

In Fig. 5.48 a comparison between calculated and experimentally measured [12] friction coefficients is given. Results for three surface specimens and two slide–to–roll ratios are given. For specimens 1 and 3 simulation results are in a very good agreement with the experimental data, considering the lack of infor-

Table 5.12: Roughness parameters of surface specimens [6] used in ball–on–disc simulations with Turbo T68 oil.

Specimen		1	2	3
Peak–to–valley height	[μm]	0.52	0.49	0.97
Wavelength	[μm]	45	19	39
RMS	[μm]	0.15	0.15	0.27

mation regarding lubricant shear thinning effects, and temperature and pressure dependence of thermophysical properties. This information is very important in conditions of high SRR values, due to large lubricant shear and temperature increase. For all four cases simulations conducted using measured roughness profiles give better results compared to experimental data than results from simulations using approximated roughness profiles. In case of specimen 2, simulation results show good agreement with the experimental data for higher entrainment speeds (above 0.7 m/s), where there is no significant asperity contact. For lower speeds, and consequently more asperity contact, simulation results considerably deviate from experimental data. Comparing the results for all three surface specimens, one could suggest that the ball with longitudinal roughness used to measure friction coefficients under designation *Specimen 2* does not correspond to the ball for which specimen 2 roughness profile was given in Fig. 5.47.

In Fig. 5.49 contact area ratios calculated over the central part of the computational domain are given for specimens 1 and 3, both with measured and approximated roughness profiles. The observed area is defined by a circle with radius equal to the Hertzian contact radius. For specimen 1, using approximated roughness results in smaller contact area for entrainment speeds higher than 0.4 m/s, while for lower speeds values of contact area overshoot the values from cases with measured roughness by up to 50%. For specimen 3, using approximated roughness profile results in larger contact contact, of up to 100%, for the whole range of entrainment speeds. Comparing the two cases with measured roughness profiles, values of contact area are larger for specimen 3 for the whole range of entrainment speeds. Interestingly, contact area ratios of both specimens converge to the same value as the speed decreases. The maximum contact area
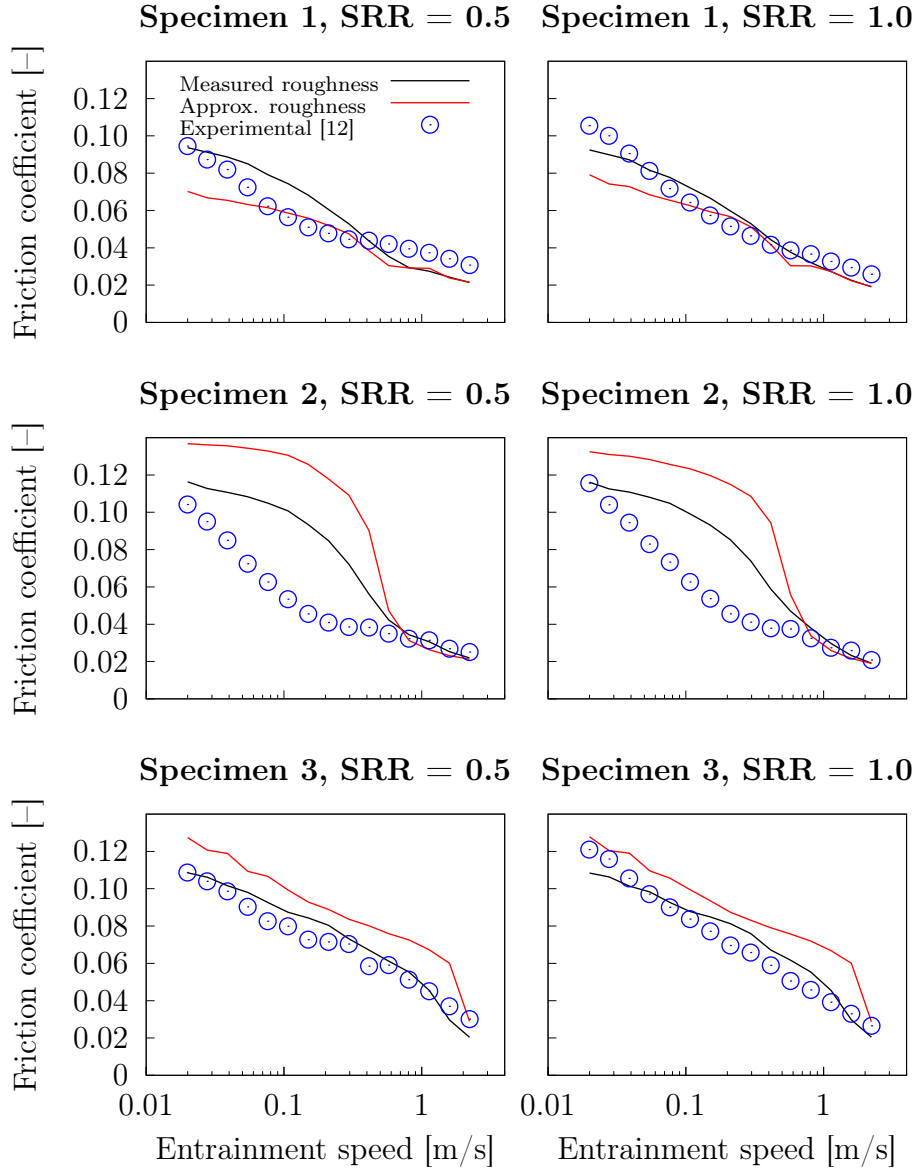
Figure 5.48: Comparison between calculated and experimentally measured friction coefficients in ball–on–disc simulations with Turbo T68 oil.

ratio for both specimens is 14% in case of measured surface profiles. In Fig. 5.50 contact areas of the test case with specimen 1 roughness are presented for four entrainment speeds. As expected, decreasing entrainment speed, and consequently hydrodynamic pressure, the contact area increases.

In Fig. 5.51 solid–to–solid contact pressures are presented for the same four cases which are depicted in Fig. 5.50. The maximum value of contact pressure is approximately 3 GPa, and is achieved for very low entrainment speeds.

In Fig. 5.52 a comparison of film hydrodynamic pressures between the two specimen 1 roughness profiles is presented. The shapes of high pressure regions under higher entrainment speeds are very similar between the two profiles indicating that the approximated roughness does contain important surface characteristics needed for calculating hydrodynamic pressures in case of specimen 1 surface, when there is no asperity contact. Additional support for this claim is given in Fig. 5.48, where using either specimen 1 roughness profiles results in very similar values of friction coefficients under high speeds. By decreasing entrainment speed, and consequently increasing the area of contact, the difference between the measured and approximated profiles is more pronounced, resulting in different friction characteristics. By comparing Figs. 5.45 and 5.52 it can be noticed that the existence of surface roughness significantly changes the shape of high pressure region, where in case of a smooth surface that shape is elliptical and smooth, while in case of a rough surface it is irregular and closer to a circular shape.

In Fig. 5.53 film temperatures for the case using specimen 1 measured roughness are given. For high entrainment speeds, under hydrodynamic regime or mixed regime with scarce contact, the film temperature decreases with declining entrainment speed. This can be observed when comparing cases with entrainment speeds of 2.2 and 1.1 m/s. When entrainment speed is decreased further, more and more load is carried by asperities which results in increased levels of boundary lubrication and heat generation. Therefore, a significant portion of boundary lubrication increases film temperatures compared to the purely hydrodynamic cases under higher entrainment speeds. This can be observed, for example, when comparing cases with speeds of 1.1 and 0.22 m/s. Case with the highest film temperatures shown in Fig. 5.53 is the case with entrainment speed

of 0.22 m/s, where the maximum film temperature reaches 150 °C in areas close to the contacting asperities. By further decreasing entrainment speed film temperature declines, even though contact area increases, due to the decrease in slip velocity between two surfaces (ball and disc) in contact.
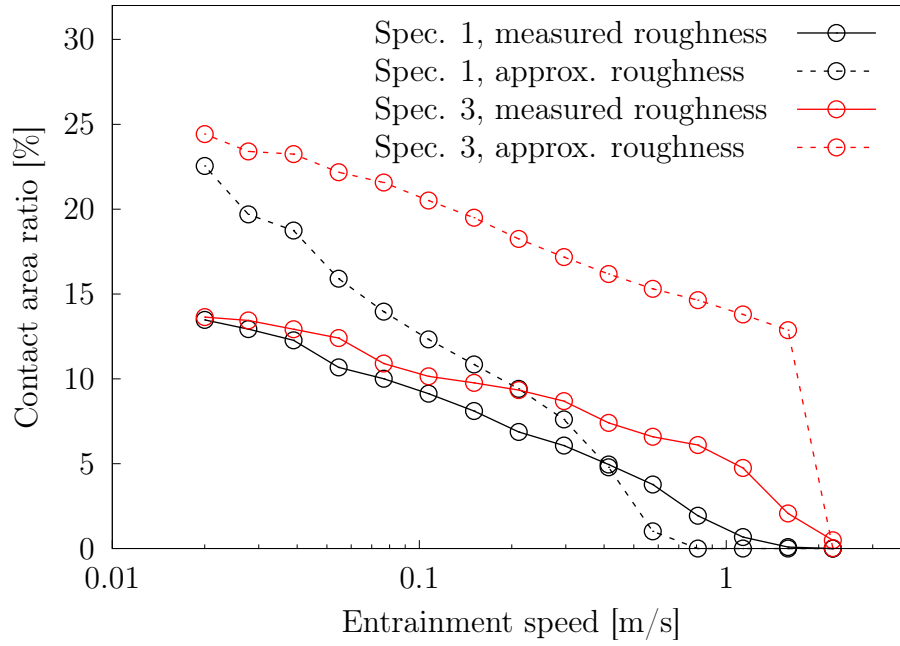
Figure 5.49: Contact area ratios for specimens 1 and 3 with SRR = 1 in ball–on–disc simulations with Turbo T68 oil.

$U_\mathrm{e} = 0.58$ m/s

$U_\mathrm{e} = 0.22$ m/s

$U_\mathrm{e} = 0.05$ m/s

$U_\mathrm{e} = 0.02$ m/s

Figure 5.50: Contact areas for specimen 1 with SRR = 1 in ball–on–disc simulations with Turbo T68 oil.

$U_{\mathrm{e}} = 0.58$ m/s $\qquad\qquad\qquad$ $U_{\mathrm{e}} = 0.21$ m/s

$U_{\mathrm{e}} = 0.05$ m/s $\qquad\qquad\qquad$ $U_{\mathrm{e}} = 0.02$ m/s

Contact pressure [GPa]

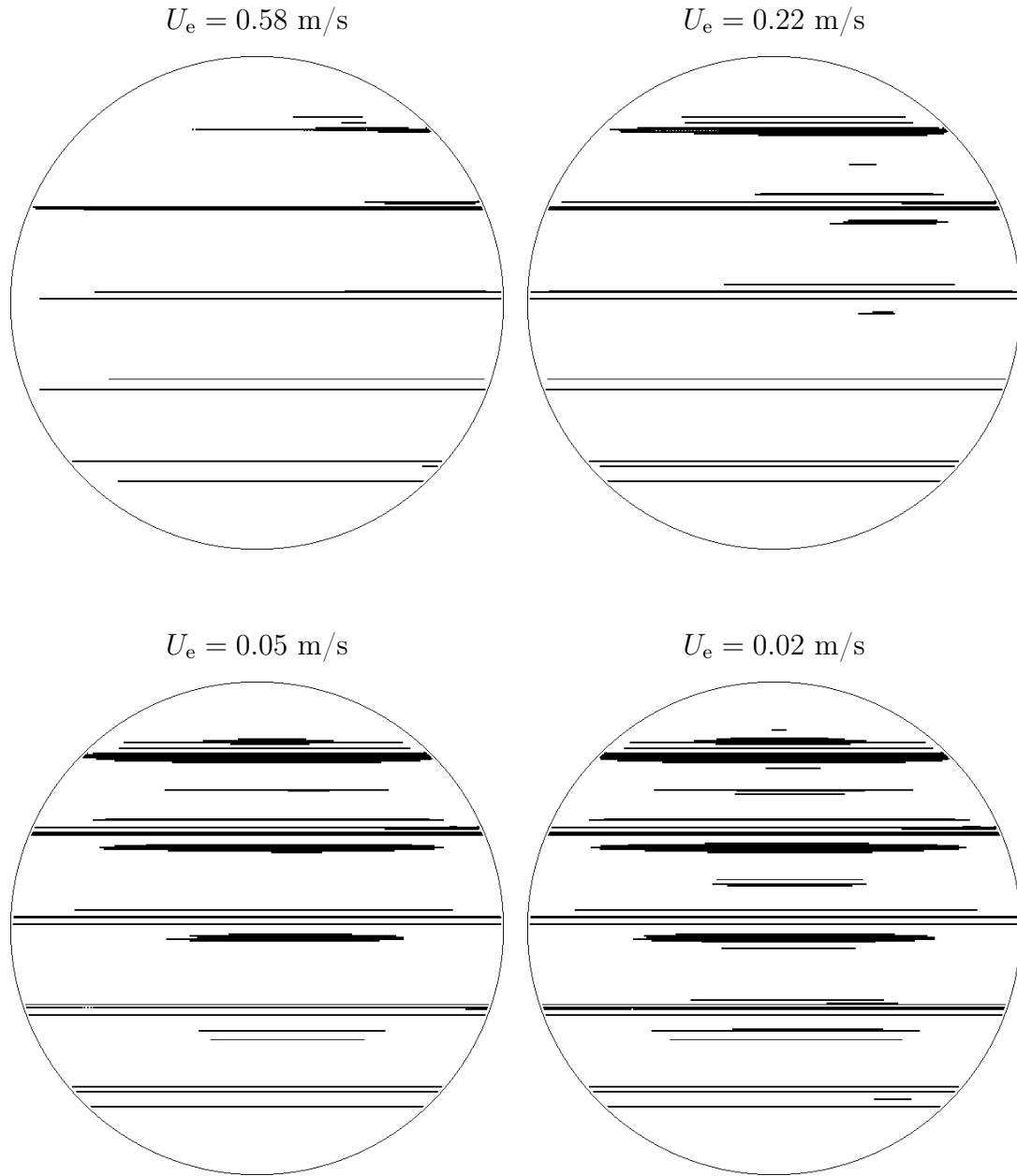0.00 $\quad$ 0.75 $\quad$ 1.50 $\quad$ 2.25 $\quad$ 3.00
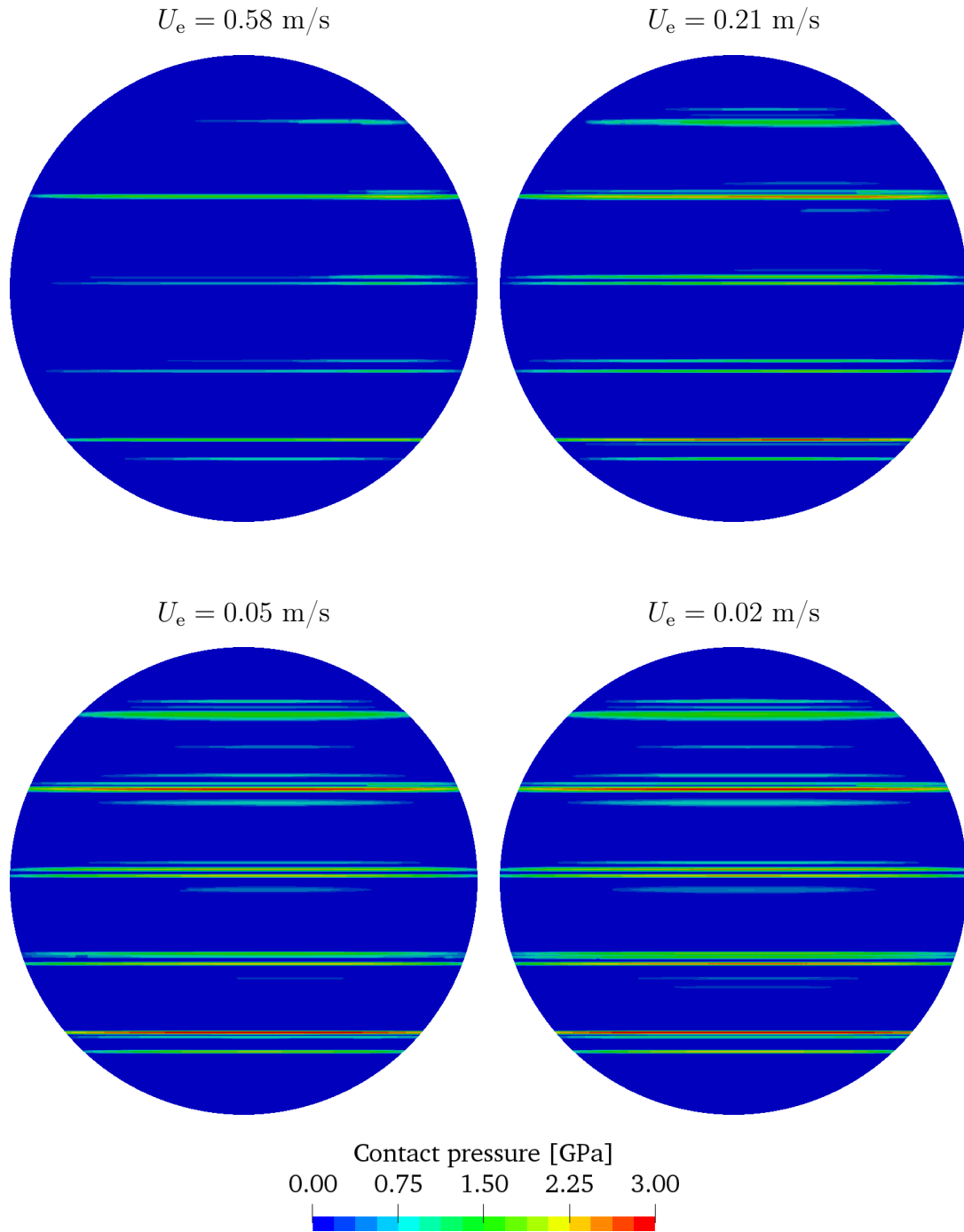
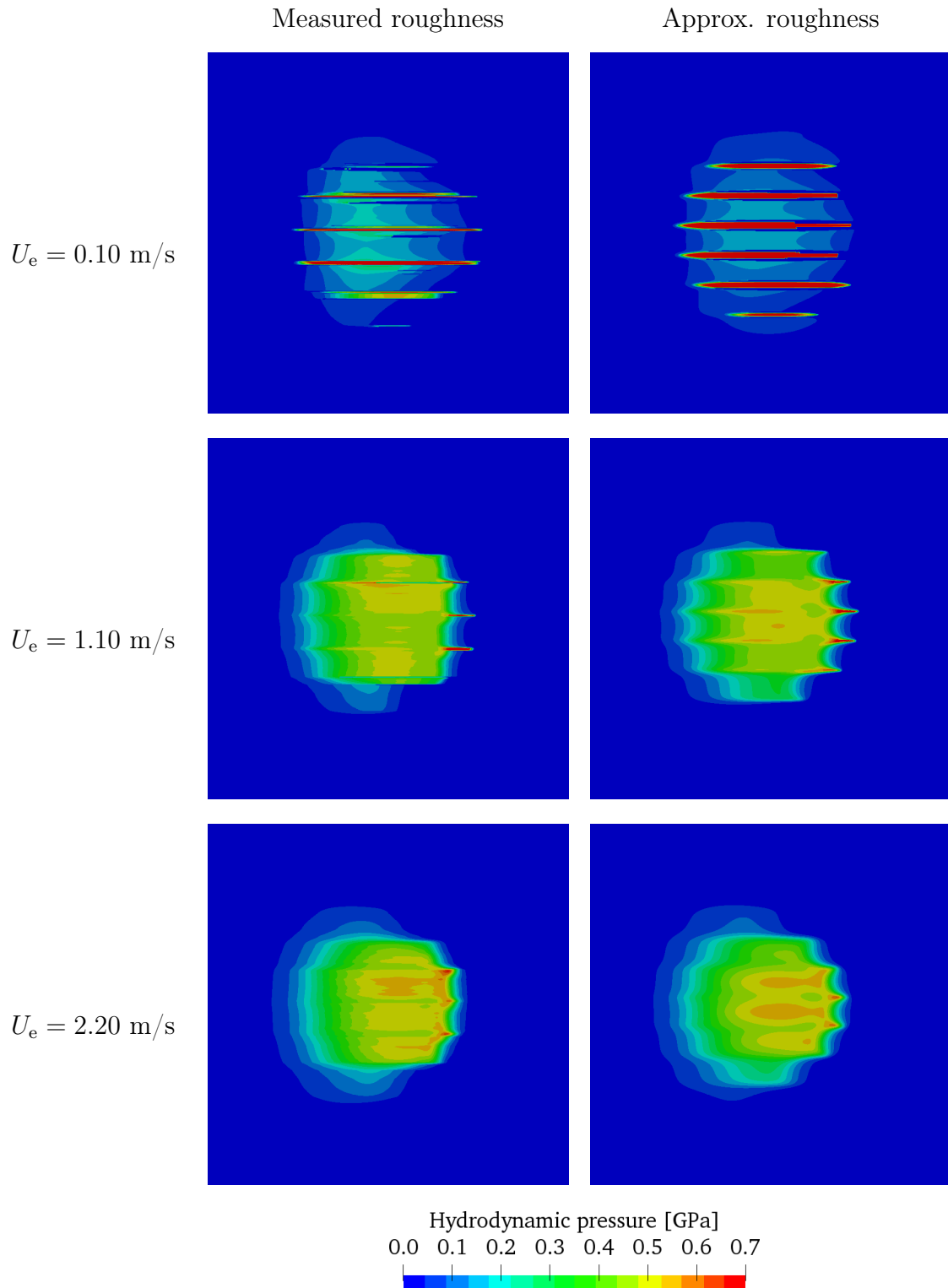Figure 5.51: Contact pressures for specimen 1 with SRR = 1 in ball–on–disc simulations with Turbo T68 oil.

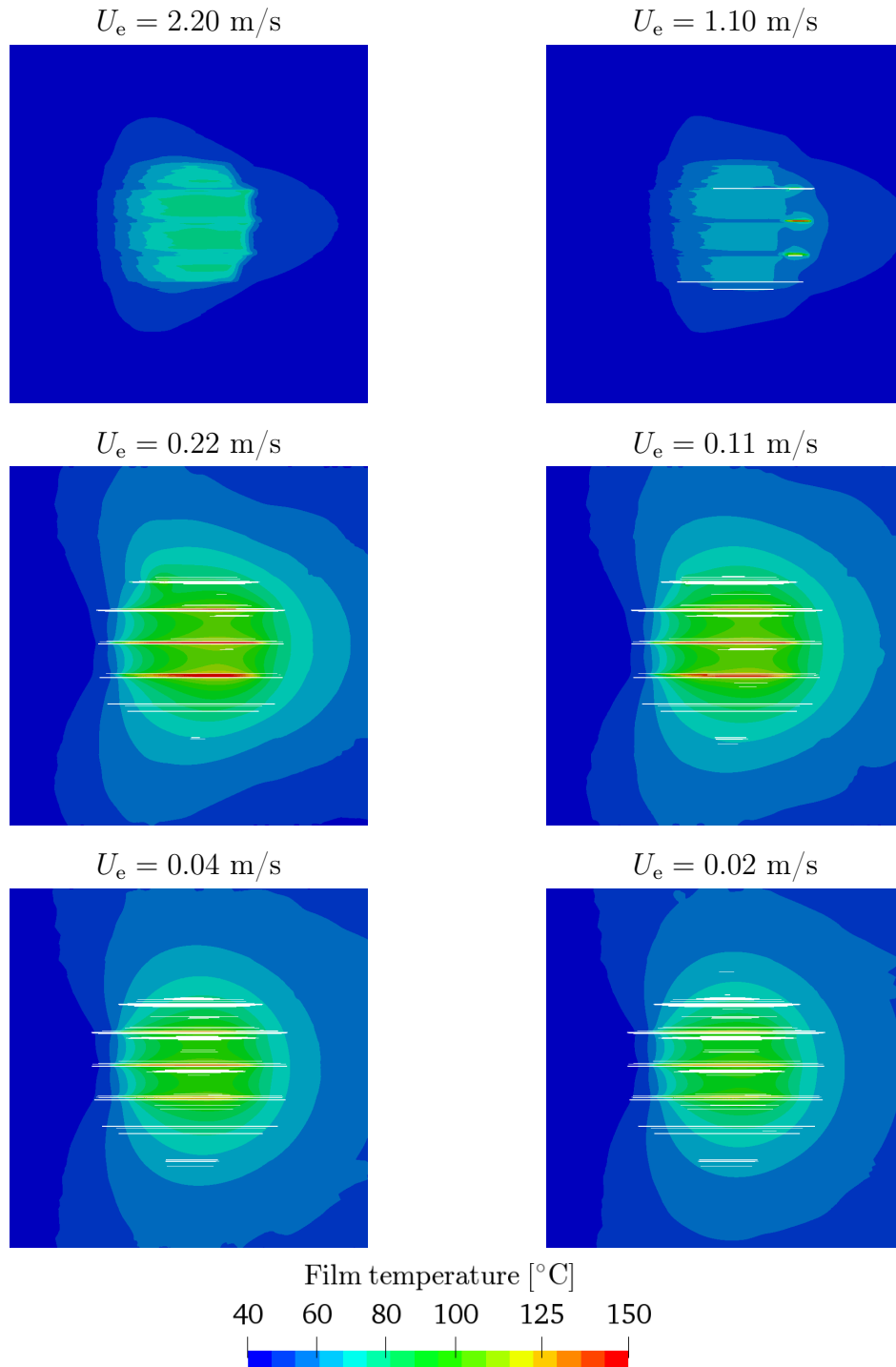Figure 5.52: Hydrodynamic pressures for specimen 1 with SRR = 1 in ball–on–disc simulations with Turbo T68 oil.

Figure 5.53: Film temperatures for specimen 1 with SRR = 1 in ball–on–disc simulations with Turbo T68 oil. White marks inside the domain denote contact areas.

5.6. Conclusion

Validation and verification of the implemented models was presented in this chapter.

First, the implementation of the Reynolds equation and cavitation algorithm was verified and validated. The first three cases (pocket slider bearing, single and twin parabolic slider bearings) were one–dimensional. For the purpose of validation the calculated pressure and density values were compared to the exact analytical solution in case of the pocket slider bearing, and to numerical solutions calculated using the LCP finite difference solver [61] implemented in Matlab® [151]. The comparison showed excellent agreement between the results. Verification was carried out by performing mesh refinement studies and calculating the cumulative error, i.e. relative deviation, of the calculated results compared to either analytical or numerical finite difference solutions. The error decreased in each case when the number of finite area faces was increased. Cases considering abrupt changes of the film thickness and film reformation boundaries usually require finer meshes in order to achieve the same accuracy as the cases with smooth film transitions which experience only rupture boundaries. The fourth case considered a two–dimensional microtexture pocket bearing with two widths, 10 mm and 300 mm. The pressure results were compared to the numerical solutions by Bertocchi et al. [3] and good agreement was achieved. In order to verify the model for two–dimensional applications the mesh refinement study was conducted. The fifth case considered is a dimple seal bearing geometry where the hydrodynamic pressure for three dimple configurations was calculated and compared to the numerical results from [4]. Again, the simulation results showed excellent agreement with the literature.

Next, the implemented elastic–perfectly–plastic deterministic contact model was validated. The validation case for purely elastic contact considered a contact between a rigid flat and deformable three–dimensional wavy surface profile made out of silicone rubber. Three mesh densities were analysed and each of them resulted in almost identical values of contact area. The results showed very good agreement with the experimentally measured contact areas [84] achieving a relative error of 4.27%, and excellent agreement with the numerical results by

Yastrebov et al. [82], with a relative error of 0.22%. The elastic–plastic contact was validated against the three–dimensional simulations of the same wavy surface geometry performed using the finite volume deformation solver. Again, the results showed good agreement, with a relative error of 3.98%.

The implemented statistical contact models were compared to the deterministic model by calculating contact area ratios and film thicknesses for three different rough surfaces. Generally, the statistical models significantly underestimated the contact area ratios for the whole range of contact pressures, and were not able to capture the full contact conditions when the material yield strength is reached. The conclusion was made that the statistical single asperity contact models should be avoided, both for the elastic and elastic–perfectly–plastic contact, in favour of deterministic contact model.

Next, the deterministic surface temperature model was validated against the exact analytical solutions of square and parabolic moving heat sources. The calculated surface temperature increase showed excellent agreement with the exact analytical solutions given by Tian and Kennedy [5].

Finally, a cumulative validation of the implemented models was carried out using numerical simulations of lubricated point contacts. The surfaces in contact considered in the simulations were surfaces of rotating ball and disc, which are the two main parts of the ball–on–disc tribometer apparatus. Two sets of simulations were conducted: simulations of hydrodynamic lubrication regime between a smooth ball and a smooth disc using Turbo T9 oil, and simulations of hydrodynamic and mixed regime between a rough ball and a smooth disc using Turbo T68 oil.

First, hydrodynamic simulations using T9 oil were presented. Calculations of minimum and central film thickness were performed for pure rolling contacts between a smooth sapphire disc and smooth steel ball for a range of entrainment speeds and two contact loads, 23 and 95 N. The results were compared with the measurements performed by Habchi et al. [10], where the authors used a ball–on–disc tribometer for measuring film thickness and friction coefficients. For the contact load of 23 N the mean relative deviations were 2.3% (minimum film thickness) and 3.0% (central film thickness), while for the contact load of 95 N the relative deviations were 13.6% and 7.8%. Calculations of friction coefficients

were performed between between steel disc and steel ball for a range of slide–to–roll ratios, two entrainment speeds (0.8 and 2 m/s) and two contact loads (38 and 154 N). The results were compared with the experimental measurements [10] and numerical calculations performed by Habchi et al. [10] and showed very good agreement with both. For the first case (38N, 0.8 m/s) the average relative deviation of friction coefficients were 0.8% from the numerical results and 7.4% from the experimental measurements, while for the second case (38 N, 2 m/s) the relative deviations were 5.9% and 11.2%, respectively. For the third case (154 N, 0.8 m/s) relative deviations were 1.8% from the experiment and 5.7% from the numerical results, while for the fourth case (154N, 2 m/s) deviations were 3.1% and 5.0%, respectively. Larger relative deviations from numerical results by Habchi et al. [10] for cases with higher entrainment speeds were expected due to the assumptions of the parabolic temperature profile and a single average viscosity value across the film thickness in the current work. A mesh refinement study was conducted with respect to the friction coefficient values for three slide–to–roll ratios. Theoretical second–order accuracy was achieved with the largest uncertainty of 0.17%.

The second set of simulations considers a lubricated contact between a smooth glass disc and a rough steel ball using Turbo T68 oil. Three different longitudinal roughnesses of steel balls were analysed. Significantly less information was available regarding Turbo T68 transport properties, compared to the Turbo T9 oil. Simulations were conducted for three surface roughness profiles, where in one set of simulations measured roughness profiles were directly used as inputs, while in the other set of simulations the sine function approximations of roughness profiles were used. Two slide–to–roll ratios were analysed and a range of entrainment speeds. For higher entrainment speeds (above 0.7 m/s) the hydrodynamic lubrication regime was achieved, while for the lower speeds the mixed regime took place. Calculated friction coefficients were compared to the experimental measurements done by Guegan et al. [12], where the authors used a ball–on–disc tribometer for measuring friction coefficients. For roughness specimens 1 and 3 simulation results showed very good agreement with the experimental data, considering the lack of information regarding lubricant shear thinning effects, and temperature and pressure dependence of thermophysical properties. Using

measured roughness inputs gave better results compared to the friction coefficient values when sine function approximations were used. Friction coefficients resulting from simulations with roughness specimen 2 showed good agreement with the experimental data for higher entrainment speeds where there is no significant asperity contact, while for the lower speeds results significantly deviate from experimental measurements.

A possibility exists that the longitudinal roughness used for measuring friction coefficients under designation *Specimen 2* does not correspond to the ball for which specimen 2 roughness profile was given in [12]. Calculated contact area ratios were compared between measured roughness profiles and sine function approximations. Using a sine function resulted in up to 100% increase of contact area ratio, compared to the measured profiles. Lubricant temperatures reached 150° in areas close to the contacting asperities.

With respect to the presented results in the current chapter the lubricated contact model is considered verified and validated.

6. Application to Metal Forming

6.1. Introduction

In this chapter the developed numerical framework for calculating lubricated rough surface contact in metal forming analysis is presented. The framework consists of previously presented and validated models, where each of them is used for calculating different pieces of the rough surface contact. The framework is implemented as a contact boundary condition for the finite volume deformation solver implemented in `foam-extend`. The implementation is tested on two metal forming processes: wire drawing and wire rolling. Different contact conditions are tested, and the results are compared to the existing penalty contact model.

6.2. Numerical Implementation

In this section the numerical implementation of previously presented and validated models in the hyperelastoplastic finite volume deformation solver [22] is presented. Models were implemented in the form of a solid contact boundary condition [8] using the `foam-extend` framework. Implementation was done in two parts: pre–runtime and runtime.

During the pre–runtime procedure, i.e. before the start of a simulation, the required contact data of the considered rough surface is calculated. The surface roughness profile or a surface scan is used as an input, together with required material properties of the surfaces considered. First, a set of surface parameters, Eqs. 4.76 to 4.78, which characterise the roughness are determined. Next, contact pressure, area ratio and film thickness are calculated for a wide range of surface separations using a contact model, either deterministic or statistical. Surface parameters and material properties are used as inputs for the selected contact models. In case of a deterministic contact modelling a full surface profile or scan is used as an input. The calculated values are stored inside interpolation tables.

During the runtime, metal forming simulation, the solid body displacement equations [22] are solved for at least two solid bodies in contact using the finite volume discretisation. At each iteration the solid body contact boundary condition is evaluated. The contact between two finite volume boundaries (patches) is determined using the GGI interface [158]. Two or more patches, expected to be in contact, are allocated into their respective GGI zones, master and slave, at the beginning of the simulation. A finite area mesh is initialised over boundary patches included in the slave zone, where all calculations considering lubricated contact are performed (e.g. Reynolds equation, film temperature equation, etc.). The first step when evaluating a contact boundary condition is determining face distances between slave and master GGI zones. In order to increase numerical stability of the calculation face distance values are explicitly under–relaxed:

$$d_\mathrm{f} = \alpha \, d_\mathrm{f}^\mathrm{n} + (1 - \alpha) \, d_\mathrm{f}^\mathrm{o}, \tag{6.1}$$

where d_f is the face distance, α is the relaxation factor, superscript $^\mathrm{n}$ denotes current calculated values while $^\mathrm{o}$ denotes values from the previous iteration. Surface velocities are obtained directly from the displacement field calculated in the previous iteration. Face distances are then used for linearly interpolating contact pressures, area ratios and film thicknesses from pre–calculated tables. Afterwards, lubricant transport properties and flow factors are calculated using previous or initial values of the film pressure, temperature and shear stress. Next, the averaged Reynolds equation, Eq. 4.5, is solved and film density is obtained, from which the pressure is calculated using a selected pressure–density relation. The film energy equation, Eq. 4.53, is solved next. Using new values of hydrodynamic pressure and shear stress, total normal contact pressure and traction are calculated:

$$P_\mathrm{tot} = P_\mathrm{a} + (1 - A_\mathrm{r})P_\mathrm{f}, \tag{6.2}$$

$$\tau_\mathrm{tot} = \mu P_\mathrm{a} + (1 - A_\mathrm{r})\tau_\mathrm{f}, \tag{6.3}$$

where P_tot is the total normal pressure of the contact, P_a is the asperity contact pressure, P_f is the film hydrodynamic pressure, A_r is the contact area ratio, τ_tot is the total traction, and τ_f is the film shear stress. Note that P_tot and

τ_{tot} represent values specific to each contact face and not the integral values of the whole contact. Using the GGI interface, total pressures and tractions are interpolated from slave to master zone faces in a conservative manner. Next, solid body displacement equations [22] are solved. If the deformation residuals are below the selected threshold positions of mesh points are updated and the solver continues to the next timestep. If the deformation residuals are above the threshold only GGI zones' topography is updated to a new configuration, and all of the steps above are repeated. The flow chart of the described procedure is presented in Fig. 6.1.

6.3.   Numerical Examples

In this section the presented lubricated contact framework is applied to two types of metal forming simulations:

- wire drawing,

- wire rolling.

In case of wire drawing a total of 20 drawing speeds are analysed. In order to show applicability of the lubricated contact model on both two–dimensional and three–dimensional cases, two types of geometries are considered: two–dimensional axisymmetric and three–dimensional quarter–symmetric geometry. Mesh refinement study is conducted in order to determine the achieved accuracy in space. Analyses are conducted for three constant values of lubricant viscosity and for actual pressure– and temperature–dependent properties of the Turbo T9 oil. Resulting drawing forces are compared with values calculated using the penalty contact model.

In case of wire rolling simulations, two rolling speeds are examined using a quarter–symmetric geometry and three mesh densities. Lubricated contact conditions, i.e. viscosity settings, are the same as in the wire drawing simulations. Results are compared with the non–lubricated penalty contact model cases.
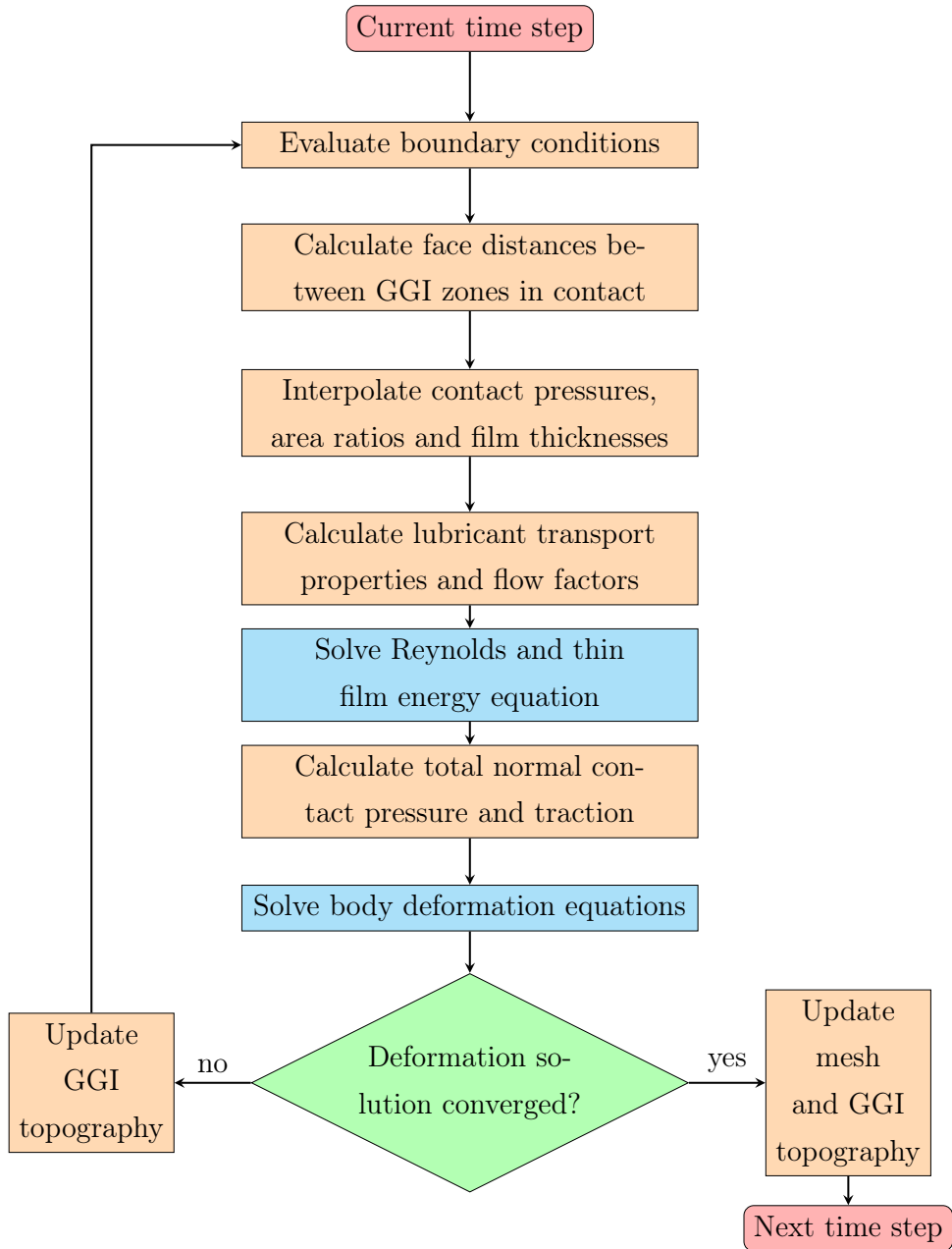
Figure 6.1: Flow chart of the lubricated contact calculation in metal forming solver.

6.3.1. Wire Drawing

In this section the lubricated contact model is applied to an isothermal wire drawing analysis. The geometry consists of a fixed die and moving wire, Fig. 6.2. The wire is pulled into the die, experiencing radial reduction and elongation in the narrowest part of the die inner cone. The area of contact between the wire and die is denoted in red in Fig. 6.3. The full geometry of the wire drawing analysis is approximated using two geometrical simplifications: axisymmetric and quarter–symmetric (Fig. 6.4), in order to reduce computational time. First, the axisymmetric cases are analysed.
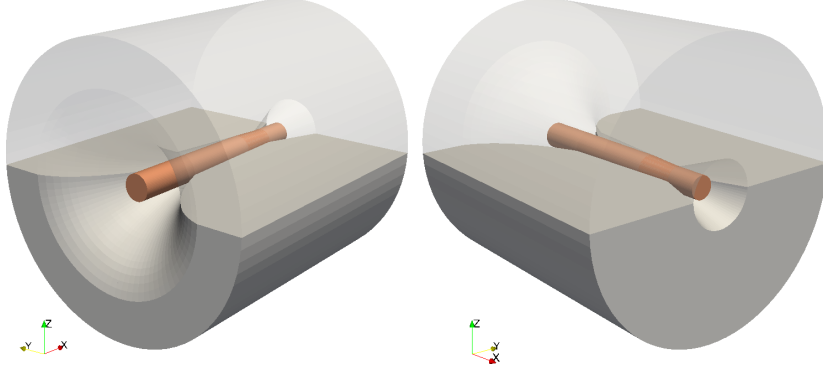

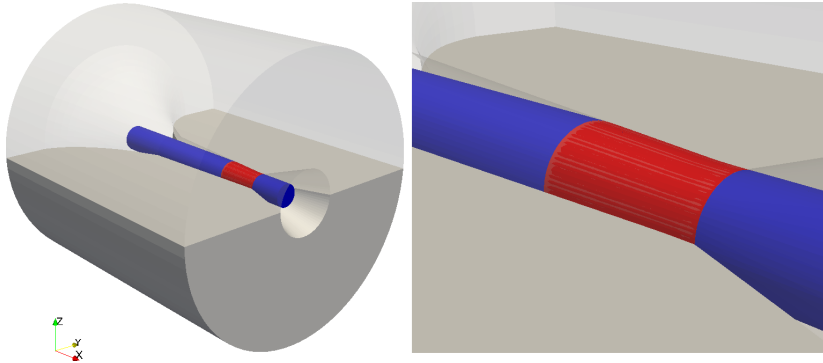Figure 6.2: Full wire drawing geometry.

Figure 6.3: Contact area (red) between the wire and the die.

Axisymmetric geometry consists of wire and die wedges, cut out from the full three–dimensional geometry. In all of the following simulations a 5° wedge angle is considered. The wire is 12 mm long with a diameter of 1.5 mm. The minimal inner diameter of the die is 1.3 mm, while the deformation angle is 6°.
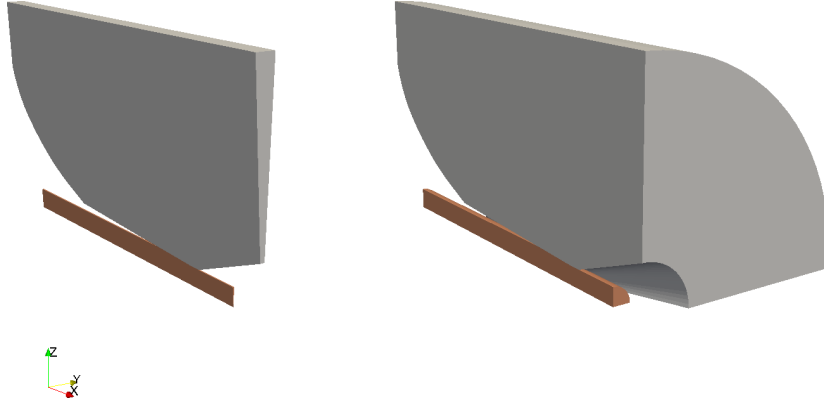
Figure 6.4: Axisymmetric (left) and quarter–symmetric (right) wire drawing geometry.

Material properties are specified in Table 6.1. Lubricant transport properties used here are of Turbo T9 oil. In addition to viscosity formulation used for T9 lubricant, Eq. 4.39, three cases with constant viscosity values (0.01, 0.1 and 1 Pa s) were considered in order to analyse the effects of different lubricant viscosities on simulation results. A constant Coulomb friction coefficient of 0.057 is assumed for characterising friction during boundary lubrication regime. Interpolation tables describing asperity contact were calculated for the given material properties and measured surfaces roughness profile depicted in Fig. 6.6.

Boundary conditions are specified in Table 6.2 and graphically presented in Fig. 6.5. The finite area mesh is initialised over the wire contact patch called `wireContact`. Several mesh densities were used, the one with 3 840 wire cells (240 finite area faces) and 1 058 die cells is shown in Fig. 6.7.

Each simulation is run for 150 timesteps, ensuring the convergence of friction force. Displacement field is updated inside a single timestep until the desired convergence is reached. The maximum number of displacement correctors per single timestep is limited to 1 000.

Wire drawing simulations were conducted for fourteen drawing speeds, ranging from 27 to 250 m/min. A comparison of friction forces between different contact conditions is given in Fig. 6.8. These values were calculated using a finite volume mesh with 1 058 die cells and 14 400 wire cells (480 finite area faces). Friction forces in case of penalty contact linearly decrease from 716 N (27 m/min) to 312 N (250 m/min). In case of the lubricated contact with Turbo

Table 6.1: Material properties of the wire and die.

Description	**Wire**	**Die**	Unit
Young's modulus	187	600	GPa
Poisson's ratio	0.3	0.24	–
Density	7 800	15 000	kg/m³
Initial yield stress	0.85	∞	GPa
Hardening of **wire**			
Plastic strain	0	0.29	–
Yield stress	0.85	1.20	GPa

Table 6.2: Boundary conditions used in axisymmetric wire drawing simulations.

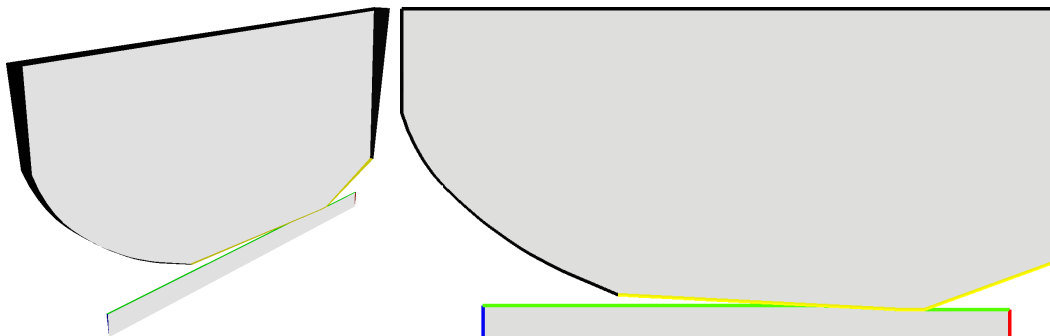| Name	Type	
wireDownstream	Fixed normal displacement velocity (drawing speed)	🟥
wireUpstream	Fixed traction (back tension)	🟦
wireContact	Fixed traction from contact model	🟩
dieContact	Fixed traction from contact model	🟨
dieFixed	Fixed zero displacement	⬛
frontAndBack	Wedge	⬜

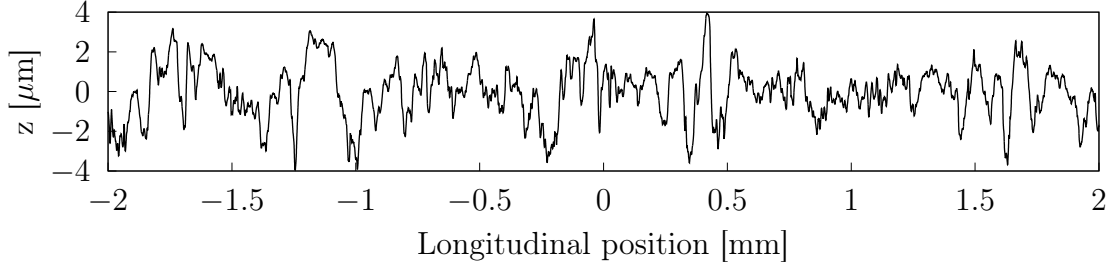Figure 6.5: With the definition of wire drawing boundary conditions [8].

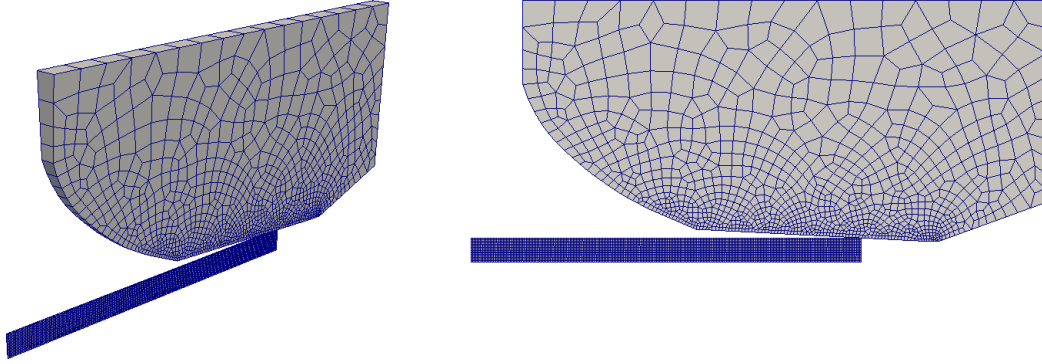Figure 6.6: Roughness profile used in wire drawing simulations.

Figure 6.7: One of the meshes used in wire drawing simulations.

T9 viscosity friction forces are slightly higher (around 2%) for the whole range of speeds, compared to the penalty contact. For cases with constant viscosity friction forces decrease with increasing lubricant viscosity. Viscosity of 0.01 Pa s gives results close to the penalty contact, with slightly lower friction forces (difference below 1%) and drawing speeds up to 100 m/min, and slightly higher forces (around 2%) above 100 m/min. For higher viscosities, friction forces are significantly lower in the whole range of drawing speeds compared to the penalty contact. Using a constant viscosity of 0.1 Pa s results in up to 8% decrease in friction force, while a constant viscosity of 1 Pa s results in up to 21% decrease compared to the penalty contact.

In Fig. 6.9 a comparison of calculated fields between three drawing speeds is presented. The maximum value of film hydrodynamic pressure is 1.2 GPa, and it is achieved at the lowest drawing speed of 44 m/min. These values are attained using viscosity properties of T9 oil. For all four lubricated contact conditions hydrodynamic pressure peaks are located at the inlet and at the outlet of the contact. Analysing the three cases with constant viscosity values, an increase of
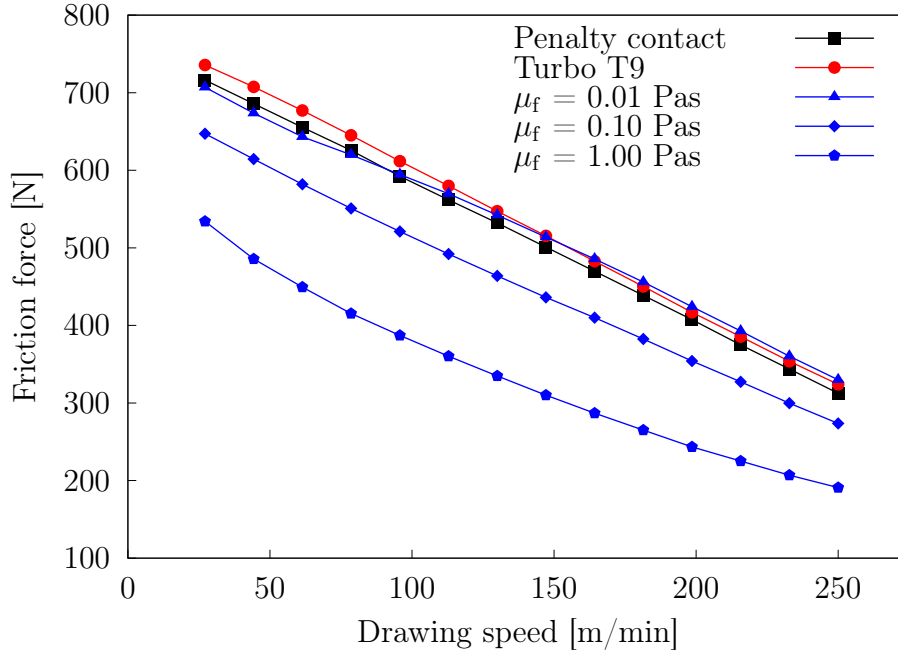
169

Figure 6.8: Comparison of friction forces calculated under different drawing speeds in axisymmetric drawing simulations.

viscosity results in higher hydrodynamic pressures, leading to larger film thicknesses, and consequently smaller contact pressures and contact area ratios. The film thickness increases at higher drawing speeds resulting in lower contact area ratios, hydrodynamic and asperity pressures. The maximum values of asperity contact pressure and contact area ratio are 0.6 GPa and 72%, respectively, both achieved at the lowest drawing speed using a constant viscosity of 0.01 Pa s. The full hydrodynamic regime is reached at 216 m/min using a constant viscosity of 1 Pa s. The film thickness ranges from 0.2 μm at the lowest speed and viscosity, up to 4 μm at the highest speed and viscosity value. Field values calculated using T9 oil properties are generally positioned between the results of simulations with 0.01 and 0.1 Pa s viscosities.

An interesting phenomenon can be observed comparing T9 with 1 Pa s cases, especially at the lowest drawing speed. A high pressure peak at the inlet is followed by a sudden pressure drop inside the contact. This pressure drop is larger when using T9 properties, compared to a constant viscosity of 1 Pa s, even though viscosity values of T9 oil inside the contact are higher (above 1 Pa s)

and film thickness at the same time is significantly smaller. One of the factors leading to larger pressure drop is relative increase in film thickness following the inlet part of the contact. This increase is more pronounced in cases of T9 oil and 0.01 Pa s viscosity, than in the case of 1 Pa s. Considering high values of viscosity of T9 oil inside the contact (above 1 Pa s) and relatively small initial value (0.011 Pa s) at the atmospheric pressure, it is concluded that a very important factor influencing the pressure drop, and thus load carrying capabilities, is the value of viscosity at the atmospheric conditions.

In order to calculate the achieved accuracy in space mesh convergence study was performed for the axisymmetric wire drawing case under a drawing speed of 79 m/min using a lubricated contact model with T9 transport properties. The study was performed systematically using nine mesh densities, and with respect to the friction force value. The test matrix is shown in Table 6.3. Uncertainty and error estimation was performed using the freely available code [156] based on the procedures suggested by Eça and Hoekstra [157].

Results of the analysis are presented in Fig. 6.10 and Table 6.4, where ϕ_0 is the extrapolated exact solution, ϕ_1 is the finest level solution, U_ϕ is the estimated uncertainty and p is the achieved accuracy in space. The results show that a second–order accuracy is achieved ($p = 1.89$), with the friction force uncertainty of 0.31%.

Table 6.3: Test matrix for the uncertainty analysis of an axisymmetric wire drawing case.

Wire cells	32	60	136	240	480	960	1 968	3 840	7 656
Die cells	36	66	147	281	537	1 058	2 178	4 133	8 390
Total cells	68	126	283	521	1 017	2 018	4 146	7 973	16 046
Friction force [N]	638.7	635.1	628.6	628.2	627.4	627.1	625.7	627.1	627.4

Table 6.4: Results of the uncertainty analysis for an axisymmetric wire drawing case.

Element	ϕ_0 [–]	ϕ_1 [–]	U_ϕ [%]	p [–]
$F_{\mathrm{f}}[N]$	626.5	627.4	0.31	1.89

In addition to the uncertainty analysis, a supplementary study is conducted in order to analyse the effect of the finite area mesh density on hydrodynamic
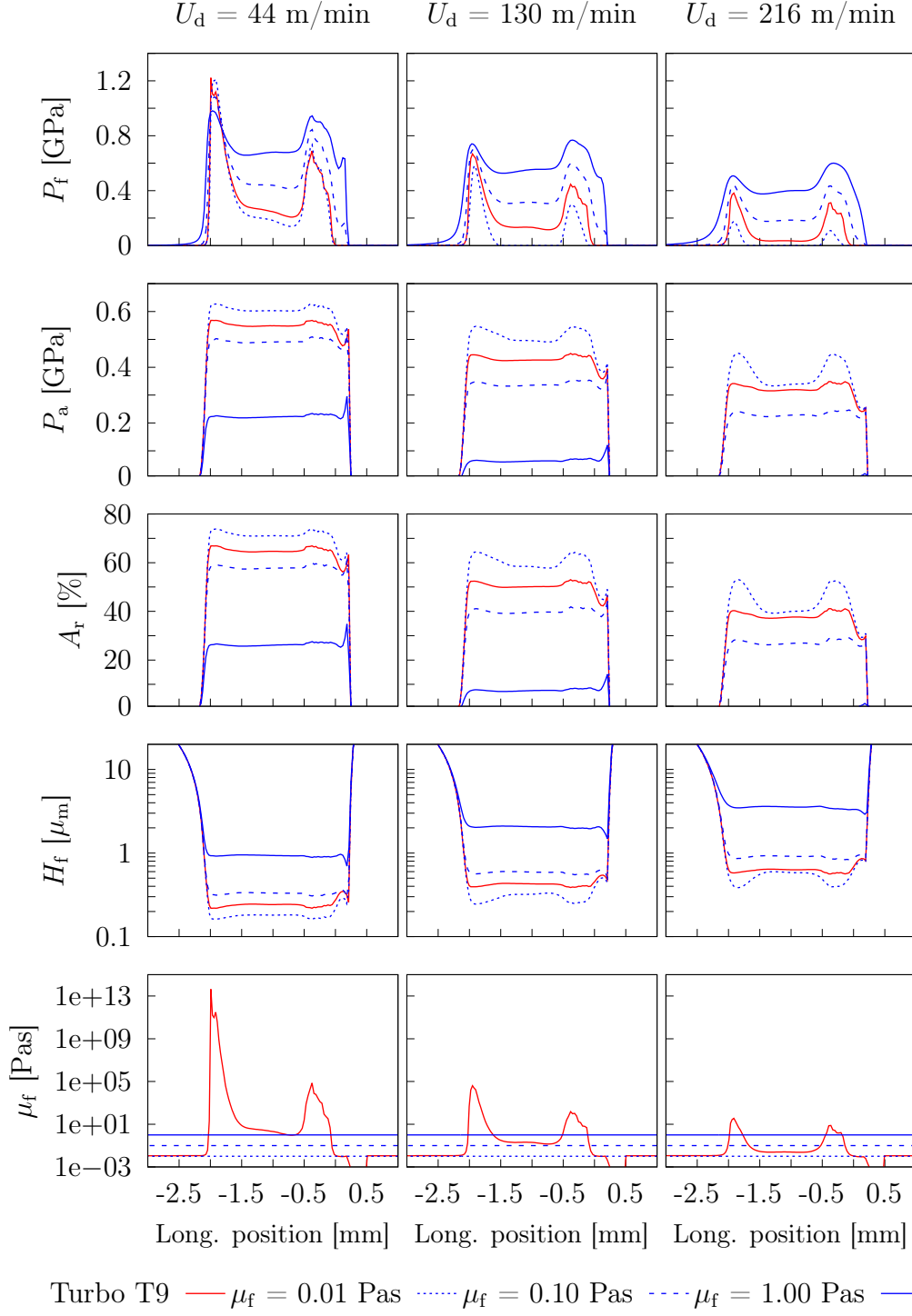
Figure 6.9: Comparison of calculated fields under three drawing speeds for axisymmetric drawing simulations. P_f – hydrodynamic pressure; P_a – asperity contact pressure; A_r – asperity contact ratio; H_f – film thickness; μ_f – film viscosity.
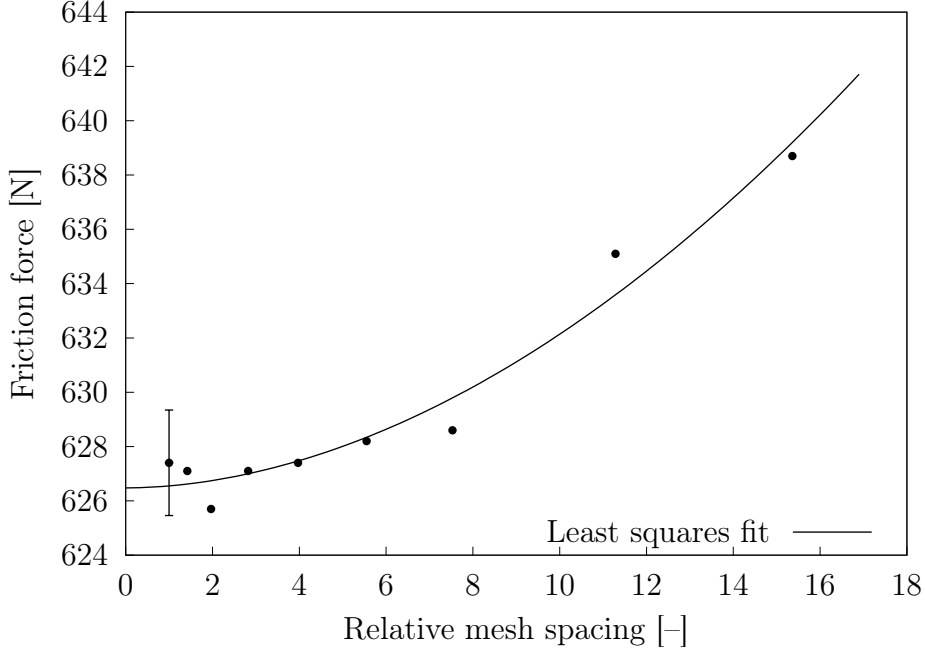
Figure 6.10: Friction forces calculated with different mesh spacings for the axisymmetric wire drawing case. Uncertainty estimate U_ϕ (Table 6.4) is depicted for the finest mesh result.

pressure. In this study the pressure profiles calculated using four additional meshes are compared. In each mesh the number of cells inside the die is constant and equal to 16 336, while the number of cells inside the wire varies: 3 840 cells (240 finite area faces), 14 400 cells (480 faces), 33 120 cells (720 faces) and 57 600 cells (960 faces).

The results of the hydrodynamic pressure for all four meshes and three drawing speeds are presented in Fig. 6.11. The two finest finite area meshes, with 720 and 960 faces, give almost identical results for all three drawing speeds. The mesh with 480 faces shows a very good agreement with finer meshes, however underpredictions of hydrodynamic pressure are visible at the centre of the contact. Using the coarsest mesh, 240 faces, results in significant deviation of pressure compared to the fine meshes.

In Fig. 6.12 a comparison of computational time required for performing axisymmetric drawing simulations between the five contact conditions is presented. All simulations were executed using a single 3.7 GHz CPU core. Computational time required for performing a single simulation using the penalty contact model
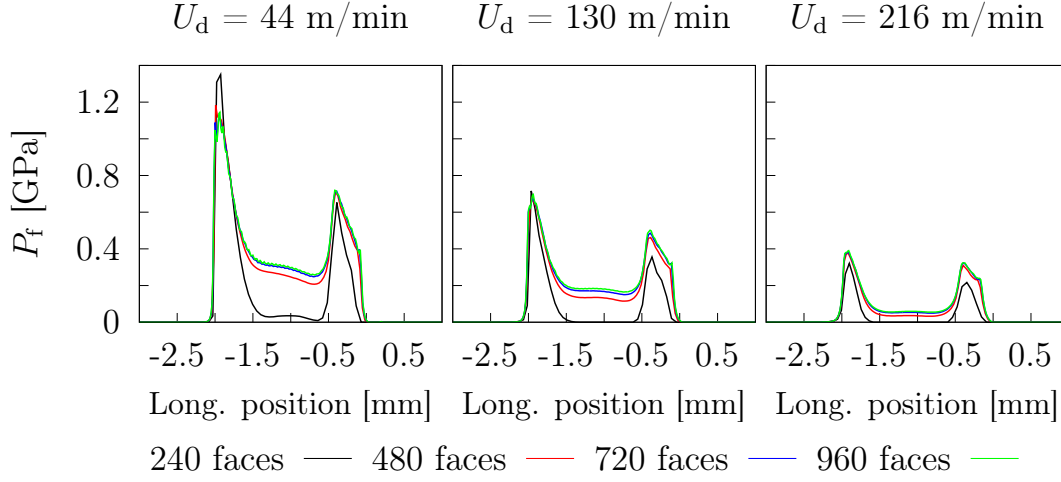
Figure 6.11: Hydrodynamic pressures calculated for four axisymmetric wire mesh densities and three drawing speeds U_d.

is between 5 000 and 6 000 s, depending on drawing speed. Using a lubricated contact model the CPU time increases from 25 to 60%, depending on the selected drawing speed. The average increase in CPU time across the whole range of drawing speeds is 38%. The largest relative difference of 60% between computational times occurs in case of the lowest drawing speed. All four lubricated contact conditions require similar computational times, with relative differences below 10%. Using a constant lubricant viscosity has no apparent efficiency gains compared to the T9 viscosity model. Considering additional calculations and non–linearities introduced into the system by the lubricated contact model an average increase of computational time by 38%, in comparison with the penalty contact, is acceptable.

In order to examine the stability of the lubricated contact model a comparison of the average number of displacement correctors per single timestep is given in Fig. 6.13. The average number of correctors in simulations using the penalty contact model ranges from 400 to 450, depending on the drawing speed. All four viscosity settings of the lubricated contact result in similar number of correctors, with relative differences under 10%. Using lubricated contact model requires from 410 to 610 displacement correctors per timestep, in average. The maximum relative increase of number of correctors when using the lubricated contact model is 32% at the drawing speed of 27 m/min, while the average increase is 10%.
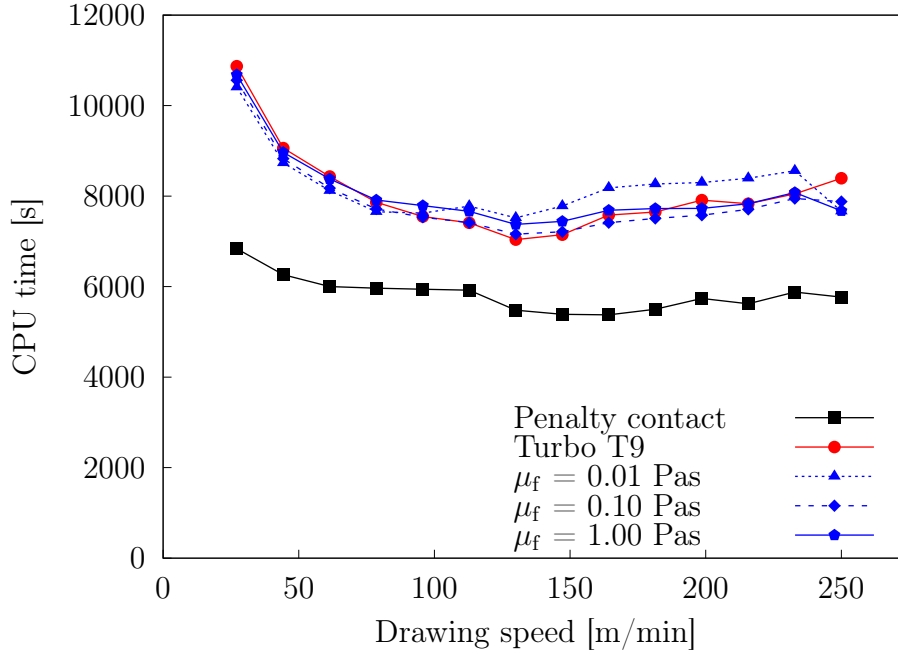
Figure 6.12: Comparison of CPU times between contact conditions for axisymmetric drawing simulations.

Considering the non–linearities introduced into the system this average increase is acceptable, i.e. the lubricated contact model can be considered fairly stable.

In order to test the applicability of the implemented model on a three–dimensional geometry quarter–symmetric simulations were conducted for three drawing speeds. A single mesh was used, consisting of 215 040 cells (7 680 finite area faces) inside the wire and 21 160 cells inside the die, Fig. 6.14. Considering the number of cells in the axial direction, this mesh corresponds to the axisymmetric mesh consisting of 14 400 cells (480 finite area faces) inside the wire and 1 058 cells inside the die. The boundary conditions are the same as in the axisymmetric case, with the only difference being symmetry boundary conditions instead of wedge.

The calculated hydrodynamic pressures for three drawing speeds are sampled along the three lines (0°, 45° and 90° angle) shown in Fig. 6.14. Sampled values are compared to the axisymmetric results in Fig. 6.15. All three quarter–symmetric pressure curves are very similar, suggesting that there are no significant pressure variations of the lubricant in the radial direction. Compar-
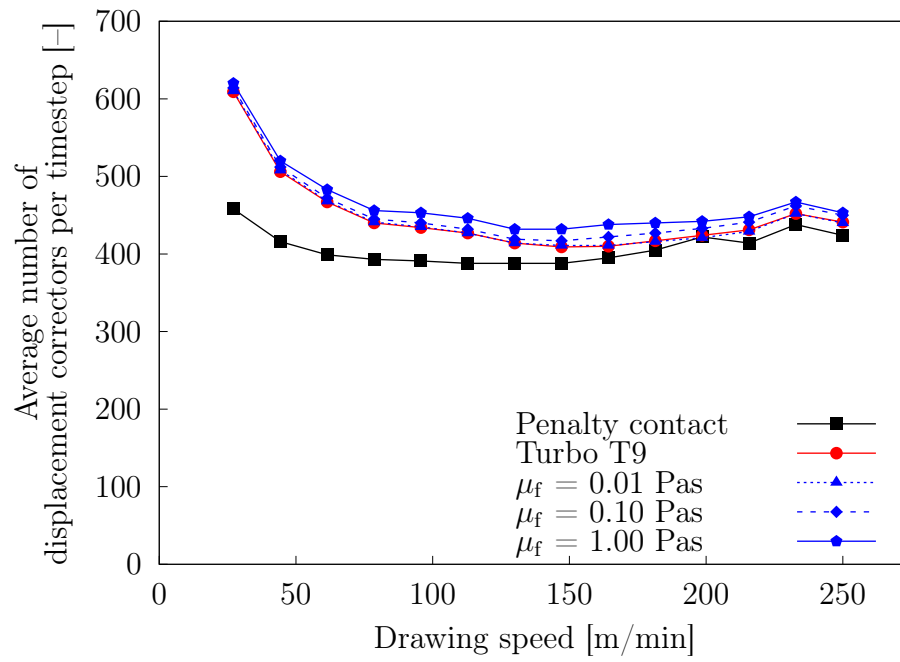
Figure 6.13: Comparison of the average number of displacement correctors per timestep for axisymmetric drawing simulations.
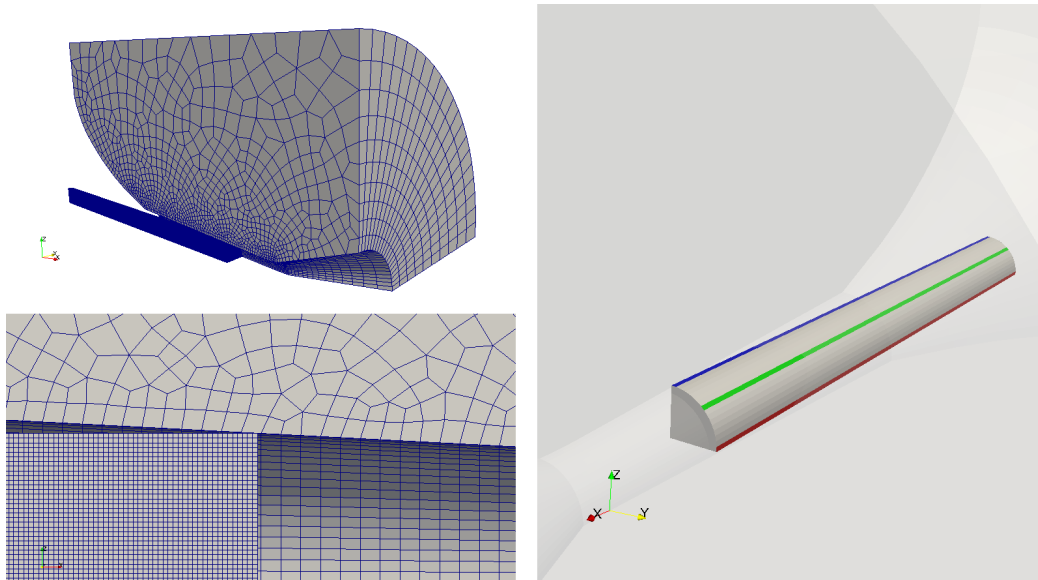

Figure 6.14: Quarter wire drawing mesh (left) and sampling lines (right).

ison to the axisymmetric results shows a very good agreement in the majority of the contact area, except at the inlet and outlet where axisymmetric simulations predict larger pressure peaks. Since axisymmetric mesh considers a single row of cells in the radial direction with two wedge boundary conditions, while quarter–symmetric mesh has 16 rows of cells with two symmetry boundary conditions where three–dimensional effects are taken into account, small differences are expected between the results.

A comparison of friction forces and computational time between axisymmetric and quarter–symmetric simulations are given in Table 6.5. All six simulations were performed using a single 3.7 GHz CPU core. The difference between values of friction forces are under 1% for all three drawing speeds, with quarter–symmetric calculations requiring 15 times more computational time than axisymmetric simulations.
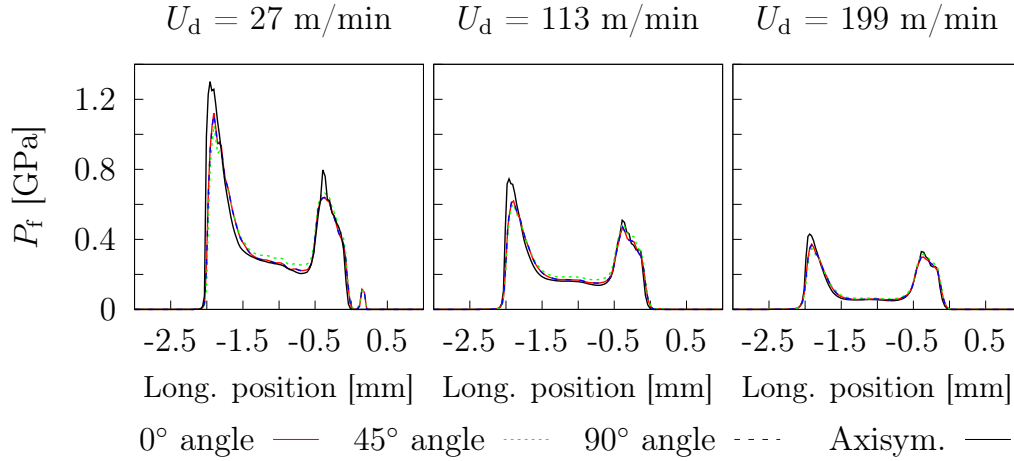
Figure 6.15: Comparison of hydrodynamic pressures P_f calculated using quarter–symmetric and axisymmetric geometries for three drawing speeds U_d.

Table 6.5: Comparison between axisymmetric and quarter–symmetric wire drawing results.

Drawing speed	Friction force [N]			Computational time [s]	
[m/min]	Axi	Quarter	Δ	Axi	Quarter
27	735.7	730.5	0.7%	5 435	84 648
113	579.9	576.7	0.6%	8 449	127 403
199	416.9	415.5	0.3%	8 650	123 909

6.3.2. Wire Rolling

In this section the lubricated contact model is applied to an isothermal wire rolling analysis. The geometry consists of two rotating rollers and one moving wire, Fig. 6.16. The wire is pulled between the rollers, where its shape is changed as it passes through. The full geometry in the analysis is approximated using a quarter–symmetric simplification, where half of the upper roller and quarter of the wire are considered.
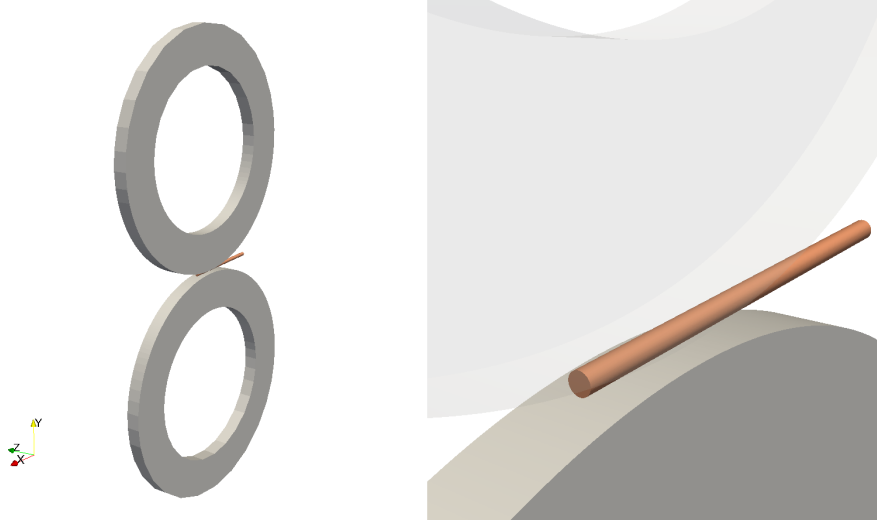
Figure 6.16: Full wire rolling geometry.

The wire is 60 mm long with a diameter of 2.71 mm. The roller is 10 mm wide with an outer radius of 178 mm and inner radius of 120 mm. The final reduction of the wire diameter is 30% in the direction orthogonal to the roller surface in contact. Material properties are specified in Table 6.6.

Lubricant transport properties and viscosity settings are the same as in the wire drawing simulations in the previous section. A Coulomb–Orowan friction law is used for characterising friction during boundary lubrication regime. A constant friction coefficient is set to 0.057 with a limiting shear stress of 1.5 GPa. Interpolation tables describing asperity contact were calculated for the given material properties and measured surfaces roughness profile depicted in Fig. 6.6.

Boundary conditions are specified in Table 6.7 and graphically presented in Fig. 6.17. The finite area mesh is initialised over the wire contact patch called

`wireContact`. Three computational meshes are used in this analysis, where mesh of the wire is systematically refined with regards to the number of finite area faces. Information considering the meshes is given in Table 6.8, with the coarsest mesh (Mesh 1) shown in Fig. 6.18. The analysis is conducted for two angular velocities, 150 and 300 rpm.

Table 6.6: Material properties of the wire and the roller.

Description	**Wire**	**Die**	Unit
Young's modulus	210	210	GPa
Poisson's ratio	0.3	0.3	–
Density	7 800	7 800	kg/m^3
Initial yield stress	1.3	∞	GPa
Hardening of **wire**			
Plastic strain	0.0 0.01 0.10 0.50 0.88		–
Yield stress	1.3 1.50 1.69 1.64 2.11		GPa

Table 6.7: Boundary conditions used in wire rolling simulations.

Name	Type	
`wireDownstream`	Fixed traction (front tension)	🟥
`wireUpstream`	Fixed traction (back tension)	🟦
`wireContact`	Fixed traction from contact model	🟩
`wireSymmetry`	Symmetry	⬛
`rollerContact`	Fixed traction from contact model	🟨
`rollerAxis`	Fixed displacement velocity (angular velocity)	⬛
`rollerSide`	Fixed zero traction	🟦
`rollerSymmetry`	Symmetry	⬛

In Fig. 6.20 a comparison of hydrodynamic pressures calculated using different viscosity settings for three mesh densities is presented. Two angular velocities of the roller are considered, where the left half of the wire represents a hydrodynamic pressure field calculated using an angular velocity of 150 rpm, while the right half represents a field calculated using an angular velocity of 300 rpm. The

Figure 6.17: With the definition of wire rolling boundary conditions.

Table 6.8: Description of meshes used in wire rolling simulations.

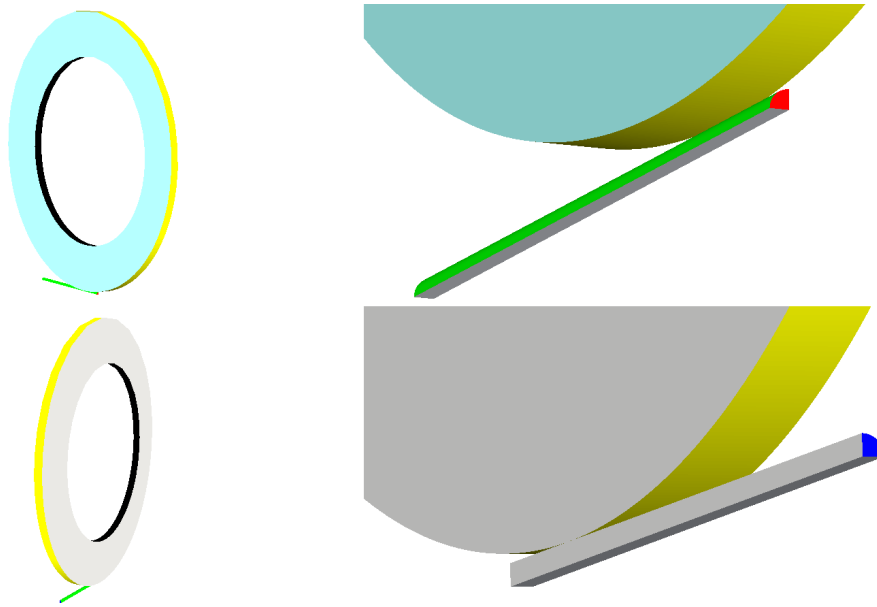| Name	Number of cells		Number of FA faces
	Roller	Wire	
Mesh 1	57 200	30 720	2 560
Mesh 2	57 200	99 792	5 544
Mesh 3	57 200	245 760	10 240
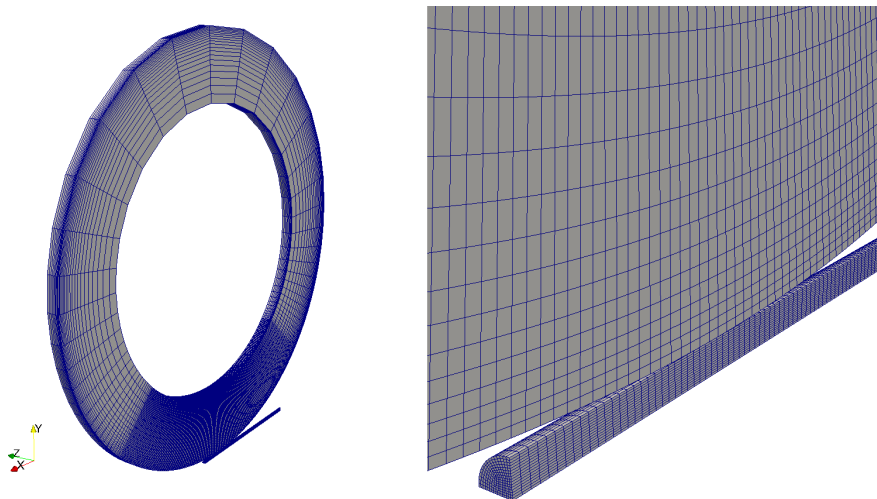
Figure 6.18: The coarsest mesh used in wire rolling simulation.

high pressure area (above 0.1 GPa) for all the cases is dominantly located at the position of the roll bite, Fig. 6.19. Inside the contact a significant pressure increase (around 1.5 GPa) can be noticed at the centre of the wire, next to the symmetry plane, only for the finest mesh (Mesh 3) and the angular velocity of 300 rpm. Hydrodynamic pressure field has a horseshoe shape, characteristic for contact pressures in wire rolling, which was also exhibited in previous analyses [22]. Hydrodynamic pressure at the sides of the contact goes up to 1 MPa, which is significantly lower compared to the pressure at the roll bite (up to 2 GPa). Similar to the wire drawing case, a constant viscosity of 0.01 Pa s gives almost the same results as the T9 viscosity settings. Increase of the area of high pressure follows the increase of both viscosity and rolling speed. The angular velocity of 300 rpm, compared to 150 rpm, results in higher pressures and larger high pressure areas for all three mesh densities and viscosity settings, which is expected. Higher values of viscosity in case of the finest mesh (Mesh 3) result in pressure increase inside the contact, next to the symmetry plane.
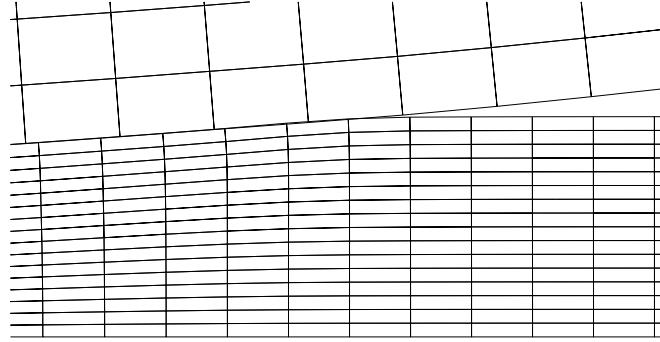
Figure 6.19: Roll bite.

In Fig. 6.21 a comparison of asperity contact pressures for two meshes and three contact conditions is presented. Note that in the case of penalty contact model there is only one contact pressure, thus it is presented here as an asperity contact pressure. The penalty contact model results in, approximately, 50% lower contact pressures inside the contact compared to the lubricated contact model. In case of the coarsest mesh (Mesh 1) high pressure areas near the roll bite have similar shapes and values for all three contact conditions. This is expected since the hydrodynamic pressure calculated using Mesh 1 is significantly lower

compared to the finer meshes (Fig. 6.20) especially for the angular velocity of 150 rpm. A slightly larger high pressure areas are exhibited at 300 rpm, compared to the lower velocity. Due to high hydrodynamic pressures at the roll bite and next to the symmetry plane, when considering the finest mesh (Mesh 3) and velocity of 300 rpm, the asperity contact pressures are significantly lower (up to 75%) in those areas of the contact.

In Fig. 6.22 a comparison of local friction coefficients is presented. The local friction coefficients are calculated by dividing the magnitude of tangential traction with the value of normal contact pressure for every contact face. The high friction region (coefficients above 0.05) is longer in the case of higher velocity (300 rpm) for each contact condition. The area of low slip conditions, and thus low friction coefficients, is located close to the exit of the contact. That area is larger and more noticeable in case of the penalty contact. Comparing lubricated contact results, the low slip area is larger and friction coefficients are lower (up to 50%) for higher angular velocity (300 rpm). In case of the penalty contact the situation is reversed, i.e. the low slip area is more dominant for the lower velocity. In case of the finest mesh (Mesh 3) and a constant viscosity of 1 Pa s low values of friction coefficients (approximately 0.03) are noticed next to the symmetry plane. This is expected due to high hydrodynamic and low asperity contact pressures in that area.

In Table 6.9 torque values of the roller calculated around the rotation axis are given for four contact conditions and three mesh densities. Using the lubricated contact model results in higher torque, up to 1.4%, compared to the penalty contact. This is expected since the areas of high hydrodynamic pressures are too small to carry significant portions of the contact load which would reduce the friction force, and consequently roller torque.

What causes the small increase of the torque, compared to the penalty contact, is the hydrodynamic pressure and shear stress at the roll bite, acting as additional resistance. If a significant hydrodynamic pressure field would form inside the contact the torque would eventually decrease below the values calculated using penalty contact. This kind of load carrying hydrodynamic pressure field forms in the drawing cases presented in the previous section, where for the higher drawing speeds and lubricant viscosities the friction coefficient is signif-

icantly smaller compared to the values calculated using penalty contact. Note that the same friction coefficient used in the penalty contact is used as a boundary lubrication friction coefficient when using the lubricated contact model. Thus, the penalty contact cases analysed here do not consider dry–friction conditions, rather pure boundary lubrication conditions.

The values of torque calculated using the finest mesh (Mesh 3) and lubricated contact model decrease (from 87.6 to 87.1 Nm) as the value of viscosity increases for the higher angular velocity (300 rpm), while for the lower velocity (150 rpm) the values of torque remain the same (87.5 Nm). The decrease of torque under higher velocity is due to an increase of hydrodynamic pressure next to the symmetry plane resulting in lubricant carrying more contact load and ultimately decreasing friction force, Figs. 6.20 and 6.22.

In Table 6.10 computational times required for performing wire rolling simulations are given. All simulations were conducted using 8 CPU cores of 3.5 GHz. Simulations with lower angular velocity (150 rpm) were run for 400 timesteps, while simulations with 300 rpm were run for 200 timesteps. The fastest simulation (Mesh 1, 300 rpm, penalty contact) ran for 2 861 seconds (47 minutes), while the slowest one (Mesh 3, 150 rpm, T9) ran for 27 198 seconds (7.5 hours). For the coarsest mesh (Mesh 1) using lubricated contact model increases CPU time from 35 to 60% compared to the penalty contact model. Using higher values of viscosity results in lower increase in CPU time. For the finest mesh (Mesh 3) lubricated contact model with constant viscosities of 0.1 and 1 Pa s is slightly faster than the penalty contact model. Overall, the average increase of compuational time when using lubricated contact model is 33%, which is in accordance with the wire drawing cases.

In order to determine the stability of lubricated contact model, compared to the penalty contact, the average number of displacement correctors per timestep is presented in Table 6.11. Interestingly, all the cases in which the finest mesh (Mesh 3) is used require up to 27% less displacement correctors compared to the penalty contact. This suggests that in the case of wire rolling simulations when very fine meshes are used the lubricated contact model is more stable than the penalty contact model. The largest increase of the number of correctors is 19%, for roller angular velocity of 150 rpm, medium mesh (Mesh 2) and T9 contact

conditions. When all the cases are considered, the average decrease in number of displacement correctors is 4%. Therefore, the lubricated contact model may be considered slightly more stable than the penalty contact model in this case.

Table 6.9: Roller torque calculated around the rotation axis. Torque values are specified in [Nm].

	Penalty		T9		$\mu_\mathrm{f} = 0.01\,\mathrm{Pa\,s}$		$\mu_\mathrm{f}\,0.1 = \mathrm{Pa\,s}$		$\mu_\mathrm{f} = 1\,\mathrm{Pa\,s}$	
rpm	150	300	150	300	150	300	150	300	150	300
Mesh 1	85.5	85.3	86.1	86.4	86.1	86.4	86.1	86.4	86.2	86.4
Mesh 2	86.4	86.3	87.4	87.3	87.4	87.3	87.4	87.3	87.4	87.2
Mesh 3	86.6	86.4	87.5	87.6	87.5	87.4	87.5	87.3	87.5	87.1

Table 6.10: Computational time required for performing wire rolling simulations using 8 CPU cores of 3.5 GHz. Computational time is expressed in [s].

	Penalty		T9		$\mu_\mathrm{f} = 0.01\,\mathrm{Pa\,s}$		$\mu_\mathrm{f} = 0.1\,\mathrm{Pa\,s}$		$\mu_\mathrm{f} = 1\,\mathrm{Pa\,s}$	
rpm	150	300	150	300	150	300	150	300	150	300
Mesh 1	2 861	2 161	4 616	3 692	4 193	3 301	4 010	3 155	3 876	3 055
Mesh 2	7 180	6 145	11 924	9 572	10 433	7 281	9 480	7 251	9 043	7 184
Mesh 3	19 662	17 297	27 198	22 260	26 787	18 270	23 162	17 277	19 107	17 096

Table 6.11: The average number of displacement correctors per timestep for wire rolling simulations.

	Penalty		T9		$\mu_\mathrm{f} = 0.01\,\mathrm{Pa\,s}$		$\mu_\mathrm{f} = 0.1\,\mathrm{Pa\,s}$		$\mu_\mathrm{f} = 1\,\mathrm{Pa\,s}$	
rpm	150	300	150	300	150	300	150	300	150	300
Mesh 1	228	265	236	260	236	259	236	267	236	259
Mesh 2	235	379	280	354	266	309	267	306	265	299
Mesh 3	314	495	304	418	302	371	301	367	299	361
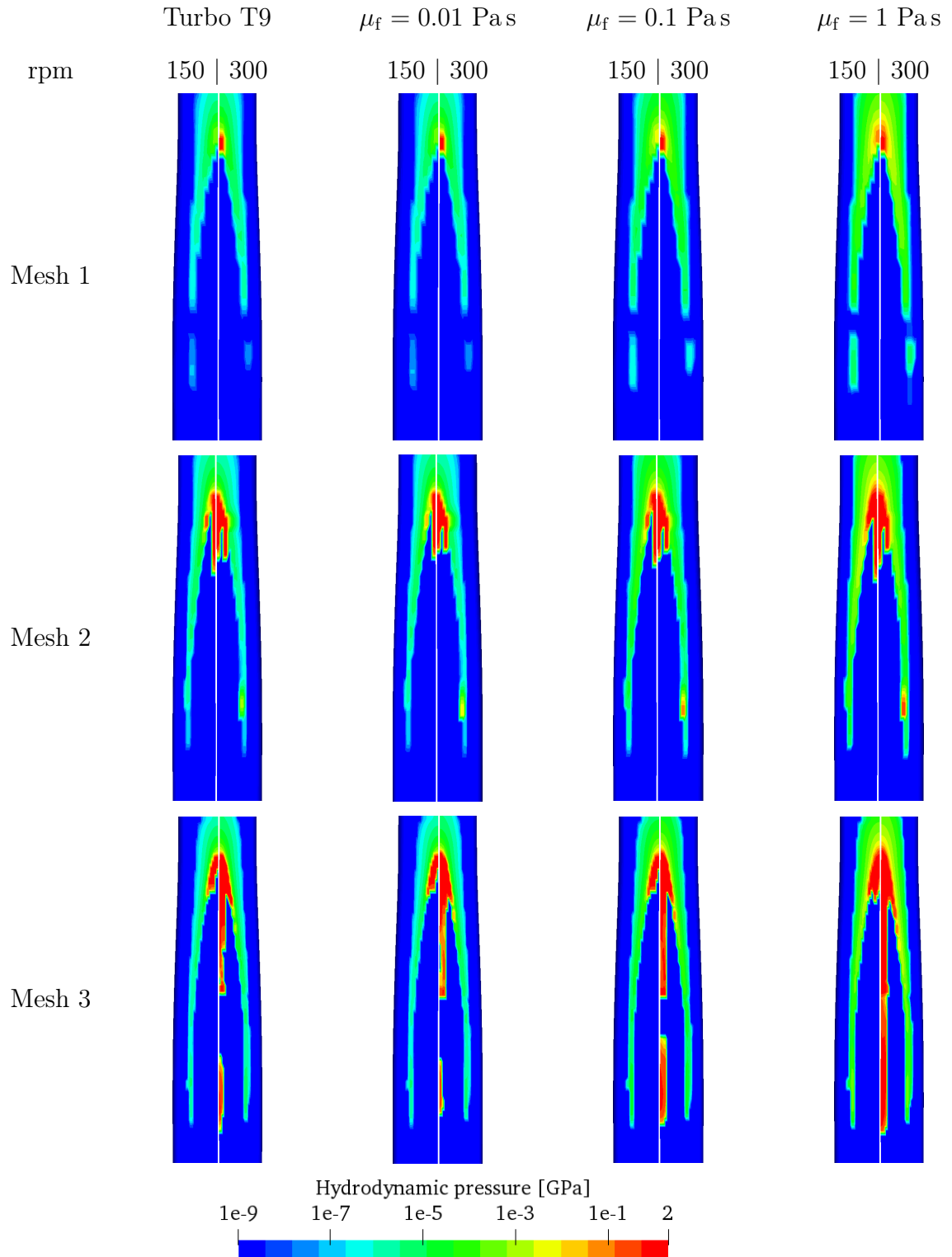
Figure 6.20: Hydrodynamic pressures calculated using different viscosity settings and three mesh densities for the wire rolling case.

Figure 6.21: Asperity contact pressure calculated using penalty contact model and lubricated contact model with different viscosity settings and two mesh densities for the wire rolling case.

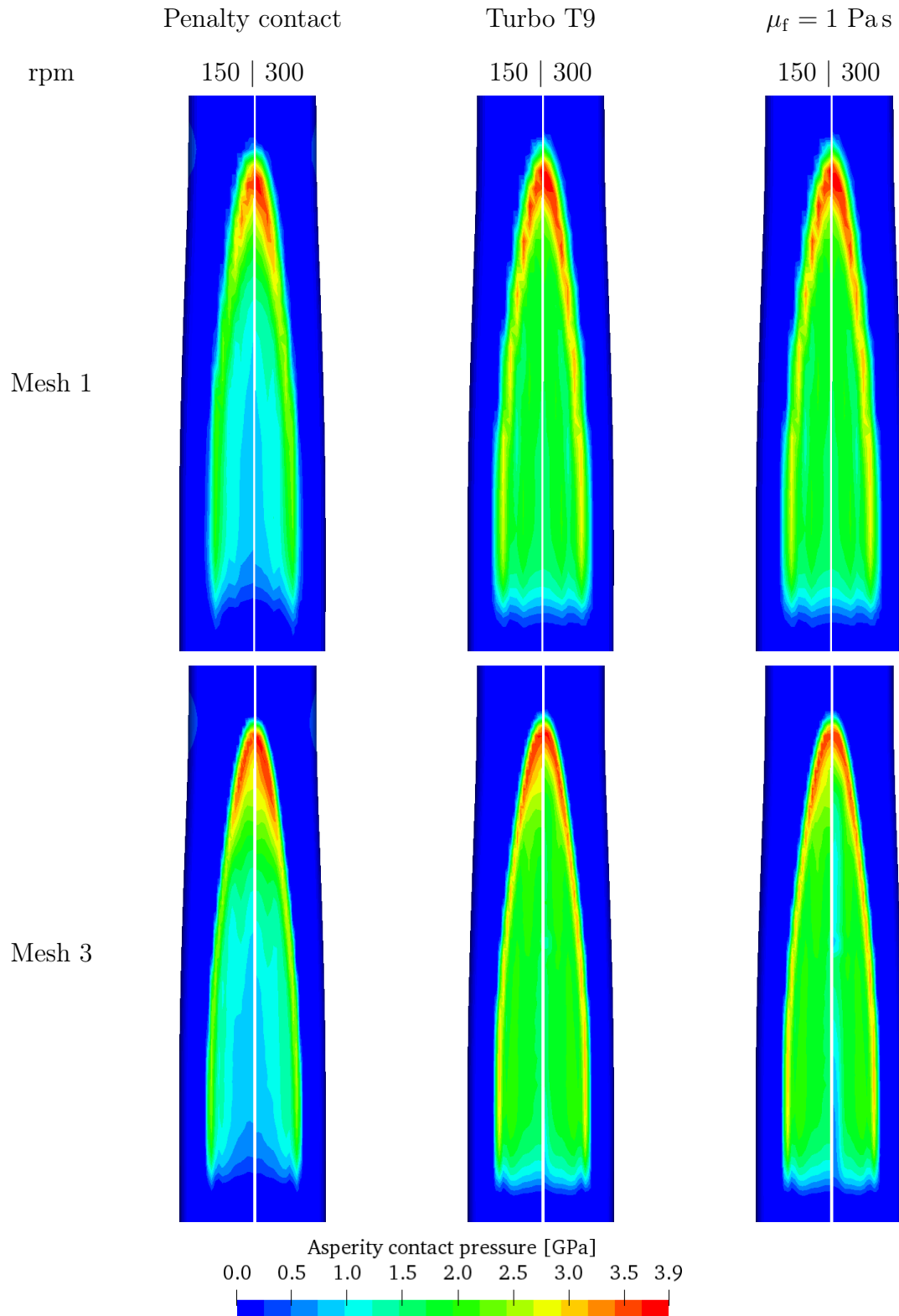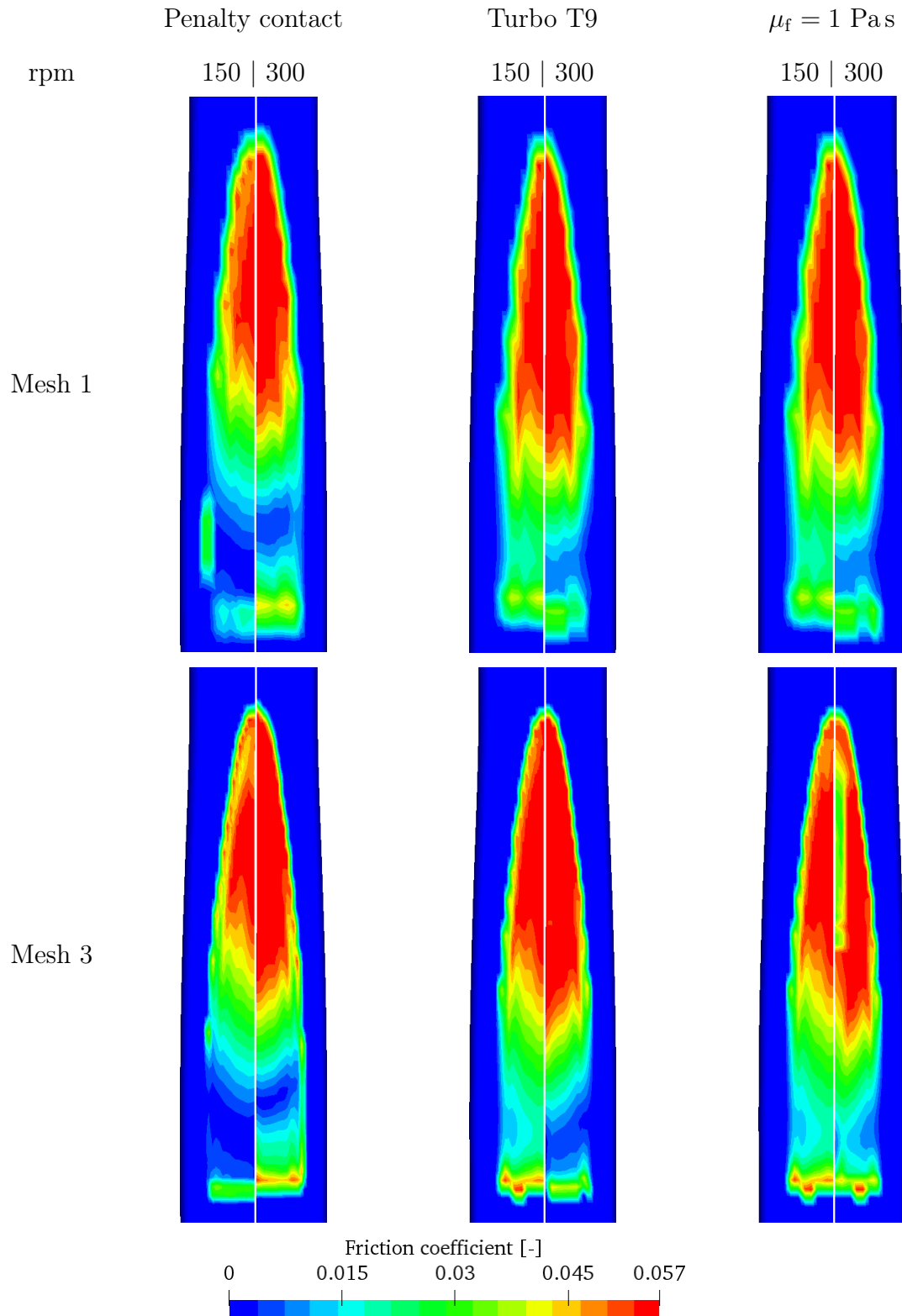Figure 6.22: Local friction coefficients calculated using penalty contact model and lubricated contact model with different viscosity settings and two mesh densities for the wire rolling case.

6.4. Conclusion

In this chapter the numerical framework for calculating lubricated rough surface contact in metal forming analysis was presented. The framework was implemented as a contact boundary condition for the hyperelastoplastic finite volume deformation solver. The implementation was done in two parts: pre–runtime and runtime. During the pre–runtime process the selected surface roughness profile is analysed, and deterministic contact model is used for calculating contact pressures, area ratios and film thicknesses for a range of nominal surface separations. The calculated values, stored in the form of interpolation tables, are used later in the runtime.

During the metal forming simulation, every time the contact boundary condition is evaluated the lubrication framework is executed. Depending on the normal distances between two surfaces contact pressures, area ratios and film thicknesses are interpolated using the pre–calculated tables. Lubricant transport properties are calculated and the Reynolds equation is solved. Calculated normal and tangential surface tractions are sent back to the deformation solver. The process is repeated until the desired convergence is reached.

The implemented framework is tested on two types of metal forming processes: wire drawing and wire rolling. Wire drawing simulations were conducted using both axisymmetric and quarter–symmetric geometries. Several drawing speeds and contact conditions were examined. For higher lubricant viscosities and wire drawing speeds the lubricant carries more contact load, resulting in the reduction of the friction force. Using finer meshes results in smaller pressure drops inside the contact. The convergence of the hydrodynamic pressure profile was achieved by refining the wire mesh. Computational time between the penalty contact and lubricated contact model was compared. Using the lubricated contact increases computational time by approximately 40%, which is an acceptable increase considering the complexity of the introduced system. The stability was tested by comparing the average number of displacement correctors between different contact conditions. The maximum increase of number of correctors was 32%, while the average increase across all contact conditions was 10%. Considering the non–linear behaviour of the lubricated contact model the increase of 10% of number of

correctors, compared to penalty contact, is acceptable. Three quarter–symmetric simulations were performed in order to test the applicability of the implemented model on a three– dimensional geometry. The results were compared to axisymmetric cases, and a very good agreement between hydrodynamic pressure profiles was achieved. The largest difference between friction forces was below 1%. A quarter–symmetric case requires, approximately, 15 times more computational time compared to the axisymmetric simulation.

Wire rolling simulations were conducted for two angular velocities (150 and 300 rpm) of the roller using the same contact conditions as in the wire drawing cases. Three mesh densities were examined. High hydrodynamic pressure is dominantly achieved in the area of the roll bite, while there was no significant pressure inside the contact. Both hydrodynamic and asperity contact pressure fields have a characteristic horseshoe shape. The calculated local friction coefficients decrease in the area of high hydrodynamic pressure, which is expected since a larger part of the load in that area is carried by the lubricant. Computational time was compared between different contact conditions, where in the case of the finest mesh the lubricated contact model is slightly faster than the penalty contact. The average increase of computational time across all cases is 33%, which is in accordance with the wire drawing simulations. Regarding stability, the average number of displacement correctors decreases by 4% when using the lubricated contact model. Thus, in the wire rolling cases the lubricated contact model can be considered slightly more stable than the penalty contact.

7. Conclusions and Future Work

With the advancement of computational resources, numerical modelling of metal forming processes is becoming a viable design tool. Existing software packages generally use sophisticated material and contact detection models, but inadequate methods for calculating microscopic contact effects and friction. These methods usually consider simple friction laws like Coulomb's or Tresca's, which are easy to implement but usually give insufficiently accurate results, especially when the contact between two surfaces is lubricated. Thus, a need exists for a numerical method that allows calculation of lubrication effects between contacting surfaces during metal forming simulations.

A numerical framework capable of calculating lubricated contact between two rough surfaces in metal forming simulations was developed. The framework was implemented as a contact boundary condition for the hyperelastoplastic finite volume deformation solver. The main features of the approach are: calculation of film thickness, hydrodynamic pressure and shear stress of the lubricant, estimation of asperity contact pressure and contact area ratio for a realistic rough surface, and calculation of temperature increase due to lubricant shear stress and asperity contact. The framework permits numerical simulations of metal forming processes with lubricated contact to be performed on a desktop PC in a reasonable amount of time.

The lubricant pressure is calculated by solving the Reynolds equation. The Reynolds equation is discretised using the Finite Area Method over a selected contact patch of the finite volume mesh. The cavitational effects are considered in a mass–conserving manner using an approach similar to Elrod–Adams algorithm. The contact between asperities is calculated with a deterministic elastic–perfectly–plastic contact model using a measured surface roughness profile or a three–dimensional surface scan as input. Contact pressures, area ratios and film thicknesses are calculated for a selected range of nominal surface separations, and stored in a form of interpolation tables. Using interpolation tables, instead of direct calculation of asperity contact, during the runtime of metal forming

simulations reduces required computational time. Temperature increase of the lubricant is calculated using a two–dimensional thin film energy equation, discretised with the Finite Area Method. The energy equation assumes a parabolic temperature profile across the film thickness. The models were thoroughly verified and validated against analytical, other numerical and experimental results.

In order to assess the accuracy of the complete numerical framework, extensive verification and validation was performed on point contact test cases, where film thickness and friction coefficients were compared to experimental results of ball–on–disc tribometer tests. The study showed that acceptable accuracy can be achieved using the implemented numerical framework, when the complete information regarding lubricant transport properties is available and surface roughness has been measured.

Finally, the numerical framework is tested on industrial–grade wire drawing and wire rolling simulations. The framework was verified by performing a mesh convergence study of the wire drawing analysis with respect to friction force. When considering wire drawing cases, the lubricated contact model exhibited an acceptable increase of computational time by 40%, compared to the penalty contact model. In wire rolling cases the average increase of computational time was slightly lower, 33%, while for very fine meshes the lubricated contact model marginally reduced the CPU time, compared with the penalty contact. The stability of the framework was assessed by comparing the average number of displacement correctors between the lubricated contact and the penalty contact model. In wire drawing cases the number of correctors increased by 10%, while in wire rolling cases there was a decrease of number of correctors by 4%. This suggests that the lubricated contact model is slightly more stable, compared to the penalty contact, in wire rolling cases.

In future study, the developed framework will be tested on a more complex metal forming cases, using different roller shapes and multiple passes. Testing on complex geometries will determine the limits of applicability, regarding efficiency and stability, of the developed framework. Additional validation will be performed on wire drawing and wire rolling cases, where the numerical results will be compared to experimental measurements of forces, torques and wire deformation. In order to perform a detailed validation of this kind, the complete

information regarding lubricant transport properties will be required. This type of information and measurements are unavailable at the present time. The framework will also be tested on cases with multiple surface contacts, where additional development of the model is expected.

Another goal of the future work is to expand the deterministic contact model to include subsurface stresses and material hardening effects. Additional work will be done to alleviate the assumption of average density and viscosity values across the film thickness and to calculate film temperature profile of arbitrary shape. Also, the contact model will be expanded to consider the evolution of surface roughness due to sliding effects.

Bibliography

[1] Željko Tuković, Metoda kontrolnih volumena na domenama promjenjivog oblika, Ph.D. thesis, Chair of Turbomachinery, Faculty of Mechanical Engineering and Naval Architecture, University of Zagreb (2005).

[2] W. R. D. Wilson, N. Marsault, Partial hydrodynamic lubrication with large fractional contact areas, Journal of Tribology 120 (1) (1998) 16. `doi:10.1115/1.2834180`.

[3] L. Bertocchi, D. Dini, M. Giacopini, M. T. Fowell, A. Baldini, Fluid film lubrication in the presence of cavitation: a mass-conserving two-dimensional formulation for compressible, piezoviscous and non-newtonian fluids, Tribology International 67 (2013) 61–71. `doi:10.1016/j.triboint.2013.05.018`.

[4] Y. Qiu, M. M. Khonsari, On the Prediction of Cavitation in Dimples Using a Mass-Conservative Algorithm, Journal of Tribology 131 (4) (2009) 041702. `doi:10.1115/1.3176994`.

[5] X. Tian, F. E. Kennedy, Maximum and average flash temperatures in sliding contacts, Journal of Tribology 116 (1) (1994) 167. `doi:10.1115/1.2927035`.

[6] J. Guegan, A. Kadiric, H. Spikes, A study of the lubrication of EHL point contact in the presence of longitudinal roughness, Tribology Letters 59 (1). `doi:10.1007/s11249-015-0549-7`.

[7] J. Guegan, Experimental investigation into the influence of roughness on friction and film thickness in ehd contacts, Ph.D. thesis (2015).

[8] V. Škurić, P. De Jaeger, H. Jasak, Lubricated elastoplastic contact model for metal forming processes in OpenFOAM, Computers & Fluids 172 (2018) 226–240. `doi:10.1016/j.compfluid.2018.06.011`.

[9] N. Patir, H. S. Cheng, Application of average flow model to lubrication between rough sliding surfaces, Journal of Lubrication Technology 101 (2) (1979) 220. `doi:10.1115/1.3453329`.

[10] W. Habchi, P. Vergne, S. Bair, O. Andersson, D. Eyheramendy, G. Morales-Espejel, Influence of pressure and temperature dependence of thermal properties of a lubricant on the behaviour of circular TEHD contacts, Tribology International 43 (10) (2010) 1842–1850. `doi:10.1016/j.triboint.2009.10.002`.

[11] S. Bair, Comment on "the relationship between friction and film thickness in EHD point contacts in the presence of longitudinal roughness" by guegan, kadiric, gabelli, & spikes, Tribology Letters 65 (3). `doi:10.1007/s11249-017-0867-z`.

[12] J. Guegan, A. Kadiric, A. Gabelli, H. Spikes, The relationship between friction and film thickness in EHD point contacts in the presence of longitudinal roughness, Tribology Letters 64 (3). `doi:10.1007/s11249-016-0768-6`.

[13] R. Boman, J.-P. Ponthot, Finite element simulation of lubricated contact in rolling using the arbitrary lagrangian–eulerian formulation, Computer Methods in Applied Mechanics and Engineering 193 (39-41) (2004) 4323–4353. `doi:10.1016/j.cma.2004.01.034`.

[14] W. R. D. Wilson, Friction and lubrication in bulk metal-forming processes, Journal of Applied Metalworking 1 (1) (1978) 7–19. `doi:10.1007/bf02833955`.

[15] H. Ou, P. Wang, B. Lu, H. Long, Finite element modelling and optimisation of net-shape metal forming processes with uncertainties, Computers & Structures 90-91 (2012) 13–27. `doi:10.1016/j.compstruc.2011.10.014`.

[16] H. Jasak, H. G. Weller, Application of the finite volume method and unstructured meshes to linear elasticity, International Journal for Numerical Methods in Engineering 48 (2) (2000) 267–287. `doi:10.1002/(sici)1097-0207(20000520)48:2<267::aid-nme884>3.0.co;2-q`.

[17] H. Jasak, H. G. Weller, Finite volume methodology for contact problems of linear elastic solids, in: Third International Conference of Croatian Society Mechanics, Cavtat, Croatia, 2000, pp. 253–260.

[18] Z. Tukovic, H. Jasak, Updated lagrangian finite volume solver for large deformation dynamic response of elastic body, Transactions of FAMENA 31 (1) (2007) 55–70.

[19] A. Karac, A. Ivankovic, Investigating the behaviour of fluid-filled polyethylene containers under base drop impact: A combined experimental/numerical approach, International Journal of Impact Engineering 36 (4) (2009) 621–631. `doi:10.1016/j.ijimpeng.2008.08.007`.

[20] P. Cardiff, A. Karač, A. Ivanković, Development of a finite volume contact solver based on the penalty method, Computational Materials Science 64 (2012) 283–284. `doi:10.1016/j.commatsci.2012.03.011`.

[21] Ž. Tuković, A. Ivanković, A. Karač, Finite-volume stress analysis in multi-material linear elastic body, International Journal for Numerical Methods in Engineering 93 (4) (2012) 400–419. `doi:10.1002/nme.4390`.
URL `https://doi.org/10.1002/nme.4390`

[22] P. Cardiff, Ž. Tuković, P. D. Jaeger, M. Clancy, A. Ivanković, A lagrangian cell-centred finite volume method for metal forming simulation, International Journal for Numerical Methods in Engineering 109 (13) (2016) 1777–1803. `doi:10.1002/nme.5345`.

[23] C. Liu, P. Hartley, C. Sturgess, G. Rowe, Simulation of the cold rolling of strip using an elastic-plastic finite element technique, International Journal of Mechanical Sciences 27 (11-12) (1985) 829–839. `doi:10.1016/0020-7403(85)90014-1`.

[24] Y.-J. Hwu, J. G. Lenard, A finite element study of flat rolling, Journal of Engineering Materials and Technology 110 (1) (1988) 22. `doi:10.1115/1.3226004`.

[25] J. P. Cescutti, E. Wey, J. L. Chenot, Finite element calculation of hot forging with continuous remeshing, in: Modelling of Metal Forming Processes, Springer Netherlands, 1988, pp. 207–216. `doi:10.1007/978-94-009-1411-7_23`.

[26] Y. Hu, W. Liu, Simulation of ring rolling process by arbitrary lagrangian eulerian finite element method, in: B. Singh, Y. Im, I. Haque, C. Altan (Eds.), Computer Modeling and Simulation of Manufacturing Processes, Vol. 20, Publ by ASME, 1990, pp. 225–240.

[27] H. Huetink, P. Vreede, J. van der Lugt, Progress in mixed eulerian-lagrangian finite element simulation of forming processes, International journal for numerical methods in engineering 30 (8) (1990) 1441–1457. `doi:10.1002/nme.1620300808`.

[28] P. Gratacos, P. Montmitonnet, C. Fromholz, J. Chenot, A plane-strain elastoplastic finite-element model for cold rolling of thin strip, International Journal of Mechanical Sciences 34 (3) (1992) 195–210. `doi:10.1016/0020-7403(92)90071-n`.

[29] C.-Y. Sa, W. R. D. Wilson, Full film lubrication of strip rolling, Journal of Tribology 116 (3) (1994) 569. `doi:10.1115/1.2928884`.

[30] Y. Liu, A. Tieu, A thermal mixed film lubrication model in cold rolling, Journal of Materials Processing Technology 130-131 (2002) 202–207. `doi:10.1016/s0924-0136(02)00720-3`.

[31] M. Khan, H. Ruan, L. Zhang, X. Zhao, X. Zhang, A new approach to the investigation of mixed lubrication in metal strip rolling, in: Proc. 7th Australasian Congress on Applied Mechanics, ACAM 7, Adelaide, Australia, 2012, pp. 1013–1021.

[32] C. Wu, L. Zhang, S. Li, Z. Jiang, P. Qu, A novel multi-scale statistical characterization of interface pressure and friction in metal strip rolling, International Journal of Mechanical Sciences 89 (2014) 391–402. `doi:10.1016/j.ijmecsci.2014.10.004`.

[33] C. Wu, L. Zhang, P. Qu, S. Li, Z. Jiang, W. Liu, Characterization of interface stresses and lubrication of rough elastic surfaces under ball-on-disc rolling, Proceedings of the Institution of Mechanical Engineers, Part J: Journal of Engineering Tribology 231 (12) (2017) 1552–1573. `doi:10.1177/1350650117700793`.

[34] H. G. Weller, G. Tabor, H. Jasak, C. Fureby, A tensorial approach to computational continuum mechanics using object-oriented techniques, Computers in Physics 12 (6) (1998) 620. `doi:10.1063/1.168744`.
URL `https://doi.org/10.1063/1.168744`

[35] O. Reynolds, On the theory of lubrication and its application to mr. beauchamp tower's experiments, including an experimental determination of the viscosity of olive oil, Philosophical Transactions of the Royal Society of London 177 (1886) 157–234.

[36] Q. J. Wang, Y. Qian, Encyclopedia of Tribology, Springer, 2013.

[37] D. Gropper, L. Wang, T. J. Harvey, Hydrodynamic lubrication of textured surfaces: A review of modeling techniques and key findings, Tribology International 94 (2016) 509–529. `doi:10.1016/j.triboint.2015.10.009`.

[38] G. Bayada, L. Chupin, Compressible fluid model for hydrodynamic lubrication cavitation, Journal of Tribology 135 (4) (2013) 041702. `doi:10.1115/1.4024298`.

[39] Y. Liu, Q. J. Wang, S. Bair, P. Vergne, A quantitative solution for the full shear-thinning EHL point contact problem including traction, Tribology Letters 28 (2) (2007) 171–181. `doi:10.1007/s11249-007-9262-5`.

[40] X. Liu, M. Jiang, P. Yang, M. Kaneta, Non-newtonian thermal analyses of point EHL contacts using the eyring model, Journal of Tribology 127 (1) (2005) 70. `doi:10.1115/1.1843161`.

[41] H. J. Kim, P. Ehret, D. Dowson, C. M. Taylor, Thermal elastohydrodynamic analysis of circular contacts part 1: Newtonian model, Proceedings of the

Institution of Mechanical Engineers, Part J: Journal of Engineering Tribology 215 (4) (2001) 339–352. `doi:10.1243/1350650011543583`.

[42] H. J. Kim, P. Ehret, D. Dowson, C. M. Taylor, Thermal elastohydrodynamic analysis of circular contacts part 2: Non-newtonian model, Proceedings of the Institution of Mechanical Engineers, Part J: Journal of Engineering Tribology 215 (4) (2001) 353–362. `doi:10.1243/1350650011543592`.

[43] X.-L. Yan, X.-L. Wang, Y.-Y. Zhang, A numerical study of fatigue life in non-newtonian thermal EHL rolling–sliding contacts with spinning, Tribology International 80 (2014) 156–165. `doi:10.1016/j.triboint.2014.07.001`.

[44] X.-L. Yan, Y.-Y. Zhang, G.-X. Xie, X.-Q. Du, F. Qin, Effects of texture orientation on the mixed thermal elastohydrodynamic lubrication and fatigue life in point contacts, Journal of Tribology 141 (1) (2018) 011501. `doi:10.1115/1.4040474`.

[45] F. Sahlin, R. Larsson, A. Almqvist, P. M. Lugt, P. Marklund, A mixed lubrication model incorporating measured surface topography. part 1: Theory of flow factors, Proceedings of the Institution of Mechanical Engineers, Part J: Journal of Engineering Tribology 224 (4) (2009) 335–351. `doi:10.1243/13506501jet658`.

[46] F. Sahlin, R. Larsson, P. Marklund, A. Almqvist, P. M. Lugt, A mixed lubrication model incorporating measured surface topography. part 2: Roughness treatment, model validation, and simulation, Proceedings of the Institution of Mechanical Engineers, Part J: Journal of Engineering Tribology 224 (4) (2009) 353–365. `doi:10.1243/13506501jet659`.

[47] X. Wang, Y. Liu, D. Zhu, Numerical solution of mixed thermal elastohydrodynamic lubrication in point contacts with three-dimensional surface roughness, Journal of Tribology 139 (1) (2016) 011501. `doi:10.1115/1.4032963`.

[48] B. J. Hamrock, S. R. Schmid, B. O. Jacobson, Fundamentals of Fluid Film Lubrication (Dekker Mechanical Engineering), CRC Press, 2004.

[49] H. Jasak, Error analysis and estimation for the finite volume method with applications to fluid flows, Ph.D. thesis, Department of Mechanical Engineering, Imperial College of Science, Technology and Medicine (1996).

[50] I. N. Bronstein, K. A. Semendjajew, G. Musiol, H. Mühlig, Taschenbuch der Mathematik., Deutsch (Harri), 2000.

[51] H. W. Swift, The Stability of Lubricating Films in Journal Bearings, Minutes of the Proceedings of the Institution of Civil Engineers 233 (1932) (1932) 267–288. `doi:10.1680/imotp.1932.13239`.

[52] W. Stieber, Das Schwimmlager: Hydrodynamische Theorie des Gleitlagers, VDI-Verlag, 1933.

[53] B. Jakobsson, L. Floberg, The finite journal bearing considering vaporization, Transactions of Chalmers University of Technology 190 (1957) 1–116, cited By :191.

[54] K. O. Olsson, Cavitation in dynamically loaded bearings, Transactions of Chalmers University of Technology 308.

[55] D. Bonneau, A. Fatu, D. Souchet, Hydrodynamic Bearings, John Wiley & Sons, Inc., Hoboken, NJ, USA, 2014. `doi:10.1002/9781119004769`.

[56] H. Elrod, M. Adams, A Computer Program for Cavitation and Starvation Problems, Cavitation and Related Phenomena in Lubrication 37 (1974) 37–41.

[57] D. Vijayaraghavan, T. G. Keith, An Efficient, Robust, and Time Accurate Numerical Scheme Applied to a Cavitation Algorithm, Journal of Tribology 112 (1) (1990) 44. `doi:10.1115/1.2920229`.

[58] F. Sahlin, A. Almqvist, R. Larsson, S. Glavatskih, A cavitation algorithm for arbitrary lubricant compressibility, Tribology International 40 (8) (2007) 1294–1300. `doi:10.1016/j.triboint.2007.02.009`.

[59] M. Fesanghary, M. M. Khonsari, A Modification of the Switch Function in the Elrod Cavitation Algorithm, Journal of Tribology 133 (2) (2011) 024501. `doi:10.1115/1.4003484`.

[60] M. Giacopini, M. T. Fowell, D. Dini, A. Strozzi, A Mass-Conserving Complementarity Formulation to Study Lubricant Films in the Presence of Cavitation, Journal of Tribology 132 (4) (2010) 041702. `doi:10.1115/1.4002215`.

[61] A. Almqvist, J. Fabricius, R. Larsson, P. Wall, A New Approach for Studying Cavitation in Lubrication, Journal of Tribology 136 (1) (2013) 011706. `doi: 10.1115/1.4025875`.

[62] A. Almqvist, P. Wall, Modelling Cavitation in (Elasto)Hydrodynamic Lubrication, in: Advances in Tribology, Vol. 2, InTech, 2016, p. 64. `doi: 10.5772/63533`.

[63] T. Woloszynski, P. Podsiadlo, G. W. Stachowiak, Efficient Solution to the Cavitation Problem in Hydrodynamic Lubrication, Tribology Letters 58 (1). `doi:10.1007/s11249-015-0487-4`.

[64] R. F. Ausas, M. Jai, G. C. Buscaglia, A Mass-Conserving Algorithm for Dynamical Lubrication Problems With Cavitation, Journal of Tribology 131 (3) (2009) 031702. `doi:10.1115/1.3142903`.

[65] A. Almqvist, On the effects of surface roughness in lubrication, Ph.D. thesis, Department of Applied Physics and Mechanical Engineering, Lulea University of Technology (2006).

[66] H. Christensen, Stochastic models for hydrodynamic lubrication of rough surfaces, Proceedings of the Institution of Mechanical Engineers 184 (1) (1969) 1013–1026. `doi:10.1243/pime_proc_1969_184_074_02`.

[67] N. Patir, H. S. Cheng, An average flow model for determining effects of three-dimensional roughness on partial hydrodynamic lubrication, Journal of Lubrication Technology 100 (1) (1978) 12. `doi:10.1115/1.3453103`.

[68] M. Sutcliffe, Friction and lubrication in metal rolling, Ph.D. thesis, Jesus College, University of Cambridge (1989).

[69] J. A. Greenwood, J. B. P. Williamson, Contact of nominally flat surfaces, Proceedings of the Royal Society of London. Series A. Mathematical and Physical Sciences 295 (1442) (1966) 300–319. `doi:10.1098/rspa.1966.0242`.

[70] R. L. Jackson, I. Green, On the modeling of elastic contact between rough surfaces, Tribology Transactions 54 (2) (2011) 300–314. `doi:10.1080/10402004.2010.542277`.

[71] J. A. Greenwood, J. H. Tripp, The elastic contact of rough spheres, Journal of Applied Mechanics 34 (1) (1967) 153. `doi:10.1115/1.3607616`.

[72] J. A. Greenwood, J. H. Tripp, The contact of two nominally flat rough surfaces, Proceedings of the Institution of Mechanical Engineers 185 (1) (1970) 625–633. `doi:10.1243/pime_proc_1970_185_069_02`.

[73] T. Hisakado, Effect of surface roughness on contact between solid surfaces, Wear 28 (2) (1974) 217–234. `doi:10.1016/0043-1648(74)90163-x`.

[74] J. I. McCool, Predicting microfracture in ceramics via a microcontact model, Journal of Tribology 108 (3) (1986) 380. `doi:10.1115/1.3261209`.

[75] W. R. Chang, I. Etsion, D. B. Bogy, An elastic-plastic model for the contact of rough surfaces, Journal of Tribology 109 (2) (1987) 257. `doi:10.1115/1.3261348`.

[76] I. Green, A transient dynamic analysis of mechanical seals including asperity contact and face deformation, Tribology Transactions 45 (3) (2002) 284–293. `doi:10.1080/10402000208982551`.

[77] R. L. Jackson, I. Green, A finite element study of elasto-plastic hemispherical contact against a rigid flat, Journal of Tribology 127 (2) (2005) 343. `doi:10.1115/1.1866166`.

[78] R. L. Jackson, I. Green, A statistical model of elasto-plastic asperity contact between rough surfaces, Tribology International 39 (9) (2006) 906–914. `doi:10.1016/j.triboint.2005.09.001`.

[79] S. S. Wadwalkar, R. L. Jackson, L. Kogut, A study of the elastic—plastic deformation of heavily deformed spherical contacts, Proceedings of the Institution of Mechanical Engineers, Part J: Journal of Engineering Tribology 224 (10) (2010) 1091–1102. `doi:10.1243/13506501jet763`.

[80] H. Peng, Z. Liu, F. Huang, R. Ma, A study of elastic–plastic contact of statistical rough surfaces, Proceedings of the Institution of Mechanical Engineers, Part J: Journal of Engineering Tribology 227 (10) (2013) 1076–1089. `doi:10.1177/1350650112474399`.

[81] J. I. McCool, Relating profile instrument measurements to the functional performance of rough surfaces, Journal of Tribology 109 (2) (1987) 264. `doi:10.1115/1.3261349`.

[82] V. A. Yastrebov, J. Durand, H. Proudhon, G. Cailletaud, Rough surface contact analysis by means of the finite element method and of a new reduced model, Comptes Rendus Mécanique 339 (7-8) (2011) 473–490. `doi:10.1016/j.crme.2011.05.006`.

[83] H. M. Westergaard, Bearing pressures and cracks, Journal of Applied Mechanics 6 (1939) A49–A53.

[84] K. Johnson, J. Greenwood, J. Higginson, The contact of elastic regular wavy surfaces, International Journal of Mechanical Sciences 27 (6) (1985) 383–396. `doi:10.1016/0020-7403(85)90029-3`.

[85] H. M. Stanley, T. Kato, An FFT-based method for rough surface contact, Journal of Tribology 119 (3) (1997) 481. `doi:10.1115/1.2833523`.

[86] A. Almqvist, F. Sahlin, R. Larsson, S. Glavatskih, On the dry elasto-plastic contact of nominally flat surfaces, Tribology International 40 (4) (2007) 574–579. `doi:10.1016/j.triboint.2005.11.008`.

[87] F. Sahlin, R. Larsson, A. Almqvist, P. M. Lugt, P. Marklund, A mixed lubrication model incorporating measured surface topography. part 1: Theory of flow factors, Proceedings of the Institution of Mechanical Engineers, Part J: Journal of Engineering Tribology 224 (4) (2009) 335–351. `doi:10.1243/13506501jet658`.

[88] W. T. Lai, H. S. Cheng, Temperature analysis in lubricated simple sliding rough contacts, ASLE Transactions 28 (3) (1985) 303–312. `doi:10.1080/05698198508981625`.

[89] H. S. Carslaw, J. C. Jaeger, Conduction of Heat in Solids (Oxford Science Publications), Oxford University Press, 1959.

[90] D. Zhu, Y.-Z. Hu, A computer program package for the prediction of EHL and mixed lubrication characteristics, friction, subsurface stresses and flash temperatures based on measured 3-d surface roughness, Tribology Transactions 44 (3) (2001) 383–390. `doi:10.1080/10402000108982471`.

[91] D. Zhu, H. S. Cheng, An analysis and computational procedure for EHL film thickness, friction and flash temperature in line and point contacts, Tribology Transactions 32 (3) (1989) 364–370. `doi:10.1080/10402008908981901`.

[92] J. Gao, S. C. Lee, X. Ai, H. Nixon, An FFT-based transient flash temperature model for general three-dimensional rough surface contacts, Journal of Tribology 122 (3) (2000) 519. `doi:10.1115/1.555395`.

[93] J. Zhao, F. Sadeghi, M. H. Hoeprich, Analysis of EHL circular contact start up: Part II—surface temperature rise model and results, Journal of Tribology 123 (1) (2001) 75. `doi:10.1115/1.1332395`.

[94] S. Liu, Q. Wang, A three-dimensional thermomechanical model of contact between non-conforming rough surfaces, Journal of Tribology 123 (1) (2001) 17. `doi:10.1115/1.1327585`.

[95] W.-Z. Wang, Y.-Z. Hu, Y. chuan Liu, H. Wang, Deterministic solutions and thermal analysis for mixed lubrication in point contacts, Tribology International 40 (4) (2007) 687–693. `doi:10.1016/j.triboint.2005.11.002`.

[96] N. Deolalikar, F. Sadeghi, S. Marble, Numerical modeling of mixed lubrication and flash temperature in EHL elliptical contacts, Journal of Tribology 130 (1) (2008) 011004. `doi:10.1115/1.2805429`.

[97] H. Salehizadeh, N. Saka, Thermal non-newtonian elastohydrodynamic lubrication of rolling line contacts, Journal of Tribology 113 (3) (1991) 481. `doi:10.1115/1.2920649`.

[98] T. Kazama, P. Ehret, C. M. Taylor, On the effects of the temperature profile approximation in thermal newtonian solutions of elastohydrodynamic

lubrication line contacts, Proceedings of the Institution of Mechanical Engineers, Part J: Journal of Engineering Tribology 215 (1) (2001) 109–120. `doi:10.1243/1350650011541666`.

[99] P. C. Sui, F. Sadeghi, Non-newtonian thermal elastohydrodynamic lubrication, Journal of Tribology 113 (2) (1991) 390. `doi:10.1115/1.2920634`.

[100] R.-T. Lee, C.-H. Hsu, W.-F. Kuo, Multilevel solution for thermal elastohydrodynamic lubrication of rolling/sliding circular contacts, Tribology International 28 (8) (1995) 541–552. `doi:10.1016/0301-679x(96)85542-3`.

[101] P. Ehret, D. Dowson, C. Taylor, Thermal effects in elliptical contacts with spin conditions, in: Tribology Series, Elsevier, 1999, pp. 685–703. `doi:10.1016/s0167-8922(99)80088-1`.

[102] K.-H. Kim, F. Sadeghi, Three-dimensional temperature distribution in EHD lubrication: Part II—point contact and numerical formulation, Journal of Tribology 115 (1) (1993) 36. `doi:10.1115/1.2920984`.

[103] A. A. Tseng, Thermal modeling of roll and strip interface in rolling processes: Part 1–review, Numerical Heat Transfer, Part A: Applications 35 (2) (1999) 115–133. `doi:10.1080/104077899275281`.

[104] A. A. Tseng, Thermal modeling of roll and strip interface in rolling processes: Part 2–simulation, Numerical Heat Transfer, Part A: Applications 35 (2) (1999) 135–154. `doi:10.1080/104077899275290`.

[105] M. Hartinger, Cfd modelling of elastohydrodynamic lubrication, Ph.D. thesis, Imperial College London, United Kingdom (2007).

[106] A. Hajishafiee, Finite-volume cfd modelling of fluid-solid interaction in ehl contacts, Ph.D. thesis, Imperial College London, United Kingdom (2013).

[107] W. Habchi, A full-system finite element approach to elastohydrodynamic lubrication problems : Application to ultra-low-viscosity fluids, Ph.D. thesis, Laboratoire de Mecanique des Contacts et des Structures, INSA, Lyon, France (2008).

[108] R. Gohar, Elastohydrodynamics, Imperial College Press, 2002.

[109] C. Roelands, Correlational aspects of the viscosity-temperature-pressure relationship of lubricating oils, Ph.D. thesis, Delft University of Technology, Netherlands (1966).

[110] L. Houpert, New results of traction force calculations in elastohydrodynamic contacts, Journal of Tribology 107 (2) (1985) 241. `doi:10.1115/1.3261033`.

[111] S. Bair, A note on the use of roelands equation to describe viscosity for EHD hertzian zone calculations, Journal of Tribology 115 (2) (1993) 333. `doi:10.1115/1.2921011`.

[112] S. Bair, The variation of viscosity with temperature and pressure for various real lubricants, Journal of Tribology 123 (2) (2001) 433. `doi:10.1115/1.1308024`.

[113] A. K. Doolittle, Studies in newtonian flow. II. the dependence of the viscosity of liquids on free-space, Journal of Applied Physics 22 (12) (1951) 1471–1475. `doi:10.1063/1.1699894`.

[114] K. L. Johnson, J. L. Tevaarwerk, Shear behaviour of elastohydrodynamic oil films, Proceedings of the Royal Society A: Mathematical, Physical and Engineering Sciences 356 (1685) (1977) 215–236. `doi:10.1098/rspa.1977.0129`.

[115] K. Sharif, S. Morris, H. Evans, R. Snidle, Comparison of non-newtonian EHL models in high sliding applications, in: Tribology Series, Elsevier, 2001, pp. 787–796. `doi:10.1016/s0167-8922(01)80159-0`.

[116] P. J. Carreau, Rheological equations from molecular network theories, Transactions of the Society of Rheology 16 (1) (1972) 99–127. `doi:10.1122/1.549276`.

[117] S. Bair, P. Vergne, M. Querry, A unified shear-thinning treatment of both film thickness and traction in EHD, Tribology Letters 18 (2) (2005) 145–152. `doi:10.1007/s11249-004-1770-y`.

[118] S. Bair, M. Khonsari, An EHD inlet zone analysis incorporating the second newtonian, Journal of Tribology 118 (2) (1996) 341. `doi:10.1115/1.2831306`.

[119] S. Bair, A rough shear-thinning correction for EHD film thickness, Tribology Transactions 47 (3) (2004) 361–365. `doi:10.1080/05698190490455519`.

[120] D. Dowson, G. R. Higginson, Elasto-Hydrodynamic Lubrication: International Series on Materials Science and Technology, Pergamon, 2014.

[121] R. Tuomas, O. Isaksson, Compressibility of oil/refrigerant lubricants in elasto-hydrodynamic contacts, Journal of Tribology 128 (1) (2006) 218. `doi:10.1115/1.2125967`.

[122] B. O. Jacobson, P. Vinet, A model for the influence of pressure on the bulk modulus and the influence of temperature on the solidification pressure for liquid lubricants, Journal of Tribology 109 (4) (1987) 709. `doi:10.1115/1.3261542`.

[123] J. R. Macdonald, Some simple isothermal equations of state, Reviews of Modern Physics 38 (4) (1966) 669–679. `doi:10.1103/revmodphys.38.669`.

[124] D. Zhu, On the thermo–elastohydrodynamic problem in elliptical contacts, Ph.D. thesis, Tsinghua University, PR China (1984).

[125] P. Yang, On the transient thermal elastohydrodynamic lubrication, Ph.D. thesis, Tsinghua University, PR China (1989).

[126] P. Wong, R. Wang, S. Lingard, Pressure and temperature dependence of the density of liquid lubricants, Wear 201 (1-2) (1996) 58–63. `doi:10.1016/s0043-1648(96)06980-3`.

[127] Ž. Tuković, H. Jasak, Simulation of free-rising bubble with soluble surfactant using moving mesh finite volume/area method, in: 6th International Conference on CFD in Oil & Gas, Metallurgical and Process Industries, SINTEF/NTNU, Trondheim, Norway, 2008.

[128] Ž. Tuković, H. Jasak, Simulation of thin liquid film flow using openfoam finite area method, in: 4th OpenFOAM Workshop, Montreal, Canada, 2009.

[129] Ž. Tuković, H. Jasak, A moving mesh finite volume interface tracking method for surface tension dominated interfacial fluid flow, Computers & Fluids 55 (2012) 70–84. `doi:10.1016/j.compfluid.2011.11.003`.

[130] P. Cardiff, Ž. Tuković, H. Jasak, A. Ivanković, A block-coupled finite volume methodology for linear elasticity and unstructured meshes, Computers & Structures 175 (2016) 100–122. `doi:10.1016/j.compstruc.2016.07.004`.

[131] M. Rauter, Ž. Tuković, A finite area scheme for shallow granular flows on three-dimensional surfaces, Computers & Fluids 166 (2018) 184–199. `doi:10.1016/j.compfluid.2018.02.017`.

[132] H. Jasak, OpenFOAM: Open source CFD in research and industry, International Journal of Naval Architecture and Ocean Engineering 1 (2) (2009) 89–94. `doi:10.2478/ijnaoe-2013-0011`.

[133] J. Peklenik, Paper 24: New developments in surface characterization and measurements by means of random process analysis, Proceedings of the Institution of Mechanical Engineers, Conference Proceedings 182 (11) (1967) 108–126. `doi:10.1243/pime_conf_1967_182_309_02`.

[134] M. N. Nounou, B. R. Bakshi, Multiscale methods for denoising and compression, in: Data Handling in Science and Technology, Elsevier, 2000, pp. 119–150. `doi:10.1016/s0922-3487(00)80030-1`.

[135] B. Bhushan, Modern Tribology Handbook, Two Volume Set (Mechanics & Materials Science), CRC Press, 2000.

[136] MATLAB Curve Fitting Toolbox, The MathWorks Inc., Natick, Massachusetts, 2018.

[137] S. Bair, C. Mary, N. Bouscharain, P. Vergne, An improved yasutomi correlation for viscosity at high pressure, Proceedings of the Institution of Mechanical Engineers, Part J: Journal of Engineering Tribology 227 (9) (2013) 1056–1060. `doi:10.1177/1350650112474394`.

[138] P. Ehret, D. Dowson, C. M. Taylor, On lubricant transport conditions in elastohydrodynamic conjuctions, Proceedings of the Royal Society of London. Series A: Mathematical, Physical and Engineering Sciences 454 (1971) (1998) 763–787. `doi:10.1098/rspa.1998.0185`.

[139] J. A. Greenwood, Two-dimensional flow of a non-newtonian lubricant, Proceedings of the Institution of Mechanical Engineers, Part J: Journal of Engineering Tribology 214 (1) (2000) 29–41. `doi:10.1243/1350650001542990`.

[140] P. Yang, S. Wen, The behavior of non-newtonian thermal EHL film in line contacts at dynamic loads, Journal of Tribology 114 (1) (1992) 81. `doi:10.1115/1.2920872`.

[141] J. Bos, Frictional heating of tribological contacts, Ph.D. thesis, University of Twente, Netherlands (11 1995).

[142] S. Liu, Q. Wang, G. Liu, A versatile method of discrete convolution and FFT (DC-FFT) for contact analyses, Wear 243 (1-2) (2000) 101–111. `doi:10.1016/s0043-1648(00)00427-0`.

[143] P. Wriggers, Computational Contact Mechanics, Springer Berlin Heidelberg, 2006. `doi:10.1007/978-3-540-32609-0`.

[144] A. A. Tseng, A numerical heat transfer analysis of strip rolling, Journal of Heat Transfer 106 (3) (1984) 512. `doi:10.1115/1.3246708`.

[145] S. Wang, A. Tseng, Macro- and micro-modelling of hot rolling of steel coupled by a micro-constitutive relationship, Materials & Design 16 (6) (1995) 315–336. `doi:10.1016/0261-3069(96)00005-2`.

[146] H. Fenech, W. M. Rohsenow, Prediction of thermal conductance of metallic surfaces in contact, Journal of Heat Transfer 85 (1) (1963) 15. `doi:10.1115/1.3686003`.

[147] GNU Scientific Library Reference Manual - 2nd Edition, Network Theory Ltd., 2006.

[148] A. E. H. Love, A Treatise on the Mathematical Theory of Elasticity (Dover Books on Engineering), Dover Publications, 2011.

[149] W. W. Chen, S. Liu, Q. J. Wang, Fast fourier transform based numerical methods for elasto-plastic contacts of nominally flat surfaces, Journal of Applied Mechanics 75 (1) (2008) 011022. `doi:10.1115/1.2755158`.

[150] V. A. Yastrebov, G. Anciaux, J.-F. Molinari, The contact of elastic regular wavy surfaces revisited, Tribology Letters 56 (1) (2014) 171–183. `doi:10.1007/s11249-014-0395-z`.

[151] MATLAB, version 9.5.0 (R2018b), The MathWorks Inc., Natick, Massachusetts, 2018.

[152] R. W. Ogden, Non-Linear Elastic Deformations (Dover Civil and Mechanical Engineering), Dover Publications, 1997.

[153] Random Surface Generator, version 1.0.1, MySimLabs, Östersund, Sweden, 2012.

[154] R. S. Dwyer-Joyce, B. W. Drinkwater, C. J. Donohoe, The measurement of lubricant–film thickness using ultrasound, Proceedings of the Royal Society of London. Series A: Mathematical, Physical and Engineering Sciences 459 (2032) (2003) 957–976. `doi:10.1098/rspa.2002.1018`.

[155] W. ten Napel, P. Klein Meuleman, T. Lubrecht, R. Bosma, L. Houpert, Traction in elastohydrodynamic lubrication at very high contact pressures., In: Eurotrib 85, 4th European Tribology Congress, (Ecully, France: Sep. 9-12, 1985) (1985) ISBN 0–444.

[156] ReFRESCO:A community based open-usage and open-source CFD code for the Maritime World., `http://www.refresco.org/verification-validation/utilitiesvv-tools/` (2018).

[157] L. Eça, M. Hoekstra, A procedure for the estimation of the numerical uncertainty of CFD calculations based on grid refinement studies, J. Comput. Phys. 262 (2014) 104–130. `doi:10.1016/j.jcp.2014.01.006`.

[158] H. Jasak, M. Beaudoin, OpenFOAM turbo tools: From general purpose CFD to turbomachinery simulations, in: ASME-JSME-KSME 2011 Joint Fluids Engineering Conference: Volume 1, Symposia – Parts A, B, C, and D, ASME, 2011. `doi:10.1115/ajk2011-05015`.

Abbreviations

SRR Slide–to–Roll Ratio. vii, viii, 143, 144, 147, 150, 153–157

WJ Wadwalkar–Jackson. 78, 79, 83, 129

WJ–D Wadwalkar–Jackson Deformable. 127

WJ–R Wadwalkar–Jackson Rigid. 127

Curriculum Vitae

Vanja Škurić, born in Kutina on April 16$^{\text{th}}$ 1990, finished high school in 2009. He started his undergraduate studies the same year at the Faculty of Mechanical Engineering and Naval Architecture in Zagreb. During his five years at the Faculty, he focused his studies towards the fields of turbomachinery and Computational Fluid Dynamics (CFD). He graduated with highest honours in 2014. He started working as a research assistant the same year, when he also began his doctoral studies. Most of his scientific CFD work has been done in the fields of lubrication, solid mechanics, multiphase flows and optimisation. He published two journal papers and presented his work at seven international conferences.

Declaration

Parts of the work presented in this thesis have been published in articles listed below.

Selected Publications

[1] V. Škurić, P. De Jaeger, H. Jasak, Model kontakta s efektima podmazi-vanja za simulacije postupka hladnog valjanja, in: P. Marović, M. Galić, L. K. Opara (Eds.), Zbornik radova Sedmog susret Hrvatskoga društva za mehaniku, Hrvatsko društvo za mehaniku, 2016, pp. 181–186.

[2] V. Škurić, P. De Jaeger, H. Jasak, Lubricated contact model for metal forming processes in OpenFOAM, in: G. Zavarise, P. Wriggers (Eds.), 5th International Conference on Computational Contact Mechanics, Universita del Salento, 2017.

[3] V. Škurić, P. De Jaeger, H. Jasak, Lubricated elastoplastic contact model for metal forming processes in OpenFOAM, Computers & Fluids 172 (2018) 226–240. `doi:10.1016/j.compfluid.2018.06.011`.

[4] V. Škurić, P. De Jaeger, H. Jasak, Lubricated contact model for cold metal rolling processes, in: J. Nobrega, H. Jasak (Eds.), OpenFOAM®: Selected Papers of the 11th Workshop, Springer, 2019, pp. 309–323.

[5] V. Škurić, H. Jasak, A. Almqvist, P. De Jaeger, Finite area algorithm for thin film cavitation in OpenFOAM, in: C. Angelov (Ed.), Proceedings from Conference for Young Researchers – Technical Sciences and Industrial Management 2019, Scientific and Technical Union of Mechanical Engineering, Bulgaria, 2019, pp. 7–11.